THESIS FOR THE DEGREE OF DOCTOR OF PHILOSOPHY

Exploration of Graphene-like 2D Materials for Energy Management and Interface Enhancement Applications

Ya Liu

Department of Microtechnology and Nanoscience

CHALMERS UNIVERSITY OF TECHNOLOGY

Gothenburg, Sweden, 2021

学校代码：10246

学　　号：17110440032

博 士 学 位 论 文

（学术学位）

石墨烯类二维材料在能源管理和界面增强领域的应用

Exploration of Graphene-like 2D Materials for
Energy Management and Interface Enhancement Applications

院　　系：　高分子科学系

专　　业：　高分子化学与物理

姓　　名：　刘亚

指 导 教 师：　刘建影 教授　（查尔姆斯理工大学）

卢红斌 教授　（复旦大学）

符益凤 副教授（查尔姆斯理工大学）

完 成 日 期：　2021 年 04 月 01 日

Exploration of Graphene-like 2D Materials for Energy Management and Interface Enhancement Applications

Ya Liu

ISBN 978-91-7905-512-7

Chalmers University of Technology

Department of Microtechnology and Nanoscience - MC2

Electronic Materials and Systems Laboratory

SE–412 96 Göteborg, Sweden

Telephone + 46 (0) 70 – 473 9605

Doktorsavhandlingar vid Chalmers tekniska högskola

ISSN 0346-718X

Ny serie nr 4979

Cover image:

The explored applications of graphene-like 2D materials in this thesis.

The man who removes a mountain begins by carrying away small stones.

千里之行始于足下

Abstract

Ever since the discovery of graphene in 2004, graphene-like 2D materials and their derivatives have attracted extensive investigations because of their exceptional physical and chemical properties. At present, the study of graphene-like 2D materials is at a stage where most of their outstanding physical and chemical properties have been discovered, but the technology for incorporating them into practical commercial products is rarely revealed. For the potential practical industrial applications of graphene-like 2D materials, energy management and interface enhancement are two of the most promising areas. So far, the behavior of the commercialized graphene-like 2D material products is far from their theoretical performance and expectations as a result of defects and π-π agglomeration, etc. In this regard, there is plenty of research room at the bottom for exploring their practical industrial applications.

At present, surface modification is the most widely used strategy to cope with agglomerations. While to be widespread in market, developing low-cost, uniform, and high-quality preparation technology, and encountering the intrinsic agglomeration issues of graphene-like 2D materials are two of the main challenges. To focus on the above two issues, we developed the functionalization method for graphene-like 2D materials, including graphene and hexagonal boron nitride, and explored their potential industrial applications in energy management and interface enhancement. Further, mass production technology and industrial demonstration for graphene and hexagonal boron nitride were explored in some chapters. The main scientific conclusions and innovations of this thesis are listed as below:

At first, Chapter 2 presents the experimental research study on using graphene-like 2D materials for energy management, especially in heat dissipation. With the rapid development of microelectronics and 5G communications, efficient heat dissipation is severely demanded for future electronics. To improve heat dissipation efficiency of electronics, based on the ultrahigh thermal conductivity of graphene-like 2D materials, this chapter explored two experimental works, including lightweight and high-performance graphene enhanced heat pipe and hexagonal boron nitride enhanced thermally conductive and electrically insulation heat spreader.

(1) *Graphene Enhanced Heat Pipe*

In this work, a unique lightweight and high thermal performance graphene heat pipe were firstly designed and developed. At first, the inner structures of graphene enhanced heat pipe were optimized, including the wicker structures, the filling volume of working fluids and the preparation of high thermal conductivity graphene film. Compared to the conventional copper-based heat pipe, our graphene enhanced heat pipe improves the specific cooling capacity more than 3 times. Further, COMSOL Multiphysics was used to establish the cooling model for graphene enhanced heat pipe. And the equation for quantifying the contribution factor from container and phase change was established. Finally, a graphene/copper composite heat pipe was studied to further improve reliability and mechanical strength.

(2) *Hexagonal Boron Nitride Enhanced Heat Spreader*

In this work, a hexagonal boron nitride based heat spreader was prepared by electrospinning with polyvinylpyrrolidone. After electrospun, the hexagonal boron nitride nanosheets are aligned along the fiber, and thus increasing the thermal conductivity. At first, the exfoliation technology was investigated. The result shows that a mixture of water and isopropanol (V_{water}:V_{IPA}=1:3) shows the highest exfoliation efficiency. With the optimized hexagonal boron nitride particle geometry and loading, the in-plane thermal conductivity of hexagonal boron nitride based heat spreader reaches 22 W m^{-1} K^{-1}, this value is comparable to most of the reported work. Particularly, such electrospinning process is constant and scalable, showing high potential for mass-production.

Chapter 3 still focuses on the application of utilizing graphene-like 2D materials for energy management but specifically in energy storage. Based on the ultrahigh electric mobility, large surface area, flexible, lightweight properties, graphene is an attractive option for energy storage. Therefore, graphene was investigated for electrical double layer capacitors and in-plane micro-supercapacitors in this chapter.

(1) *Graphene Enhanced Electric Double-layer Capacitor*

In this work, a scalable soft template strategy was developed to prepare graphene foam with high electrochemical performance as electrode for supercapacitors. The specific surface areas and wettability of graphene foam is tailored by doping. Further, density functional theory simulation reveals why increasing the polarity of graphene largely

improves its wettability. Afterwards, the unique porous structure, low ohm resistance, and high electrical conductivity largely improve the electrochemical performance of graphene foam electrodes and thus achieve ultrahigh specific capacity (550 F g^{-1}), cycling stability (96.1% capacity retention after 10 000 cycles at a high current density of 10 A g^{-1}), and outstanding rate capability (308 F g^{-1} at 100 A g^{-1}).

(2) *Graphene Based In-plane Micro-supercapacitor*

In this work, graphene assembled film was used to replace the conventional silicon wafer for fabricating flexible and high thermal performance micro-supercapacitors. The result shows that such replacement decreases the surface temperature of micro-supercapacitors by 4 °C, and the graphene based micro-supercapacitor present a similar electrochemical behavior with the referenced silicon based micro-supercapacitor. In addition, the graphene assembled film substrate can work as heat spreader for micro-supercapacitor, thus saving spaces and optimizing the following packaging procedures. This work paves the way for utilizing graphene assembled film in semiconductors.

Chapter 4 presents the application of using functional graphene-like 2D materials for interface enhancements due to their high Young's module, large surface area, anti-friction, etc. Graphene-like 2D materials enhanced composites and bio-application are two of the main categories for the commercialization of interface enhancement. However, the graphene-like 2D materials suffer from π-π agglomeration, which leads to poor dispersibility in solvents and matrix. As a result, graphene-like 2D materials enhanced composites exhibit lower property than their theoretical expectations. At present, surface functionalization is the most effective strategy to encounter the π-π agglomeration. Therefore, this chapter explored the application of using functional graphene-like 2D materials in composites, including graphene enhanced water-borne epoxy coatings and hexagonal boron nitride enhanced cement repair materials.

(1) *Graphene Enhanced Water-borne Epoxy Coating*

Graphene was used to lower the coefficient of friction and extend the lifetime of the water-borne epoxy coating in this work. To improve the dispersibility and the compatibility with epoxy, p-hydroxybenzene diazonium salt was prepared to functional graphene. With the optimized geometry and loading, 30 times less coefficient of friction than graphene-free coatings were achieved. And the wear-out time is more than 2 times longer than the three commercial graphene oxide enhanced coatings. This result is

confirmed by Applied Nanosurface AB, Sweden. Besides, mass production technology up to 300 g per batch was developed for the functional graphene. The geometry of graphene was optimized, and the result shows that with the same functional groups, the larger graphene sheets show higher tribological performance than their smaller encounters. Finally, this functionalization strategy was further developed to improve the dispersibility of carbon nanotubes too.

(2) *Hexagonal Boron Nitride Enhanced Cement Repair Material*

This work explored the application of using hexagonal boron nitride to enhance cement repair materials. To improve the dispersibility in cement repair materials and the adhesion with substrates, hexagonal boron nitride was functionalized by carboxymethyl cellulose. After functionalization, the surface zeta potential of hexagonal boron nitride decrease from -5.61 mV to -55.07 mV, and thus largely improves its dispersibility. Results show the incorporation of hexagonal boron nitride improve mechanical strength of cement repair materials by contributing to forming alite. Besides, for the repair material containing h-BN, most of the failure happened at the interface repair material/concrete, while the failure is mainly happening in the concrete for the sample containing FBN. Cooperated with a local cement company (Lanark AB), this work has demonstrated the commercial application as repair materials for walls.

Besides, we studied the functional graphene quantum dots for mRNA based drug delivery platform. After complexed with mRNA, the transfection efficiency of the graphene quantum dots based drug delivery platform is 25% with a formation concentration as 4000 ng mL^{-1}. A comparable transfection efficiency could be achieved at much lower doses if the ratio between the carrier and the cargo is optimized. This graphene quantum dots based drug delivery platform exhibits excellent processability. This work describes a potentially strategy for prepare stable and effective mRNA delivery systems.

Keywords: Graphene-like 2D materials, Energy Management, Interface Enhancement, Industrial Application

Category Number: O631

List of Publications

Appended Papers

This thesis is based on the following appended papers and manuscript:

[1] **Ya Liu**, Xiaoli Zhao, Cancan Wang, Long Zhang, Mengxiong Li, Yunmei Pan, Yifeng Fu, Johan Liu*, Hongbin Lu*. Egg albumen templated graphene foams for high-performance supercapacitor electrodes and electrochemical sensors. *Journal of Materials Chemistry A*, 2018, 6(37): 18267-18275.

[2] **Ya Liu**, Shujing Chen, Yifeng Fu, Davide Mencarelli, Luca Pierantoni, Hongbin Lu*, Johan Liu*. A lightweight and high thermal performance graphene heat pipe. *NanoSelect*, 2020, 2: 1-9.

[3] **Ya Liu**, Chao Xia, Abdelhafid Zehri, Lilei Ye, Nan Wang, Boris Zhmud, Hongbin Lu*, Johan Liu*. Surface Modification of Graphene for Use as a Structural Fortifier in Water-Borne Epoxy Coatings. *Coatings*, 2019, 9(11): 754.

[4] **Ya Liu**, Changhong Zhao, Alan Sabrish, Lilei Ye, Xiaoqiu Wu, Hongbin Lu*, Johan Liu*. A novel graphene quantum dot-based mRNA delivery platform. Chemistry Open, 2021, 10: 1-7.

[5] **Ya Liu**, Nan Wang, Lilei Ye, Abdelhafid Zehri, Andereas Nylander, Amos Nkansah, Hongbin Lu*, Johan Liu*. Thermally Conductive and Electrically Insulating PVP/Boron Nitride Composite Films for Heat Spreader. *IMAPS Nordic Conference on Microelectronics Packaging (NordPac)*, 2019.

[6] **Ya Liu**, Nan Wang, Lilei Ye, Hongbin Lu*, Johan Liu*. Effect of Boron Nitride Particle Geometry on the Thermal Conductivity of a Boron Nitride Enhanced Polymer Composite Film. *The 25th edition of the International Workshop on Thermal Investigation of ICs and Systems (Therminic)*, 2019.

Other Contributions:

[1] **Ya Liu**, Thiringer Torbjörn, Nan Wang, Yifeng Fu, Hongbin Lu*, Johan Liu*. Graphene Based Thermal Management System for Electric Vehicle Battery Cooling. *8th Electronics System-Integration Technology Conference (ESTC)*, 2020.

[2] Yifeng Fu, Josef Hansson, **Ya Liu**, Shujing Chen, Abdelhafid Zehri, Majid Kabiri Samani, Nan Wang, Yuxiang Ni, Yan Zhang, Zhibin Zhang, and Qianlong Wang, Mengxiong Li, Hongbin Lu, Marianna Sledzinska, Torres Sotomayor, Sebastian Volz, Alexander Balandin, Xiangfan Xu, Johan Liu. Graphene Related Materials for Thermal Management. *2D Materials*, 2019, 7(1): 012001.

[3] Changhong Zhao, Xuebin Song, **Ya Liu**, Yifeng Fu, Lilei Ye, Nan Wang, Fan Wang, Lu Li, Mohsen Mohammadniaei, Min Zhang, Qiqing Zhang*, Johan Liu*. Synthesis of Graphene Quantum Dots and Their Applications in Drug Delivery. *Journal of Nanobiotechnology*. 2020, 18: 142.

[4] Mengxiong Li, Jiangwei Liu, Shaoxue Pan, Jiajia Zhang, **Ya Liu**, Johan Liu, Hongbin Lu*. Highly Oriented Graphite Aerogel Fabricated by Confined Liquid-phase Expansion for Anisotropically Thermally Conductive Epoxy Composites. *ACS Applied Materials & Interfaces*, 2020, 12(24): 27476-27484.

[5] Nan Wang, **Ya Liu**, Shujing Chen, Lilei Ye, Johan Liu*. Highly Thermal Conductive and Electrically Insulated Graphene Based Thermal Interface Material with Long-Term Reliability. *IEEE 69th Electronic Components and Technology Conference (ECTC)*. 2019.

CONTENTS

CHAPTER 1

Introduction

1.1 Background

2D materials have become one of the most significant discoveries in the past decades because of the thriving development of nanoscience and nanotechnology. Theoretically, 2D materials are the thinnest materials consisting of only one single layer of atoms. While the lateral size of 2D material can larger than few micros[1]. Graphene is the most well-known 2D materials, composed of a freestanding single atomic layer of graphite atoms, and these graphite atoms are aligned in hexagonal structures within the 2D plane. Generally, graphene was discovered by Geim and his co-works at Manchester University in 2004, through the so-called scotch tape method[1]. Since then, this revolutionary discovery has added a new dimension of research in materials science, biotechnology, and physics, etc.[1-5] Inspired by the remarkable properties of graphene, a dozen of other 2D materials are isolated from their bulk encounters in the past 10 years, including hexagonal boron nitride (h-BN)[6], MXene[7], covalent-organic frameworks (COFs)[8], metal-organic frame works (MOFs)[9], black phosphorene (b-P)[10], transition metal dichalcogenides (TMDCs)[11], graphitic carbon nitride (g-C_3N_v)[12], black arsenic phosphorene (b-AsP)[13], layered double hydroxides (LDHs)[14], etc.[15] Further, the unique single-layer feature endows 2D materials unprecedented physical, electronic, and chemical properties[24, 25], such as the extraordinary Young's modulus, high thermal conductivity, ultrahigh ratio of lateral size, etc.[15, 26] Thus, enormous exploration has been paid to develop high efficiency preparations and explore revolutionary applications for 2D materials. To name a few, both graphene and hexagonal boron nitride have been extensively investigated as conductive fillers for heat dissipations in electronics[27]. Graphene has shown significant advantages to improve the specific capacity for Lithium-ion batteries and supercapacitors[15]. The COFs and MOFs have been reported as promising candidates for carbon dioxide absorptions and hydrogen storages. Graphene reinforcing polymers, such as epoxy, polyurethane (PU), etc., have attracted constant attention from vendors and downstream companies, such as Applied Co., Ltd., Dassi bikes Ltd., etc.[28]

At present, some of the graphene-like 2D materials based applications are close to production levels, including graphene enhanced helmet, biosensor, transistor array, etc. To implement the exceptional properties of graphene-like 2D materials, many high-tech companies are attempting to commercialize these revolutionary materials. In addition, large consortiums, such as the Graphene Flagship in Europe, have been launched to provide long-term fund ing for supporting the widely spread of graphene-like 2D materials on markets[16]. Nowadays, the study of graphene-like 2D materials is at a stage where most of their remarkable properties have been discovered, but the technology for bridging the academic concept to the practical industrial application is rarely revealed[17]. In practice, the behavior of graphene-like 2D materials is far from reaching their theoretical values. Ideally, graphene-like 2D material is a plane of atoms bonded by pure sp^2 hybridized forces. However, realistically, graphene-like 2D materials severely differ from this concept and vary in thickness, structural defects, and geometry. This may be because the inconsistent production approaches and the lack of corresponding uniform industrial standards. These deviations significantly change the structural, chemical, and electronic properties of graphene-like 2D materials. As a result, the graphene-like 2D materials products usually present properties far below the expectation where their intrinsic properties are critically demanded. Take graphene for example, its mechanical, thermal and electrical performances are severely reduced when increasing structural defe cts or the thickness[18-23]. For instance, the Young's modulus of the pristine graphene reaches 1 TPa, while the Young's modulus of graphene oxides or reduced graphene oxides usually decrease to 250 GPa[23]. Practically, graphene enhanced composites usually exhibit tensile strengthless less than 150 Mpa[23, 24].

To widespread on the market, new revolutionary solutions should either create new market opportunities or present significant performance improvement. For graphene-like 2D materials, a moderate enhancement in performance is not enough to replace the heavily invested and well-established conventional technology within the industry. In this regard, this thesis explored new applications for graphene-like 2D materials. Meantime, functionalization was used to encounter the intrinsic π-π agglomeration for largely improving the behaviors of graphene-like 2D materials based products, thus verifying their practical industrial applications. Based on the experimentally result, in some chapters, mass production technology and industrial demonstration were developed for functional graphene and hexagonal boron nitride.

1.2 Graphene-like 2D Materials

Figure 1-1 (a) presents the chemical structures of the typical 2D materials, including graphene, hexagonal boron nitride (h-BN)[6], MXene[7], covalent-organic frameworks (COFs)[8], metal-organic frameworks (MOFs)[9], black phosphorene (b-P)[10], transition metal dichalcogenides (TMDCs)[11], and layered double hydroxides (LDHs)[14, 15]. In particular, graphene-like 2D materials contains graphene, h-BN, and their derives. Typically, in graphene-like 2D materials, the single-layer atoms form hexagonal crystals in a honeycomb configuration by sp^2 hybridized forces within the 2D plane[15]. As shown in Figure 1-1 (b), the bond length between C-C is 0.141 nm, and atomic force microscope measurement (AFM) verifies the thickness of single-layer graphene is 0.335 nm, exactly the thickness of one layer of carbon atom[30].

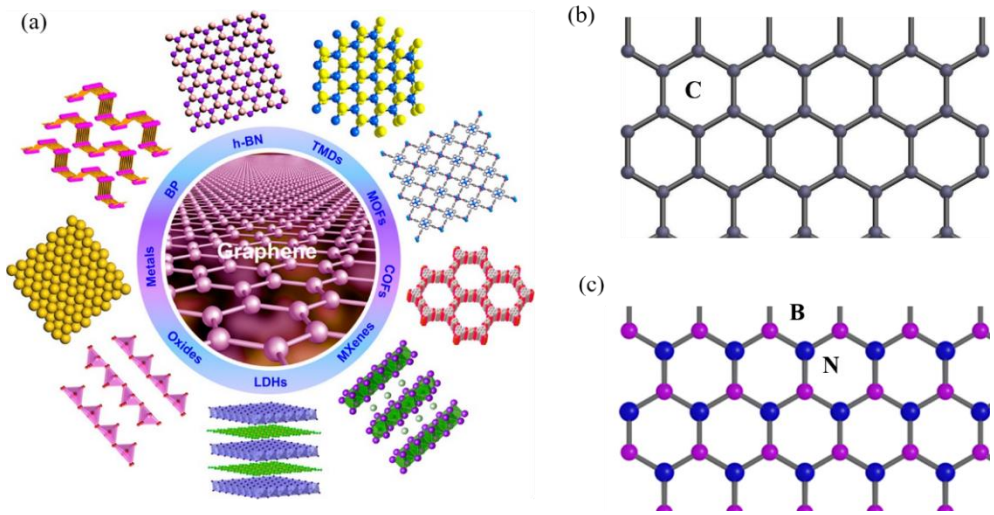

Figure 1-1. (a) Schematic illustration of typical 2D materials. (b) The schematic crystal lattice of graphene. (c) The schematic crystal lattice of hexagonal boron nitride[29]. (Reproduced with the permission from the American Chemical Society).

Because of the unique 2D atom alignment, graphene exhibits distinguished properties in friction, strength, electrical, thermal, optical, etc. For instance, the breaking and tensile strength of graphene reach 60 GPa and 125 GPa, which is 200 times stronger than the stainless steel[31]. The elastic modulus of graphene is as high as 1.1 Tpa[32]. Further, graphene shows a thermal conductivity up to 5000 W m^{-1} K^{-1} under room temperature, and exhibits zero bandgap property with a linear dispersion relationship near the Dirac point[1]. The carrier mobility of graphene goes up to 2×10^5 cm^2 V^{-1} S^{-1}. Theoretically, the specific surface area of graphene reaches 2630 m^2 g^{-1}. Unsurprisingly, these

distinctive properties of graphene have attracted extensive interest in energy storage, heat dissipation, interface enhancement, drug delivery, etc.[33-35]

Recently, the study of graphene focuses on either commercialization or exploring its new physical and chemical properties at the atomic level. In the last decade, the graphene industry has witnessed a boom in both preparations and applications, see Figure 1-2. The production of graphene has increased more than 100 times in the past 10 years[35], and a wide range of graphene products is commercially available in the market, involving graphene powder, graphene oxide dispersion, graphene film, graphene assembled film, etc.[36]

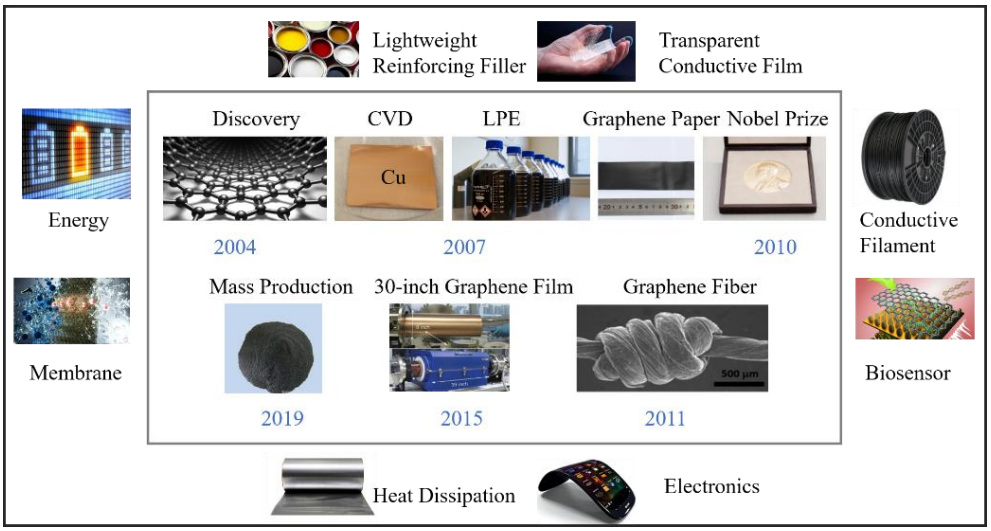

Figure 1-2. A timeline of landmarks for graphene-like 2D materials investigation and commercialization[36]. (Reproduced with the permission from the Spring Nature Ltd. and the American Chemical Society.)

However, there are only limited graphene-based products that have veraciously met the requirement of market. The property of graphene products is far below the theoretical behaviors of pristine graphene[36]. In this regard, there are two main challenges for developing graphene based products from lab to market. At first, the unique property of monolayer graphene drastically deteriorates while increasing the thickness or defects. But the preparation of single-layer graphene is both time and energy assuming. Therefore, the mass production of low-cost, high-quality, single-layer graphene products is one of the most critical challenges for their large-scale industrial applications. Secondly, graphene flakes severely suffer from the automatic agglomeration due to their large surface area and the strong Van der Waals forces between adjacent layers. In this

regard, functionalization would be a favorable strategy to encounter the agglomeration issues, and thus improve graphene's dispersibility.

Similar to graphene's lattice structure, the monolayer hexagonal boron nitride (h-BN) is composed of alternating nitrogen and boron atoms, see Figure 1-1 (b). The h-BN is generally referred to as 'white graphene' because its agglomeration is white powders or blocks[32, 37]. The interlayer spacing between adjacent hexagonal boron nitride layers is 0.333 nm, and the bond length of B-N is 0.145 nm[32]. Due to the absence of dangling bonds and the strong in-plane B-N covalent bonds, h-BN shows similar excellent mechanical, chemical and thermal properties with graphene[37]. In contrast, the h-BN presents remarkably different electronic properties with graphene. For example, pristine graphene exhibits high electronic conductivity, while h-BN is highly electronically insulated. This is because the bandgap of graphene is zero, while the bandgap of h-BN is 5.97 eV[38]. Thus, h-BN presents dielectric breakdown field up to 7.94 mV cm^{-1}, which is comparable to the conventionally used SiO_2 based dielectrics[38]. Besides, the thermal conductivity of h-BN is 751 W m^{-1} K^{-1} at room temperature[39]. Although lower than graphene, the thermal conductivity of h-BN is higher than the majority of metals (i.e. Copper: 380 W m^{-1} K^{-1}, Aluminum 237 W m^{-1} K^{-1}) and conventional ceramics (i.e. Alumina: 30 W m^{-1} K^{-1}, Aluminum Nitride: 321 W m^{-1} K^{-1})[32]. With these distinctive advantages, h-BN is widely studied for thermal management in electronics, such as electrical insulation thermal interface materials and heat spreaders, etc.[37]

On the other hand, the electrical structures of h-BN can be tailored by doping, hybridization, functionalization, or substitution, etc.[39] Thus, hexagonal boron nitride-graphene heterojunctions have been extensively studied for future high performance and stable graphene based electronics[40]. Despite the extensive progress in the past decade, the mass production and the poor dispersibility of h-BN are two of the severe challenges limits its industrial applications. Currently, ball milling is the most feasible strategy to achieve large scale hexagonal boron nitride nanoflakes. However, ball milling is both time and energy assuming with relatively small size productions.

1.3 Synthesis of Graphene-like 2D Materials

Until now, many methods were developed to produce mono- and multi-layer graphene-like 2D materials, especially aiming at mass production of high quality and large lateral size nanosheets[40]. Generally, these methods can be classified as bottom-up (chemical

vapor deposition, polymerization, etc.)[25] and top-down approaches (mechanical exfoliation, liquid-phase exfoliation, etc.)[1]. In the bottom-up methods, the synthesis is achieved from liquid or gaseous precursors[41], such as methane, ethylene, borazine, ammonia, etc. While in top-down methods, bulk size crystals are converted into their smallest compositional parts through mechanical/chemical exfoliation,[42, 43] plasma etching,[44] laser ablation[45], and unzipping of nanotubes, etc.[46, 47]

1.3.1 Chemical Vapor Deposition

In chemical vapor deposition (CVD), atoms in the precursors are self-assembled into their corresponding hexagonal structures, see Figure 1-3 (a). For graphene, it grows on metallic substrates by carbon sources decomposes under high temperature. The carbon sources can be solids (i.e. polymers, sucrose, camphor, etc.), liquids (i.e. ethanol, hexane, turpentine oil, benzene, etc.) or gases (i.e. methane, ethylene, acetylene, etc.)[48]. And the metallic substrates can be Co,[49] Ni, Au, Cu,[50] Pd,[51] Pt, Ir, Ru, Re, Rh, Ge[52], etc.[51] Traditionally, Ni and Cu are widely utilized as catalyst-type substrates for graphene growth because of their low cost and excellent catalytic property[40]. While hexagonal boron nitride has been extensive growth on transaction metals, such as Pt, Ru, Ph, Nu, Ni, Pd, SiO_2/Si, etc.[53] Typically, borazine and ammonia are widely used as B and N sources for hexagonal boron nitride growth. The CVD technique enables the synthesis of high quality, uniform and large area 2D materials on various substrates[53-55]. Compared to other methods, the CVD method offers few defects, better control of the number of layers and large surface area with long-range ordering. Recently, the roll-to-roll CVD routes has been developed to mass production graphene, see Figure 1-3 (b)[56].

After growth, transfer methods, including bubble-mediated transfer, dry transfer, electrochemical transfer, roller-assisted transfer, and support-free transfer strategies have been developed to obtain free-standing or on-substrate CVD products, see Figure 1-3 (c).

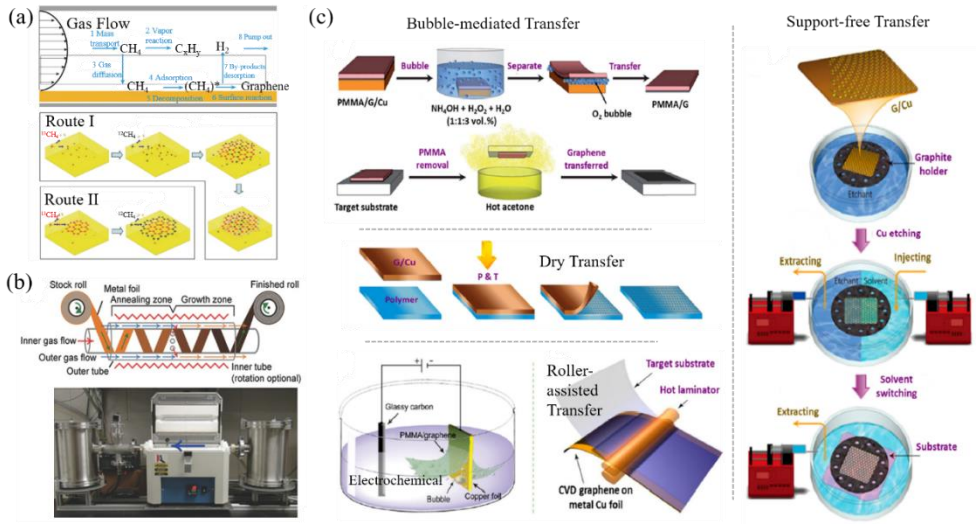

Figure 1-3. (a) The schematic presentation of CVD growth of graphene-like 2D materials. (b) The schematic and optical images of continuous roll-to-roll growth graphene. (c) The schematic transfer methods of CVD growth of graphene-like 2D materials.

Especially, the synthesis procedure of CVD methods can be optimized to control the crystalline structure, layers, and lateral geometry of graphene-like 2D materials for specific applications, such as on-chip fabrications and constructive transparent film. However, the high cost of CVD method needs to be decreased for widespread applications[25].

1.3.2 Mechanical Exfoliation

Mechanical exfoliation, the so-called "scotch tape method", is the earliest reported technology to extract few-layer graphene sheets from graphitic bulks[1, 57], see Figure 1-4. In mechanical exfoliation, few-layers graphene is obtained by repeating attach and remove the adhesive tape on bulk sources[48, 58-61]. In principle, the external force is required up to 300 nN μm^{-2} for exfoliating a single atom layer graphene[61]. This mechanical exfoliation method has utilized to successfully obtain monolayers of graphene[15], h-BN[57], MoS_2[59], $NbSe_2$[57], WS_2[60], $Bi_2Sr_2CaCu_2O_x$[60] from their bulks[56]. In mechanical exfoliation, the geometry of 2D nanosheets is largely limited by the size of pristine raw materials[40]. In addition to directly mechanical cleavage, ball milling, shear forces, and sonication technology have been explored to improve the production yield of nanosheets for both graphene and h-BN. For example, ammonia borane (NH_3BH_3), potassium hydroxide (KOH), sodium hydroxide (NaOH), sodium

chloride (NaCl) has been utilized to ball mixing with h-BN powder to produce 2D h-BN nanosheets[62]. While ball mixing, binding energy and surface tension are two of the dominants for achieving high efficiency. In this regard, isopropyl alcohol was demonstrated as an excellent exfoliation media for h-BN[40]. In addition, 55% ethanol/water solution and thionyl chloride ($SOCl_2$) have been reported to produce a higher yield of h-BN nanosheets[63, 64].

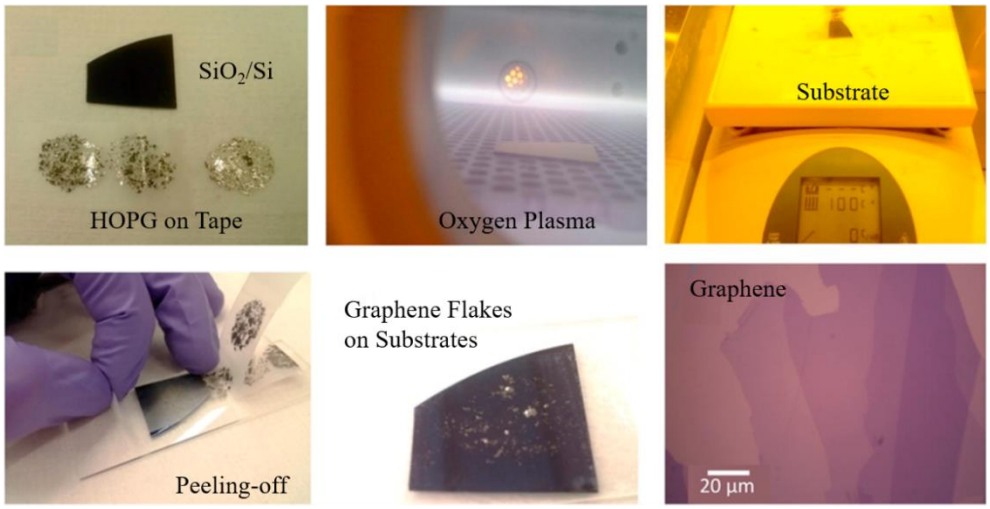

Figure 1-4. Schematic images of the scotch tape method[57]. (Reproduced with the permission from the Institute of Physics Publishing.)

Although the mechanical exfoliation method is simple and can produce relatively high quality nanosheets, it is a low yield technology with poor reproducibility and the exfoliated flake geometry is limited to hundreds of micrometers[65]. Therefore, mechanical exfoliation technology is only suitable for laboratory studies and cannot be utilized for mass production[61].

1.3.3 Liquid-Phase Exfoliation

Alternatively, the liquid-phase exfoliation method provides the possibility to mass-produce single and few layers of 2D nanosheets including graphene, h-BN, $MoTe_2$, WS_2, $NbSe_2$, MoS_2, $NiTe_2$, Bi_2Te_3, etc.[56] from their bulks at a relatively low cost[66, 67]. In this method, oxidation, intercalation, ion exchange and ultrasonic cleavage are the four main functions[56], see Figure 1-5. Taking graphene oxide for example, the space of graphitic layers is enlarged by strong oxidation (H_2O_2, $KMnO_4$, H_2SO_4, etc.) or the intercalation of large size molecules or metal atoms (compared to the interlayer distance)[48]. According to the reported experimental results, a solvent with 40-50 mJ m^{-2} surface

tension benefits for achieving a high-efficiency exfoliation for graphene oxide[69]. Based on such theory, many solvents have been developed as the exfoliation media for graphene oxide, including dimethylformamide (DMF), n-methy1-2-pyrrolidone (NMP), ethanol, N, N-dimethylacetamide (DMA), etc., and their mixture solutions[68] Furthermore, sodium hydroxide (NaOH) can improve the exfoliation efficiency through intercalating into 2D layers, and thus weaken the Van der Waals force[70]. Until now, the liquid phase exfoliation method has developed the commercial preparation strategy for graphene oxide because of its high efficiency and the possibility to obtain large geometry sheets up to 10 μm[56]. The liquid phase exfoliation was initially utilized to prepare mono- and few-layer h-BN in 2008, where the h-BN powder was sonicated in 1,2-dichloroethane solution[71]. After that, water, isopropyl, ethanol, etc., have been demonstrated to be able to exfoliate h-BN. Compared to graphene, the exfoliation efficiency for h-BN is relatively low, thus this method is not widely developed for its mass-production.

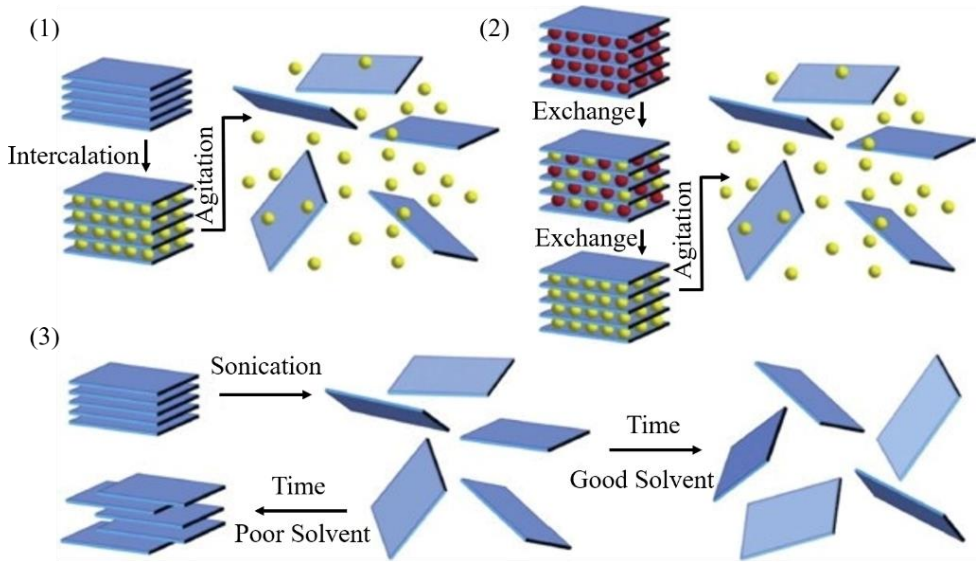

Figure 1-5. Schematic process for the liquid-phase exfoliation [67]. (Reproduced with the permission from Science.)

Alternatively, controlled electrochemical exfoliation is another liquid exfoliation method for preparing graphene-like 2D materials. It is conducted by applying a positive potential (e.g. 10 V, 15 min) on graphite. In electrochemical exfoliation, reducer involving sodium borohydride ($NaBH_4$), hydroiodic acid (HI), hydrazine (N_2H_4), and ascorbic acid (vitamin C), etc., are needed to decrease defects within the 2D plane[72]. In addition, unzipping of hexagonal nanotubes, such as carbon nanotubes and boron nitride

nanotubes, is another liquid phase exfoliation method for the synthesis of graphene-like 2D materials[73, 74]. However, the high cost, low yield, and low reproducibility property decrease the researcher's interest in this unzipping method.

1.3.4 Wet Chemical Synthesis

The wet chemical synthesis method is mainly used for preparing hexagonal boron nitride nanosheets (BNNS). This method provides a possible mass production route for BNNS[40]. Figure1-6 (a) presents the optical images of hexagonal boron nitride dispersion prepared by wet chemical synthesis. Usually, the BNNS can be obtained by heating urea ($CO(NH_2)_2$) and boric acid (H_3BO_3) at 900 °C under nitrogen atmosphere through the below chemical reactions[74]:

$$2H_3BO_3 \xrightarrow{\Delta} B_2O_3 + 3H_2O$$

$$CO(NH_2)_2 \xrightarrow{\Delta} NH_3 + HNCO$$

$$B_2O_3 + 2\,NH_3 \xrightarrow{\Delta} 2BN + 3H_2O$$

As shown in Figure 1-6 (b, c), the quality of BNNS can be controlled by tailoring the molar ratio of the B and N contained sources, such as H_3BO_3 and $CO(NH_2)_2$.

BNNS can also be synthesized from sodium azide (NaN_3), ammonium chloride (NH_4Cl) and sodium tetrafluoroborate ($NaBF_4$) in an autoclave at a relatively low temperature, e.g. 300 °C, through the following chemical reactions[75]:

$$NaBF_4 + 3NaN_3 + 3\,NH_4Cl \xrightarrow{\Delta} BN + 3NaCl + NaF + 3NH_3 + 4N_2 + 3\,HF$$

Other sources, such as B_2O_3 + Zn + $N_2H_4 \cdot 2HCl$[76], H_3BO_3 + CH_4N_2O + NaN_3 + NH_4Cl[77], and B_2O_3 + MoO_3 + Graphene[78], etc. have also been developed for exfoliating BNNS.

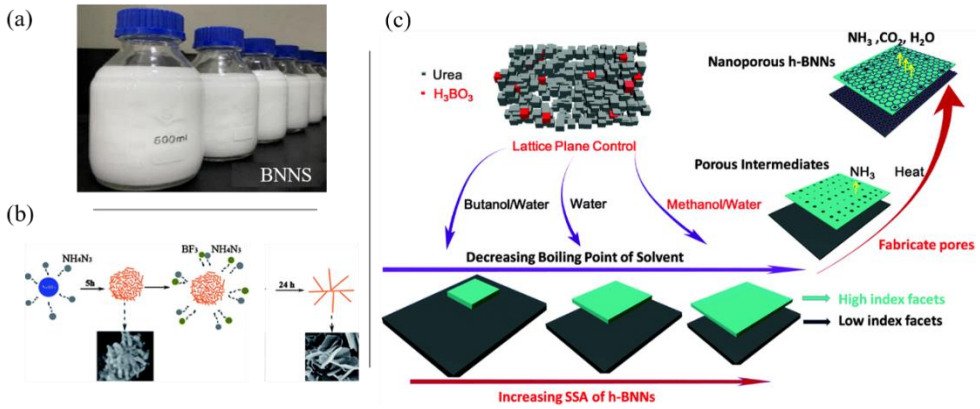

Figure 1-6. (a) Optical images of BNNS dispersion. (b) Schematic mechanism of synthesis BNNS from NH_4N_3 and BF_3. (c) Schematic mechanism of synthesis BNNS from H_3BO_3 and $CO(NH_2)_2$. (Reproduced with the permission from Nano Research.)

1.3.5 Reduction of Graphene Oxide

Graphene oxide (GO) can be prepared through oxidation by alkali metal compounds and strong acids[79-82]. However, this oxidation evitable introduces many defects on graphene, and result in lower conductivity and Young's modulus. In this regard, the reduction technology is developed to remove the oxygen-containing groups on the graphene oxide, such as chemical reduction, thermal reduction, and UV light reduction, etc.[103] After reduction, the reduced graphene oxide (RGO) exhibits similar physical and chemical properties with the pristine graphene, see Figure 1-7 (a, b, c)[83]. In chemical reduction, GO is reduced by using reductive chemicals, such as hydrochloric (HCl), hydrazine (N_2H_4)[84-86], sodium borohydride ($NaBH_4$)[87, 88], hydrobromic (HBr), and hydroiodic acid (HI)[88], etc.[83, 89, 103] While in thermal reduction, the GO is suffering from high temperature, normally around or above 1000 °C, under H_2, Ar_2, N_2H_4, N_2, or a mixture of them[90, 103]. Finally, the excessive functional groups in GO can be removed by exposure to UV light or microwave. Among these three methods, chemical and thermal reduction can be used to mass-produce RGO[91, 103].

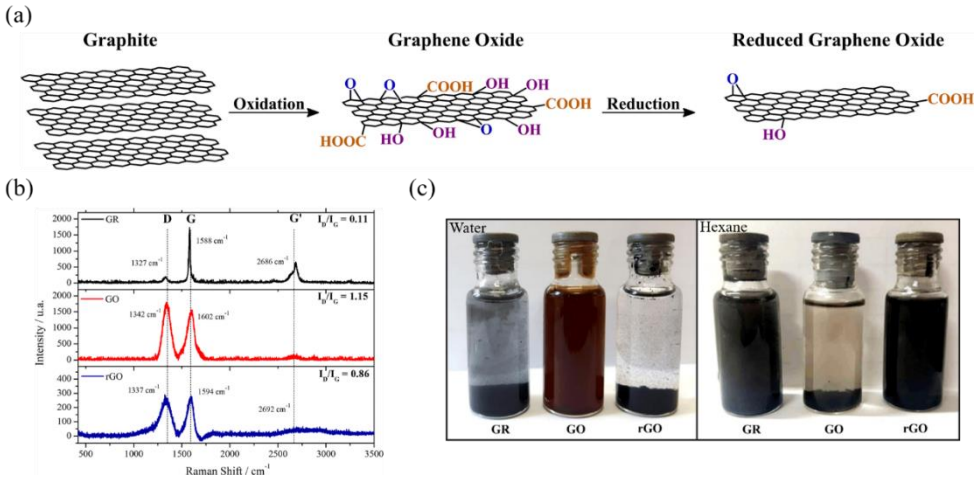

Figure 1-7. (a) Schematic mechanism of synthesis reduced graphene oxide. (b) The Raman spectrum of graphene, graphene oxide and reduced graphene oxide. (c) The optical images of the dispersion of graphene, graphene oxide and reduced graphene oxide in water and hexane. (Reproduced with the permission from Nano Research.)

1.3.6 Others

Apart from the above-mentioned methods, some other approaches have been investigated to exfoliate graphene-like 2D materials, including physical vapor deposition (PVD)[92], pulsed laser deposition (PLD)[93], pyrolysis of compounds[94], microwave irradiation-assisted exfoliation[95], microwave-based solvothermal process[96], high-pressure microfluidization[97], magnetic stirring-assisted ultrasonication[98], liquid exfoliation combined with fast quenching[99], etc. But the interests in these methods are limited because of the lack of mass production possibility, high cost, or lower product quality, etc.

1.4 Functionalization of Graphene-like 2D Materials

Until now, graphene-like 2D materials have been extensively explored for various applications in energy management, mechanical reinforcement, electronics, sensors, gas separation, catalysis, biomedicine, water remediation, etc.[29] On one hand, defects, such as edges, grain boundaries, doping, vacancies significantly decrease the outstanding property of pristine graphene-like 2D materials possesses. For example, the point vacancy and edges could lead to structural distortions, resulting in significantly reducing work function and bandgap[100]. On the other hand, these defects provide an opportunity to control the physical and chemical properties of graphene-like 2D materials through

tailoring their concentration and the type of defects[101]. For instance, functionalization with oxygen-containing groups has been widely utilized to improve the dispersibility of graphene-like 2D materials in solvent, polymer, or metal substrates. The functional groups can be hydroxyl, carboxyl, epoxy groups, etc. Moreover, doping with heteroatoms is an effective approach to tailor the band gap and improve the wettability of graphene-like 2D materials for energy storages and catalysts.

Secondly, the graphene-like 2D sheets inevitably suffer from agglomeration, which dramatically decreases their physical and chemical performance[102]. For example, the Raman measurement shows that single-layer graphene can deliver a Young's module up to 1 TPa, while the GO or RGO typically exhibits tensile strength less than 250 Gpa[103]. In this regard, effective functionalization and dispersion of graphene-like nanosheets are of critical importance[104]. By functionalization, both physical and chemical properties of graphene-like 2D materials can be tuned[56]. For instance, chemical doping of graphene can convert graphene from electrical conduction into insulation, and hydroxyl, carboxyl groups have been demonstrated to successfully tailoring graphene-like 2D sheets from hydrophobic to hydrophilic[15]. Compared to their pristine encounters, the stability and electrical property of graphene-like 2D sheets showed a remarkable improvement after functionalization[103]. Therefore, functionalization provides a possibility to solve the poor interface and π-π stacking issues for graphene-like 2D materials, and thus improves the possibility to achieve their theoretical properties. Usually, the surface functionalization of graphene-like 2D materials is categorized as covalent and non-covalent functionalization.

1.4.1 Covalent Functionalization

Covalent functionalization is the most convenient method in terms of solution processing for surface modification of graphene-like 2D materials. In covalent functionalization, strong acid or oxidants with hydrophilic species, such as amine, isocyanate, esters, carboxyl, epoxy, and hydroxyl groups are grafted on the defects or edges of graphene-like 2D materials by C-C coupling[103, 105]. The solvent for covalent functionalized graphene-like 2D materials can be water, acetone, ethylene glycol,1-propanol, ethanol, dimethylformamide (DMF), N-methyl pyrrolidone (NMP), etc.[106] After functionalization, these negatively charged oxygenated groups allow to form a stable colloidal dispersion of graphene-like 2D materials in several solvents by providing

solvation and electrostatic repulsion[105]. However, the introduction of these oxygenated groups increases defects and disrupts the π-π conjugation, and thus weaken the physical and chemical properties of the pristine graphene-like 2D materials. For instance, the electrical conductivity of pristine graphene goes up to 7200 S m^{-1} with an electric mobility reaching 2.5×10^5 S m^{-1} while GO shows electrical insulated behavior[105]. Figure 1-8 presents the feasible covalent functionalization routes for graphene-like 2D materials, including reduction, diazonium reaction, with sodium azide, with lithium aluminum hydride ($LiAlH_4$), with organic isocyanates, through acylation reaction, esterification, nucleophilic ring-opening reaction, etc.[106]

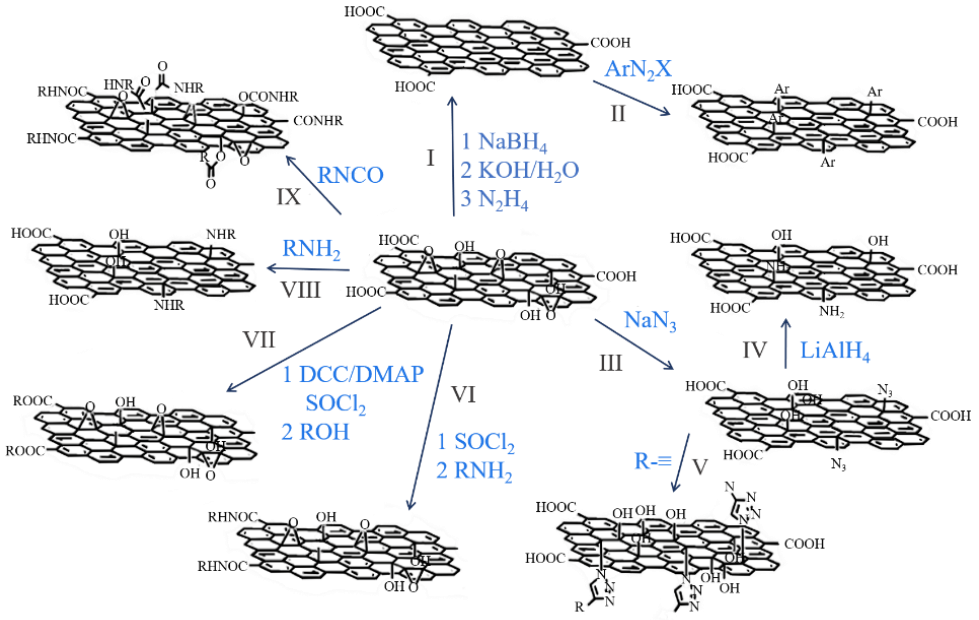

Figure 1-8. Schematic representation of covalent functionalization of graphene-like 2D materials. I: Reduction. II: Diazonium reaction. III: With sodium azide. IV: With $LiAlH_4$. V: Click chemistry reaction. VI: Acylation reaction. VII: Esterification. VIII: Nucleophilic ring-opening reaction. IX: With organic isocyanates[106]. (Reproduced with the permission from the Royal Society of Chemistry.)

Among all of these routes, acylation reaction (reaction VI) is one of the most widely used approaches to graft molecular moieties with graphene-like 2D materials[107]. For example, by the acylation methods, the carboxylic groups can be bonded to amino-functionalized groups to obtain nitrogen contains graphene oxide (NGO). Then the NGO can be conveniently tethered to a large number of chemicals with hydroxyl groups or epoxy groups (Reaction VIII)[108]. Except for small organic molecules, graphene can be modified by polymers with hydroxyl groups, after activated by amino-containing groups,

such as N-hydroxybenzotriazole (HOBT), N, N-4-(dimethylamino)-pyridine (DMAP), thionyl chloride ($SOCl_2$), or dicyclohexylcarbodiimide (DCC), etc., see reaction VII[109]. In reaction III and IV, sodium azide is used to modify GO with a further reduction to form amino groups[110].

1.4.2 Non-covalent Functionalization

Non-covalent functionalization is a well-known strategy to functionalize graphene-like 2D nanomaterials by wrapping, π-π stacking, or Van der Waals forces[111-113]. Before being used in graphene-like 2D materials, this technique has been widely studied for the functionalization of carbon nanotubes. Unlike covalent functionalization, the extended π-π conjugation after non-covalent functionalization is not disrupted. Until now, a variety of modifying agents, involving pyrene derivatives, sodium dodecylbenzene sulfonate surfactant (SDBS), amine-terminated polymers, etc., have been demonstrated to have π-π interaction with graphene-like 2D materials for non-covalent functionalization. Until now, non-covalent functionalization has been utilized to obtain stable graphene-like 2D sheets dispersion for applications in composites, biotechnology, energy management, etc.[114] For example, a blood-compatible graphene/heparin conjugate has been prepared through noncovalent modification of graphene by heparin[114]. After functionalized by polyethylene glycol, poly(propylene imine), etc., graphene can be homogenously dispersed in ethanol or distilled water[115].

1.4.3 Heteroatom Doping

Heteroatom doping is to replace the original atoms in graphene-like 2D materials with heteroatoms but not disrupt the original hexagonal structure. The introduction of heteroatoms to graphene-like 2D materials ends up with significant changes in their pristine properties. For instance, the introduction of N, S, O, etc., on graphene structure can effectively increase the wettability by interrupting the homogenous electron distributions within the 2D in-plane. To meet the practical requirement in semiconducting applications, doping is widely used to tailor the bandgap of graphene and hexagonal boron nitride while maintaining their original honeycomb-like structures[116]. Many efforts, such as doping boron nitride nanosheets (BNNS) with carbon and oxygen atoms, were described to narrow bandgaps. For example, the bandgap of h-BN reduces about 30% after exposed to oxygen plasma[116]. Both

theoretically and experimentally have proved the possibility of tuning the bandgap of the boron nitride nanosheets by doping.

1.5 Applications of Graphene-like 2D Materials

Recently, efforts have been focused on exploring the commercial application for graphene-like 2D materials, such as energy management, interface enhancement, bio and electrochemical sensors, gas or liquid absorbers, transistors, water separation, etc.[117] However, in some cases, the use of pristine graphene-like 2D materials is problematic because of the process difficulty and the agglomeration between adjacent nanosheets. To end these issues, functionalized graphene-like 2D materials in the aforementioned areas has been extensively developed.

1.5.1 Graphene-like 2D Materials for Energy Management

Energy management is a major industry that requires the consumption of graphene-like 2D materials in large quantities. In the past decades, chip manufacturers have been increasing the number of transistors with shrunk sizes to achieve higher clock frequency and component density. As a result, the pursuit for high integration dramatically increased power consumption in integrated circuits, and thus leads to a great challenge on heat dissipations[118]. Nowadays, the heat flux at local hotspots has exceeded 1000 W cm^{-2} in insulated gate bipolar transistors (IGBT). Such high heat flux in a seal and limited room is a big threat to the reliability of the electronics and will significantly shorten their lifetime[118]. Among the unique properties of graphene-like 2D materials, their high thermal conductivity coupled with their flexibility and lightweight properties, present great potential to address the thermal management challenge in electronics. So far, the reported thermal conductivity of the freestanding single layer graphene and hexagonal boron nitride reaches 4000 and 751 W m^{-1} K^{-1} at room temperature, respectively[114], which is far better than conventional polymers, metals, and ceramics. Until now, a multitude of graphene-like 2D materials or their derivatives based products have been developed for thermal managements, including graphene (or h-BN) films, graphene (or h-BN) assembled films, graphene fibers, graphene foams, graphene laminations, etc. Practically, these materials are usually developed as nanofluid, heat spreaders, and thermal interface materials (TIMs), see Figure 1-9[119]. While for thermal management, the alignment of graphene-like 2D materials heavily determines the thermal conductivity of their composites. Because of the well-aligned graphene-like 2D sheets contribute to

build thermal conductive pathway and decrease thermal interface resistance. Recently, continually graphene films roller has been fabricated from the exfoliated graphene flakes in suspension following by graphitization and further mechanical densifications. This method delivery graphene assembled films with a thermal conductivity up to 1500 W m^{-1} K^{-1}, and thus shows great potentials in thermal management. Meanwhile, the unique electrical insulation property of hexagonal boron nitride makes it strategically ideal for heat dissipation in electronics, especially where electrical conduction is not allowed. The electrical insulation property allows the hexagonal boron nitride based products to directly contact with circuits when applied as a heat spreader or thermal interface materials[119]. However, the poor dispersibility and fragile property of h-BN limits its wide applications in heat dissipation.

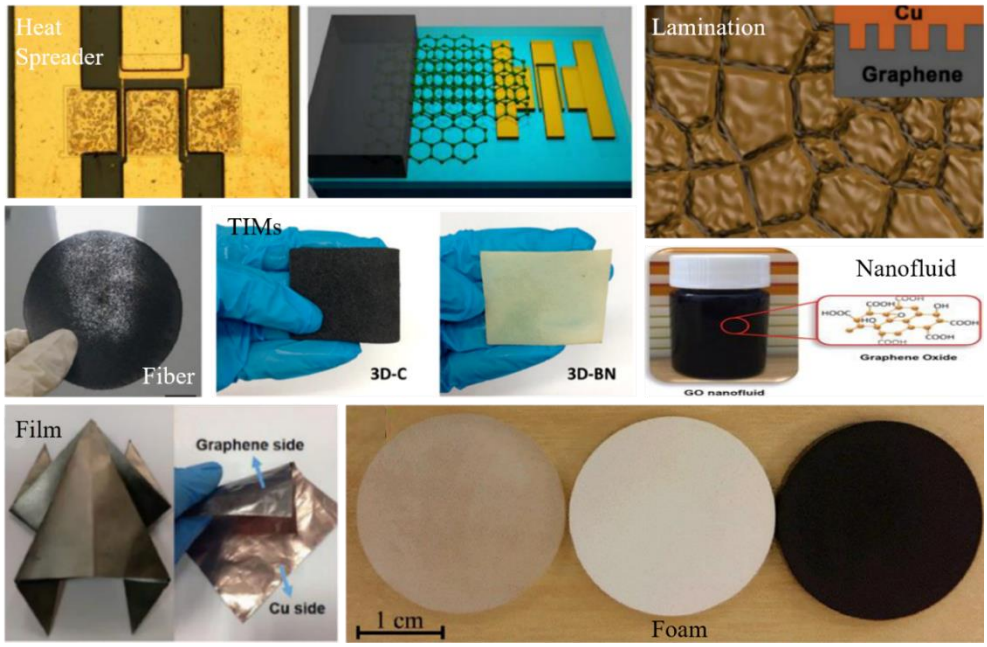

Figure 1-9. The applications of using graphene-like 2D materials for heat dissipation.

Alternatively, graphene offers exceptionally high electrical conductivity and electrochemically stability. Coupled with the lightweight and ultrahigh ratio surface area (2630 m^2 g^{-1})[120] properties, graphene is an ideal option for energy storage, such as Lithium-ion battery, solar cell, fuel cell, and supercapacitor, see Figure 1-10[117], to meet the challenge of ever-increasing global energy consumption[121]. For example, the theoretical capacitance of graphene is calculated as 550 F g^{-1}, which shows overwhelming advantages as supercapacitor implementation[122]. For supercapacitor, the amount of charges or ions stored per unit mass is directly proportional to the available

surface area of electrodes. Because of the ultrahigh surface area of graphene, the research is focused on how to make full utilization of the intrinsic surface capacitance of graphene for supercapacitors. The supercapacitors with graphene-based electrodes and a mesoporous structure exhibit a specific energy density up to 85.6 W h kg^{-1}[123]. Laser-scribed graphene films that have been used directly as electrodes without binder, conductive additives or metal current collectors, have shown energy densities of up to 1.36 mW h cm^{-3} and power densities of 20 W cm^{-3}[124]. Indeed, the graphene based supercapacitor market is one of the first commercialized graphene technologies[114, 125]. The graphene ultracapacitors have been reported to reduce the elevator energy consumption by half and are currently used throughout Europe.

In addition, graphene has been studied as a conductive agent for electrodes to improve rate capability and cyclability because of their high electron mobility. For example, graphene is combined with common cathode materials, such as $LiCoO_2$, $LiMn_2O_4$ and $LiFePO_4$, to prepare cathode electrodes. Owing to the improved electrical and thermal conductivity of graphene, the path for the transport of charge and heat is much shortened in comparison to conventional additives such as carbon black. Improvement of up to 160% of the discharge capacity is observed with graphene enhanced electrodes[126]. Also, graphene can form a skeleton or matrix to resolve the issues associated with poor rate performance, low coulomb efficiency and fast capacity decay by encapsulating active components[127-129]. Currently, commercial batteries with graphene and graphene-Si composite electrodes are under development. Until now, battery manufacturers have been developing graphene battery technology with ‘graphene ball’ materials that enable five times faster charging speeds than standard Lithium-ion batteries[130], and this technology is expected to be adopted in mobile phone products in the near future.

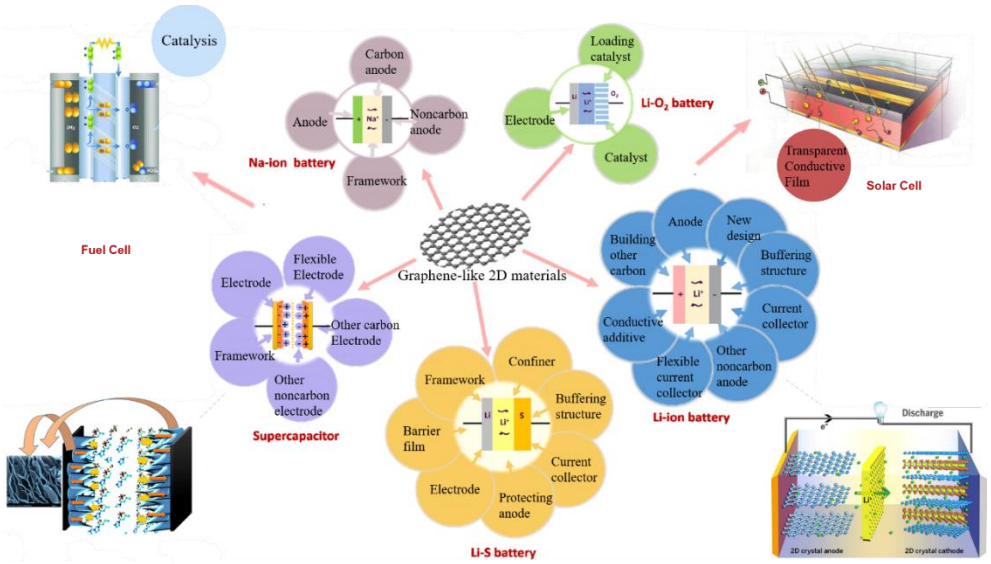

Figure 1-10. The applications of using graphene-like 2D materials for energy storage.

Alternatively, fiber-shaped reduced graphene oxide surfactant modified graphene, metal oxides/hydroxides or conductive polymers with graphene, graphene sheets and 3D graphene have also been investigated for energy storages[117]. The graphitic carbon shows a good arrangement of graphene layer and high crystallinity, which improves the intercalation for batteries. In this regard, graphene has been extensively investigated as cathodes, catalysts, electrolyte membranes, flow plates, dye sensitizers, etc.

1.5.2 Graphene-like 2D Materials for Interface Enhancement

Due to the outstanding mechanical strength, elasticity, conductivity, high surface area, anti-corrosion and lightweight properties, etc., graphene-like 2D materials have been widely studied as scaffolds or enhanced additives in composites, see Figure 1-11. Theoretically, the incorporation of a small amount of graphene-like 2D materials particles in the matrix of metals, polymers, or ceramics can significantly enhance their physical properties. For instance, only 0.5 wt.% of graphene-like 2D materials particles in epoxy resin improves the fracture toughness up to 40%[131]. The electrical conductivity of epoxy is enhanced by 8 orders of magnitude from 10^{-8} S m^{-1} to 1 S m^{-1}[132], and thermal conductivity is enhanced by 167 times to 33 W m^{-1} K^{-1} by adding graphene nanosheets[133, 134]. Until now, a few graphene enhanced products have been commercialized[36]. For example, tennis racquets with a graphene-based composite were first commercialized. Following this success, ski equipment, bicycles, helmets and shoes with graphene as the reinforcement agents are in production, see Table 1-1. The chemical

inertness and the special layered structure of graphene have also been utilized for anti-corrosion purposes[135]. The incorporation of graphene nanoparticles into coatings creates a corrugated path for the permeation of oxidants, and thus be able to delay the oxidation process. The graphene-based coatings have been demonstrated to outperform conventional zinc phosphate-based materials for anti-corrosion[136] and are commercially available now.

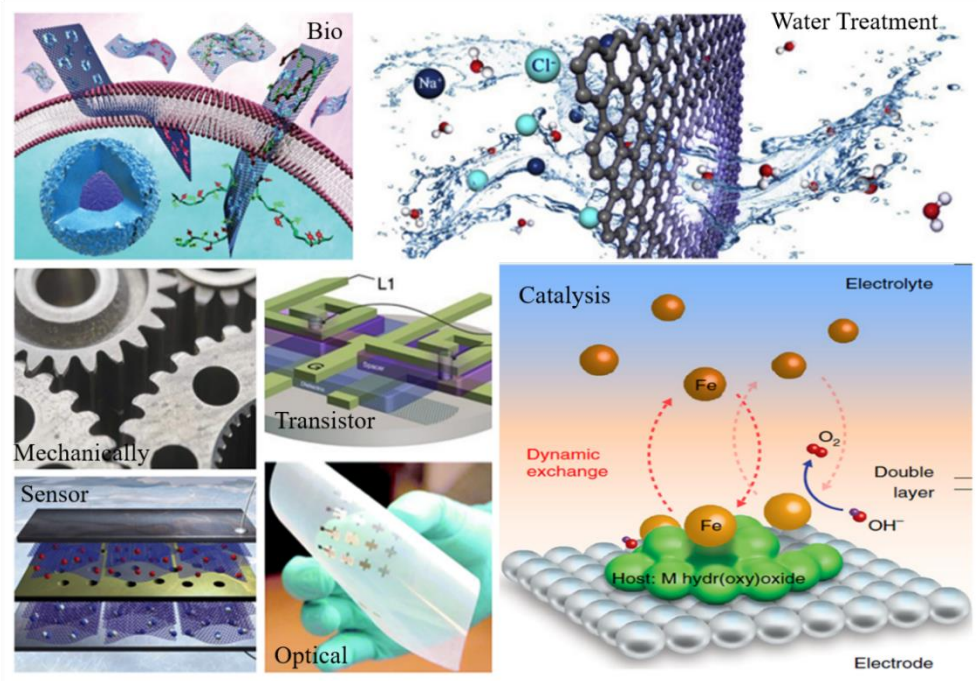

Figure 1-11. The applications of using graphene-like 2D materials for interface enhancements.

Additionally, graphene nanoflakes can assemble into freestanding foil-like paper. In such graphene assembled paper, graphene materials form a unique layer structure interlocked together in parallel, allowing effective load distribution. The Young's modulus and fracture strength of the graphene paper go up to 42 GPa and 120 MPa[137], superior to those of other paper-like materials, for example, graphite foil or bucky paper[138, 139]. Meanwhile, graphene can also be fabricated as fibers through spinning, a similar process to the production of conventional synthetic fibers[140, 141]. Similar with graphene paper, the graphene flakes form into interconnected networks but in the form of a fiber. The Young's modulus of the graphene fiber reaches 120 GPa, and the tensile strength of the graphene fiber is measured up to 1.2 GPa[141-143]. Coupled with the outstanding electrical conductivity (>10^5 S m^{-1})[140, 144-146], thermal conductivity (>1400 W m^{-1} K^{-1})[143, 146] and high-temperature stability, graphene assembled papers and fibers

provide the structurally robust platforms for various applications in light-weight reinforcement, conductive textiles, heat spreaders, etc.

Table 1-1. Available graphene-based products in the market. (Reproduced with the permission from the Springer Nature Ltd. Publishing.)[36]

Property	Company	Product (Model)	Features
Thermal	Huawei	Smartphone (Mate 20 X)	Graphene heat sink
Thermal	TeamGroup	Solid-state drives	Graphene heat spreader
Thermal, mechanical	Momodesign	Helmet (FGTR 1.0)	Graphene film for heat dissipation
Thermal, mechanical	Directa Plus/Colmar	Apparel (G+ series)	Graphene-assisted heat management and heat distribution
Mechanical	HEAD	Tennis racquet, Ski (GrapheneXT)	Graphene for light weight, flexibility and robustness
Mechanical	Dassi	Bicycle (Interceptor)	Graphene in frameset for light weight and stiffness
Mechanical	inov-8	Shoes (G-series)	Graphene for improved elasticity, strength and durability
Mechanical	ZOLO	Earphone (Liberty series)	Graphene-enhanced audio drivers
Mechanical	Richard Mille	Watch (RM 50-03)	Graphene for light-weight chronograph
Electrical	Nanomedical diagnostics	Biosensor (Agile)	Graphene FET as a biochemical sensor
Electrical	Graphenea	Transistors (GFET-S10)	FETs on SiO_2 with CVD graphene
Optical, electrical, mechanical	Chongqing	Smartphone	Graphene Technology Flexible touch screen for mobile phone
Optical	Emberion	Photodetector	Graphene-based photodetector
Optical, electrical	Graphene Flagship	Modulator and Detector	All-graphene optical communication link at 25 Gb s^{-1}
Optical, electrical	Galapad	Smartphone (Galapad Settler)	Graphene-based touch screen enabling better light transmission
Chemical	Applied	Additives for painting/coating	Graphene for anti-corrosion and for blocking moisture penetration
Chemical	Cal Battery	Lithium battery electrode	Silicon-graphene composite anode

1.6 Challenges for Commercialization of Graphene-like 2D Materials

Although several trials have been conducted to commercialize graphene-like 2D materials, these products currently in the market are significantly below their pristine single layer encounters[17]. In principle, structural defects and agglomeration significantly weaken the chemical and physical properties of graphene-like 2D materials[22, 23]. Until now, the most efficient and reliable approach to avoid agglomeration is to functionalize the graphene-like 2D materials before incorporating them with the matrix. This pre-functionalization contributes to forming chemical bonders with the matrix, and thus be able to encounter the Van der Waals forces[147, 148]. Until now, extensively investigations have been carried out regarding using the functionalized graphene-like 2D materials as a reinforcing unit for improving the conductivity, superhydrophobic, thermal dispassion, and mechanical performance in composites[117]. Usually, the functionalized graphene-like 2D materials-based composites are prepared by in-situ polymerization, solution blending, melt blending, and building sandwich structures[148]. Functionalized graphene-like 2D materials have been demonstrated as effective filler for a variety of polymers, ceramics, and metals, including polythene (PE), polyvinyl butyral (PVB), poly(methyl methacrylate) (PMMA), poly(N-isopropyl acrylamide) (PNIPAM), polystyrene (PS), poly (ethylene-vinyl acetate) (PEVA), polyurethane (PU), epoxy, polycarbonates (PC), poly(vinyl alcohol) (PVA), silicon nitride (Si_3N_4), copper (Cu), aluminum (Al), etc. for a variety of functions, such as anti-corrosion, electrical conductivity, elastic strength, extension strength, Young's module, thermal conductivity, etc.[116, 149-155] For instance, the extension strength of PMMA, PU, epoxy, PS is remarkably increased to 2-10 times with less than 1wt.% graphene loading[106]. The thermal conductivity of epoxy can be increased about 6 times after incorporated with graphene[150]. The electrical conductivity of PP, PE, PC, etc., is significantly improved more than 300% after using graphene as enhanced fillers[151]. A 53% tensile strength of Alumina was achieved after sintering with graphene[152].

However, one of the fundamental challenges for graphene-like 2D materials commercialization is their run-to-run variations in terms of product quality, defects, thickness and doping. For instance, the quantity of graphene is largely nonuniform by various vendors, and a recent study has found that products from most vendors are not of optimal quality for most graphene applications[17]. This large statistical variation in

the quality of graphene and lack of standards detriments the commercialization of graphene-like 2D materials. To this end, a series of characterization approaches have been developed and reported, which allowing manufacturers to control and check the quality by meticulous characterization of grown or transferred graphene-like 2D materials. However, most techniques developed in academics are limited in inspection area and throughput, which is hard to meet the requirement for industrial adoption. Some key parameters that require quality control are microscopic defects such as grain boundaries, contamination, doping, etc., macroscopic defects such as tears and wrinkles, thickness uniformity, and require assessment in a non-destructive manner.

In summary, bridging the gap between the commercially available products and the pristine graphene-like 2D materials is essential to reach the expectations for industrial applications. Further efforts should be made to incorporate cost-effective industrial-scale production, quality control, explore new killer applications or achieve significant performance improvement by using graphene-like 2D materials.

1.7 This Thesis

At present, most of the outstanding physical and chemical properties of graphene-like 2D materials have been discovered, and their commercialization is the new focus. Until now, a wide range of graphene-like 2D materials based products are available in the market, such as graphene powder, hexagonal boron nitride dispersion, graphene oxide dispersion, graphene film, graphene assembled film, etc. However, these graphene-like 2D materials based products severely differ from the academic definitions of pristine graphene-like 2D materials and vary in thickness, structural defect, and lateral size. As a result of defects and π-π agglomeration, the graphene-like 2D materials based products present properties far below the expectation where their intrinsic properties are critically demanded. To improve the behavior of graphene-like 2D materials, surface functionalization is widely used to encounter the π-π agglomerations between adjacent layers.

To widespread on the market, new revolutionary solutions should either create new market opportunities or present significant performance improvement. For graphene-like 2D materials, a moderate enhancement in performance is not enough to replace the heavily invested and well-established conventional technology within the industry. Thus, these products severely lack convincement to replace the established mature technology

that has been heavily invested in the past decades. At present, the main challenges for the commercialization of graphene-like 2D materials are exploring new killer applications, developing low-cost, uniform, and high-quality preparation technology, and encountering the intrinsic π-π agglomeration issues. To focus on these issues, we investigated the functionalization strategies for graphene and hexagonal boron nitride in this thesis, and explored their potential industrial applications in energy management and interface enhancement, two of the most promising areas for the commercialization of graphene-like 2D materials. Afterwards, mass production technology and industrial demonstration for functional graphene and hexagonal boron nitride were explored in some chapters. The layout of this thesis is listed as below:

Chapter 1 introduces in detail the research area as graphene-like 2D materials. Firstly, a basic overview of graphene-like 2D materials is provided. Secondly, the synthesis, functionalization approaches of graphene-like 2D materials, and their recent development are presented. Finally, the applications and challenges for the commercialization of graphene-like 2D materials in terms of scalable progress are exhibited. The application and challenge parts motivate the experimental work in this thesis.

Chapters 2 presents the experimental researches on using graphene-like 2D materials for energy management, specifically in heat dissipation. To provide efficient heat dissipation strategy for the electronics and 5G communications, this chapter studied two experimental works, including lightweight and high-performance graphene enhanced heat pipe and hexagonal boron nitride enhanced thermal conductive and electrical insulation heat spreader.

(1) *Graphene Enhanced Heat Pipe*

A lightweight and high thermal transfer coefficient graphene heat pipe was firstly developed in this work. The inner structures of graphene enhanced heat pipe, including preparation for high thermal conductivity graphene film, optimization of wicker structure, and filling volume of the working fluid were investigated. The result indicates the graphene heat pipe exhibits more than 3 times higher specific cooling capacity than the commercial copper-based heat pipe. COMSOL Multiphysics was used to calculate the contribution factor from the container, and thus explain the function of graphene in heat pipes. Finally, to improve the reliability, the interface between graphene and copper

was optimized and the graphene/copper composite heat pipe improves 2 times higher thermal transfer coefficient than the reference commercial products.

(2) *Hexagonal Boron Nitride Enhanced Heat Spreader*

In this work, a scalable hexagonal boron nitride based heat spreader was prepared by electrospinning with polyvinylpyrrolidone. With the optimized hexagonal boron nitride geometry and loading, the in-plane thermal conductivity of hexagonal boron nitride based heat spreader reaches 22 W m^{-1} K^{-1}, this value beats most of the reported work regarding electrically insulation heat spreaders.

Chapter 3 investigated the application of using graphene-like 2D materials for energy management, specifically in supercapacitors. Graphene has shown attractive applications in energy storage because of its ultrahigh electric mobility, large surface area, lightweight properties, etc. Accordingly, in this chapter, graphene was studied for the electrical double layer capacitors and the in-plane micro-supercapacitors.

(1) *Graphene Enhanced Electric Double-layer Capacitor*

In this work, a scalable graphene foam preparation technology was developed to realize high-performance supercapacitors through tailoring specific surface areas and wettability. The unique porous structure, low ohm resistance, doping and high electrical conductivity largely improve the electrochemical performance of graphene foam electrodes. Further, density functional theory simulation was firstly used to reveal the reason why increasing polarity in graphene improves wettability.

(2) *Graphene Based In-plane Micro-supercapacitor*

In this work, graphene assembled film was used to replace the conventional silicon wafer to fabricate flexible and high thermal performance micro-supercapacitors. The result shows that such replacement decreases the surface temperature by 4 °C but will not influence the electrochemical behavior of micro-supercapacitors.

Chapter 4 presents the application of using functional graphene-like 2D materials for interface enhancements, one of the most developed area for graphene-like 2D materials. This chapter contains three research works, including graphene enhanced water-borne epoxy coatings, graphene enhanced mRNA drug delivery platform and hexagonal boron nitride enhanced cement repair materials.

(1) *Graphene Enhanced Water-borne Epoxy Coating*

Graphene was used to lower the coefficient of friction and extend the lifetime of the water-borne epoxy coating in this work. To improve the dispersibility of graphene and improve its compatibility with epoxy, p-hydroxybenzene diazonium salt was prepared to functional graphene by Sandmeyer reaction. In addition, amino groups on functional graphene can bond with epoxy to further improve the mechanical strength of coatings. With optimized geometry and loading, 30 times less coefficient of friction than graphene-free coatings were achieved. And the wear-out time is more than 2 times higher than the commercial products. Finally, mass production technology up to 300 g per batch was developed for preparing functional graphene. This functionalization strategy was further developed for carbon nanotubes to improve their dispersion too.

(2) *Hexagonal Boron Nitride Enhanced Cement Repair Material*

In this work, a mixture of nanoscale and microscale functional hexagonal boron nitride was prepared for improving the strength of cement repair materials. Compared to pristine hexagonal boron nitride particles, functional hexagonal boron nitride largely improves the dispersion in cement repair materials matrix and the adhesion with substrates. Together with a local cement company, this work has demonstrated the commercial application as repair materials for walls.

Besides, we investigated functional graphene quantum dots for mRNA based drug delivery platform. To interact with cells, the zeta potential of graphene quantum dots was tailored to positive by functionalized with polyethyleneimine. The transfection efficiency for functional graphene quantum dots and mRNA complexes is 25% with a formulation concentration of 4000 ng mL^{-1}, but comparable transfection efficiencies could be achieved at much lower doses if the ratio between the carrier and the cargo was optimized. This work describes a potentially interesting preparation method for stable and effective mRNA delivery systems.

Finally, in chapter 5 I give a summary of the experimental work this thesis is based on, and in chapter 6 I provide an outlook of the challenge and future work for graphene-like 2D materials commercialization.

Reference

[1] Novoselov K. S., Geim A. K., Morozov S. V., et al. Electric field effect in atomically thin carbon films [J]. Science, 2004, 306(5696): 666-669.

[2] Dreyer D. R., Park S., Bielawski C. W., et al. The chemistry of graphene oxide [J]. Chem. Soc. Rev., 2010, 39(1): 228-240.

[3] Wang G. X., Yang J., Park J., et al. Facile synthesis and characterization of graphene nanosheets [J]. J. Phy. Chem. C, 2008, 112(22): 8192-8195.

[4] Wang G. X., Shen X. P., Wang B., et al. Synthesis and characterisation of hydrophilic and organophilic graphene nanosheets [J]. Carbon, 2009, 47(5): 1359-1364.

[5] Li X. L., Wang X. R., Zhang L., et al. Chemically derived, ultrasmooth graphene nanoribbon semiconductors [J]. Science, 2008, 319(5867): 1229-1232.

[6] Weng Q. H., Wang X. B., Wang X., et al. Functionalized hexagonal boron nitride nanomaterials: emerging properties and applications [J]. Chem. Soc. Rev., 2016, 45(14): 3989-4012.

[7] Anasori B., Lukatskaya M. R., Gogotsi Y. 2D metal carbides and nitrides (MXenes) for energy storage [J]. Nat. Rev. Mater., 2017, 2(2): 17.

[8] Colson J. W., Woll A. R., Mukherjee A., et al. Oriented 2D covalent organic framework thin films on single-layer graphene [J]. Science, 2011, 332(6026): 228-231.

[9] Rodenas T., Luz I., Prieto G., et al. Metal-organic framework nanosheets in polymer composite materials for gas separation [J]. Nat. Mater., 2015, 14(1): 48-55.

[10] Ling X., Wang H., Huang S. X., et al. The renaissance of black phosphorus [J]. Proc. Natl. Acad. Sci. U. S. A., 2015, 112(15): 4523-4530.

[11] Wang Q. H., Kalantar K., Kis A., et al. Electronics and optoelectronics of two-dimensional transition metal dichalcogenides [J]. Nat. Nanotechnol., 2012, 7(11): 699-712.

[12] Zheng Y., Liu J., Liang J., et al. Graphitic carbon nitride materials: controllable synthesis and applications in fuel cells and photocatalysis [J]. Energy Environ. Sci., 2012, 5(5): 6717-6731.

[13] Liu B. L., Kopf M., Abbas A. N., et al. Black arsenic-phosphorus: layered anisotropic infrared semiconductors with highly tunable compositions and properties [J]. Adv. Mater., 2015, 27(30): 4423-4429.

[14] Wang Q., O'Hare D. Recent advances in the synthesis and application of layered double hydroxide (LDH) nanosheets [J]. Chem. Rev., 2012, 112(7): 4124-4155.
[15] Cai X. K., Luo Y. T., Liu B., et al. Preparation of 2D material dispersions and their applications [J]. Chem. Soc. Rev., 2018, 47(16): 6224-6266.
[16] Ferrari A. C., Bonaccorso F., Fal'ko V., et al. Science and technology roadmap for graphene, related two-dimensional crystals, and hybrid systems [J]. Nanoscale, 2015, 7(11): 4598-4810.
[17] Kauling A. P., Seefeldt A. T., Pisoni D. P., et al. The worldwide graphene flake production [J]. Advan. Mater., 2018, 30(44): 1803784.
[18] Ghosh S., Bao W. Z., Nika D. L., et al. Dimensional crossover of thermal transport in few-layer graphene [J]. Nat. Mater., 2010, 9(7): 555-558.
[19] Serov A. Y., Ong Z. Y., Pop E. Effect of grain boundaries on thermal transport in graphene [J]. Appl. Phys. Lett., 2013, 102(3):3881.
[20] Lindsay L., Broido D. A., Mingo N. Flexural phonons and thermal transport in multilayer graphene and graphite [J]. Phys. Rev. B, 2011, 83(23): 1417-1425.
[21] Yu Q. K., Jauregui L. A., Wu W., et al. Control and characterization of individual grains and grain boundaries in graphene grown by chemical vapour deposition [J]. Nat. Mater., 2011, 10(6): 443-449.
[22] Huang P. Y., Ruiz-Vargas C. S., Zande A. M., et al. Grains and grain boundaries in single-layer graphene atomic patchwork quilts [J]. Nature, 2011, 469(7330): 389-392.
[23] Zandiatashbar A., Lee G. H., An S. J., et al. Effect of defects on the intrinsic strength and stiffness of graphene [J]. Nat. Commun., 2014, 5(9): 3186.
[24] Zhang H. Ultrathin two-dimensional nanomaterials [J]. Acs Nano, 2015, 9(10): 9451-9469.
[25] Tan C. L., Cao X. H., Wu X. J., et al. Recent advances in ultrathin two-dimensional nanomaterials [J]. Chem. Rev., 2017, 117(9): 6225-6331.
[26] Dai Z. H., Liu L. Q., Zhang Z. Strain engineering of 2D materials: issues and opportunities at the interface [J]. Adv. Mater., 2019, 31(45): 11.
[27] Cai Q., Scullion D., Gan W., et al. High thermal conductivity of high-quality monolayer boron nitride and its thermal expansion [J]. Sci. Adv., 2019, 5(6): eaav0129.
[28] Huang Y. J., Qin Y. W., Zhou Y., et al. Polypropylene/graphene oxide nanocomposites prepared by in situ ziegler-natta polymerization [J]. Chem. Mater., 2010, 22(13): 4096-4102.

[29] Tan C. L., Cao X. H., Wu X. J., et al. Recent advances in ultrathin two-dimensional nanomaterials [J]. Chemical Reviews, 2017, 9(117): 6225-6331.
[30] Gupta A., Chen G., Joshi P., et al. Raman scattering from high-frequency phonons in supported n-graphene layer films [J]. Nano Lett., 2006, 6(12): 2667-2673.
[31] Li J. L., Kudin K. N., McAllister M. J., et al. Oxygen-driven unzipping of graphitic materials [J]. Phys. Rev. Lett., 2006, 96(17): 176101.
[32] Wang J. G., Ma F. C., Sun M. T. Graphene, hexagonal boron nitride, and their heterostructures: properties and applications [J]. RSC Adv., 2017, 7(7): 16801-16822.
[33] Geim. Graphene: status and prospects [J]. Science, 2009, 324(5934): 1530-1534.
[34] Bonaccorso F., Sun Z., Hasan T., et al. Graphene photonics and optoelectronics [J]. Nat. Photonics, 2010, 4(9): 611-622.
[35] Zurutuza A., Marinelli C. Challenges and opportunities in graphene commercialization [J]. Nat. Nanotechnol., 2014, 9(10): 730-734.
[36] Kong W., Kum H., Bae S. H., et al. Path towards graphene commercialization from lab to market [J]. Nat. Nanotechnol., 2019, 14(10): 927-938.
[37] Dean C. R., Young A. F., Meric I., et al. Boron nitride substrates for high-quality graphene electronics [J]. Nat. Nanotechnol., 2010, 5(10): 722-726.
[38] Li X. M., Tao L., Chen Z. F., et al. Graphene and related two-dimensional materials: structure-property relationships for electronics and optoelectronics [J]. Appl. Phys. Rev., 2017, 4(2): 021306.
[39] Jo I., Pettes M. T., Kim J., et al. Thermal conductivity and phonon transport in suspended few-layer hexagonal boron nitride [J]. Nano Lett., 2013, 13(2): 550-554.
[40] Zhang K. L., Feng Y. L., Wang F., et al. Two dimensional hexagonal boron nitride (2D-hBN): synthesis, properties and applications [J]. J. Mater. Chem. C, 2017, 5(46): 11992-12022.
[41] Cai J. M., Ruffieux P., Jaafar R., et al. Atomically precise bottom-up fabrication of graphene nanoribbons [J]. Nature, 2010, 466(7305): 470-473.
[42] Park S., Ruoff R. S. Chemical methods for the production of graphenes [J]. Nat. Nanotechnol., 2009, 4(4): 217-224.
[43] Huang Y., Sutter E., Shi N. N., et al. Reliable exfoliation of large-area high-quality flakes of graphene and other two-dimensional materials [J]. Acs Nano, 2015, 9(11): 10612-10620.

[44] Zhang L. F., Feng S. P., Xiao S. Q., et al. Layer-controllable graphene by plasma thinning and post-annealing [J]. Appl. Surf. Sci., 2018, 441: 639-646.

[45] Russo P., Liang R., Jabari E., et al. Single-step synthesis of graphene quantum dots by femtosecond laser ablation of graphene oxide dispersions [J]. Nanoscale, 2016, 8(16): 8863-8877.

[46] Jiao L. Y., Wang X. R., Diankov G., et al. Facile synthesis of high-quality graphene nanoribbons [J]. Nat. Nanotechnol., 2011, 6(2): 132-132.

[47] Kosynkin D. V., Higginbotham A. L., Sinitskii A., et al. Longitudinal unzipping of carbon nanotubes to form graphene nanoribbons [J]. Nature, 2009, 458(7240): 872-875.

[48] Kumar R., Sahoo S., Joanni E., et al. Recent progress in the synthesis of graphene and derived materials for next generation electrodes of high performance lithium ion batteries [J]. Prog. Energy Combust. Sci., 2019, 75: 100786.

[49] Kairi M. I., Zuhan M. K. N. M., Khavarian M., et al. Co-synthesis of large-area graphene and syngas via CVD method from greenhouse gases [J]. Mater. Lett., 2018, 227: 132-135.

[50] Ge X. M., Zhang Y. H., Chen L. X., et al. Mechanism of SiO_x particles formation during CVD graphene growth on Cu substrates [J]. Carbon, 2018, 139: 989-998.

[51] Dhall S., Kumar M., Bhatnagar M., et al. Dual gas sensing properties of graphene-Pd/SnO_2 composites for H_2 and ethanol: role of nanoparticles-graphene interface [J]. Inter. J. Hydrogen Energ., 2018, 43(37): 17921-17927.

[52] Gaspare L. D., Scaparro A. M., Fanfoni M., et al. Early stage of CVD graphene synthesis on Ge(001) substrate [J]. Carbon, 2018, 134: 183-188.

[53] Corso M., Auwarter W., Muntwiler M., et al. Boron nitride nanomesh [J]. Science, 2004, 303(5655): 217-220.

[54] Muller Frank., Stowe K., Sachdev H. Symmetry versus commensurability: epitaxial growth of hexagonal boron nitride on Pt (111) from B-trichloroborazine ($ClBNH)_3$ [J]. Chem. Mater., 2005,17(13): 3464-3467.

[55] Rokuta E., Hasegawa Y., Itoh A., et al. Vibrational spectra of the monolayer films of hexagonal boron nitride and graphite on faceted Ni (755) [J]. Surf. Sci., 1999, 427-428(1): 97-101.

[56] Gupta A., Sakthivel T., Seal S. Recent development in 2D materials beyond graphene [J]. Prog. Mater. Sci., 2015, 73: 44-126.

[57] Novoselov K. S., Jiang D., Schedin F., et al. Two-dimensional atomic crystals [J]. Proc. Natl. Acad. Sci., 2005, 102(30): 10451-10453.

[58] Hiura H., Ebbesen T. W., Fujita J., et al. Role of sp3 defect structures in graphite and carbon nanotibes [J]. Nature, 1994, 367(6459): 148-151.

[59] Miremadi B. K., Morrison S. R. High activity catalyst from exfoliated MoS_2 [J]. J. Catal., 1987, 103(2): 334-345.

[60] Thripuranthaka N., Late D. J. Temperature dependent pingle-Layer WS_2 [J]. Acs Appl. Mater. Inter., 2013, 6(2): 1158-1163.

[61] Jiao L. Y., Zhang L., Wang X. R., et al. Narrow graphene nanoribbons from carbon nanotubes [J]. Nature, 2009, 458(7240): 877-880.

[62] Pacile D., Meyer J. C., Girit C. O., et al. The two-dimensional phase of boron nitride: few-atomic-layer sheets and suspended membranes [J]. Appl. Phys. Lett., 2008, 92(13): 133107.

[63] Cao L., Emami S., Lafdi K. Large-scale exfoliation of hexagonal boron nitride nanosheets in liquid phase [J]. Mater. Express, 2014, 4(2): 165-171.

[64] Sun W. L., Meng Y., Fu Q. R., et al. High-yield production of boron nitride nanosheet and its uses as a catalyst support for hydrogenation of nitroaromatics [J]. Acs Appl. Mater. Inter., 2016, 8(15): 9881-9888.

[65] Huang Y., Sutter E., Shi N. N., et al. Reliable exfoliation of large-area high-quality flakes of graphene and other two-dimensional materials [J]. Acs Nano, 2015, 9(11): 10612-10620.

[66] Parvez K., Li R. J., Puniredd S. R., et al. Electrochemically exfoliated graphene as solution-processable, highly conductive electrodes for organic electronics [J]. Acs Nano, 2013, 7(4): 3598-3606.

[67] Nicolosi V., Chhowalla M., Kanatxidis M. G., et al. Liquid exfoliation of layered materials [J]. Science, 2013, 340(6139): 1420.

[68] Guardia L., Fernandez-Merino M. J., Paredes J. I., et al. High-throughput production of pristine graphene in an aqueous dispersion assisted by non-ionic surfactants [J]. Carbon, 2011, 49(5): 1653-1662.

[69] Hernandez Y., Nicolosi V., Lotya M., et al. High-yield production of graphene by liquid-phase exfoliation of graphite [J]. Nat. Nanotechnol., 2008, 3(9): 563-568.

[70] Liu W. W., Wang J. N. Direct exfoliation of graphene in organic solvents with addition of NaOH [J]. Chem. Commun., 2011, 47(24): 6888-6890.

[71] Han W. Q., Wu L. J., Zhu Y. M., et al. Structure of chemically derived mono- and few-atomic-layer boron nitride sheets [J]. Appl. Phys. Lett., 2008, 93(22): 223103.

[72] Zhou F., Huang H. B., Xiao C. H., et al. Electrochemically scalable production of fluorine-modified graphene for flexible and high-energy ionogel-based microsupercapacitors [J]. J. Am. Chem. Soc., 2018, 140(26): 8198-8205.

[73] Zeng H. B., Zhi C. Y., Zhang Z. H., et al. "White graphenes": boron nitride nanoribbons via boron nitride nanotube unwrapping [J]. Nano Lett., 2010, 10(12): 5049-5055.

[74] Charlier J. C., Blase X., De V. A., et al. Microscopic growth mechanism for carbon and boron-nitride nanotubes [J]. Appl. Phys. A., 1999, 68(3): 267-273.

[75] Lian G., Zhang X., Tan. M., et al. Facile synthesis of 3D boron nitride nanoflowers composed of vertically aligned nanoflakes and fabrication of graphene-like BN by exfoliation [J]. J. Mater. Chem., 2011, 21(25): 9201-9207.

[76] Zhao. Z., Yang Z., Wen Y., et al. Facile synthesis and characterization of hexagonal boron nitride nanoplates by two-steps route [J]. J. Am. Ceram. Soc., 2011, 94(12): 4496-5001.

[77] Pacile D., Meyer L. C., Girit C. O., et al. The two-dimensional phase of boron nitride: few-atomic-layer sheets and suspended membranes [J]. Appl. Phys. Lett., 2008, 92(13): 133107.

[78] Han W. Q., Yu H. G., Liu Z. Convert graphene sheets to boron nitride and boron nitride-carbon sheets via a carbon-substitution reaction [J]. Appl. Phys. Lett., 2011, 98(20): 2031112.

[79] Erickson K. J., Gibb A. L., Sinitskii A., et al. Longitudinal splitting of boron nitride nanotubes for the facile synthesis of high quality boron nitride nanoribbons [J]. Nano Lett., 2011, 11(8): 3221-3226.

[80] Hummers W. S., Offeman R. E. Preparation of graphitic oxide [J]. J. Am. Chem. Soc., 1958, 80(6): 1339-1339.

[81] Ulrich H., Ernst k. Untersuchungen über graphitoxyd [J]. Ze. Anorg. Allg. Chem., 2010, 234(4): 311-336.

[82] Staudenmaier L. Verfahren zur darstellung der graphitsure [J]. Eur. J. Inorg. Chem., 1898, 31(2): 1481-1487.

[83] Chua C. K., Pumera M. Chua, C. K., et al. Chemical reduction of graphene oxide: a synthetic chemistry viewpoint. Chem. Soc. Rev. [J]. Chem. Soc. Rev., 2013, 43(1): 291-312.

[84] Gilje S., Han S., Wang M., et al. A chemical route to graphene for device applications [J]. Nano Lett., 2007, 7(11): 3394-3398.

[85] Chen H., Muller M. B., Gilmore K. J., et al. Mechanically strong, electrically conductive, and biocompatible graphene paper [J]. Adv. Mater., 2010, 20(18): 3557-3561.

[86] Qi X. Y., Pu K. Y., Li H., et al. Amphiphilic graphene composites [J]. Angew Chem. Int. Edit., 2010, 49(49): 9426-9429.

[87] Shin H. J., Kim K. K., Benayad A., et al. Efficient reduction of graphite oxide by sodium borohydride and its effect on electrical conductance [J]. Adv. Funct. Mater., 2009, 19(12): 1987-1992.

[88] Gao W., Alemany L. B., Ci L. J., et al. New insights into the structure and reduction of graphite oxide [J]. Nature Chem., 2009, 1(5): 403-408.

[89] Pei S. F., Zhao J. P., Du J. H., et al. Direct reduction of graphene oxide films into highly conductive and flexible graphene films by hydrohalic acids [J]. Carbon, 2010, 48(15): 4466-4474.

[90] Tang H. X., Ehlert G. J., Lin Y. R., et al. Highly efficient synthesis of graphene nanocomposites [J]. Nano Lett., 2012, 12(1): 84-90.

[91] Wu T. S., Liu S., Li H. L., et al. Production of reduced graphene oxide by UV irradiation [J]. J. Nanosci. Nanotechno., 2011, 11(11): 10078-10081.

[92] Sutter P., Lahiri J., Zahl P., et al. Scalable synthesis of uniform few-layer hexagonal boron nitride dielectric films [J]. Nano Lett., 2013, 13(1): 276-281.

[93] Glavin N. R., Jespersen M. L., Check M. H., et al. Synthesis of few-layer, large area hexagonal-boron nitride by pulsed laser deposition [J]. Thin Solid Films, 2014, 572: 245-250.

[94] Zhu W. S., Dai B. L., Wu P. W., et al. Graphene-analogue hexagonal BN supported with tungsten-based ionic liquid for oxidative desulfurization of fuels [J]. Acs Sustain. Chem. & Eng., 2015, 3(1): 186-194.

[95] Song L. C., Yu G. A., Wang H. T., et al. Synthesis, characterization and properties of transition metal Pd/Pt[60] fullerene complexes containing phosphane ligands crystal structure of [$Pd(\eta^2\text{-}C_{60})\{Ph_2PCH_2(CH_2OCH_2)_2CH_2PPh_2\}$] [J]. Eur. J. Inorg. Chem., 2004, 2004(4): 866-871.

[96] Lu C. C., Liu Z. Characterization of the binding strengths between boronic acids and cis-diol-containing biomolecules by affinity capillary electrophoresis [J]. Methods Molecul. Biolog., 2015, 1286(3): 297-307.

[97] Hilmi Y., Yapmcak G., Oye D., et al. Nanoscopic characterization of two-dimensional (2D) boron nitride nanosheets (BNNSs) produced by microfluidization [J]. Ceram. Int., 2012, 38(3): 2187-2193.

[98] Hao Y. M., Lou S. Y., Zhou S. M., et al. Structural, optical, and magnetic studies of manganese-doped zinc oxide hierarchical microspheres by self-assembly of nanoparticles [J]. Nanoscale Res. Lett., 2012, 7(1): 100.

[99] Zahedi P., Karami Z., Rezaeian I., et al. Preparation and performance evaluation of tetracycline hydrochloride loaded wound dressing mats based on electrospun nanofibrous poly(lactic acid)/poly(-caprolactone) blends [J]. J. Appl. Polym. Sci., 2012, 124(5): 4174-4183.

[100] Alem N., Louie S., Zettl A., et al. Defects in two dimensional crystals: An ultra-high resolution aberration-corrected electron microscopy study [J]. Microsc. Microanal., 2012, 18(S2): 1516-1517.

[101] Azevedo S., Kaschny J. R., Castilho C. M. C. D., et al. Electronic structure of defects in a boron nitride monolayer [J]. Eur. Phys. J. B, 2009, 67(4): 507-512.

[102] Liu Y., Zhao X. L., Wang C. C., et al. Egg albumen templated graphene foams for high-performance supercapacitor electrodes and electrochemical sensors [J]. J. Mater. Chem. A, 2018, 6(37): 18267-18275.

[103] Lau K. T., Hui D., Bhattacharyya D. Graphene-based materials and their composites: A review on production, applications and product limitations [J]. Compos. Part B- Eng., 2018, 142: 200-220.

[104] Kuila T., Bose S., Mishra A. K., et al. Chemical functionalization of graphene and its applications [J]. Prog. Mater. Sci., 2012, 57(7): 1061-1105.

[105] Loh K. P., Bao Q. L., Ang P. K., et al. The chemistry of graphene [J]. J. Mater. Chem., 2010, 20(12): 2277-2289.

[106] Marques P., Gonalves G., Cruz S., et al. Functionalized graphene nanocomposites [M]. Adv. Nanocompos. Technolog. 2011.

[107] Niyogi S., Bekyarova E., Itkis M. E., et al. Solution properties of graphite and graphene [J]. J. Am. Chem. Soc., 2006, 128(24): 7720-7721.

[108] Wang S., Chia P. J., Chua L. L., et al. Band-like transport in surface-functionalized highly solution-processable graphene nanosheets [J]. Adv. Mater., 2008, 20(18): 3440-3446.

[109] Veca, L. M., Lu F. S., Meziani M. J., et al. Polymer functionalization and solubilization of carbon nanosheets [J]. Chem. Commu., 2009,18: 2565-2567.

[110] Salvio R., Krabbenborg S., Naber W. J. M., et al. The formation of large-area conducting graphene-like platelets [J]. Chemistry, 2010, 15(33): 8235-8240.

[111] Xu Y. X., Zhao L., Bai H., et al. Chemically converted graphene induced molecular flattening of 5,10,15,20-tetrakis(1-methyl-4-pyridinio)porphyrin and its application for optical detection of cadmium(II) ions [J]. J. Am. Chem. Soc., 2009, 131(37): 13490-13497.

[112] Wang X. R., Tabakman S. M., Dai H. J. Atomic layer deposition of metal oxides on pristine and functionalized graphene [J]. J. Am. Chem. Soc., 2008, 130(26): 8152-8153.

[113] Wang Q. H., Hersam M. C. Room-temperature molecular-resolution characterization of self-assembled organic monolayers on epitaxial graphene [J]. Nat. Chem., 2009, 1(3): 206-211.

[114] Lee D. Y., Khatun Z., Lee J. H., et al. Blood compatible graphene/heparin conjugate through noncovalent chemistry [J]. Macromolecules, 2011, 12(2): 336-341.

[115] Hua B., Xu Y. X., Lu Z., et al. Non-covalent functionalization of graphene sheets by sulfonated polyaniline [J]. Chem. Commun., 2009, 13(13): 1667-1669.

[116] Weng Q. H., Wang X. B., Wang X., et al. Functionalized hexagonal boron nitride nanomaterials: emerging properties and applications [J]. Chem. Soc. Rev., 2016, 45(14): 3989-4012.

[117] Olabi A. G., Abdelkareem M. A., Wilberforce T., et al. Application of graphene in energy storage device - A review [J]. Renew. Sust. Energ. Rev., 2021, 135: 110026.

[118] Fu Y. F., Hansson J., Liu Y., et al. Graphene related materials for thermal management [J]. 2D Mater., 2020, 7(1): 012001.

[119] Tao O. Y., Chen Y. P., Xie Y. E., et al. Thermal transport in hexagonal boron nitride nanoribbons [J]. Nanotechnology, 2010, 21(24): 245701.

[120] Ivanovskii A. L. Graphene-based and graphene-like materials [J]. Russ. Chem. Rev., 2012, 81(7): 571-605.

[121] Bonaccorso F., Colombo L., Yu G. H., et al. Graphene, related two-dimensional crystals, and hybrid systems for energy conversion and storage [J]. Science, 2015, 347(6217): 1246501.

[122] Xia J. L., Chen F., Li J. H., et al. Measurement of the quantum capacitance of graphene [J]. Nat. Nanotechnol., 2009, 4(8): 505-509.

[123] Liu C. G., Yu Z. N., Neff D., et al. Graphene-based supercapacitor with an ultrahigh energy density [J]. Nano Lett., 2010, 10(12): 4863-4868.

[124] El-Kady M. F., Strong V., Dubin S., et al. Laser scribing of high-performance and flexible graphene-based electrochemical capacitors [J]. Science, 2012, 335(6074): 1326-1330.

[125] Kong L. P., Zhang C. F., Wang J. T., et al. Free-standing T-Nb_2O_5/graphene composite papers with ultrahigh gravimetric/volumetric capacitance for Li-ion intercalation pseudocapacitor [J]. Acs Nano, 2015, 9(11): 11200-11208.

[126] Kucinskis G., Bajars G., Kleperis J. Graphene in lithium ion battery cathode materials: A review [J]. J. Power Sources, 2013, 240: 66-79.

[127] Zhao J., Zhou G. M., Yan K., et al. Air-stable and freestanding lithium alloy/graphene foil as an alternative to lithium metal anodes [J]. Nat. Nanotechnol., 2017, 12(10): 993-999.

[128] Fang R. P., Zhao S. Y., Pei S. F., et al. Toward more reliable lithium-sulfur batteries: an all-graphene cathode structure [J]. Acs Nano, 2016, 10(9): 8676-8682.

[129] Zhu J. X., Yang D., Yin Z. Y., et al. Graphene and graphene-based materials for energy storage applications [J]. Small, 2014, 10(17): 3480-3498.

[130] Son I. H., Park J. H., Park S., et al. Graphene balls for lithium rechargeable batteries with fast charging and high volumetric energy densities [J]. Nat. Commun., 2017, 8: 1561.

[131] Chandrasekaran S., Sato N., Tolle F., et al. Fracture toughness and failure mechanism of graphene based epoxy composites [J]. Compos. Sci. Technol., 2014, 97: 90-99.

[132] Liang J. J., Wang Y., Huang Y., et al. Electromagnetic interference shielding of graphene/epoxy composites [J]. Carbon, 2009, 47(3): 922-925.

[133] Lee J. H., Lee E. K., Joo W. J., et al. Wafer-scale growth of single-crystal monolayer graphene on reusable hydrogen-terminated germanium [J]. Science, 2014, 344(6181): 286-289.

[134] Li Q., Guo F. Y., Li W. W., et al. Ultrahigh thermal conductivity of assembled aligned multi layer graphene/epoxy composite [J]. Chem. Mater., 2014, 26(15): 4459-4465.

[135] Ding R., Li W., Wang X., et al. A brief review of corrosion protective films and coatings based on graphene and graphene oxide [J]. J. Alloy. Compd., 2018, 764: 1039-1055.

[136] Ramezanzadeh B., Moghadam M. H. M., Shohani N., et al. Effects of highly crystalline and conductive polyaniline/graphene oxide composites on the corrosion protection performance of a zinc-rich epoxy coating [J]. Chem. Eng. J., 2017, 320: 363-375.

[137] Dikin D. A., Stankovich S., Zimney E. J., et al. Preparation and characterization of graphene oxide paper [J]. Nature, 2007, 448(7152): 457-460.

[138] Zhang X., Sreekumar T. V., Liu T., et al. Properties and structure of nitric acid oxidized single wall carbon nanotube films [J]. J. Phys. Chem. B, 2004, 108(42): 16435-16440.

[139] Dowell M. B., Howard R. A. Tensile and compressive properties of flexible graphite foils [J]. Carbon, 1986, 24(3): 311-323.

[140] Xu Z., Gao C. Graphene chiral liquid crystals and macroscopic assembled fibres [J]. Nat. Commun., 2011, 2: 571.

[141] Xiang C. S., Young C. C., Wang X., et al. Large flake graphene oxide fibers with unconventional 100% knot efficiency and highly aligned small flake graphene oxide fibers [J]. Adv. Mater., 2013, 25(33): 4592-4597.

[142] Hu X. Z., Xu Z., Liu Z., et al. Liquid crystal self-templating approach to ultrastrong and tough biomimic composites [J]. Scientific Rep., 2013, 3(8): 2374.

[143] Xin G. Q., Yao T. K., Sun H. T., et al. Highly thermally conductive and mechanically strong graphene fibers [J]. Science, 2015, 349(6252): 1083-1087.

[144] Xie L., Shan B., Xu H., et al. Aqueous nanocoating approach to strong natural microfibers with tunable electrical conductivity for wearable electronic textiles [J]. Acs Appl. Mater. Inter., 2018, 1(5): 2406-2413.

[145] Valles C., Nunez J. D., Benito A. M., et al. Flexible conductive graphene paper obtained by direct and gentle annealing of graphene oxide paper [J]. Carbon, 2012, 50(3): 835-844.

[146] Lin X. Y., Shen X., Zheng Q. B., et al. Fabrication of highly-aligned, conductive, and strong graphene papers using ultralarge graphene oxide sheets [J]. Acs Nano, 2012, 6(12): 10708-10719.

[147] Xin G. Q., Sun H. T., Hu T., et al. Large-area freestanding graphene paper for superior thermal management [J]. Adv. Mater., 2014, 26(26): 4521-4526.

[148] Huang X., Qi X. Y., Boey F., et al. Graphene-based composites [J]. Chem. Soc. Rev., 2012, 41(2): 666-686.

[149] Khan U., May P., O'Neill A., et al. Polymer reinforcement using liquid-exfoliated boron nitride nanosheets [J]. Nanoscale, 2013, 5(2): 581-587.
[150] Coleman J. N., Lotya M., O'Neill A., et al. Two-dimensional nanosheets produced by liquid exfoliation of layered materials [J]. Science, 2011, 331(6017): 568-571.
[151] Wang X. B., Zhi C. Y., Li L., et al. "Chemical blowing" of thin-walled bubbles: high-throughput fabrication of large-area, few-layered BN and Cx-BN nanosheets [J]. Adv. Mater., 2011, 23(35): 4072-4076.

CHAPTER 2

Graphene-like 2D Materials for Heat Dissipation

2.1 Introduction

In the past decades, the pursuit for high integration and performance in integrated circuits was dramatically increased, thus intiates severely challenges for heat dissipations. Although the slowdown of Moore's law releases some stress, the heat dissipation requirement in electronics is still in great demand and the non-uniform local over-heating issues inside chips remains unsolved[1]. For example, the power density of hotspots in insulated gate bipolar transistors has exceeded 1000 W cm^{-2}[2, 3]. Recently, the exceptional thermal conductivity of graphene has motivated extensive investigation on using graphene-like 2D materials and their derivatives for heat dissipations. Theoretically, the in-plane thermal conductivity of the single-layer graphene sheet reaches 5000 W m^{-1} K^{-1}, while the reported experimentally thermal conductivity of the monolayer graphene ranges from 2000 to 3000 W m^{-1} K^{-1}[3, 4]. To date, graphene has been widely studied as heat spreaders[5, 6], thermal interface materials[7], laminations[8, 9], nanofluids[10, 11], and thermally conductive fillers[12], etc. The utilizing of graphene in these applications has been demonstrated to cool down copious substrates, such as field-effect transistors, hotspots, etc.[13]

Compared with thermal interface materials and heat spreaders, the phase change possesses overwhelming advantages as ultrahigh thermal conductivity. For instance, the water evaporation exhibits a thermal conductivity up to 8000-10000 W m^{-1} K^{-1}, while the thermal conductivity of graphene based heat spreaders and thermal interface materials is usually below 1000-1800 and 5-150 W m^{-1} K^{-1}, respectively[14]. Accordingly, the phase change process is expected to be constant and recyclable. Therefore, the graphene-based heat pipe could be an ideal strategy for heat dissipations as it combines the advantage of fast thermal conduction of graphene, high cooling capacity of phase change, and recyclable.

Secondly, the interest in using hexagonal boron nitride for heat dissipation in electronics and batteries is constantly increasing, especially where electrical insulation is critically

demanded. The hexagonal boron nitride shows relatively high thermal conductivity (751 W m^{-1} K^{-1}) and outstanding electrical insulation property (bandgap 5.97 eV)[10]. However, the hexagonal boron nitride shows poor processibility and exhibits even worse compatibility than graphene. To cope with these issues, effective dispersions and well alignment of the boron nitride nanosheets are two of the main fundamental challenges for using hexagonal boron nitride as thermally conductive fillers.

In this chapter, graphene heat pipe was firstly designed to broaden the application of using graphene in heat dissipations. The inner structures of graphene heat pipes were optimized by preparation of high thermal conductivity graphene film, optimization of the wicker structures, and tailoring the working fluid. Results show our graphene enhanced heat pipe improves the specific cooling capacity 3.5 times more than the referenced commercial copper-based heat pipe. Meantime, the COMSOL Multiphysics was used to build the contribution equation to quantity heat removed by phase change in the graphene enhanced heat pipe. Finally, to further increase the reliability of graphene enhanced heat pipe, graphene/copper composite heat pipes were developed. To decrease the thermal interface resistance, the electroplating technology and the interface between graphene and copper were optimized.

Secondly, a hexagonal boron nitride based high thermal conductive while electrically insulation heat spreader was developed by electrospinning in this chapter. With the optimized exfoliation technology, geometry, and the loading of hexagonal boron nitride, the in-plane thermal conductivity of our hexagonal boron nitride based heat spreader goes up to 22 W m^{-1} K^{-1}. In a simulated heat package, the hexagonal boron nitride based heat spreader decreases the temperature on the heater by 5 ℃ than the reference one without using any heat dissipation solutions.

2.2 Graphene Enhanced Heat Pipe

2.2.1 Introduction

The heat pipe is widely used as a cooling strategy for electronics due to its high thermal transfer coefficient. Conventionally, in a heat pipe, the working fluid is sealed in a metal container with capillary wick structures on the inner wall, and the heat is mainly removed by the evaporation-condensation circulation of the working fluid[15-18, 20]. Structurally, a heat pipe can be divided into the evaporator section, the adiabatic section, and the condenser section, as shown in Figure 2-1 (a). When heat enters the heat pipe, the

working fluid in the evaporator section (right) is evaporated and the vapor flow moves towards the condenser section (left)[20]. Meantime, the external cooling media, such as heat sink or cooling water, are connected to the condenser section for condensing the vapor. After that, the vapor is transferred into liquid working fluids and can be delivered to the evaporator section by the capillary force from wicker structures[19, 20]. Therefore, the heat can be constantly removed from the evaporation section by phase changes[19, 20]. Conventionally, three wicker structures are long-established in heat pipes: sintered porous copper powder, screen mesh, and grooved sink, see Figure 2-1 (b).

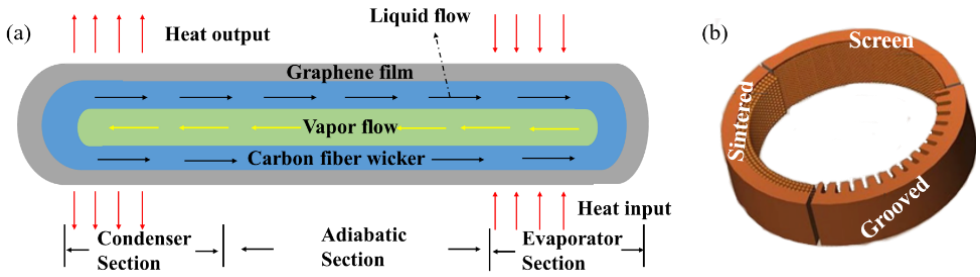

Figure 2-1. (a) The operating mechanism of the graphene enhanced heat pipe. (b) The conventional wick structure in heat pipes.

Currently, most of the heat pipes are composed of titanium[21], aluminum[20, 21, 22], tungsten[21], stainless[21], copper[20, 21], etc.[20, 23]. However, these conventional metals are not capable to meet the cooling requirements for the fast growing mobile devices, where lightweight has become one of the main concerns[20, 21, 24]. To lighten heat pipes, new strategies such as carbon fiber based wick structures, metal/polymer composites, and light-metals have been developed[20, 21]. However, the introduction of polymers severely decreases thermal conductivities[20, 23], while light-metal has corrosion risk[20, 25]. To this end, graphene assembled films present tremendous benefits for heat pipes[26], such as anti-corrosion property, lightweight, and exceptional in-plane thermal conductivity (up to 2500 W m^{-1} K^{-1} at room temperature)[27-38], more than 10 times higher than that of the conventional metals[33-36].

Herein, a new type of graphene enhanced heat pipe with an improved cooling capacity was developed[20]. The graphene enhanced heat pipe is composed of three main parts: graphene assembled film (container), carbon fiber bunch (wick structure), and water/ethanol solution (working fluid). The result shows the graphene enhanced heat pipe achieved a specific thermal transfer coefficient as high as 7230 W m^{-1} K^{-1} g^{-1}[20].

Next, the COMSOL Multiphysics was used to establish the cooling model for graphene enhanced heat pipe[20]. Finally, a graphene/copper composite heat pipe was fabricated to further improve the mechanical strength and reliability of graphene enhanced heat pipes. To decrease thermal interface resistance and increase mechanical reliability, the interface between graphene and copper was tailored by tungsten [20].

2.2.2 Materials and Experiments

2.2.2.1 Materials

Table 2-1. Materials

Name	Specifications	Manufacturers
Graphene Assembled Film (GF)	/	SHT Smart High Tech AB
Carbon Fiber Mesh (CFM)	/	Fibre Glast developments Co., Ltd.
Carbon Fiber Bunch (CFB)	/	Fibre Glast developments Co., Ltd.
Acetone	99.9 wt.%	Sigma-Aldrich (Sweden) Trading Co., Ltd.
Absolute Ethanol	99.8 wt.%	Sigma-Aldrich (Sweden) Trading Co., Ltd.
Bright Copper Plating Solution	/	Tifoo-Electroplating & Surface Technology Co., Ltd.

2.2.2.2 Experiments

(1) Preparation of Graphene Assembled Film

The graphene oxide slurry (10 mg mL^{-1}) was coated on a thin aluminum substrate, and dried under 80 °C through a thermal panel for 24 h. After peeled-off, the isolated graphene oxide film was annealed at 2850 °C for 60 min. Finally, the graphitized film was densified under 500-2000 KN pressure for 6 h[20].

(2) Fabrication of Graphene Enhanced Heat Pipe

Before using as wick structures, a 10 wt.% acetone solution was used to remove the polymers on the carbon fiber bunch, following by oxidization at 50 W for 1 min. Then the carbon fiber bunch was adhered to the graphene assembled film and rolled into a tube, holden by a copper spiral. Next, one end of the graphene tube was soaked into epoxy solution. After curing, the graphene enhanced heat pipe was sealed and filled with working fluids by the device shown in Figure 2-2[20].

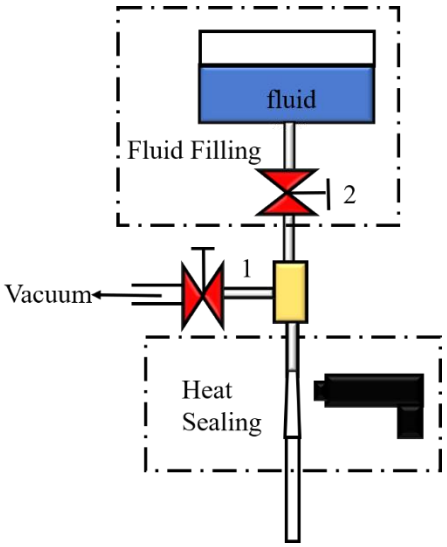

Figure 2-2. The vacuum set-up for preparing graphene enhanced heat pipe.

(3) Preparation of Graphene/Copper Composite Film

At first, a thin layer of tungsten (W) was sputtered on two sides of the graphene assembled film at 300 W under Ar_2 atmosphere (Nordiko 2000, Nordiko Technical Service Ltd., Hampshire, UK). After that, the graphene assembled film was electroplated under 0.5 A in a bright copper solution (Tifoo-Electroplating & Surface Technology, Germany). In a working situation, the copper plate was connected to the positive of the direct current (DC) power supplier while graphene assembled film works as the negative electrode. The residue electroplating solution was removed by distilled water. After drying, two pieces of 30 μm copper film was attached on the two sides of the graphene/copper film, following by sintering at 950 °C for 1 h under Ar_2 atmosphere. Afterwards, the graphene/copper composite film was pressed under 45 Mpa for 60 min (Operator, Dongyi Manufacturing Technology Ltd., Wuxi, China)[20].

(4) Preparation of Graphene/Copper Heat Pipe

At first, the micro tunnel was printed on graphene/copper composite film by mechanical press to work as wick structure for the graphene/copper heat pipe. After that, the graphene/copper composite film was welded into a tube using solder paste (Kester R276, Itasca, Italy). After that, the graphene/copper composite heat pipe was fabricated by the same fabrication approaches as the graphene enhanced heat pipe[20].

(5) Simulation

Cooling capacities of the conduction and the phase change in the graphene enhanced heat pipe was quantitatively determined by COMSOL Multiphysics. To verify the contribution from the graphene assembled film, the in-plane thermal conductivity of wall was defined as 400, 900 and 1400 W m^{-1} K^{-1}. To simplify the model, the effective thermal conductivities (k_{eff}) of the porous wick structure were given by

$$k_{eff} = \frac{k_f\left(k_f+k_s-(1-\varphi)(k_f-k_s)\right)}{k_f+k_s+(1-\varphi)(k_f-k_s)} \quad 2\text{-}1$$

where φ is the effective porosity of wick structure, k_s is the thermal conductivity of crystal carbon, k_f is the thermal conductivity of the working fluid.

The vapor density (ρ_v), the inlet flow and the outlet flow (p) were given by[20]:

$$\rho_v = \frac{p}{R_s T} \quad 2\text{-}2$$

$$p = p_{sat}(T) = p_{ref} \cdot exp\left(\frac{\lambda}{R_s}\left(\frac{1}{T_{ref}} - \frac{1}{T}\right)\right) \quad 2\text{-}3$$

Where R_s represents the gas constant (8.315 J mol^{-1} K^{-1}), T is the temperature, T_{ref} is the evaporation temperature of the mixture solution, and p_{ref} represents the room pressure[20].

2.2.2.3 Characterization

(1) Field Emission Scanning Electron Microscopy (FESEM)

The micro morphologies were observed under FESEM (Ultra 55, Zeiss, Germany). The sample was attached to the conductive tape for measurement.

(2) In-plane Thermal Conductivity

The in-plane thermal diffusivity (D, mm^2 s^{-1}) of the graphene assembled films were determined by the laser flash method (LFA-467, NETZSCH, Germany), see Figure 2-

3 (a). The sample was cut into Φ 25 mm and coated with graphite. In this method, the thermal diffusivity (D) is calculated from the equation as below:

$$D = 0.1388 \times d^2/t_{1/2} \quad 2\text{-}4$$

Where, $t_{1/2}$is the half maximum (s), d is the thickness of the sample (mm)[20].

The density (ρ, g cm^{-1}) was calculated by weight divided volume. Thermal conductivity $k_{\parallel}$ (W m^{-1} K^{-1}) was given by[39]

$$k_{\parallel} = \rho \times C_p \times D \quad 2\text{-}5$$

(3) Through-plane Thermal Conductivity

The through-plane thermal conductivity of graphene assembled film was determined by a steady-state heat-flow method, see Figure 2-3 (b). The sample was cut into Φ 20 mm.

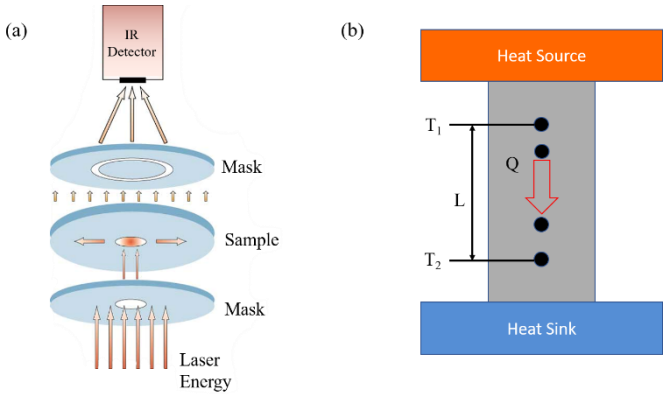

Figure 2-3. (a) Schematic working principle of the laser flash method for in-plane thermal conductivity. (b) Schematic working principle of the steady-state heat-flow method for through-plane thermal conductivity.

In the steady-state heat-flow method, the total thermal resistance of samples with varied thicknesses was measured as R by the following equation:

$$R = R_{c1} + R_{c2} + C/k_{\perp} \quad 2\text{-}6$$

Where, R_{c1} and R_{c2} represent the thermal interface resistance on top and bottom surface, C represents the thickness, $k_{\perp}$ is the through-plane thermal conductivity, respectively[39].

(4) Small Angle X-Ray Scattering (SAXS)

SAXS was used to reveal the alignment of graphene flakes in the graphene assembled film through Mat: Nordic SAXS/WAXS/GISAXS instrument (SAXSLAB, USA). The images were recorded using a 2D Pilatus 1M hybrid pixel detector using exposure times

between 0.5-5 s in transmission mode. For measurement, the graphene assembled film is cut into 1×1 cm and mounted on the sample holder by a transparent tape[20].

(5) X-Ray Diffraction (XRD)

XRD patterns were performed on a diffractometer (X'Pert PRO, Panalytical B.V., Netherlands) operating in the θ-2θ mode, with a Cu Kα radiation source (λ = 1.5406 Å).

(6) X-Ray Images

X-ray images were captured using a high-speed flat panel X-Ray detector at 9 keV photon energy.

(7) Infrared Thermograph

An infrared thermograph camera (A655SC, FLIR, USA) was used to visualize thermal dissipation performances. The thermal diffusivity of graphite was calibrated as 0.98. A DC power supply (Agilent E3612A) was used to provide heat. The sample was attached to the heater by a thin layer of thermal greases (TG100, Loctite, 3 W m^{-1} K^{-1}, China)[39].

(8) Heat Dissipation Performance

To record temperature distribution on the heat pipe, five thermal couples were attached at the position of 1-5 using scotch tapes, see Figure 2-4 (a, b). A DC power supply (Agilent E3612A) was used to provide heat. While measurement, two ends of the heat pipe were fixed in the aluminum and copper block, and the interspaces were perfused with thermal greases (TG100, Loctite, 3 W m^{-1} K^{-1}, China), see Figure 2-4 (a). To prevent thermal leakage, a thick thermal insulation foam was covered at the evaporator and adiabatic section of the testing set-up[20]. All data were obtained under the steady-state mode.

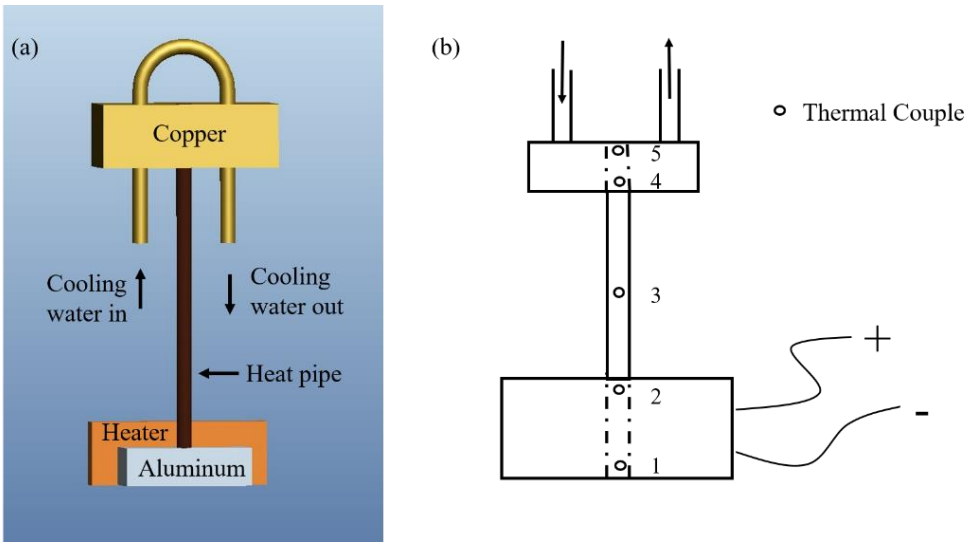

Figure 2-4. (a) Schematic illustration of the setup for heat pipe measurement. (b) Thermal couple positions on the heat pipe.

The specific thermal transfer coefficient (ϱ) was calculated by:

$$\varrho = \frac{Q}{A(T_{hi}-T_{ci})m} \quad 2\text{-}7$$

$$T_{hi} = T_{ho} - \frac{Q ln(\frac{d_o}{d_i})}{2\pi k L_h} \quad 2\text{-}8$$

$$T_{ci} = T_{co} - \frac{Q ln\left(\frac{d_o}{d_i}\right)}{2\pi k L_c} \quad 2\text{-}9$$

Where Q represents the heat loading, m represents the weight, L_c, L_h corresponds to the length of the condenser and evaporation section, d_i, d_o is the inner and outer diameter of the heat pipe, k represents the thermal conductivity, T_{ho}, T_{co} represent the out-wall temperature of the evaporation section and the condenser section[18, 20] and A corresponds to the cross-section area[20].

2.2.3 Results and Discussions

2.2.3.1 Preparation of Graphene Enhanced Heat Pipe

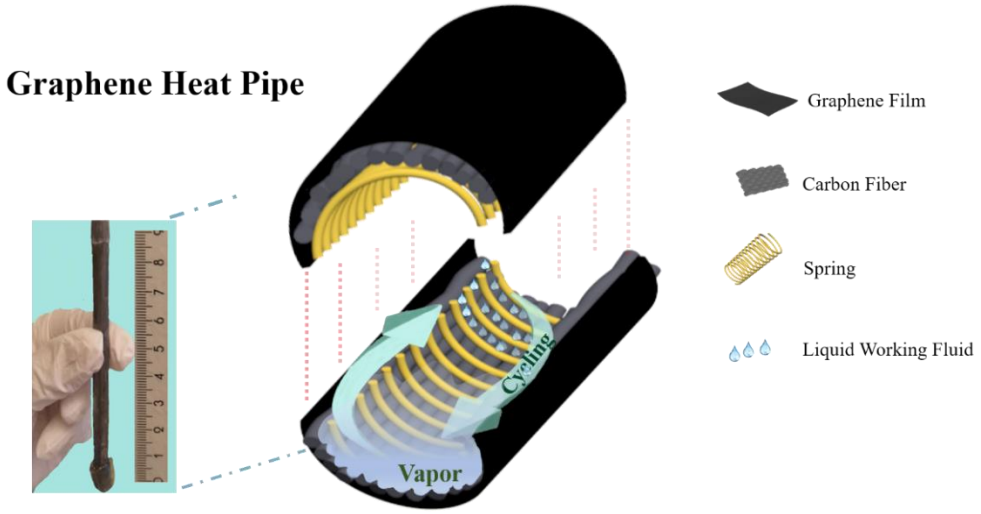

Figure 2-5. The optical and schematic images of the graphene enhanced heat pipe.

The detailed structures of our graphene enhanced heat pipe are presented in Figure 2-5. In which, the graphene assembled film, the carbon fiber, the ethanol/water solution works as the container, the wicker, and the working fluid, respectively[20].

At First, the small angel X-Ray scattering was used to analyze the alignment of the graphene flakes in graphene assembled film for improving thermal conductivity, see Figure 2-6. The thermal conductivity of graphene assembled film is highly related to the alignment of graphene flake. A well-aligned graphene flakes provide more thermal transfer pathways, and thus contributing to increase thermal conductivity[40-42].

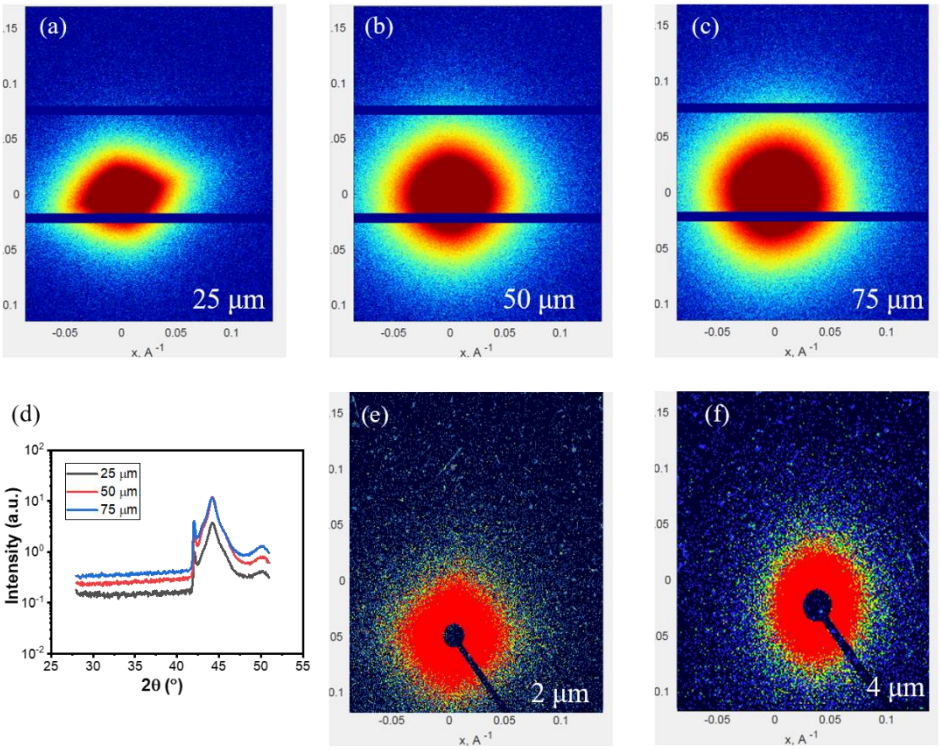

Figure 2-6. (a) The SAXS image of the graphene assembled film with thicknesses of 25 μm. (b) The SAXS image of the graphene assembled film with thicknesses of 50 μm. (c) The SAXS image of the graphene assembled film with thicknesses of 75 μm. (d) The XRD patterns of the graphene assembled film with thicknesses of 25, 50, and 75 μm. (e) The SAXS image of the graphene assembled film with thicknesses of 2 μm. (f) The SAXS image of the graphene assembled film with thicknesses of 4 μm.

Furthermore, the heat transfer model was established to explain why the alignment of graphene flakes can improve thermal conductivity. The biaxial orientated graphene layers are contacted by a face-to-face method (F-F), while mostly point-point (P-P) and line-line (L-L) contacts is observed in random and uniaxial orientated graphene layers[4, 20], as shown in Figure 2-7 (a-c). Compared to the P-P and L-L contact, the F-F contact provides more thermal transfer pathway and lower thermal interfaces between graphene flakes.

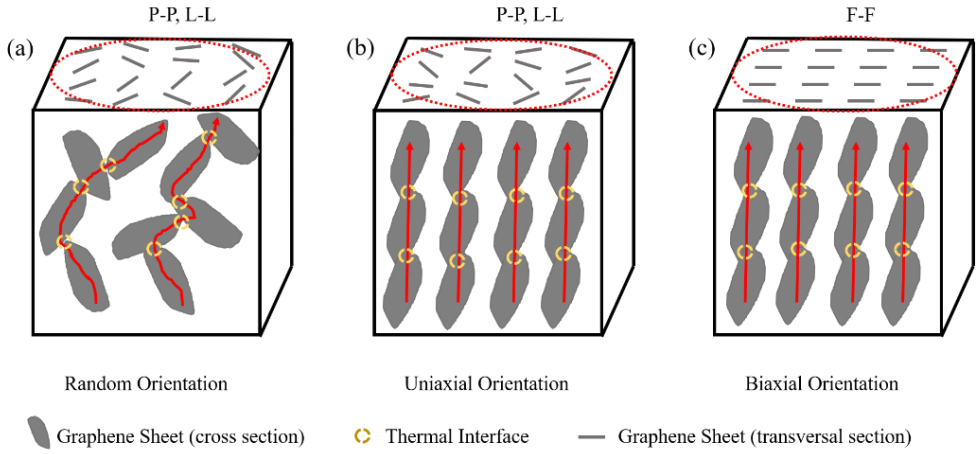

Figure 2-7. (a) The random aligned graphene sheets. (b) The uniaxial aligned graphene sheets. (c) The biaxial aligned graphene sheets.

Secondly, three wick structures, involving carbon fiber bunch (CFB), carbon fiber mesh (CFM) and O_2 plasma-treated graphene film (GF) were studied to optimize the cooling capacity of graphene enhanced heat pipe. The critical heat flux increased by wick structure in GF, CFM and CFB are calculated as 34.04, 52.57 and 100.12 J, indicating the CFB would be the best choice for graphene enhanced heat pipe among the three candidates. To verify this hypothesis, three graphene enhanced heat pipes with the same geometry but using GF, CFM and CFB as wicker structures were prepared. As expected, the experimental results show that the graphene enhanced heat pipe with the CFB wick structure shows the shortest start-up time and the highest specific thermal transfer coefficient, see Figure 2-8 (a, b)[20].

Further, coupled with the saturated evaporation pressure, graphene enhanced heat pipe with various amounts of working fluids (15, 30, 45, 60 vol.%, $V_{Ethanol}$: V_{Water} =4:1) were studied to optimize the filling volume. The result shows the specific thermal transfer coefficient increases at first while increasing the filling volume because of the improvement of the latent cooling capacity of working fluids. When the filling volume is higher than 30 vol.%, owning to the improved vapor pressure and backflow resistance, the specific thermal transfer coefficient starts to decrease when further increasing the fil ling volume, see Figure 2-8 (c)[16, 20].

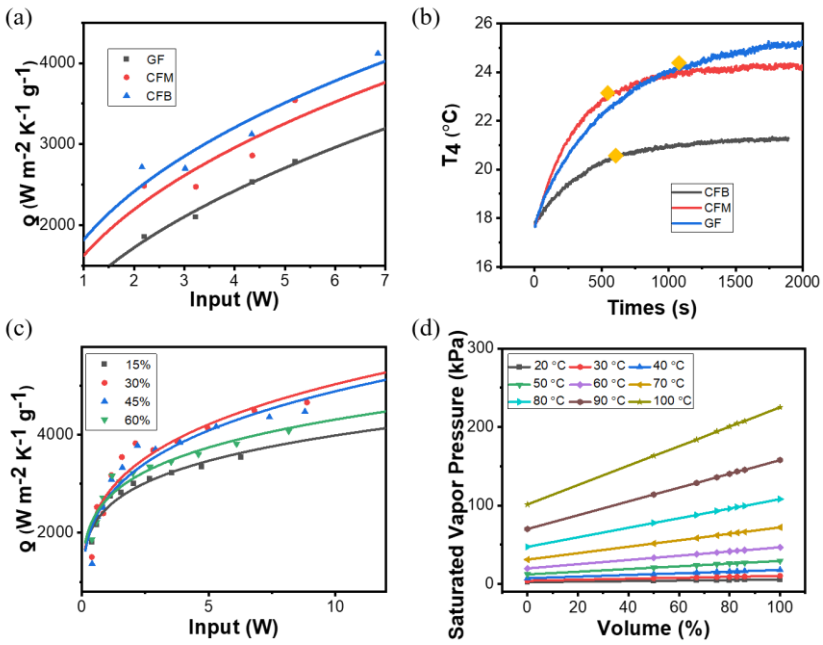

Figure 2-8. (a) The thermal transfer coefficient of graphene enhanced heat pipe with three wickers. (b) The start-up time of graphene enhanced heat pipe with three wicker structures. (c) The thermal transfer coefficient of graphene enhanced heat pipe with various working fluid loadings. (d) The saturated vapor pressure of water/ethanol mixture solutions.

2.2.3.2 Heat Dissipation Performance of Graphene Enhanced Heat Pipe

With the above optimized container, wicker structure and working fluid volume, graphene enhanced heat pipe with 6 mm outer-diameter and various lengths (90, 130, 150 mm) were fabricated to study its heat dissipation behaviors. With a 10 W heat loading, the cooling capacity increases with shortening the graphene enhanced heat pipe, and reaches 7230 W m^{-2} K^{-1} g^{-1}, see Figure 2-9 (a-e)[22, 43]. A 90 mm graphene enhanced heat pipe cools the heater 44 °C with a 15.4 min start-up time, see Figure 2-9 (f).

To compare with the commercialized products, a commercialized copper-based heat pipe with the same geometry (CHP, Spread Fast AB, Sweden) was used as a reference, see Figure 2-9 (g). Results show the specific cooling capacity of the graphene enhanced heat pipe is 3.5 times higher than the referenced commercial copper based heat pipe[20], while shortens the start-up time by approximately 35%, see Figure 2-9 (h, i).

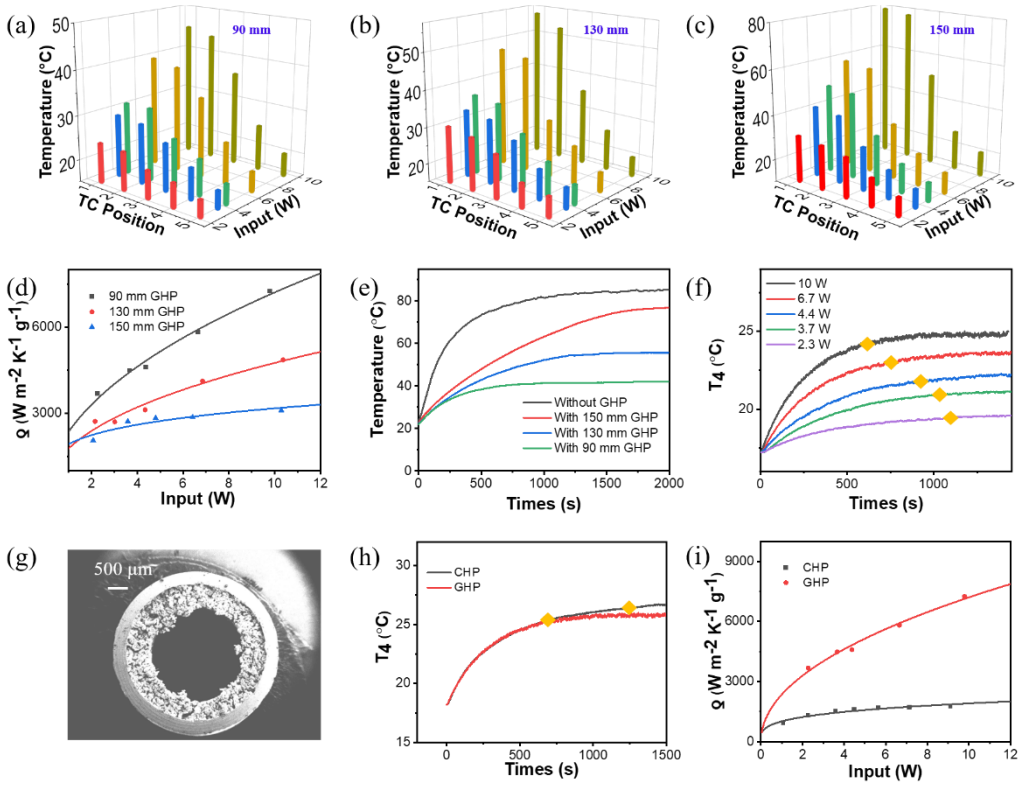

Figure 2-9. (a) The temperature distribution of the 90 mm graphene enhanced heat pipe. (b) The temperature distribution of the 130 mm graphene enhanced heat pipe. (c) The temperature distribution of the 150 mm graphene enhanced heat pipe. (d) The cooling capacity of the 90, 130, and 150 mm graphene enhanced heat pipe. (e) The temperature on the heater. (f) The start-up time of the 90 mm graphene enhanced heat pipe. (g) The cross-section SEM image of the commercialized copper based heat pipe. (h) The start-up time of the graphene enhanced heat pipe and the commercialized copper based heat pipe. (i) The cooling capacity of the graphene enhanced heat pipe and the commercialized copper based heat pipe.

2.2.3.3 Heat Transfer Modelling of Graphene Enhanced Heat Pipe

The COMSOL Multiphysics solver was used to establish the heat transfer model for the graphene enhanced heat pipes. Models with the same geometry of experiments have been created, see Figure 2-10 (a)[20]. Particularly, unlike the significant anisotropic thermal conductivity of graphene assembled film, the graphene enhanced heat pipes exhibit similar performance with the isotropic or anisotropic parameters, see Figure 2-10 (b). The simulation results imply that improving the thermal conductivity of the container effectively enhance the cooling capacity of graphene enhanced heat pipes. To establish the equation between the thermal conductivity and the thermal transfer coefficient, we define the contribution factor as γ.

Herein we use the conduction to present the cooling capacity of the container. To exclude phase changes, empty graphene enhanced heat pipes were simulated, and the result is shown in Figure 2-10 (c, d). Accordingly, the contribution factor from the conduction (γ_c) is given by

$$\gamma_c = \frac{Q_c}{Q_c+Q_p} \quad 2\text{-}10$$

$$\gamma_c = \frac{Qe/A\Delta T_e}{Qf/A\Delta T_f} = \frac{Qe/\Delta T_e}{Qf/\Delta T_f} \quad 2\text{-}11$$

Where Q_p, Q_c is the heat delivered by the phase change and the conduction, Qe, Qf is the heat delivered by empty and filled graphene enhanced heat pipes, A represents the cross-section area, ΔT_f is the difference in temperature between the condenser and evaporator section in the filled graphene enhanced heat pipe, ΔT_e is the difference in temperature between the condenser and evaporator section in the empty graphene enhanced heat pipe[20].

Further, according to the Riedel equation and the definition of the thermal conductivity,

$$Q_c = A\Delta Tk/L \quad 2\text{-}12$$

$$Q_p = 1.093mR_sT_c\ln(P_c-1)/18(0.93-T_b) \quad 2\text{-}13$$

where R_s is the gas constant (8.315 J mol^{-1} K^{-1}), T_b is known, represents the reduced temperature at boiling point, P_c is the critical pressure, T_c is the tested temperature, m is the weight of the working fluid, L corresponds to the length of the heat pipe, k represents the thermal conductivity, ΔT is the temperature difference between the evaporator and the condenser section[20, 44, 45].

Therefore, equation 2-11 is rewritten as

$$\gamma_c = A\Delta T\lambda(0.93-T_b)/[(0.93T_bA\Delta T\lambda L)+1.093mRT_cLln(P_c-1)] \quad 2\text{-}14$$

While assigned the physical values,

$$\gamma_c = 1.44\lambda(0.93-T_b)/[(0.0168\lambda+191T_cln(P_c-1)] \quad 2\text{-}15$$

Because of $191T_cln(P_c-1) \gg 0.0168\lambda$, the equation 2-11 can be simplified as[20]

$$\gamma_c = 1.44\lambda(0.93-T_b)/191T_cln(P_c-1) \quad 2\text{-}16$$

Therefore, equation 2-16 indicates the heat dissipated by phase change is mainly determined by the inner structure of the heat pipe, involving inner pressure, wick structure, volume, diameter and working fluid[17]. In addition, the γ_c can be improved by increasing the thermal conductivity of the container.

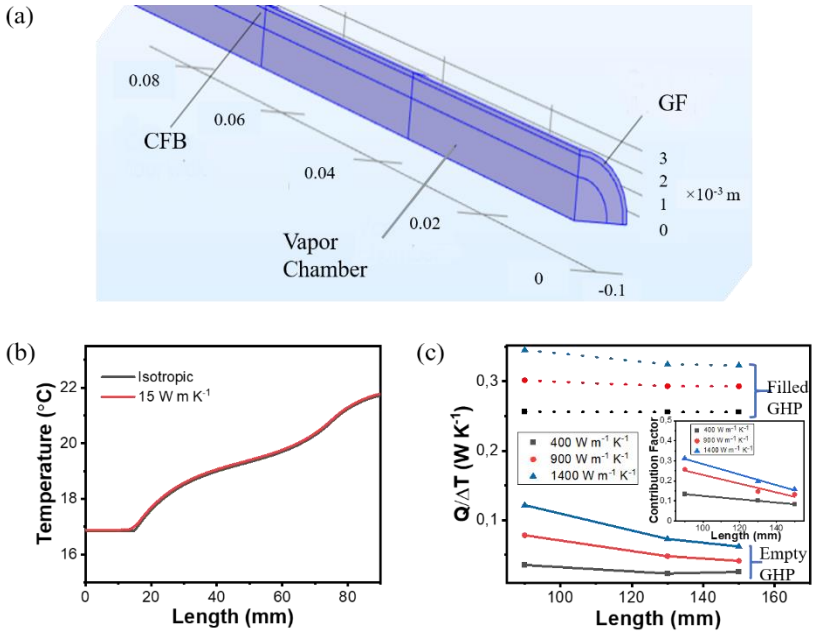

Figure 2-10. (a) The model of graphene enhanced heat pipe. (b) The temperature distribution of the graphene enhanced heat pipe with isotropic and anisotropic graphene assembled film (λ //:1400 W m^{-1} K^{-1}, λ ⊥:15 W m^{-1} K^{-1}). (c) The cooling capability of the conduction and phase change, the inset is the $\gamma_c$with various heat pipe lengths.

2.2.3.4 Graphene/Copper Composite Heat Pipe

To further improve the mechanical strength and reliability of graphene enhanced heat pipe, graphene/copper composite heat pipe was prepared by a similar method. At first, tungsten (W) was sputtered as interface materials for graphene and copper. After sintering, a typical peak of WC was observed on the XRD patterns, indicating the improved bonding at the interface between copper and graphene film, see Figure 2-11. Such WC alloy can strengthen graphene/copper composite film and decrease the thermal resistance within the sandwich structures.

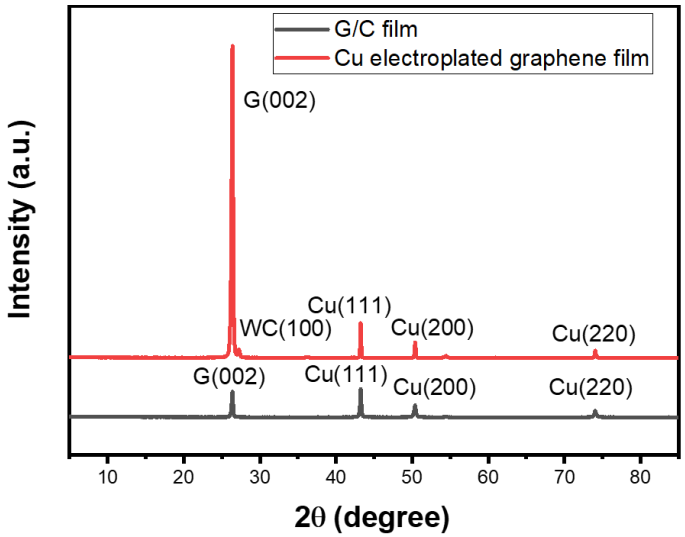

Figure 2-11. The XRD pattern of graphene/copper composite film with and without tungsten as interface materials.

The thickness of graphene/copper composite film is about 80 μm, while the thickness of tungsten is controlled at approximately 6 nm, which is too thin to be observed under the SEM. Compared to the reference one without tungsten bonding, a tight bonding between graphene and copper was observed. While an obvious gap was observed between graphene and copper layer in the reference graphene/copper film, which copper was electroplated on the graphene assembled film without bonding materials, see Figure 2-12 (a, b).

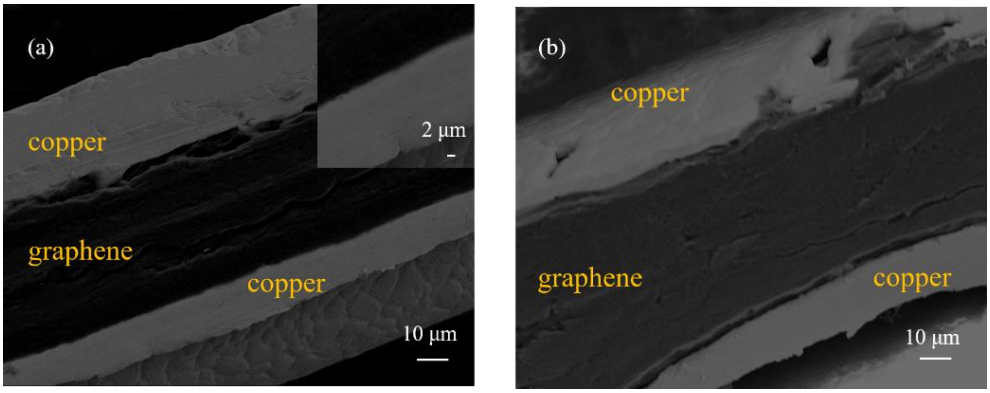

Figure 2-12. (a) The cross-section SEM photography of graphene/copper composite film with tungsten as interface materials. (b) The cross-section SEM photography of the reference graphene/copper film without tungsten as interface materials.

With the optimized thickness of tungsten and electroplated copper, the thermal conductivity of the graphene/copper composite film is as high as 1026 W m K^{-1}, as shown in Figure 2-13 (a, b). To visualize the thermal dissipation property of such graphene/copper heat spreader, the graphene/copper composite film was used to cool a printed circuit board (PCB), see Figure 2-13 (c, d). After integration with the graphene/copper heat spreader and heat sink, the temperature on the PCB is cooled 28 °C, indicating an improved cooling capacity of the graphene/copper composite film.

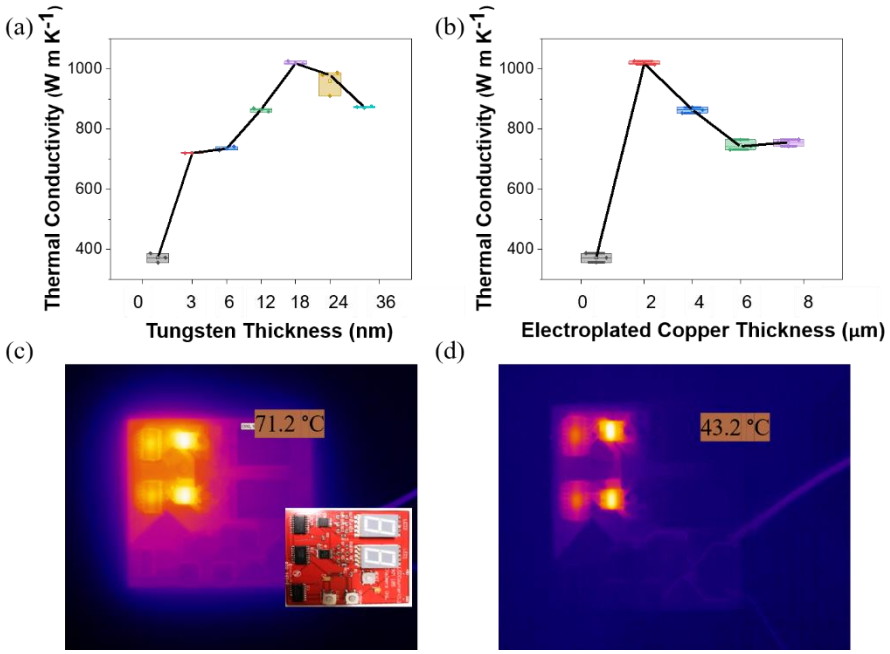

Figure 2-13. (a) Thermal conductivity of graphene/copper film with various tungsten thicknesses. (b) Thermal conductivity of graphene/copper film with various electroplating copper thicknesses. (c) Infrared image of the PCB with 3W heat loading (the image inset is the PCB). (d) Infrared image of the PCB with graphene/copper heat spreader and heat sink.

Then the surface motograph of the graphene/copper composite film was studied by X-Ray digital radiography. After composited with copper, the surface becomes densify and no porous was found, as shown in Figure 2-14 (a, b). With an input power of 10 W, compared with the reference copper-based heat pipe, the graphene/copper composite heat pipe demonstrated a 40% shorter start-up time and 2 times higher specific thermal transfer coefficient, see Figure 2-14 (c, d).

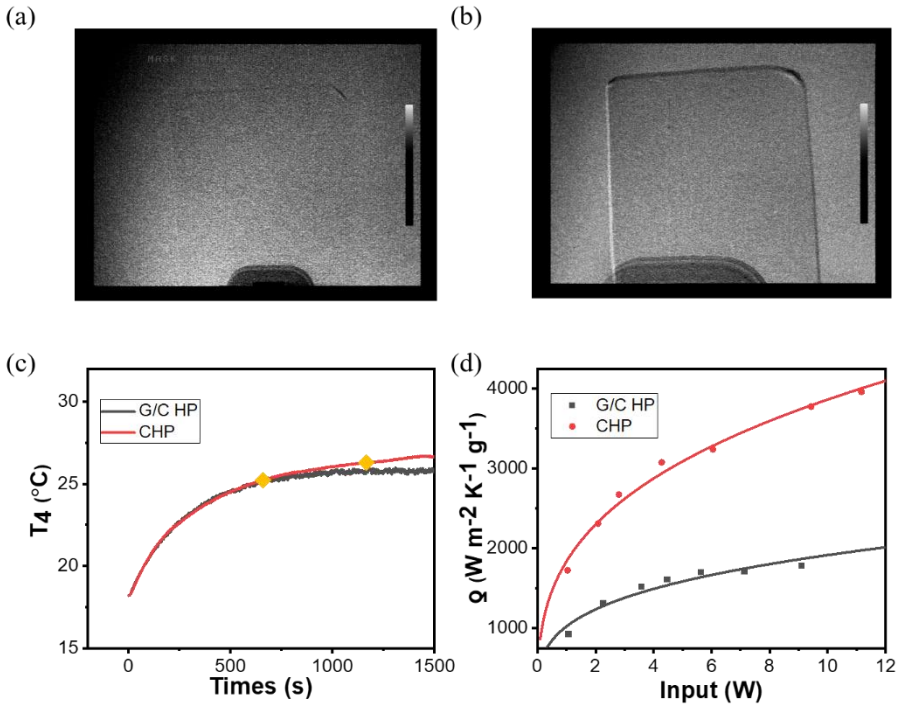

Figure 2-14. (a) The X-Ray image of graphene film. (b) The X-Ray image of graphene/copper film. (c) The start-up time of graphene/copper composite heat pipe and commercial copper-based heat pipe. (d) The specific thermal transfer efficiency of graphene/copper composite heat pipe and commercial copper-based heat pipe.

2.3 Hexagonal Boron Nitride Enhanced Heat Spreader

2.3.1 Introduction

With the rapid development of heat dissipation requirement in electronics and 5G communications, the interest in high thermal conductivity while electrically non-conductive material has significantly increased as they won't disturb the function of circuits when removing heat[47]. Currently, polymers have been widely developed for electrically non-conductive applications due to their flexibility and excellent electrical insulation properties[48]. However, the intrinsic thermal conductivity of polymers, such as epoxy and polyethylene, is usually below 1-2 W m^{-1} K^{-1}, which far below the thermal conductivity requirement for thermal interface materials (> 20 W m^{-1} K^{-1}), needless to say for heat spreaders (> 1000 W m^{-1} K^{-1})[48]. In this regard, incorporating thermal conductive while electrically insulative particles, for example, diamond, hexagonal boron nitride (h-BN), alumina (Al_2O_3), and aluminum nitride (AlN), etc., into the matrix is an effective strategy to improve the thermal conductivity of polymers[49]. Therefore,

the hexagonal boron nitride exhibits attractive advantages for thermally conductive while electrically insulation applications. The hexagonal boron nitride presents a thermal conductivity up to 751 W m^{-1} K^{-1} with a wide bandgap (5.97 eV), thus ensure high electrically insulation property. Meantime, building interconnected networks and aligning the conductive particles are two of the most effective strategies to achieve high thermal conductivity composites. Therefore, preparing conductive fillers into highly aligned fibers would be an effective strategy to realize high thermal conductivities.

In this work, h-BN were spun with polyvinylpyrrolidone (PVP) to prepare PVP/h-BN fibers. At first, the exfoliation technology and the geometry of the hexagonal boron nitride were optimized, and the result shows that nanoscale hexagonal boron nitride particles contribute to achieving higher thermal conductivity than the microscales. Further mechanical compression and UV-light curing were used to achieve a uniform PVP/h-BN composite film with improved mechanical strength. With the optimized hexagonal boron nitride particle geometry and loading, the in-plane thermal conductivity of the hexagonal boron nitride based heat spreader reaches 22 W m^{-1} K^{-1}, this value is comparable to most of the reported work. Notably, the electrospinning process is simple and scalable, exhibiting high potential for commercialization.

2.3.2 Materials and Experiments

2.3.2.1 Materials

Table 2-2. Materials

Name	Specifications	Manufacturers
Hexagonal Boron Nitride (h-BN)	99 wt.%	3M Technical Ceramics (U.S.A.) Co., Ltd.
Polyvinylpyrrolidone (PVP)	/	Sigma-Aldrich (Sweden) Trading Co., Ltd.
Carboxymethylcellulose Sodium (CMC)	/	Sigma-Aldrich (Sweden) Trading Co., Ltd.
Isopropanol (IPA)	98 wt.%	Sigma-Aldrich (Sweden) Trading Co., Ltd.
Absolute Ethanol	99.8 wt.%	Sigma-Aldrich (Sweden) Trading Co., Ltd.

2.3.2.2 Experiments

(1) Preparation of h-BN Nanosheets

The h-BN nanosheets (BNNS) are prepared by tip sonicated (VEVOR FS-1800N, Shanghai VEVOR Machinery Equipment Co., Ltd.) h-BN powder in the deionized water and isopropanol solution for 1 h with a frequency of 200 kHz. After that, the unexfoliated h-BN particles were removed by using a high-speed refrigerated centrifuge at 8000 rpm (CR22N, Hitachi Koki Himac Co., Ltd.), and the exfoliated BNNS were collected at 10000 rpm for 30 min.

(2) Preparation of PVP/h-BN Films

At first, 10 g BNNS powder was dissolved in 500 mL PVP solution (5-20 g mL^{-1}) at 50 °C. While electrospinning, the voltage was 13 kV, and the work distance between the collector and spinneret was 15 cm, see Figure 2-15. The injection flow was 0.3 mL h^{-1} controlled by a syringe pump. The fibers were spun with a 10% ambient humidity at room temperature. The aluminum foil coated on the connector was used to connect the fiber. After electro-spun, the PVPY/h-BN fibers can be easily removed by peeling off from the aluminum foil. After peeling off, the freestanding PVP/h-BN fibers suffer from mechanical press under 15 Mpa for 10 min to be densified.

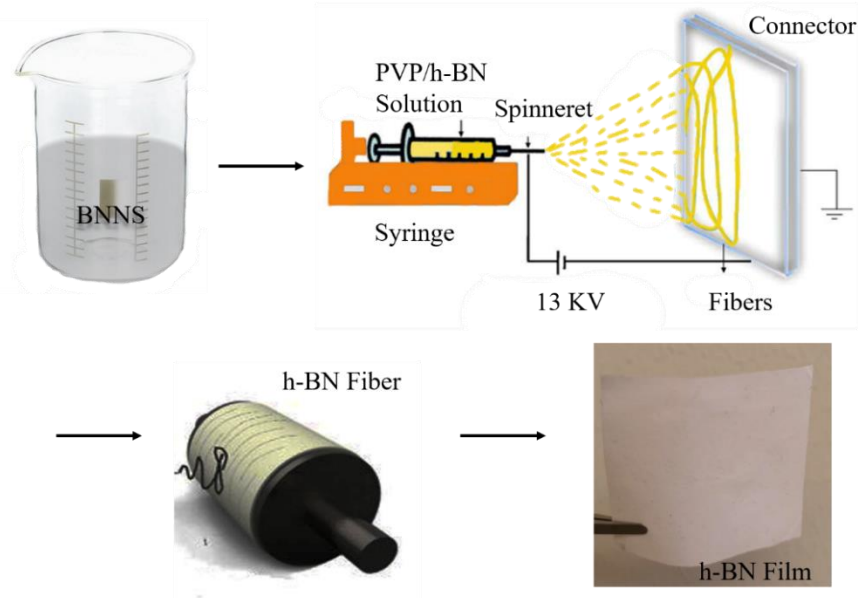

Figure 2-15. Schematic of the preparation of PVP/h-BN fiber by electrospinning.

(3) Preparation of h-BN/CMC Film

For fabrication of CMC composite film, CMC powder (M.W 700000) was dissolved in distilled water at 50 ℃ at first. Then the BNNS dispersion (10 mg mL^{-1}) was dropped into the CMC solution. After that, the CMC solution with BNNS was cast into a Φ25 cm cell-culture dish. After drying under 60 ℃, the free-standing CMC/BNNS composite film is obtained by peeling off from the cell-culture dish.

2.3.2.3 Characterization

(1) Field Emission Scanning Electron Microscopy (FESEM)

FESEM observation was conducted on a Zeiss Supra 60 VP microscope to assess the alignment of the electrospun fiber. The acceleration voltage is 15 kV. To observe the alignment of h-BN in the PVP/h-BN fiber, the samples were sintered at 600 ℃ for 3 h to expose the bare h-BN scaffolds.

(2) Transmission Electron Microscopy (TEM)

TEM (Tecnai G^2 20, USA) is operated at an acceleration voltage of 200 kV to show the microstructure of graphene oxide sheets. The tested solution is diluted to 1 mg mL^{-1}, and dropped on lacey support films, and further dried under 60 ℃ in an oven.

(3) Specific Heat Capacity

Specific heat capacity (C_p, J Kg^{-1} K^{-1}) analysis was performed using the transient plane source method (TPS 2500s, Hot disk, Sweden) with a Kapton Sensor (14.67 mm). The sample was cut into Φ5 cm.

(4) In-plane Thermal Conductivity

The in-plane thermal diffusivities (D, mm^2 s^{-1}) were determined by the laser flash method (LFA-467, NETZSCH, Germany), see Figure 2-16 (a). The sample was coated with graphite. In this method, the thermal diffusivity (D) is given by:

$$D = 0.1388 \times d^2/t_{1/2} \quad \text{2-17}$$

Where, $t_{1/2}$is the half maximum (s), d is the thickness of the sample (mm)[20].

The density (ρ, g cm^{-1}) was calculated by weight divided volume. Thermal conductivity $k_{\parallel}$ (W m^{-1} K^{-1}) was given by[39]

$$k_{\parallel} = \rho \times C_p \times D \quad \text{2-18}$$

(5) Through-plane Thermal Conductivity

The through-plane thermal conductivity was determined by the steady-state heat-flow strategy, see Figure 2-16 (b).

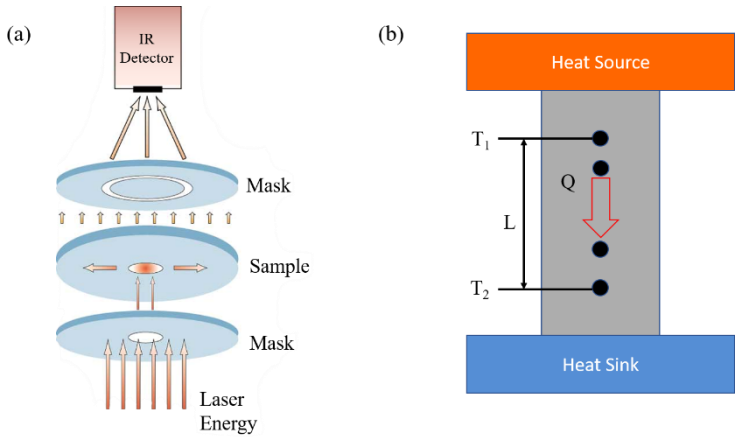

Figure 2-16. (a) Schematic representation of the laser flash method. (b) Schematic representation of the steady-state heat-flow method.

In this method, the total thermal resistance of samples with varied thicknesses was measured as R by the following equation:

$$R = R_{c1} + R_{c2} + C/k_{\perp} \quad 2\text{-}19$$

Where, R_{c1} and R_{c2} is the interface thermal resistance on top and bottom surface, $k_{\perp}$ is the through-plane thermal conductivity, C is the thickness[39].

(6) Thermal Dissipation Performance

The surface temperature profile was captured by infrared thermography (FLIR-A655 SC). A model similar to the thermal package in practical applications was used to determine the cooling performance of the PVP/h-BN heat spreader, see Figure 2-17. The diffusivity was calibrated as 0.98. While measuring, a DC heater (RS component Co., Ltd., Sweden) was used as the heat source, which was connected to a DC power supply (E3612A, Agilent, USA). The sample was attached to the heat mat by a thin layer of thermal grease (TG100, Loctite, 3 W m^{-1} K^{-1}, China). Plastic foams were used on the bottom and up to minimize thermal leakages.

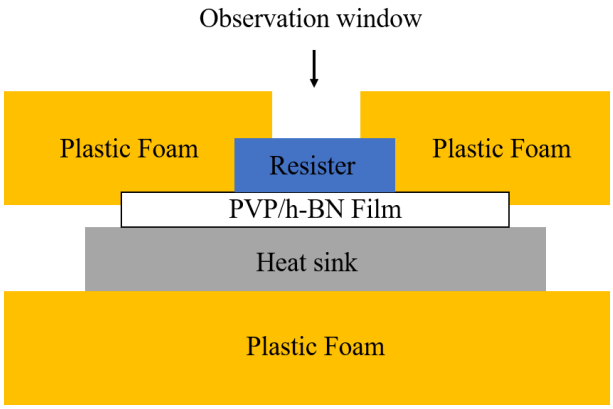

Figure 2-17. The setup for infrared thermal camera measurement.

2.3.3 Results and Discussions

2.3.3.1 Preparation of Hexagonal Boron Nitride Nanosheets

A water/isopropanol solution was used as the media for exfoliating boron nitride nanosheets (BNNS). Because the exfoliation efficiency is largely dependent on the surface tension of the solvent, the solvent volume ratio between distilled water and isopropanol is optimized at first. Results show that 30 vol.% isopropanol solution provides the most stable and highest exfoliation efficiency for BNNS, see Figure 2-18 (a, b).

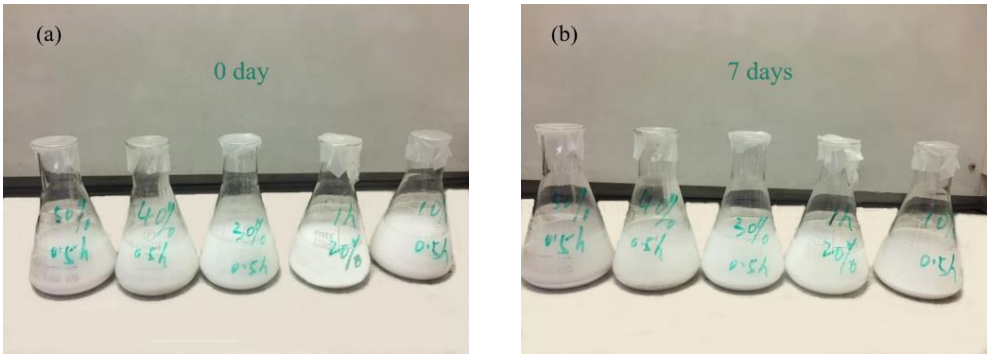

Figure 2-18. Optical images of the h-BN dispersion with different solvents (a) 0 day after exfoliation and (b) seven days after exfoliation.

Next, the SEM and the AFM were used to observe the morphology of the h-BN and BNNS. The pristine h-BN flakes show a size around 1-5 μm with a layer accumulation structure, as shown in Figure 2-19 (a, b).

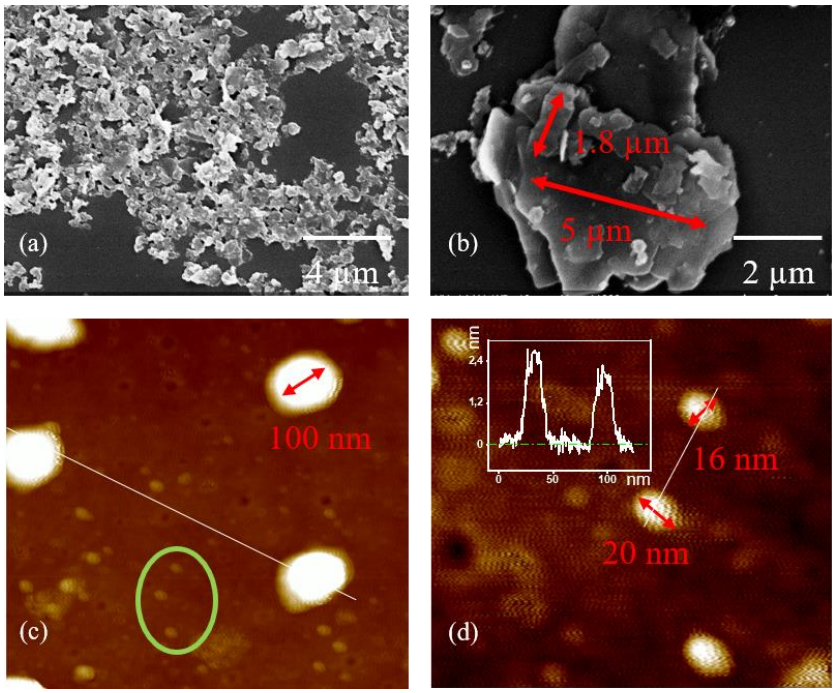

Figure 2-19. (a) The SEM photography of the unexfoliated h-BN powder. (b) The high-resolution SEM photography of the unexfoliated BN powder. (c) The AFM image of BNNS. (d) The high-resolution AFM image of BNNS, the insets are height profiles.

After mechanical exfoliation, the morphology of h-BN changed from irregular polygon to ellipse after strong mechanical exfoliation, and the edge of pristine h-BN sheets becomes smooth. As shown in Figure 2-19 (c, d), the geometry of BNNS is 10-100 nm with a thickness of about 2-20 nm. Accordingly, the thickness of a single-layer atom is around 0.33 nm, the prepared BNNS are piled up by a few to tens layers of single layer h-BN nanosheets[46].

Figure 2-20 (a) is the XPS full survey of BNNS. Except for boron and nitride, a significant oxygen peak can be observed at the position of 531 eV. XPS peak analyses were used to further understand the chemical structure of oxygen. As shown in Figure 3-20 (b, c), oxygen is introduced to h-BN sheets after exfoliation. Both boron and nitride have combined with oxygen with the specific peaks at 198 eV and 405 eV, respectively.

To study the influence of h-BN geometry, BNNS/CMC composite films were explored at first. FTIR was used to analyze the chemical bonding between CMC and BNNS, as shown in Figure 2-20 (d). Compared with CMC-BN, the peak at the position of 1598 cm^{-1} disappear on the FTIR spectra of CMC-BNNS. This peak corresponding to the C=O group, indicating the covalent binding between CMC and BNNS.

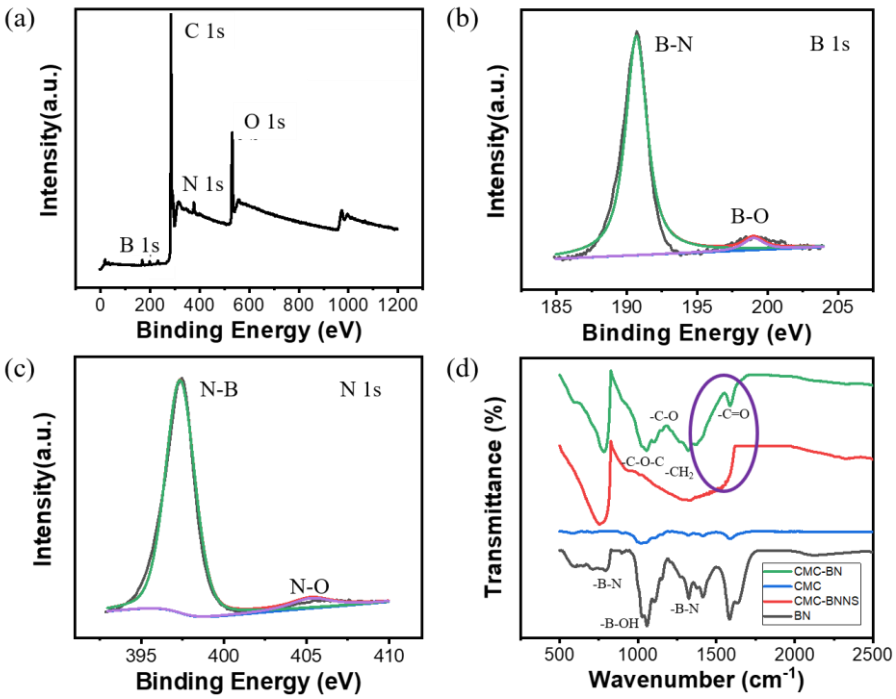

Figure 2-20. (a) The XPS full survey of BNNS. (b) The B 1s XPS spectra. (c) The N 1s XPS spectra. (d) The FTIR spectrum of pristine BN, CMC, CMC/h-BN, and CMC/BNNS.

With an additive loading from 0 to 5 wt.%, the CMC/BNNS shows the highest in-plane thermal conductivity, while CMC/h-BN shows the lowest in-plane thermal conductivity, as shown in Figure 2-21 (a, b). Thus, the BNNS shows overwhelming advantages as conductive fillers than BN and BN+BNNS composites.

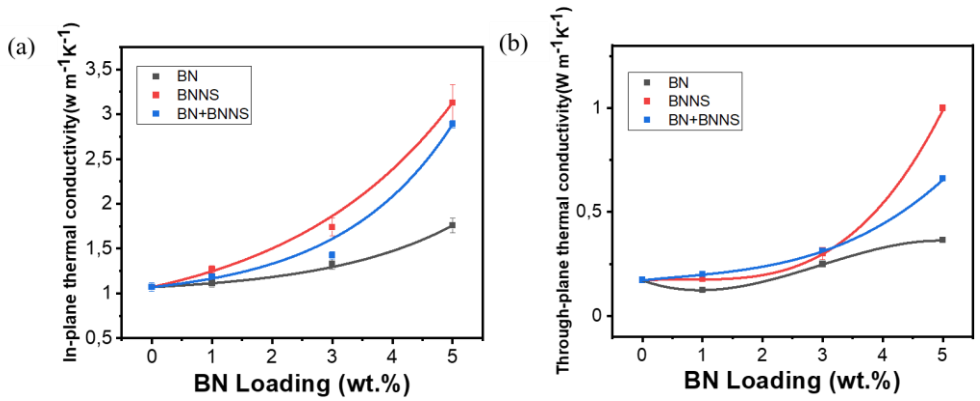

Figure 2-21. (a) The in-plane thermal conductivity of the unexfoliated BN, BNNS, and BN+BNNS based composite film with different BN loading. (b) The through-plane thermal conductivity of the unexfoliated BN, BNNS and BN+BNNS based composite film with different BN loading.

2.3.3.2 Preparation of Hexagonal Boron Nitride Based Fiber

As shown in Figure 2-22 (a, b), the diameter of the PVP/h-BN fiber is 6 μm.

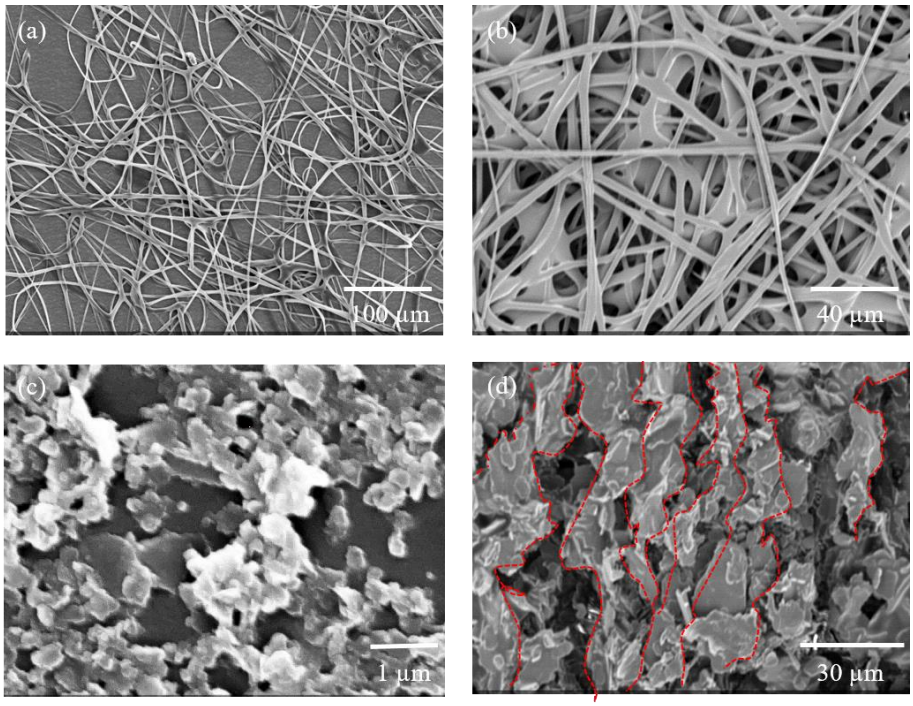

Figure 2-22. The morphology of PVP/h-BN fiber with (a) low and (b) high resolutions. (c) The morphology of h-BN composite film by mechanical pressing h-BN powder. (d) The morphology of h-BN fiber film (after sintering at 600 °C for 3 h). The inset is the element mapping of h-BN film.

To verify the alignment of the BNNS in PVP/h-BN fibers, the PVP/h-BN fiber was calcinated to expose the BNNS frameworks. In comparison, the PVP/h-BN electrospinning solution was dried under the same sintering. As shown in Figure 2-22 (c, d), the h-BN sheets in PVP/h-BN fiber are well aligned and form an interconnected network, while the BNNS randomly aligned in the reference one. Therefore, the electrospinning can effectively align the BNNS for improving thermal conductivity.

2.3.3.3 Heat Dissipation Performance of Hexagonal Boron Nitride Enhanced Heat Spreader

The heat capacity of the PVP/h-BN is measured as 0.77 J Kg^{-1} K^{-1} by hot disk, as shown in Figure 2-23 (a). Similar with graphene, the in-plane thermal conductivity of PVP/h-BN composite film decreased with increasing film thickness, which is a result of the increase of thermal interface resistance between BNNS and adjacent layers.

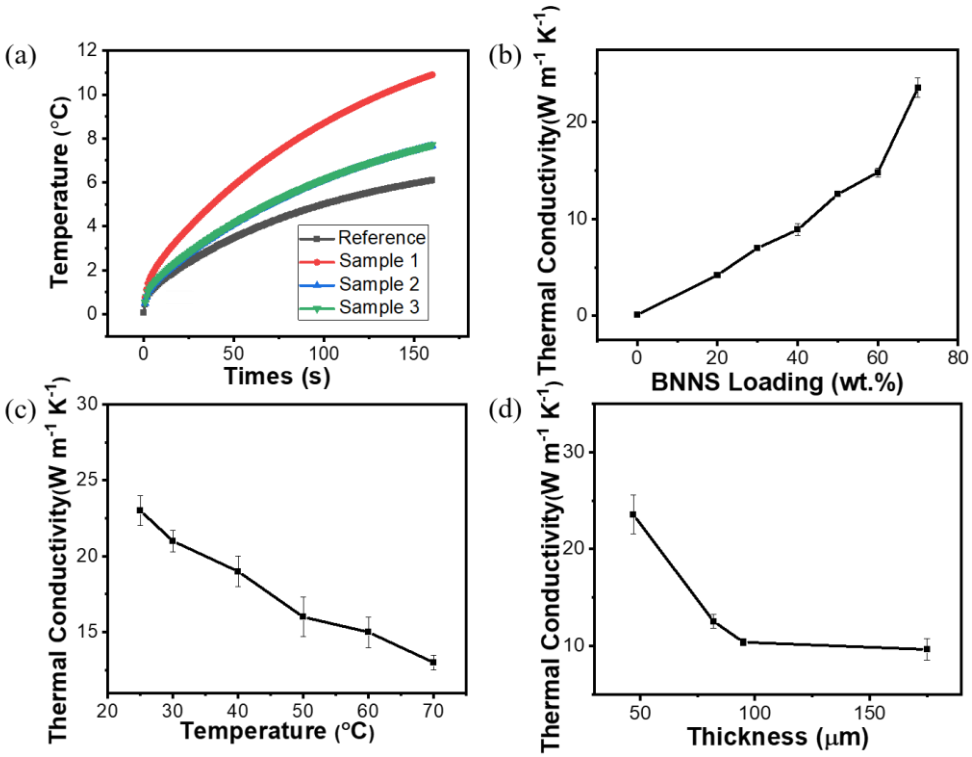

Figure 2-23. (a) The heat capacity of PVP/h-BN composite film. (b) The in-plane thermal conductivity of PVP/h-BN composite film with different BNNS loading. (c) The in-plane thermal conductivity of PVP/h-BN composite film at different temperatures. (d) The in-plane thermal conductivity of PVP/h-BN film with various thicknesses.

As shown in Figure 2-23 (b, d), the in-plane thermal conductivity of this PVP/h-BN film reaches 22 W m^{-1} K^{-1} at a thickness of 40 μm with 70 wt.% h-BN loadings. Notably, with the electrospinning process, the filler loading of PVP/h-BN composite film can go up to 70 wt.% without breaking, which is 3 times higher than that of the casting method. However, the thermal conductivity of the PVP/h-BN heat spreader decreases with increasing temperature in the range 20-70 °C, see Figure 2-23 (c).

Similarly, the through-plane thermal conductivity of PVP/h-BN composite film reduces when increasing the film thickness, as shown in Figure 2-24 (a). Unlike in-plane behaviors, the through-plane thermal conductivity of the PVP/h-BN composite film reaches a maximum of is 0.485 W m^{-1} K^{-1} at 60 wt.% h-BN loadings, more than 5 times higher than the referenced PVP fiber, see Figure 2-24 (b). Notably, if measured by the laser flash method, the thermal conductivity of the same PVP/h-BN composite film is 7 W m^{-1} K^{-1}. Although the laser flash method is the most widely used method to evaluate thermal conductivity in publications, it loses accurateness when determining the

through-plane thermal conductivity for relatively thin films. For example, the minimax thickness for graphene film is approximately a few hundred micrometers. As to the through-plane thermal conductivity, results by the steady-state method are more correspond to practical applications. While in the steady-state method, the thickness changes after mechanical pressed should take into consideration for calculation. Thus, the through-plane thermal conductivity is a reference, the practical cooling capability is usually determined by an infrared camera.

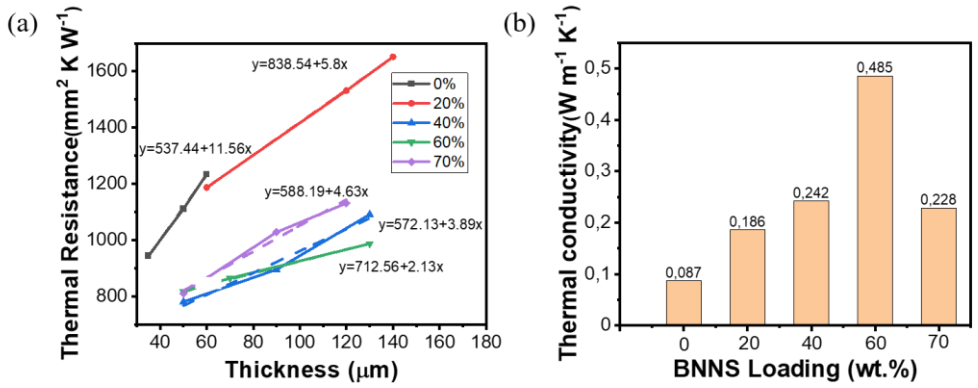

Figure 2-24. (a) Thermal resistance and its linear fit curves of PVP/h-BN film with different h-BN loading. (b) Extracted through-plane thermal conductivities of PVP/h-BN films with different h-BN loading.

Finally, to verify the heat dissipation performance in practical applications, the PVP/h-BN composite film was used as a heat spreader to cool down a thermal resister in a simulated environment of thermal package. Consequently, the case with oriented PVP/h-BN fibers manages to cool the resister by 10 °C than the reference case, see Figure 2-25 (a, b). This demonstrates that our PVP/h-BN film presents outstanding cooling capacity while using as heat spreaders for thermal packages.

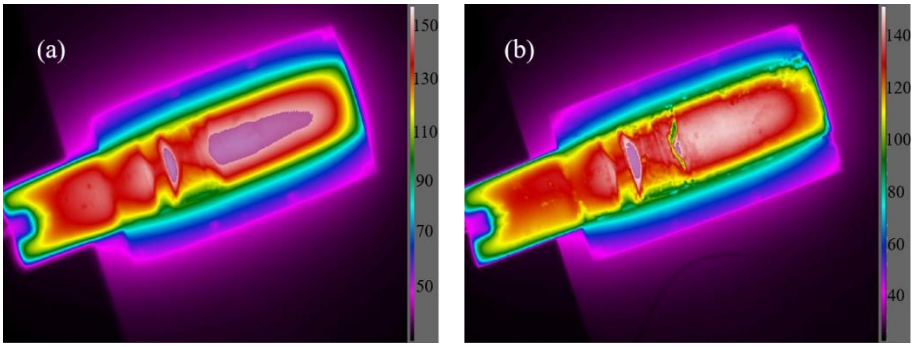

Figure 2-25. (a) The temperature distribution profile of a 4 W heater with PVP/h-BN composite film. (b) The temperature distribution profile of a 4 W heater without PVP/h-BN composite film.

2.4 Summary

In this chapter, we have explored the application of using graphene-like 2D materials for heat dissipation.

At first, we have demonstrated, for the first time, the application of using graphene as constructive parts in heat pipes for cooling purposes. With an optimized wick structure, the graphene enhanced heat pipe exhibits a specific thermal transfer coefficient as high as 7230 W m^{-2} K^{-1} g^{-1}, which is 3.5 times higher than the well-designed commercial copper-based heat pipe. In addition, a heat transfer model was built to evaluate the heat transfer model for the graphene enhanced heat pipe. Further, to improve the reliability of graphene enhanced heat pipe, graphene/copper composite heat pipe was fabricated with an optimized interface between graphene and copper. This work broadens the possibility of using graphene for heat dissipation, especially in situations where lightweight is required as a priority, such as power systems, avionics, space electronics, automotive electronics, etc.

Secondly, we prepared a non-conductive thermal heat spreader using a PVP/h-BN composite film by electrospinning. At an h-BN loading of 70 wt.%, the prepared PVP/h-BN composite film exhibits an in-plane thermal conductivity up to 22 W m^{-1} K^{-1}, higher than the industrial requirement for electrically heat spreaders. Whereas more than 5 times improved through-plane thermal conductivity was achieved at a 60 wt.% h-BN loading. The heat spreading performance was demonstrated for the PVP/h-BN composite film by deploying it between a heater and heatsink, similar to the thermal package in practical applications. The result shows the integration of the PVP/h-BN composite film decreased the temperature by 10 ℃. Thus, this electrospinning method extends the application of polymer based composite film as a non-conductive heat spreader.

Reference

[1] Fu Y. F., Hansson J., Liu Y., et al. Graphene related materials for thermal management [J]. 2D Mater., 2020, 7(1): 012001.

[2] Manno M., Yang B., Khanna S., et al. Microcontact-enhanced thermoelectric cooling of ultrahigh heat flux hotspots [J]. IEEE T. Comp. Pack. Man., 2015, 5(12): 1775-1783.

[3] Chen S. S., Moore A. L., Cai W. W., et al. Raman measurements of thermal transport in suspended monolayer graphene of variable sizes in vacuum and gaseous environments [J]. Acs Nano, 2010, 5(1): 321-328.

[4] Cai W., Moore A. L., Zhu Y., et al. Thermal transport in suspended and supported monolayer graphene grown by chemical vapor deposition [J]. Nano Lett., 2010, 10(5): 1645-1651.

[5] Han N., Viet C. T., Han M., et al. Improved heat dissipation in gallium nitride light-emitting diodes with embedded graphene oxide pattern [J]. Nat. Commun., 2013, 4: 1452.

[6] Xin G. Q., Sun H. T., Hu T., et al. Large-area freestanding graphene paper for superior thermal management [J]. Adv. Mater., 2014, 26(26): 4521-4526.

[7] Liang Q., Yao X., Wang W., et al. A three-dimensional vertically aligned functionalized multilayer graphene architecture: an approach for graphene-based thermal interfacial materials [J]. Acs Nano, 2011, 5(3): 2392-2401.

[8] Malekpour H., Chang K. H., Chen J. C., et al. Thermal conductivity of graphene laminate [J]. Nano Lett., 2014, 14(9): 5155-5161.

[9] Goli P., Ning H., Li X., et al. Thermal properties of graphene-copper-graphene heterogeneous films [J]. Nano Lett., 2014, 14(3): 1497-1503.

[10] Zhang H. B., Zheng W. G., Yan Q., et al. Electrically conductive polyethylene terephthalate/graphene nanocomposites prepared by melt compounding [J]. Polymer, 2010, 51(5): 1191-1196.

[11] Sadeghinezhad E., Mehrali M., Rosen M. A., et al. Experimental investigation of the effect of graphene nanofluids on heat pipe thermal performance [J]. Appl. Therm. Eng., 2016, 100: 775-787.

[12] Shtein M., Nadiv R., Buzaglo M., et al. Graphene-based hybrid composites for efficient thermal management of electronic devices [J]. Acs Appl. Mater. Inter., 2015, 7(42): 23725-23730.

[13] Zhang Y., Edwards M., Samani M. K., et al. Characterization and simulation of liquid phase exfoliated graphene-based films for heat spreading applications [J]. Carbon, 2016, 195-201.

[14] Savvatimskiy A. I. Measurements of the melting point of graphite and the properties of liquid carbon (a review for 1963–2003) [J]. Carbon, 2005, 43(6): 1115-1142.

[15] Trefethen L. On the surface tension pumping of liquids or a possible role of the candlewick in space exploration [J]. GE Tech. Info., 1962, 615: D114.

[16] Zohuri B. Heat pipe design and technology [M]. Boca Raton, 2011.
[17] Zohuri B., Heat pipe design and technology: modern applications for practical thermal management [M]. Springer, 2016.
[18] Yang X., Yan Y., Mullen D. Recent developments of lightweight, high performance heat pipes [J]. Appl. Therm. Eng., 2012, 33: 1-14.
[19] Vasiliev L. L. Heat pipes in modern heat exchangers [J]. Appl. Therm. Eng., 2005, 25(1): 1-19.
[20] Liu Y., Chen S. J., Fu Y. F., et al. A light-weight and high thermal performance graphene heat pipe [J]. Nano Select, 2020, 2(2): 364-372.
[21] Rassamakin B., Khairnasov S., Zaripov V., et al. Aluminum heat pipes applied in solar collectors [J]. Sol. Energy, 2013, 94: 145-154.
[22] Zuo Z., Faghri A. A network thermodynamic analysis of the heat pipe [J]. Int. J. Heat Mass Tran., 1998, 41(11): 1473-1484.
[23] Czerwinski F. Magnesium alloys: corrosion and surface treatments [M]. Academic, 2011.
[24] Narendra B. N., Kamath H. C. Materials used in heat pipe [J]. Mater. Today Proceedings, 2015, 2(4-5): 1469-1478.
[25] Xin G., Yao T., Sun H., et al. Highly thermally conductive and mechanically strong graphene fibers [J]. Science, 2015, 349(6252): 1083-1087.
[26] Xiong Z., Wang X., Lee K. H. K., et al. Thermal transport in supported graphene nanomesh [J]. Acs Appl. Mater. Inter., 2018, 10(11): 9211-9215.
[27] Pulizzi F., Bubnova O., Milana S., et al. Graphene in the making [J]. Nat. Nanotechnol., 2019, 14(10): 914-918.
[28] Cai Q., Scullion D., Gan W., et al. High thermal conductivity of high-quality monolayer boron nitride and its thermal expansion [J]. Sci. Adv., 2019, 5(6): eaav0129.
[29] Tritt T. M. Thermal conductivity: theory, properties, and applications [M]. Springer, 2005.
[30] Barani Z., Mohammadzadeh A., Geremew A., et al. Thermal properties of the binary-filler hybrid composites with graphene and copper nanoparticles [J]. Adv. Funct. Mater., 2020, 30(8): 1904008.
[31] Meng X., Pan H., Zhu C., et al. Coupled chiral structure in graphene-based film for ultrahigh thermal conductivity in both in-plane and through-plane directions [J]. Acs Appl. Mater. Inter., 2018, 10(26): 22611-22622.

[32] Xu Y., Li Z., Duan W. Thermal and thermoelectric properties of graphene [J]. Small, 2014, 10(11): 2182-2199.
[33] Wang N., Samani M. K., Li H., et al. Tailoring the thermal and mechanical properties of graphene film by structural engineering [J]. Small, 2018, 14(29): 1801346.
[34] Peng L., Xu Z., Liu Z., et al. Ultrahigh thermal conductive yet superflexible graphene films [J]. Adv. Mater., 2017, 29(27): 1700589.
[35] Sastri V. S. Green corrosion inhibitors: theory and practice [M]. John Wiley & Sons, 2012.
[36] Böhm S. Graphene against corrosion [J]. Nat. Nanotechnol., 2014, 9(10): 741-742.
[37] Seol J. H., Jo I., Moore A. L., et al. Two-dimensional phonon transport in supported graphene [J]. Science, 2010, 328(5975): 213-216.
[38] Yao G., Duan T., Chi E., et al. Microbeam two-dimensional small-angle X-ray scattering investigating the effects of reduced graphene oxide on local microstructures of high-density polyethylene/reduced graphene oxide nanocomposite bars [J]. Roy. Soc. Open Sci., 2019, 6(2): 181866.
[39] Liu Y., Wang N., Ye L., et al., Thermally conductive and electrically insulating PVP/Boron nitride composite films for heat spreader [C]. International Microelectronics Assembly and Packaging Society, 2019, 1-5.
[40] Vazquez G., Alvarez E., Navaza J. M. Surface tension of alcohol water + water from 20 to 50 °C [J]. J. Chem. Eng. Data, 1995, 40(3): 611-614.
[41] Chi S. Heat pipe theory and practice [M]. Hemi, 1976.
[42] Lokteva I., Koof M., Walther M., et al. Monitoring nanocrystal self-assembly in real time using in situ small-angle X-ray scattering [J]. Small, 2019, 15(20): 1900438.
[43] Wang S., Zhang W., Zhang X., et al. Study on start-up characteristics of loop heat pipe under low-power [J]. Int. J. Heat Mass Tran., 2011, 54(4): 1002-1007.
[44] Tye R. P., Thermal conductivity [M]. Academic Press, 1969.
[45] Vetere A. The riedel equation [J]. Ind. Eng. Chem. Res., 1991, 30(11): 2487-2492.
[46] Nemes-Incze P., Osváth Z., Kamarás K., et al. Anomalies in thickness measurements of graphene and few layer graphite crystals by tapping mode atomic force microscopy [J]. Carbon, 2008, 46(11): 1435-1442.
[47] Vu M. C., Kim I. H., Choi W. K., et al. Highly flexible graphene derivative hybrid film: an outstanding nonflammable thermally conductive yet electrically insulating

material for efficient thermal management [J]. Acs Appl. Mater. Inter., 2020, 12(23): 26413-26423.

[48] Wang Y., Wu W., Drum M. R. D., et al. Achieving a 3D thermally conductive while electrically insulating network in polybenzoxazine with a novel hybrid filler composed of boron nitride and carbon nanotubes [J]. Polymers, 2020, 12(10): 2331.

[49] Ralphs M., Kong W., Wang R. Y., et al. Thermal conductivity enhancement of soft polymer composites through magnetically induced percolation and particle-particle contact engineering [J]. Adv. Mater. Interfaces, 2019, 6 (6): 1801857.

CHAPTER 3

Graphene-like 2D Materials for Energy Storage

3.1 Introduction

The large theoretical surface area (2630 m^2 g^{-1}) and ultrahigh electrical conductivity of graphene-like 2D materials have attracted extensive investigation in energy storage, such as Lithium-ion batteries and supercapacitors[1]. Compared to the Lithium-ion battery, the supercapacitor shows advantages as rapid discharge-charge, safe working, low cost, and high-power density, etc.[2] In the supercapacitor, energy is stored by forming a double layer of conductive electrodes and released by the positive and negative ions moves between the electrodes[2, 3]. Therefore, the capacity is largely related to the surface area of electrodes. For this reason, graphene shows great potential to boost the capacity of supercapacitor s due to its ultrahigh electrical conductivity and large surface area[3].

While with the rapid development of consumer electronics, the requirement for thinner, lighter, and flexible supercapacitors is drastically increased. Compared to the traditional three electrodes supercapacitor, the micro-supercapacitor (MSCs) possesses remarkable advantages of ultra-small volume and high electrochemical capacity[15]. Although the MSCs and conventional supercapacitors share the same working principle, the MSCs predominately use an on-chip interdigitated structure while conventional supercapacitors employ vertical sandwich structures[2]. Generally, the width of electrodes in MSCs is within a micrometer scale, such as 25 μm[16]. Coupled with the urgent demand for replacing silicon wafers in next-generation silicon transistors, graphene is highly expected as the alternative for silicon because of its high field velocity[17].

This chapter described two methods of using graphene for supercapacitors, involving 3D graphene foam enhanced supercapacitors electrodes and graphene film enhanced MSCs. In 3D graphene foam enhanced supercapacitors, N, S, Si doping was used to improve its wettability in electrolytes. Density Functional Theory indicates that the introduction of heteroatoms effectively interrupts the balanced electron distribution, and thus improves the electrochemical properties. In MSCs, this work firstly explored the

possibility of replacing silicon wafers with flat graphene assembled films, which were commercialized by some vendors in a small batch. Additionally, the microelectronic severely suffers from heat dissipation issues. The replacement of silicon wafer with graphene assembled film can largely improve heat dissipation of microelectronic because the thermal conductivity of graphene assembled film is more than 10 times (1500-2000 W m^{-1} K^{-1}) higher than that of the silicon wafer (130 W m^{-1} K^{-1}). In this regard, the graphene assembled film can work as a heat spreader for the following package process, thus decreases the cost and saves spaces for microelectronics.

3.2 Graphene Enhanced Electric Double-Layer Capacitor

3.2.1 Introduction

In terms of the working mechanism, supercapacitor s can be mainly divided into two types: pseudocapacitors and electric double-layer capacitors (EDLCs)[4-6]. The pseudocapacitors are called faradic capacitors. In principle, the pseudocapacitors store energy through the redox reaction between the active materials and the electrolytes, a faradic process[1]. While in EDLCs, energy is stored and released by forming a double layer of conductive electrodes and ion adsorptions in between them, see Figure 3-1[2, 3]. In EDLCs, no electron transfers across the electrode, thus is so-called non-faradic process.

For EDLCs, the specific capacity (C in F g^{-1}) of each electrode is calculated by the equation as below[8]:

$$C = \varepsilon_r \varepsilon_o A/dm \qquad 3\text{-}1$$

where ε_r is the relative permittivity, ε_o is the vacuum permittivity (8.85×10^{-12} F m^{-1}), d represents the Debye length, m is the mass of active materials, and A is the specific surface area of the electrode[9, 10].

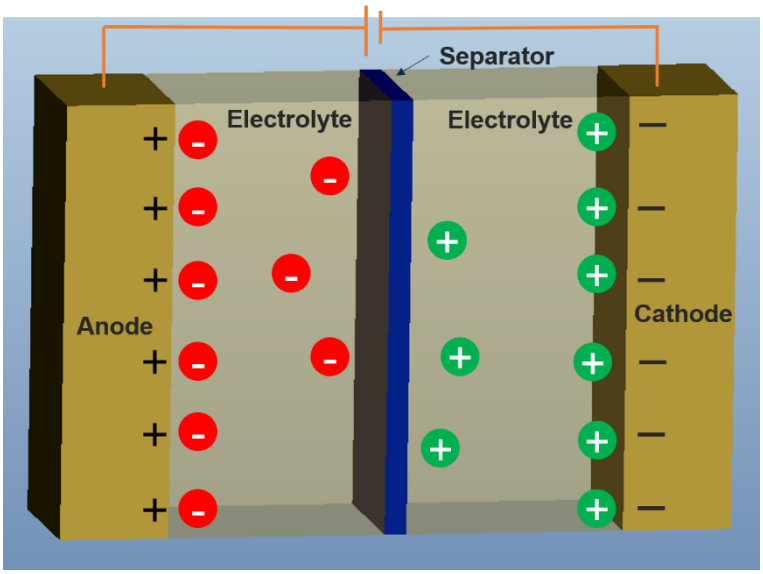

Figure 3-1. Schematic representation of supercapacitors.

Therefore, a large specific area and lower Debye length contribute to improving the specific capacity of EDLCs[11]. For this reason, graphene shows great potential to boost the capacity of supercapacitors due to its ultrahigh conductivity and large surface area[3].

On the other hand, although graphene displays attractive electrical performance, a single piece of graphene is too delicate to generate significant functions in supercapacitors[18]. In addition, graphene sheets inevitably suffer from agglomeration and weak interface contact with electrolytes[8]. These two features dramatically decrease the realistic electrochemical capacity of graphene as electrodes. For example, theoretical calculation indicates graphene can deliver a gravimetric capacitance up to 550 F g^{-1}, while the specific capacity of graphene based supercapacitor usually below 150 F g^{-1}[3, 8]. To cope with these re-stacking and poor wettability issues, building 3D dimensional hydrophilic structures is one of the effective strategies to improve the specific capacity of graphene based supercapacitors[3].

In this section, a simple soft foam template strategy was used to prepare highly hydrophilic graphene foam as an electrode in the supercapacitor. The unique porous structure, low ohm resistance, doping and high electrical mobility largely increase the electrochemical behaviors and thus achieve ultrahigh specific capacitance, excellent cycling stability, and rate capability. Density functional theory simulation firstly reveals the reason why increase polarity in graphene can improve wettability.

3.2.2 Materials and Experiments

3.2.2.1 Materials

Table 3-1. Materials

Name	Specifications	Manufacturers
Flake Graphite	95 wt.%, 100-mesh	Sigma-Aldrich (Shanghai) Trading Co., Ltd.
Potassium Permanganate ($KMnO_4$)	Analytically	Sinopharm Chemical Reagent Co., Ltd.
Concentrated Sulfuric Acid (H_2SO_4)	98 wt.%	Sinopharm Chemical Reagent Co., Ltd.
Hydrogen Peroxide (KOH)	30 wt.%	Sinopharm Chemical Reagent Co., Ltd.
Egg Albumen	/	
Nickel Foam	/	Sinopharm Chemical Reagent Co., Ltd.
Acetone ($(CH_3)_2CO$)	99 wt.%	Sinopharm Chemical Reagent Co., Ltd.
Hydrochloric Acid (HCl)	37 wt.%	Sinopharm Chemical Reagent Co., Ltd.
Absolute Ethanol (C_2H_6O)	99.8 wt.%	Sinopharm Chemical Reagent Co., Ltd.
Polytetrafluoroethylene (PTFE) Solution	60 wt.%	Sigma-Aldrich (Shanghai) Trading Co., Ltd.

3.2.2.2 Experiments

(1) Preparation of Graphene Oxide

At first, graphite powder (13 g) and $KMnO_4$ (39 g) were homogenously dispersed in 500 mL concentrated sulfuric acid within an ice bath for deep oxidation. Next, 78 mL H_2O_2 was added into the suspension to intermediate the soluble sulfate and reduce the residual oxidants. Then the graphene oxide was collected by centrifugation at 10000 rpm

until the pH value become seven. Finally, the purified graphene oxide was suffered from mechanical exfoliation to achieve a 2 wt.% graphene oxide dispersion[8].

(2) Preparation of Graphene Foam

In a typical procedure, the egg albumen foam was prepared by strong mechanical stirring (6000 rpm, 20 min)[8]. Then, a graphene oxide dispersion (2-10 mg mL^{-1}) was added into the foams to obtain a uniform soft graphene oxide foam. Subsequently, the graphene oxide foam was dried under 60 °C for 2 h. After that, the solidified graphene oxide foam was calcinated at 600-900 °C under a nitrogen atmosphere for 2 h. As a result, the graphene oxide foam was reduced to graphene foam. Simultaneously, the egg albumen was removed by chemical decompositions[8].

(3) Preparation of Graphene Foam Electrode

At first, the nickel foam was subsequently ultrasonicated in $(CH_3)_2CO$ (10 min), HCl (10 min), C_2H_6O (30 min), and H_2O (30 min). After drying, the nickel foam was annealed at 1000 °C for 2 h under a nitrogen atmosphere[8]. After that, the oxidates on nickel foam are believed to be removed. Then the graphene oxide foam slurry was homogeneously coated on the nickel foam to be solidified (Ni-GOF). After that, the Ni-GOF was annealed for 2 h under a nitrogen atmosphere to obtain freestanding graphene foam electrodes (GF-Ni). The mass loading of graphene was calculated as 0.7 mg. As a reference, graphene foam was mixed with 0.5 wt.% PTFE solution to fabricate reference electrodes[8].

3.2.2.3 Characterization

(1) Rheological Behaviors

Rheological performances were carried out on a HAAKE MARS III rotary rheometer (Thermo Fisher, USA) under frequency sweep and steady shear scanning mode. The oscillation frequency sweep was performed at 25 °C from 20 to 0.1 Hz[8].

(2) Fourier Transform Infrared Spectroscopy (FTIR)

The chemical structures were identified by FTIR (NEXUS 6700, Thermo Fisher, USA), scanning from 4000 to 500 cm^{-1}. The sample is prepared by grounding with KBr powder for 10 min and pressed into pellet under 10 Mpa for 1 min[8].

(3) Field Emission Scanning Electron Microscopy (FESEM)

The micro morphologies were observed under FESEM (Ultra 55, Zeiss, Germany) with acceleration voltage 6-12 KV. The sample was attached to the conductive tape[8].

(4) Energy Dispersive X-Ray Spectroscopy (EDX)

EDX is conducted with FESEM (Ultra 55, Zeiss, Germany) under acceleration voltage 6-12 KV, and EDX (IXRF, USA) to analyze the element distributions[8].

(5) Transmission Electron Microscopy (TEM)

TEM (Tecnai G^2 20, USA) is operated at an acceleration voltage of 200 kV to show the microstructure of graphene oxide sheets. To prepare the sample, the graphene solution is dispersed by ultrasonic, diluted to 1 mg mL^{-1}, and dropped on lacey support films with further drying under 60 °C[8].

(6) X-Ray Photoelectron Spectroscopy (XPS)

XPS was carried out on an AXIS Ultra DLD system with an Al Kα source. The energy calibration of the spectrometer was performed using C 1s peak at 284.8 eV[8].

(7) N_2 Adsorption-Desorption Isotherms

Adsorption-desorption isotherms of N_2 were measured at 77 K by an N_2 adsorption system (Auto Sorb 1, Quanta chrome Corporation, USA). The sample was heated from room temperature to 1000 °C at a rate of 5 °C min^{-1} in the air[8].

(8) Dynamic Water Contact Angles

Dynamic water contact angles were performed using an OCA20 contact angle instrument. The volume of droplet is 20 μL[8].

(9) Thermogravimetric Analyzer (TGA)

TGA was performed on a thermogravimetric analyzer (TGA2, Mettler Toledo, USA) at a rate of 10 °C min^{-1} from room temperature to 800 °C under nitrogen atmosphere[8].

(10) X-Ray Diffraction (XRD)

XRD patterns were operated by a diffractometer (X'Pert PRO, Panalytical, Netherlands). The wavelength of the Cu Ka source is 1.5406 Å[8].

(11) Electrical Conductivity

The electrical conductivity of graphene foam was carried out on a four-point probe system (ST2262). The electrical conductivity is calculated from the equation as below:

$$\sigma = \frac{1}{R \times \delta} \quad 3\text{-}2$$

Where δ is the thickness of the sample, R is bulk resistance, and σ is electrical conductivity[8].

(12) Electrochemical Measurements

A three-electrodes system was used to investigate the electrochemical performance of our graphene foam electrodes (CHI660D, Chenhua Instruments, China). Conventionally, 6 M KOH solution was chosen as the electrolyte. The Pt wire was used as the counter electrode and an Ag/AgCl electrode works as the reference electrode. Electrochemical properties of the obtained graphene foam electrodes were determined by chronopotentiometry (CP), electrochemical impedance spectroscopy (EIS), cyclic voltammetry (CV), and cycling stability. The specific capacity was calculated from the equation as below:

$$C = \frac{I \times \Delta t}{m \times \Delta V} \quad 3\text{-}3$$

where m is the mass of the active material (g), ΔV is the potential change (V), Δt is the discharge time (s), and I is the current loaded (A)[8].

3.2.3 Results and Discussions

3.2.3.1 Preparation of Graphene Foam

The preparation of graphene foams is schematically presented in Figure 3-2. To optimize the specific capacity of graphene foam electrode, the soft graphene oxide foam was annealed under 400, 600, 800, 900 and 1000 °C, respectively. The obtained sample is marked as GF-400, GF-600, GF-800, GF-900 and GF-1000.

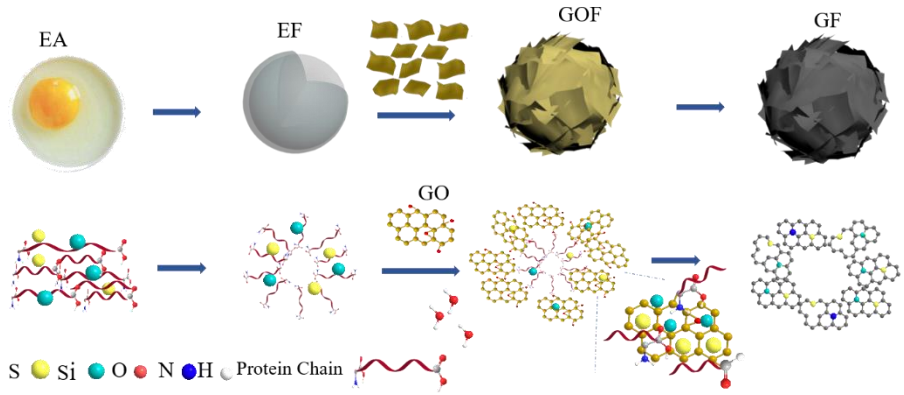

Figure 3-2. Schematic illustration of the preparation of the graphene foam.

As shown in Figure 3-3 (a), the graphene foam consists of interconnected honeycomb-like porous structures. After dispersed in water, the graphene foam exhibits typical 2D layer micrography under TEM, see Figure 3-3 (b). The diameter of pores distributes from hundreds of microns to several nanometers. Further, C, O, S and Si are observed incorporated with graphene, as shown in Figure 3-3 (c)[8].

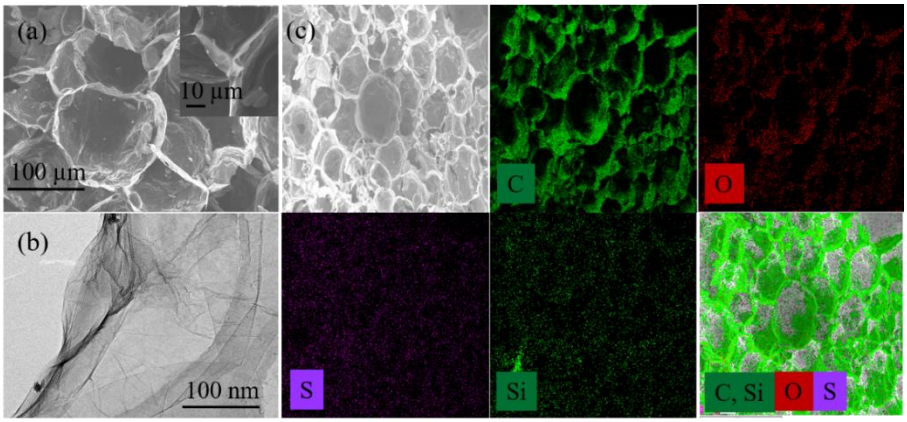

Figure 3-3. (a) The SEM image of the graphene foam (the image on the right corner is a high-resolution SEM image). (b) The TEM image of the graphene foam. (c) The SEM and element mapping micrography of the graphene foam.

Further, a typical IV isotherm with a small hysteresis at high relative pressure (*P/P0*=0.9) was observed in the nitrogen adsorption/desorption isotherm, suggesting the coexistence of mesopores and macropores in the graphene foam. Density functional theory calculation suggests that the pores centered at 4 nm. As expected, the surface area of graphene foam is as high as 1020 m^2 g^{-1}, see Figure 3-4 (b, c). According to the specific capacity equation, such a high surface area multiscale porous structure benefits for achieving high electrochemical capacities[8].

Further, FTIR provides evidence that egg albumen was completely decomposed after calcination. As shown in Figure 3-4 (a), the characterization peaks at 650 to 3000 cm^{-1} on egg foam disappear after calcination.

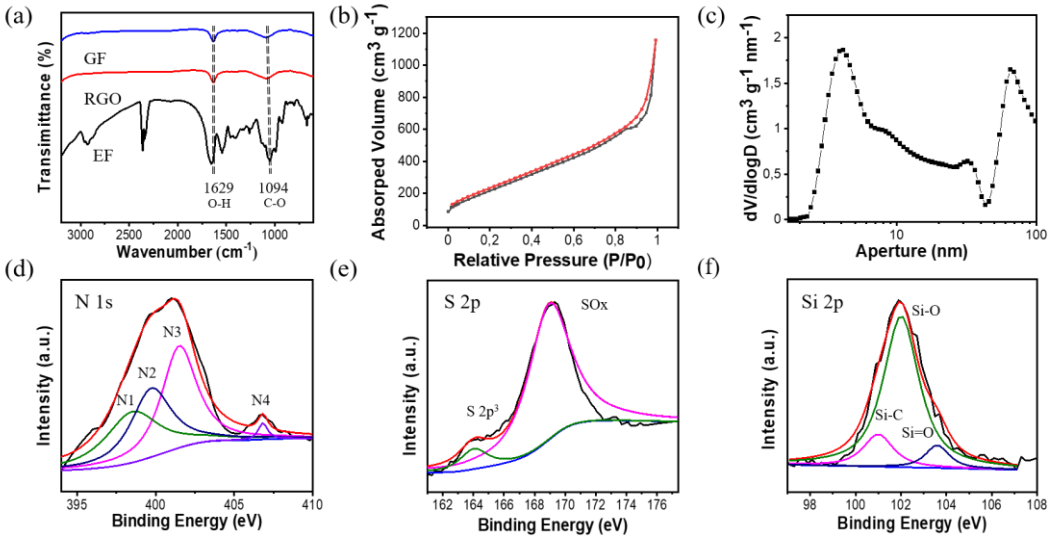

Figure 3-4. (a) The FTIR spectrum of the graphene foam, the reduced graphene oxide and the egg foam. (b) The nitrogen adsorption/desorption isotherms of the graphene foam. (c) The pore size distributions of the graphene foam. (d) The high-resolution XPS spectrum of the N 1s. (e) The high-resolution XPS spectrum of the S 2p. (f) The high-resolution XPS spectrum of the Si 2p.

However, the EDS loses resolution to identify relatively small atomic number elements for example N, with a little dose. To this end, XPS was utilized to identify these atoms[8]. As presented in Figure 3-4 (d), the N 1s phase in graphene foam can be resolved into four different modes, corresponding to the oxidized nitrogen (406.8 eV), graphitic (401.5 eV), pyrrolic (399.7 eV) and pyridinic (398.5 eV)[8]. In addition, the Si 2p spectrum can be divided into three characteristic peaks of Si=O (103.6 eV), Si-C (102.1 eV), and Si-O (100.96 eV), see Figure 3-4 (f)[8]. And the S 2p peak can be resolved into two peaks of S-O (168.9 eV) and s^2p^3 (-C-S-C-, 163.9 eV), see Figure 3-4 (e)[8]. The relative content of N, S, and Si for GF-800 determined by elemental analysis is 4.87, 0.32, and 6.69 wt.%[8]. The N, S, and Si doping with graphene would improve the wettability with electrolytes through generating new electronic states and introducing oxygen-containing functional groups and thus improving the specific capacity[8].

3.2.3.2 Wettability of Graphene Foam

Dynamic water contact angle tests were used to confirm the influence of doping on wettability. An improved hydrophilic was observed in all the graphene foam than the reduced graphene oxide with a far smaller initial wetting angle, see Figure 3-5[8]. These results verify an expected improved wettability of graphene foam by N, S and Si doping. This improved wettability is expected to enhance the specific capacity for graphene electrodes because of EDLCs store energy by adsorbing electrolytes on the surface of electrodes[8].

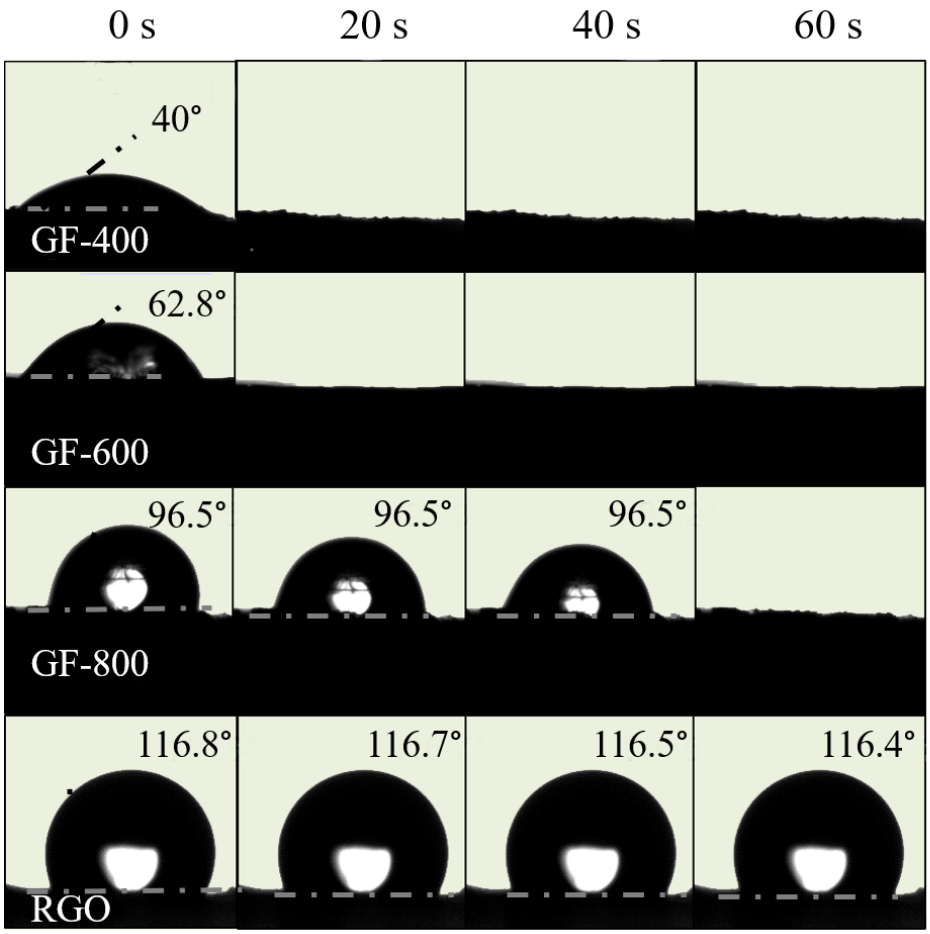

Figure 3-5. The wetting angle of the graphene foam annealed at various temperatures and reduced graphene oxide (RGO).

Next, density functional theory calculations were performed to explain why N, S, and Si doping improve wettability from the electronic structure level with the CASTEP mode. While modeling, a 3 × 3 × 1 supercell was built, and the energy cutoff was set at 380 eV. After doping with C, S, and Si atoms, both bond length of -C-C- (1.42 °A) and the bond

angle of -C-C-C-(120°) changed, and the regular hexagonal honeycomb structures reform slightly in the in-plane direction.

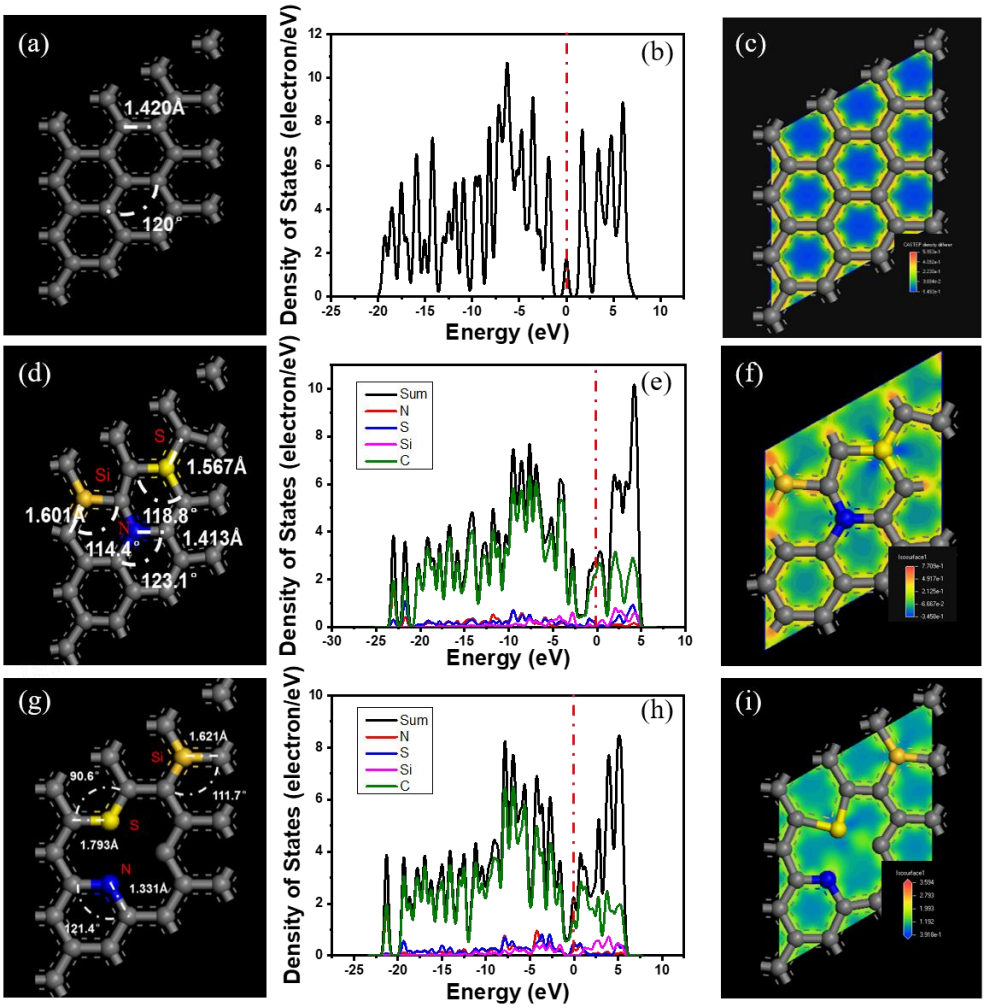

Figure 3-6. (a) The relaxed atomic structures (RAS) of the un-doped graphene. (b) The partial densities of states (DOS) of the un-doped graphene. (c) The charge density distributions (CDD) of the un-doped graphene (d) The RAS of doped flawless graphene. (e) The partial DOS of states of doped flawless graphene. (f) The CDD of doped flawless graphene. (g) The RAS of doped defective graphene. (h) The partial DOS of states of doped defective graphene. (i) The CDD of doped defective graphene[8].

In addition, defects on the graphene sheets affect their crystal structures with more sophisticated electronic states at the position close to the Fermi energy, see Figure 3-6 (a-i). Consequently, the wettability of graphene is improved as a result of the disrupted electronic distribution in graphene and the improved polarity within 2D structures[8].

3.2.3.3 Electrochemical Performance of Graphene Foam

To verify the improved specific capacity, we next investigated the supercapacitor performance of the graphene foam. To avoid the influence of $Ni(OH)_2$ and oxides, nickel foam was washed with $(CH_3)_2CO$, HCl, C_2H_6O and H_2O, followed by annealing at 1000 °C for 2 h under a nitrogen atmosphere at first. XRD diffractions for graphene oxide, graphene foam, nickel foams (before and after annealing at 800 ˚C) were carried out to verify whether $Ni(OH)_2$ and oxides residue after annealing. As shown in Figure 3-7 (a, b), the sharp diffraction peak at 10˚ on pristine graphene oxide, disappears after thermal reduction, suggesting that oxygen-containing groups have been removed in graphene foam. Proverbially, two dominated broad and weak peaks at the position of 2 θ = 43° and 24° are attributed to the (100) and (002) reflections of the graphitic carbon layers. The porous structure and chemical doping are able to broaden the peak width of (002)[19]. After calcination, the peaks of nickel foams match well with the peaks of original nickel foams. This result confirms that nickel foams keep stable during heating[8].

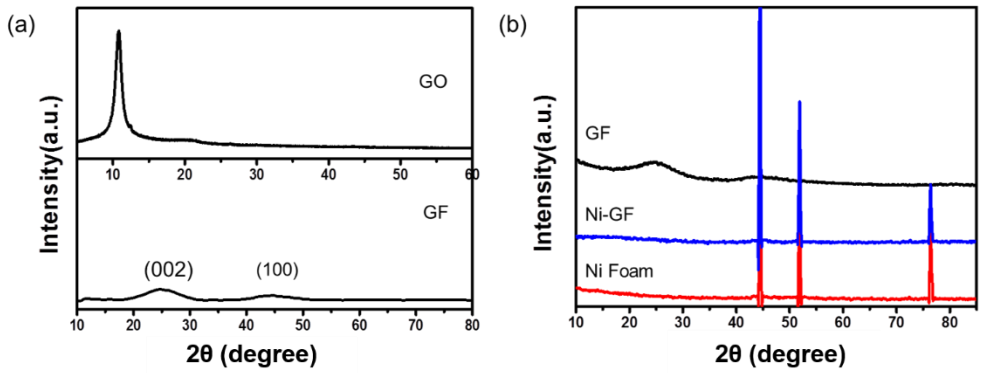

Figure 3-7. (a) The XRD patterns of graphene oxide and graphene foam. (b) The XRD patterns of graphene foam, Ni-GF and Ni foam.

As shown in Figure 3-8 (a), the graphene electrode exhibits a typical EDLCs behavior with a square-like CV curve from -1 to 0 V, and thus the capacity can be totally contributed to the graphene foam[8]. In addition, the capacitance of graphene foam electrode increases at first while increasing the calcination temperature from 400 to 800 °C. This is because the graphene oxide is reduced, and the inactive egg albumen is decomposed during annealing. After 800 °C, the specific capacity decreases when further increasing annealing temperature owning to re-stacking of graphene sheets. Therefore, the balance between surface area and conductivity is critical to optimize the

capacity of graphene foam electrodes. In particular, the specific capacitance of graphene foam (GF-800) reaches 534 F g^{-1} at 1 A g^{-1}, as shown in Figure 3-8 (b). This value is almost equivalent to the theoretical capacity of graphene (550 F g^{-1})[8]. The specific capacity of GF-800 remains at 308 F g^{-1} even at 100 A g^{-1} with nearly no IR drops. In addition, the graphene foam electrode remains 96.1% capacity after 10 000 cycles at a high current density of 10 A g^{-1}, see Figure 3-8 (c, d, e). Compared to the reported work, our graphene foam electrodes push the boundary of specific capacity in carbon-based electrodes for supercapacitor, see Figure 3-8 (f). Therefore, the GF-800 shows promising potential as an electrode for supercapacitor[8].

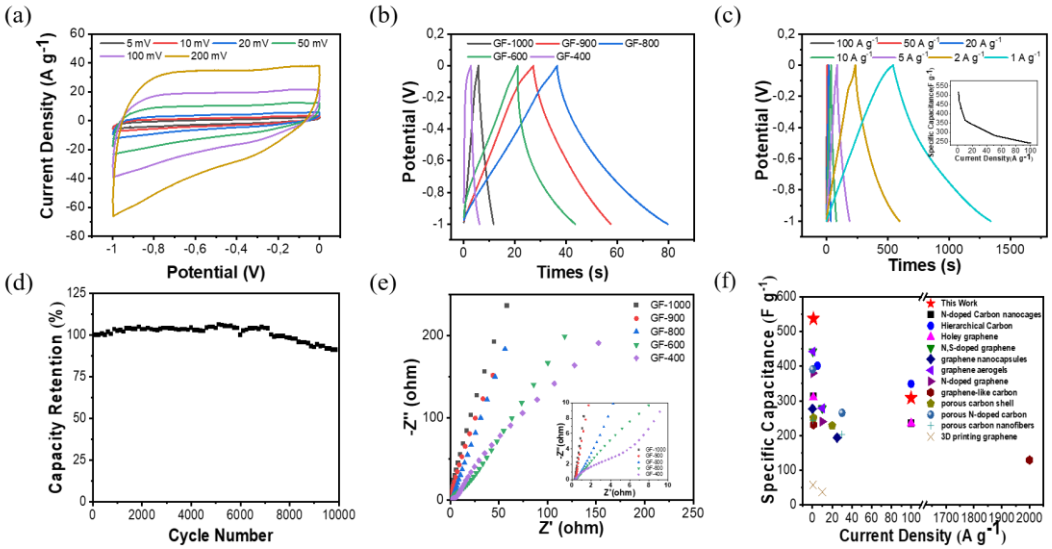

Figure 3-8. (a) The CV curves of graphene foam annealed at 800 °C at various scanning rates. (b) The CP curves of graphene foam annealed at various temperatures at 10 A g^{-1}. (c) The rate behaviors of graphene foam annealed at 800 °C. (d) The cycling performance of graphene foam annealed at 800 °C at 10 A g^{-1}. (e) The Nyquist plots of graphene foam annealed at various temperatures. The image at the right corner presents high-frequency regions. (f) The comparison of specific capacitance of GF-800 with reported work[8].

To figure out the origin of the ultrahigh performance of GF-800 as a supercapacitor electrode, a reduced graphene oxide (RGO) electrode under the same conditions but without the egg albumen template was prepared. In comparison, the RGO electrode exhibits only 147 F g^{-1} at 1 A g^{-1}, indicating that the interconnected pores and element doping largely contributes to the capacity, see Figure 3-9 (a)[8]. While the capacity of GF-PTFE (90 wt.% active material) goes up to 471 A g^{-1} at 1 A g^{-1}, suggesting the porous freestanding structure largely contributes to the capacity, see Figure 3-9 (c). Further, in

the Nyquist plots, the GF-800 exhibits a vertical slope with an ohmic resistance less than 0.3 Ω, suggesting that fast ion diffusion and electron transfer. The super-low ohmic resistance would arise from the improved wettability and the high electrical conductivity (6.99×10^5 S m^{-1} by the four-probe method). Moreover, a close to -90° phase angle in the low-frequency region is observed in Bode Plots, see Figure 3-9 (b). From the Nyquist plots, the GF-800 shows the fastest time constants. Accordingly, the fastest charge-discharge rate in GF-800 leads to the highest specific capacity[8]. Coupled with improved wettability, 3D porous structure, low ohm resistance and high electrical conductivity, the GF-800 results in ultrahigh capacity for micro-supercapacitors.

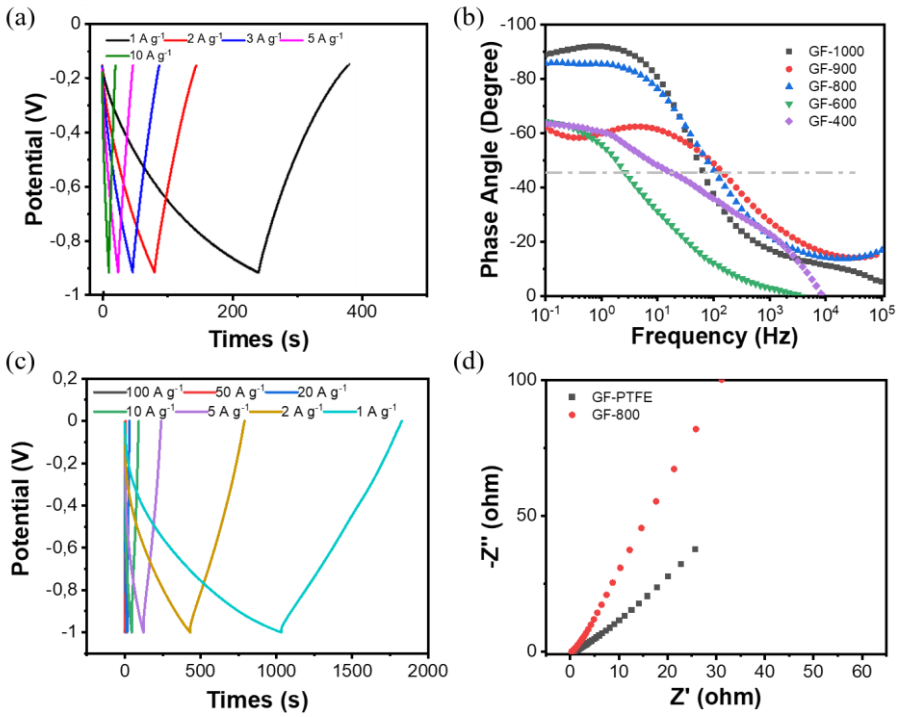

Figure 3-9. (a) The CP curves of reduced graphene oxide. (b) The Bode plots of graphene foam annealed at various temperatures. (c) The CP curves of the reference GF800-PTFE. (d) The Nyquist plots of graphene foam annealed at 800 ℃ and the reference GF800-PTFE.

3.3 Graphene Based In-plane Micro-Supercapacitor

3.3.1 Introduction

As the geometry of portable electronics becomes smaller, the demand for low-power integrated circuits for miniature embedded microelectromechanical systems (MEMS) is sharply increased in medical[20], biological[21] and environmental[22], etc. Among these micropower systems, micro-supercapacitors (MSCs) possess distinguish advantages of

long lifetime, high charge/discharge rates, and high peak power, etc.[2] As shown in Figure 3-10 (a), compared to the Lithium thin-film battery, MSCs have higher power density and stability but low energy density. Among all of the micropower systems, the activated MSCs exhibit the best power density and energy density. For the self-power system, the output from energy harvesters is typically pulsed rather than constant. Thus, it requires the storage unit has a good capability of rapid charging with low resistance. Taking the relatively low energy density demand and ultra-long lifetime into consideration, MSCs is a more suitable storage solution in miniaturized self-power systems. Although MSCs and conventional supercapacitors share the same working principle, MSCs predominately use an on-chip interdigitated structure while conventional supercapacitors employ vertical sandwich structures, see Figure 3-10 (b). A typical in-plane MSCs fabrication process is illustrated in Figure 3-10 (c). The main steps include photolithography, metal deposition and lift-off. These procedures are highly similar to the standard fabricating procedures of the metal-oxide-semiconductor field-effect transistor (MOSFET) and the MEMs, two of the most important basic units in microelectronics.

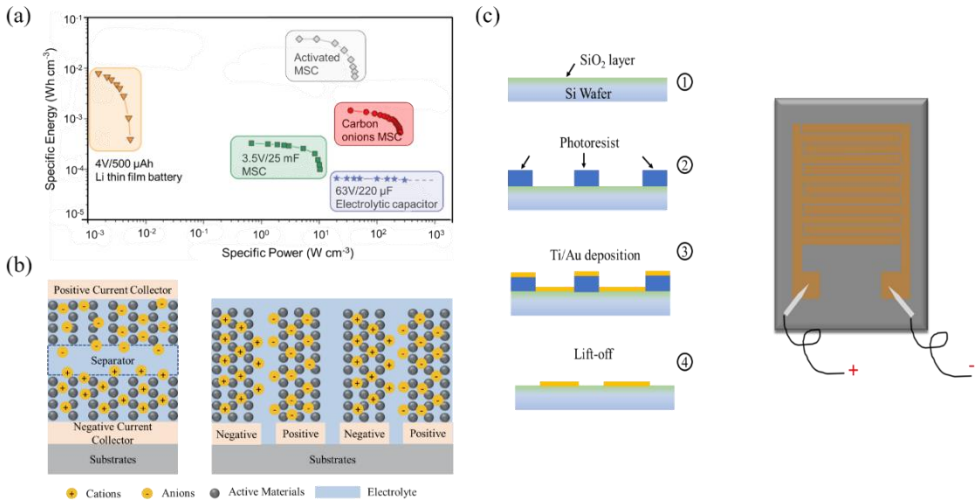

Figure 3-10. (a) Comparative Ragone plot of various micro power systems[2]. (b) Schematic image of the EDLCs (left) and the MSCs (right). (c) Schematic drawing of fabrication procedures (left) and the in-plane structure (right) of MSCs[2].

Currently, the study of graphene enhanced MSCs focuses on using graphene as electrodes to increase the energy and power density[23, 24]. For instance, laser patterning and laser scribing methods have been used to prepared graphene, graphene/CNTs

electrodes for MSCs[24, 25]. The reduced graphene oxide (RGO) coated MSCs are extensively developed because of the high density of chemically active defect sites, scalability, low-cost and wet-chemical properties of RGO[26, 27]. Although the mass production of graphene oxide is scalable, it suffers from decomposition when exposed to an environment high than 70 °C[28].

However, the microelectronics severely suffer from heat dissipation issues, while far too little attention has been paid to the heat dissipation for MSCs. Coupled with the urgent demand for replacing silicon wafers with graphene in next-generation silicon transistors because of its high field velocity of graphene[17]. The replacement of silicon wafer with graphene assembled film can largely improve heat dissipation of microelectronic because the thermal conductivity of graphene assembled film is more than 10 times (1500-2000 W $m^{-1}K^{-1}$) higher than that of the silicon wafer (130 W $m^{-1}K^{-1}$). Thus, the graphene assembled film can work as a heat spreader for the following package process, thus saves space and optimizes packaging procedure for microelectronics.

In this work, graphene assembled film was utilized to replace silicon wafer as a substrate for MSCs. Compared to the conventional silicon wafer, graphene shows overwhelming advantages for heat dissipation and flexibility. The result shows such replacement significantly improves the heat dissipation of MSCs but will not influence the electrochemical behaviors of MSCs. This work may broaden the applications of using graphene for semiconductors.

3.3.2 Materials and Experiments

3.3.2.1 Materials

Table 3-2. Materials

Name	Specifications	Manufacturers
Graphene Assembled Film	/	SHT Smart High-Tech AB
maN-400	/	Micro Resist Technology
Microposit MF-319 Developer	/	Dow Chemistry Co., Ltd.
N,N-Dimethylfluoride (DMF)	99.9 wt.%	Sigma-Aldrich (Sweden) Trading Co., Ltd.
RGO	10 wt.%	Graphenea Technology
1-Ethyl-3-methylimidazolium bis(trifluoromethylsulfonyl)imide (EMIM-TFSI)	97 wt.%	Sigma-Aldrich (Sweden) Trading Co.,Ltd.

3.3.2.2 Experiments

(1) Preparation of Flat Graphene Film

The raw graphene assembled film was provided by the SHT Smart High-Tech AB. Then the graphene assembled film suffered from mechanical pressed under 45 MPa for 6 h (Operator 2008SFX, Dongyi Manufacturing Technology Co., Ltd., China) until the density of graphene film became 1.8 g cm^{-3}. The scanning electron microscope (SEM) images are carried out on a Zeiss Supra 60 VP (Germany) under 10 KV. The roughness of the graphene assembled film was captured on an optical surface profiler (Wyko NT 1100, Veeco, USA). After that, a 200 nm SiO_2 was sputtered on the graphene film to separate the graphene substrate and micro supercapacitor circuits by Sputtering (FHR MS 150, NORDIKO, UK) under the Ar_2 atmosphere.

(2) Preparation of Shadow Masking

The fabrication of the MSCs utilizes the principle of shadow masking the electrode surface with a layer of current collectors. For such purpose, a shadow mask was fabricated using a 2 inches Si wafer of thickness 280 μm. A SiO_2 layer of 400 nm was thermally grown on it using a mixture of H_2O and $SiCl_4$ gases. A negative photoresist maN-400 was spin-coated on the substrate as a hard mask for etching SiO_2 at 2000 rpm

at an acceleration of 1000 rpm. After exposed to UV-light for 50 s, the MSCs patterns were resolved, following developed by MF319 and hard-baked. Afterward, the exposed SiO_2 was etched by exposure to a mixture of CHF_3 and CF_4. A wafer etching was performed on the exposed Si surface using deep reactive ion etching involving SF_6 plasma for 240 min. Finally, the photoresist was removed by mR-REM400 and the shadow mask was ready for use.

(3) Preparation of Graphene Based MSCs

For MSCs fabrication on the graphite paper substrate, a two inched Si wafer was used as a carrier. A photoresist was spin located on the surface and then the graphite paper with SiO_2 insulating surface was applied on it before any form of baking. The carrier was then soft-baked at 100 °C to strengthen the adhesion on the surface. In particular, reduced graphene oxide was chosen as the electrode material. The reduced graphene oxide was dissolved in N, N-dimethyl fluoride (DMF) to achieve a solution density of 10 g L^{-1}. The solution was sonicated for 15 min at 35 kHz for a good dispersion before spin coating. The solution was then spin-coated on the graphite paper surface at a spin speed of 500 rpm at a low acceleration of 100 $rpms^{-1}$ for five times. The electrodes were then dried in ambient atmospheric conditions for solvent evaporation. For the current collectors, using the shadow mask previously fabricated, a layer of Au/Ti (100/20 nm) was evaporated on the surface of the wafer. The exposed reduced graphene oxide was then etched using O_2 plasma at 100 W. Finally, the wafer was heated at a high temperature of 400 °C to dissociate the graphite surface from the Si carrier wafer. For electrochemical characterization, EMIM-TFSI, chosen as an electrolyte owing to its high electrical conductivity and temperature tolerance, was dropped onto the MSCs.

3.3.2.3 Characterization

(1) Field Emission Scanning Electron Microscopy (FESEM)

The morphologies were observed under FESEM (Ultra 55, Zeiss, Germany) with acceleration voltage 6-12 KV. The sample was attached to the conductive tape for measurement.

(2) Optical Microscopy

Microstructures of MSCs were determined by optical microscopy to identify the geometry of fingers.

(3) Optical Surface Profiler

The surface roughness was determined on an optical surface profiler (Wyko NT 1100, Veeco, USA). The sample was attached to a silicon wafer with double-sided tape for roughness measurement. Fifteen measurements per sample were made on three different positions for all three magnifications.

(4) Thermal Dissipation Performance

Infrared thermography (A655SC, FLIR, USA) was used to visualize the thermal dissipation performance of the graphene film based MSCs. The diffusivity was calibrated as 0.98. While measuring, a DC heater (RS component Co., Ltd., Sweden) was used as the heat source, which was connected to a DC power supply (E3612A, Agilent, USA). The MSCs were attached to the heat mat by a thin layer of thermal grease (TG100, Loctite, 3 W m^{-1} K^{-1}, China).

(5) Electrochemical Measurements

Electrochemical measurements were carried out with a setup in Figure 3-11. The two needles connect with positive and negative electrodes. Electrochemical performances of the obtained graphene foam electrodes were analyzed by chronopotentiometry (CP), electrochemical impedance spectroscopy (EIS), cyclic voltammetry (CV), and cycling stability. The capacitance was calculated from discharge curves (-1.0 V to 0 V) as the graphene electrode was used as the negative electrode in supercapacitors. The specific capacity was calculated from the equation as below:

$$C = \frac{I \times \Delta t}{m \times \Delta V} \qquad 3\text{-}4$$

where m is the mass of the active material (g), ΔV is the potential change (V), Δt is the discharge time (s), and I is the current loaded (A)[8].

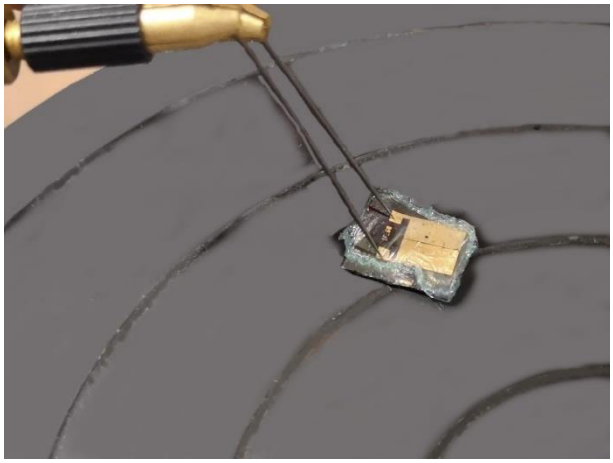

Figure 3-11. Measurement set-up for electrochemical performance.

(6) Thermal Dissipation Performance

The surface temperature profile was captured by infrared thermography (FLIR-A655 SC). Samples were cut into the size as 40 × 50 mm, were pressed in-between a heater and an aluminum heat sink to demonstrate its performance as a heat spreader, as shown in Figure 3-12. The heater was connected to a DC power supply with the input power kept constant at about 4 W. The diffusivity was calibrated as 0.98. While measuring, a DC heater (RS component Co., Ltd., Sweden) was used as the heat source, which was connected to a DC power supply (E3612A, Agilent, USA). The MSCs were attached to the heat mat by a thin layer of thermal grease (TG100, Loctite, 3 W m^{-1} K^{-1}, China). Plastic foams were used on the bottom and up to minimize heat leakages.

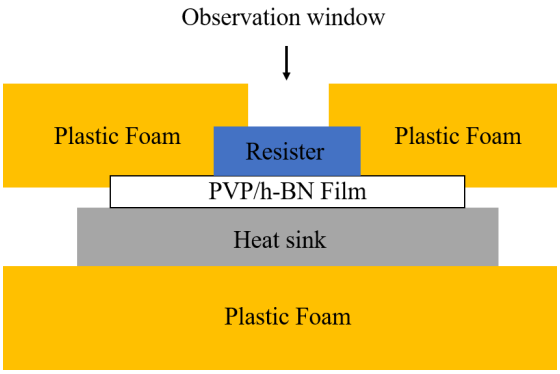

Figure 3-12. The setup for infrared thermal camera measurement.

3.3.3 Results and Discussions

3.3.3.1 Preparation of Graphene Based In-plane Micro-Supercapacitor

The typical fabrication procedure of graphene based MSCs is illustrated in Figure 3-13. To avoid short, a thin layer of SiO_2 was coated on graphene assembled film to isolate graphene and MSCs. As a reference, the same MSCs arrays were fabricated on a 2 inches silicon wafer.

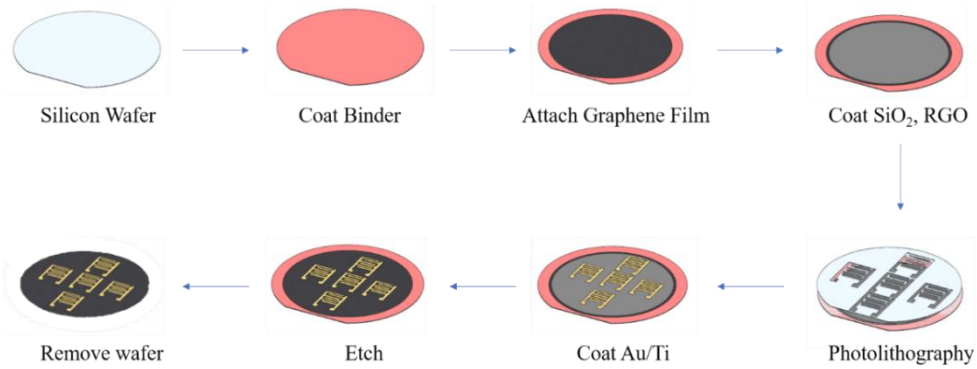

Figure 3-13. Schematic drawing of fabrication procedures of graphene enhanced MSCs.

Figure 3-14 presents the optical images of our graphene based MSCs. With the shadow masking technology, the in-plane MSCs structures can be transferred on the graphene film, with no short, see Figure 3-14 (a-g). In the MSCs, the length of one electrode is 500 μm, while the distance between adjacent electrodes is 16 μm. On a two inches wafer, 20 MSCs were fabricated. As shown in Figure 3-14 (h-j), the graphene based MSCs are flexible and can be simply twisted.

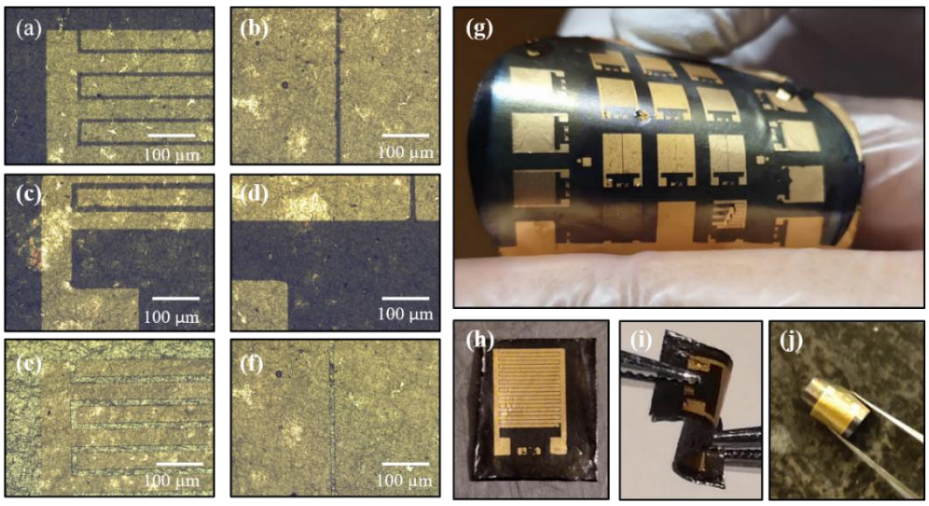

Figure 3-14. Microscopic images of graphene based flexible MSCs.

3.3.3.2 Electrochemical and Thermal Performance of Graphene Based In-plane Micro-Supercapacitor

With the extensive development of MSCs, the energy density in MSCs should be largely increased. As a result, the thermal performance of MSCs can be one of the key limits for future MSCs, following Moore's law and similar to the development trend of the electric vehicle battery.

Firstly, we measured the electrochemical behavior of graphene based MSCs and the reference silicon based MSCs. As expected, the MSCs fabricated on the graphene assembled film and the silicon wafer show similar specific capacity and resistance because of the similar electrode structures, see Figure 3-15 (a, b). After coated with reduced graphene oxide, our MSCs exhibits a specific capacity up to 167 F cm^{-2}, which improved more than 1.5 times than the reported 100 F cm^{-2}.

To demonstrate the thermal dissipation property of using graphene film as a substrate for MSCs, a 12 W heat was loaded on graphene film and silicon wafer based MSCs array. Compared to the MSCs on a silicon wafer, the heating element with graphene film based MSCs is 4 °C cooler, demonstrating the super thermal conductivity of graphene film, see Figure 3-15 (c, d). Compared to the silicon wafer, the in-plane thermal conductivity of the graphene assembled film is improved 10 times (1400 W m^{-1} K^{-1}). Thus, the graphene assembled film integrates the function of both substrate and heat spreader. On the other hand, the temperature of 12 MSCs on graphene film is similar while the MSCs on silicon wafer exhibit a wide temperature distribution of 12 MSCs. Such phenomenon indicates temperature distributed on graphene MSCs is obviously homogenous than the MSCs on a silicon wafer, verifying the heat spreader hypothesis. This is because the super high in-plane thermal conductivity of graphene film works as a heat spreader for MSCs.

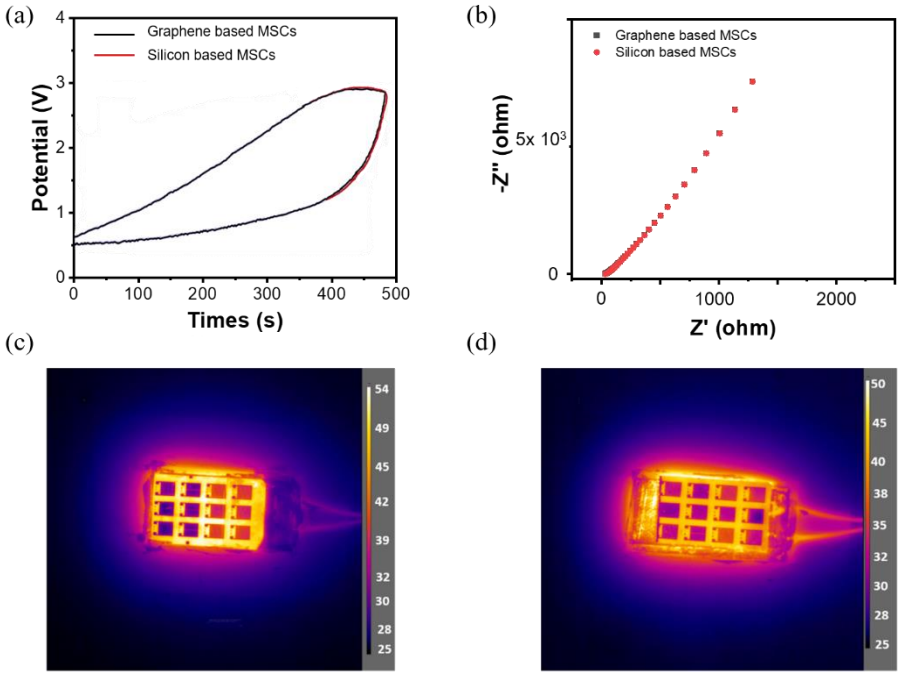

Figure 3-15. (a) The CV curves of graphene assembled film based MSCs and silicon based MSCs. (b) The Nyquist plots of graphene assembled film based MSCs and silicon based MSCs. (c) The infrared image of silicon based MSCs. (d) Infrared thermography of graphene based MSCs.

3.4 Summary

In this chapter, we explored the application of using graphene for supercapacitors, including electric double-layer capacitors and in-plane micro-supercapacitor.

At first, a scalable graphene foam preparation technology was developed to realize high performance supercapacitor through tailoring specific areas and wettability. The unique porous structure, low ohm resistance, doping and high electrical conductivity largely improve the specific gravimetric capacity, cycling stability and rate capability. Further, density functional theory simulation was firstly used to reveal the reason why increasing the polarity of graphene improves its wettability.

In addition, flexible in-plane micro-supercapacitors were fabricated by replacing silicon wafers with graphene assembled films. By this replacement, the graphene based MSCs can be used as wearable energy devices and the heat dissipation performance of MSCs is drastically improved without influence its electrochemical behaviors. This work demonstrates the possibility of using graphene in the semiconductor industry, which provides a new application for graphene-like 2D materials.

Reference

[1] Cao X. H., Shi Y. M., Shi W. H., et al. Preparation of novel 3D graphene networks for supercapacitor applications [J]. Small, 2011, 7(22): 3163-3168.

[2] Xiong G. P., Meng C. Z., Reifenberger R. G., et al. A review of graphene-based electrochemical microsupercapacitors [J]. Electroanal., 2014, 26(1): 30-51.

[3] Lee J. H., Park N., Kim B. G., et al. Restacking-inhibited 3D reduced graphene oxide for high performance supercapacitor electrodes [J]. Acs Nano, 2013, 7(10): 9366-9374.

[4] Su Y. H., Lin Y. H., Tseng Y. H., et al. Postinjection gelation of an electrolyte with high storage permittivity and low loss permittivity for electrochemical capacitors [J]. J. Power Source, 2021, 481:228869.

[5] Pesaran A. A. Battery thermal models for hybrid vehicle simulations [J]. J. Power Source, 2002, 110(2): 377-382.

[6] Kumar H., Sharma R., Yadav A., et al. Recent advancement made in the field of reduced graphene oxide-based nanocomposites used in the energy storage devices: a review [J]. J. Energy Storage, 2021, 33: 102032.

[7] Liu Y., Jiang S. P., Shao Z. Intercalation pseudocapacitance in electrochemical energy storage: recent advances in fundamental understanding and materials development [J]. Mater. Today Adv., 2020, 7: 100072.

[8] Liu Y., Zhao X., Wang C., et al. Egg albumen templated graphene foams for high-performance supercapacitor electrodes and electrochemical sensors [J]. J. Mater. Chem. A, 2018, 6(37): 18267-18275.

[9] Simon P., Gogotsi Y. Materials for electrochemical capacitors [J]. Nat. Mater., 2008, 7(11): 845-854.

[10] Zhang L. L., Zhao X. S. Carbon-based materials as supercapacitor electrodes [J]. Chem. Soc. Rev., 2009, 38(9): 2520-2531.

[11] Pandolfe A. G., Hollenkamp A. F. Carbon properties and their role in supercapacitors [J]. J. Power Sources, 2006, 157(1): 11-27.

[12] Song R. Y., Park J. H., Sivakkumar S. R., et al. Supercapacitive properties of polyaniline/Nafion/hydrous RuO_2 composite electrodes [J]. J. Power Sources, 2007, 166(1): 297-301.

[13] Yu G., Hu L., Vosgueritchian M., et al. Solution-processed graphene/MnO_2 nanostructured textiles for high-performance electrochemical capacitors [J]. Nano Lett., 2011, 11(7): 2905-2911.

[14] Li H., Wang J., Chu Q., et al. Theoretical and experimental specific capacitance of polyaniline in sulfuric acid [J]. J. Power Sources, 2009, 190(2): 578-586.
[15] Zhang H. X., Cao Y. D., Chee M. O. L., et al. Recent advances in micro-supercapacitors [J]. Nanoscale, 2019, 11(13): 5807-5821.
[16] Zoski C. G. Ultramicroelectrodes: design, fabrication, and characterization [J]. Electroanal., 2015, 14(15): 1041-1051.
[17] Kong W., Kum H., Bae S. H., et al. Path towards graphene commercialization from lab to market [J]. Nat. Nanotechnol., 2019, 14(10): 927-938.
[18] Qin Z., Jung G. S., Kang M. J., et al. The mechanics and design of a lightweight three-dimensional graphene assembly [J]. Sci. Adv., 2017, 3(1): e1601536.
[19] Xiong Z., Liao C., Han W., et al. Mechanically tough large-area hierarchical porous graphene films for high-performance flexible supercapacitor applications [J]. Adv. Mater., 2015, 27(30): 4469-4475.
[20] Nieder A. Miniature stereo radio transmitter for simultaneous recording of multiple single-neuron signals from behaving owls [J]. J. Neurosci. Meth., 2000, 101(2): 157-164.
[21] Mohseni P., Najafi K., Eliades S. J., et al. Wireless multichannel biopotential recording using an integrated FM telemetry circuit [C]. International Conference of the IEEE Engineering in Medicine & Biology Society, 2005.
[22] Hautefeuille M., O'Flynn B., Peters F., et al. Miniaturised multi-MEMS sensor development [J]. Microelectronics Reliab., 2009, 49(6): 621-626.
[23] Xiong G., Meng C., Reifenberger R. G., et al. Graphitic petal electrodes for all-solid-state flexible supercapacitors [J]. Adv. Energy Mater., 2014, 4(3): 1300515.
[24] Gao W., Singh N., Song L., et al. Direct laser writing of micro-supercapacitors on hydrated graphite oxide films [J]. Nat. Nanotechnol., 2011, 6(8): 496-500.
[25] El-Kady M. F., Kaner R. B. Scalable fabrication of high-power graphene micro-supercapacitors for flexible and on-chip energy storage [J]. Nat. Commun., 2013, 4: 1475.
[26] Byon H. R., Lee S. W., Chen S., et al. Thin films of carbon nanotubes and chemically reduced graphenes for electrochemical micro-capacitors [J]. Carbon, 2011, 49(2): 457-467.
[27] Liu C., Yu Z., Neff D., et al. Graphene-based supercapacitor with an ultrahigh energy density [J]. Nano Lett., 2010, 10(12): 4863-4868.

[28] Jung I., Field D. A., Clark N. J., et al. Reduction kinetics of graphene oxide determined by electrical transport measurements and temperature programmed desorption [J]. J. Phy. Chem. C, 2009, 113(43): 18480-18486.

CHAPTER 4

Graphene-like 2D Materials for Interface Enhancement Applications

4.1 Introduction

The arena of using graphene-like 2D materials to enhance composites has bloomed in last decades because of their remarkable properties of high Young's module, anti-corrosion, lightweight, large surface area, etc.[1, 2] At present, the incorporation of graphene-like 2D materials as nanofillers has demonstrated overall improvements in mechanical, thermal and electrical properties, even a few of them have been commercialized.[3] While using as an enhancement nanofiller, the dispersion of graphene-like 2D materials in the matrix heavily determines the property of composites[3-5]. At present, surface modification, including covalent and non-covalent methods, is one of the most effective approaches to improve the dispersibility of graphene-like 2D materials in matrix[3, 4]. Usually, the functional groups are highly determined by the fundamental physical and chemical properties of the matrix and the applications. For instance, to improve the mechanical properties of coatings and cement repair materials, chemicals with hydrophilic functional groups, such as hydroxyl, amino, or carboxyl, are utilized to functionalize graphene-like 2D materials and improve their dispersibility in the matrix. While positive charged functional chemicals, such as polyethylenimine (PEI), are widely used to control the zeta potential of graphene-like 2D materials for drug deliveries. In this chapter, surface modification of graphene and hexagonal boron nitride were studied for their interface enhancement applications, including water-borne epoxy coatings, cement repair materials and mRNA drug delivery platforms.

As to graphene enhanced water-borne epoxy coatings, functional graphene was used to lower the coefficient of friction (COF) and extend the lifetime for the Tricolit TSC Coating, a commercialized waterborne epoxy coating. The geometry of graphene nanoparticles was optimized, and the result shows more than 2 times higher tribological properties, and smooth surfaces are achieved by adding 1 wt.% functional graphene. The

mass production technology up to 300 g per batch was developed for preparing functional graphene.

Secondly, functional hexagonal boron nitride was prepared for improving the strength of cement repair materials. After functionalized with carboxymethyl cellulose, the functional hexagonal boron nitride is able to improve the adhesion between the substrates and the repair materials. This work has demonstrated the commercial application to repair walls for five-start projects.

Thirdly, functional graphene quantum dots were used to deliver intact and functional mRNA to Huh-7 hepatocarcinoma (liver) cells. To interact with cells, the zeta potential of graphene quantum dots was tailored to positive by functionalization with PEI. The transfection efficiency for functional graphene quantum dots and mRNA complexes was as high as 25%.

4.2 Graphene Enhanced Water-borne Epoxy Coating

4.2.1 Introduction

At present, the water-borne epoxy coatings have emerged as an effective solution for protecting substrates, such as bearing, gearing, etc., from friction loss, and thus extend their lifetimes[10, 11]. However, the wear resistance of water-borne epoxy coatings is limited and can hardly meet the requirement for long lifetime applications[13]. To address this issue, nano-fillers, such as graphene oxide[17], silicon dioxide[13], carbon nanotubes[15], nano-diamond[14], graphene[16], etc., enhanced coatings is considered as an effective strategy for improving wear-resistances of water-borne epoxy coatings[10, 11].

Compared to conventional materials, graphene-like 2D materials offer overwhelming benefits for tribological protections, such as atomically smooth surface, remarkable mechanical stiffness, easy shear capability, high fracture strength, chemical inertness, etc.[18-20] While for the application of using graphene-like 2D materials in water-borne coatings, the encountered challenge is how to achieve a homogenous formulation[10]. Because graphene-like 2D materials are usually hydrophobic and inherently suffer from agglomeration by the strong π-π interaction between adjacent sheets. To this end, graphene-like 2D materials are usually pre-functionalized by chemicals with hydrophilic or active groups[11]. After functionalization, both the dispersibility and the mechanical

strength of the graphene-like 2D materials is significantly improved because of the introduction of hydrophilic groups on the 2D in-plane sheets[10, 21, 22]. For instance, a nearly 300% improvement of storage modulus of epoxy can be achieved by adding only 2% hydroxyl functional graphene[10]. Therefore, it is highly attractive to utilize functional graphene-like 2D materials for improving the tribological performance of water-borne epoxy-based coatings.

In this work, functional graphene was used to lower the coefficient of friction (COF) and extend the lifetime for the Tricolit TSC Coatings, a commercialized waterborne epoxy coating. To improve the dispersibility of graphene, graphene was functionalized by p-hydroxybenzene diazonium chloride with an active hydroxyl group at first. Results show that 15 times lower COF was achieved. Compared with three referenced commercialized products, the functional graphene enhanced Tricolit TSC Coatings exhibit more than 2 times longer lifetime. Finally, mass production technology up to 300 g per batch was developed for the functional graphene. This functionalization strategy was further developed to improve the dispersibility of carbon nanotubes too.

4.2.2 Materials and Experiments

4.2.2.1 Materials

Table 4-1. Materials

Name	Specifications	Manufacturers
Graphene Powder	1 μm	Carbonene
Sulfanilic acid	98 wt.%	Sigma-Aldrich (Sweden) Trading Co., Ltd.
Sodium Nitrite ($NaNO_2$)	99 wt.%	Sigma-Aldrich (Sweden) Trading Co., Ltd.
Hydrochloric Acid (HCl)	37 wt.%	Sigma-Aldrich (Sweden) Trading Co., Ltd.
Tricolit TSC Coating	/	Applied Nano Surfaces AB
Graphene Oxide (GO)	10 wt.%	Applied Graphene Materials UK Ltd.

4.2.2.2 Experiments

(1) Preparation of Hydroxybenzene Diazonium Salt

In an ice-water bath (0-4 °C), 10 mL 0.2 M sodium nitrite and 3 g aminophenol were dissolved into 100 mL distilled water. After that, 20 mL 30 wt.% hydrochloric acid was dropped into the dispersion to activate the diazotization reaction. Finally, the hydroxybenzene diazonium salt (DS) was isolated by centrifugated at 10000 rpm[10].

(2) Preparation of Functionalized Graphene

To prevent the reaction between the diazo group and the phenolic hydroxyl group, the pH value of DS solution was adjusted to 2 by adding hydrochloric acid. Then the hydroxybenzene diazonium salt solution (2 g 0.5 wt.%) was slowly dropped into the graphene dispersion (20 mg mL^{-1}) at 50 °C for 8 h (pH=10). Afterward, the functional graphene was collected by centrifugation at 8000 rpm, 30 min for 3 times[10].

(3) Formulation of Functionalized Graphene Enhanced Tricolit TSC Coating

At first, the functional graphene dispersion (50 mg mL^{-1}) was mixture with the Tricolit TSC Coatings. After that, the epoxy slurry with functional graphene was sprayed on a 10 × 5 cm stainless steel plate. After that, the sprayed plate was cured at 50 °C (45 min), 90 °C (60 min), 120 °C (60 min), and 250 °C (30 min)[10].

4.2.2.3 Characterization

(1) Transmission Electron Microscopy (TEM)

TEM (Tecnai G^2 20, USA) is operated at an acceleration voltage of 200 kV to show the microstructure of graphene oxide sheets. The sample dispersion is diluted to 1 mg mL^{-1}, and dropped on lacey support films with further drying under 60 °C in an oven[10].

(2) Field Emission Scanning Electron Microscopy (FESEM)

The micro morphologies were observed under FESEM (Ultra 55, Zeiss, Germany) with acceleration voltage 6-12 KV. The sample was attached to the conductive tape for measurement[10].

(3) X-Ray Photoelectron Spectroscopy (XPS)

XPS (PHI 5000 VersaProbe III, Kanagawa, Japan) was performed to identify the chemical structures of graphene and functionalized graphene using an Al Kα source (hν

= 1486.6 eV). The sample powder was spread on conductive double-sided carbon tape. The energy was calibrated using C 1s peak (284.8 eV)[10].

(4) Fourier Transform Infrared Spectroscopy (FTIR)

The chemical structures were identified by FTIR (NEXUS 6700, Thermo Fisher, USA) scanning from 4000 to 500 cm^{-1}. The sample is prepared by grounding with KBr powder for 10 min and pressed into pellet under 10 Mpa for 1 min[10].

(5) Thermogravimetric Analyzer (TGA)

TGA was performed on a thermogravimetric analyzer (PerkinElmer, Pyris 1, USA) from 60 to 600 °C under nitrogen atmosphere[10]. The heating rate is 10 °C min^{-1}.

(6) Tribological Tests

A reciprocating ball-on-disc test rig was used for friction tests, see Figure 4-1 (a). The stroke length and the load for lubricated friction tests were 10 mm and 3 N, using velocity ramps (10 circles, 0 to 100 to 0 rpm) with motor oil (0W-40, Castrol Edge, Germany), see Figure 4-1 (b). The stroke length and the load for dry abrasion tests were 10 mm and 4 N, using a constant velocity of 200 rpm for 30 min. A customized rig (resembling to ASTM D-4060) was used for Wear tests, see Figure 4-1 (c). The rotating speed and the load for the nylon ring are 130 rpm and 1N[10].

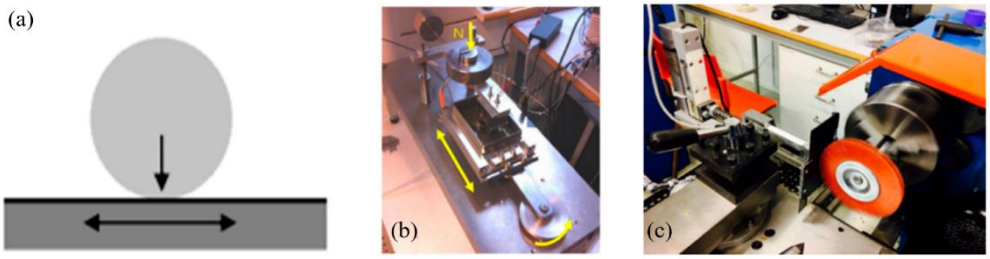

Figure 4-1. (a) Schematic presentation of the friction test setup. (b) The optical image of the tribological test rig. (c) The optical image of the abrasion test rig.

4.2.3 Results and Discussions

4.2.3.1 Preparation of Functionalized Graphene

The high active p-hydroxybenzene diazonium salt was prepared by a typical diazotization reaction, see Figure 4-2[10]. At first, nitrous acid reacts with the hydrogen ion in mineral acid to form the nitrosonium ion. When the nitrosonium ion meets

aromatic amine, its positive charge shifts on the nitrogen of aromatic amine to form N-nitrosamine as nitrogen attached with aromatic amine gives its long pair of electrons to nitrosonium ion. After that, protonation of N-nitrosamine takes place followed by deprotonation of it. Which gives rise to diazohydroxide. Finally, the diazohydroxide protonates to form diazonium salt. Based on this diazotization mechanism, aminophenol, $NaNO_2$, and HCl were choose as reactants to obtain diazonium salt for graphene functionalization. Notably, the diazonium salt should be prepared just before the next step of surface modification due to the diazonium salt's high tendency to decompose. The chemical reaction schematic diagram is as follows.

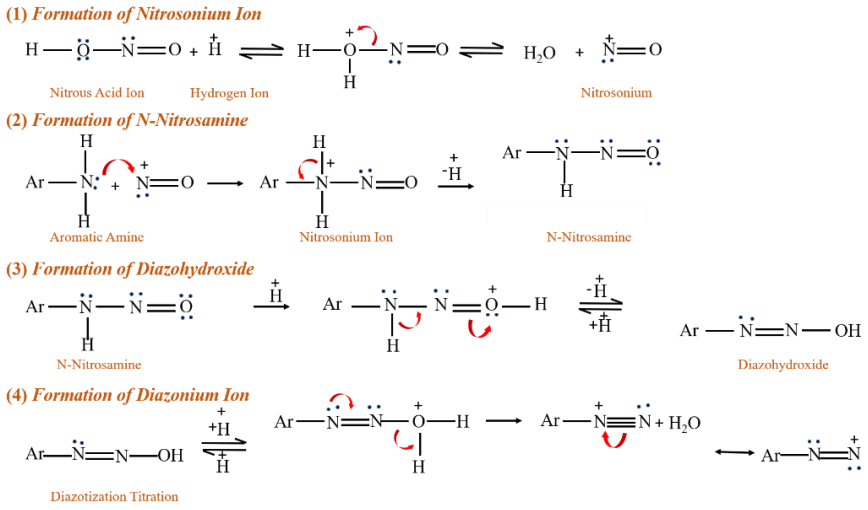

Figure 4-2. Schematic illustration of the mechanism of diazotization reaction.

After that, the p-hydroxybenzene diazonium chloride can react with the defects on graphene to prepare hydrophilic functional graphene. The preparation for functional graphene is shown in Figure 4-3.

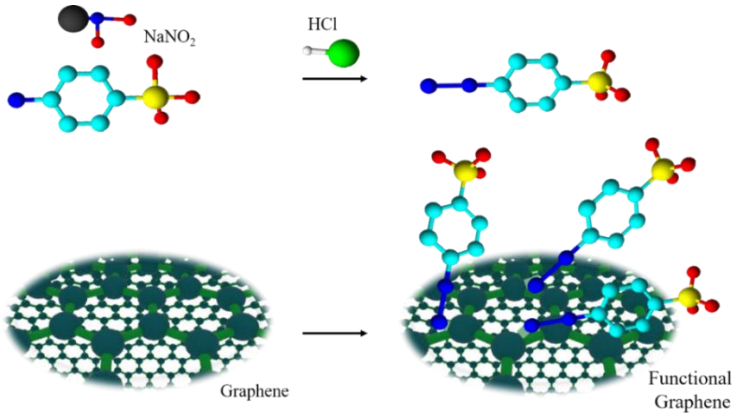

Figure 4-3. Schematic presentation of the preparation of functional graphene.

The FTIR spectroscopy was used to characterize the chemical structures of the functional graphene (FG) and the pristine graphene. A small peak at 1201 cm^{-1} corresponds to C-O stretching vibrations is observed at the FTIR spectrum of the unfunctional graphene, see Figure 4-4 (a). This peak indicates the presence of oxidized sites on the unfunctional graphene. These oxidized sites can provide possible reaction sites for functionalization. The peak at 2120 cm^{-1} disappears after functionalization, indicating the N≡N stretching vibrations in the p-hydroxybenzene diazonium salt are broken and may graft with the oxidized site on graphene sheets. Other evidence peaks are at 1061, 1191, 1564, and 1734 cm^{-1}, represents the existence of C-O, C-O (phenol), C=C (phenol), and C=O groups from the aromatic rings[10].

TGA provides evidence to further verify the functionalization of graphene, see Figure 4-4 (b). TGA curves of pristine graphene show a slight weight loss of 1 wt.%, while a significant weight loss of 3.5 wt.% is observed on the functional graphene at around 200 °C, corresponding to the decomposition of functional phenolic agents.

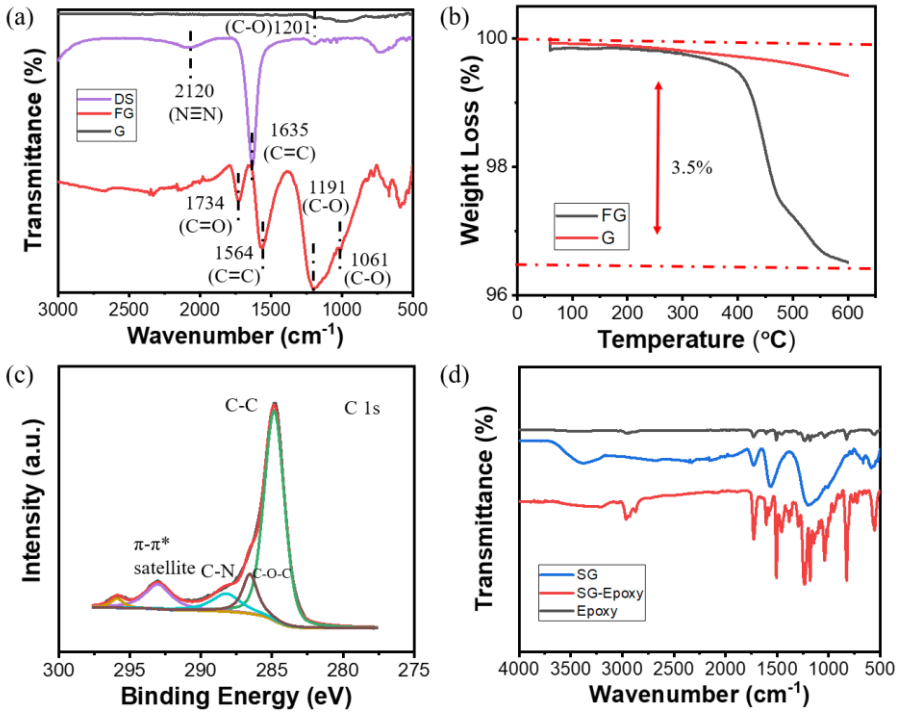

Figure 4-4. (a) The FTIR spectrum of the functional graphene and pristine graphene platelet. (b) The weight loss of the functional graphene by TGA. (c) The XPS spectrum of C 1s in the functional graphene. (d) The FTIR spectrum of the Tricolit TSC Coatings and functional graphene enhanced the Tricolit TSC Coatings.

Further, the XPS provides more evidence on the bonding between the aminophenol moiety and the graphene. The C 1s peak can be divided into four peaks, corresponding to π-π satellite (293 eV), C-N (288.2 eV), C-O-C (286 eV), and C-C (284.8 eV), see Figure 4-4 (c). All these above demonstrate the functionalization of graphene with p-hydroxybenzene diazonium salt[10].

Moreover, the peak at 3300 cm^{-1} on functional graphene, corresponding to the hydroxyl groups, disappears after curing with the functional graphene. This behavior indicates that functional graphene can work as the reactive cross-linker for epoxy coatings as expected, see Figure 4-4 (d)[24].

Take all the above characterizations into consideration, one feasible mechanism for p-hydroxybenzene diazonium salt functional graphene is represented in Figure 4-5. Similar to the well-known methylation reaction between the diazomethane and the carboxylic acid[10, 23], a heteropolar bond between diazonium moieties and the carboxyl is formed by ion exchange at first, following by the release of nitrogen from diazonium carboxylate[10].

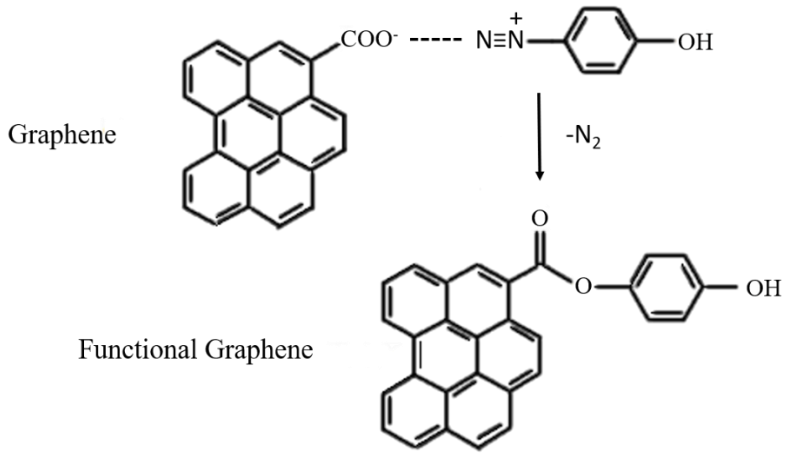

Figure 4-5. The mechanism of the p-hydroxybenzene diazonium salt functional graphene.

Afterward, the TEM was used to observe the micromorphology of the functional graphene. The unfunctional mechanical exfoliated graphene is composed of 10 layers of single-layer graphene, as shown in Figure 4-6 (a, b). After functionalization, the crystal structure of functional graphene was not as sharp as pristine graphene and lattice fringes are cannot even been observed, see Figure 4-6 (c, d)[10].

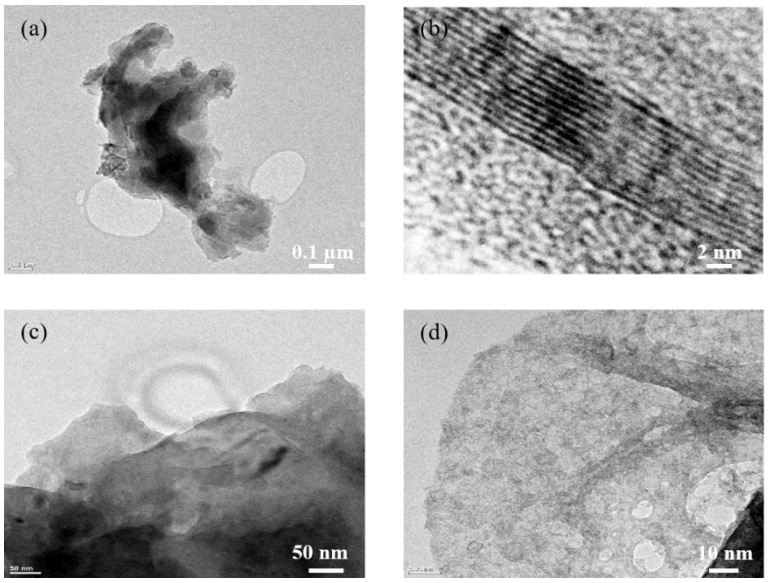

Figure 4-6. (a) The low-resolution TEM image of the pristine mechanical exfoliated graphene. (b) The high-resolution TEM image of the pristine mechanical exfoliated graphene. (c) The low-resolution TEM image of the diazonium salt functionalized graphene. (d) The high-resolution TEM image of the diazonium salt functionalized graphene.

4.2.3.2 Tribological Performance of Functionalized Graphene Enhanced Tricolit TSC Coatings

To optimize the geometry of functional graphene for the Tricolit TSC coatings, three batches of functional graphene with an average particle geometry of 3-6 μm (FG1), 1-3 μm (FG2), and 0.5-1 μm (FG3), were prepared respectively. As a reference, three commercial products, CNR, SNR, and graphene oxide (GO) was formulated with the Tricolit TSC coatings, respectively.

After dried, both the graphene and the reference GO enhanced Tricolit TSC coatings present a smooth surface on the aluminum substrate, see Figure 4-7 (a). Compared to the reference GO, the FG1 enhanced Tricolit TSC coatings show an improved dispersibility in the Tricolit TSC Coatings with a more homogenously surface after curing.

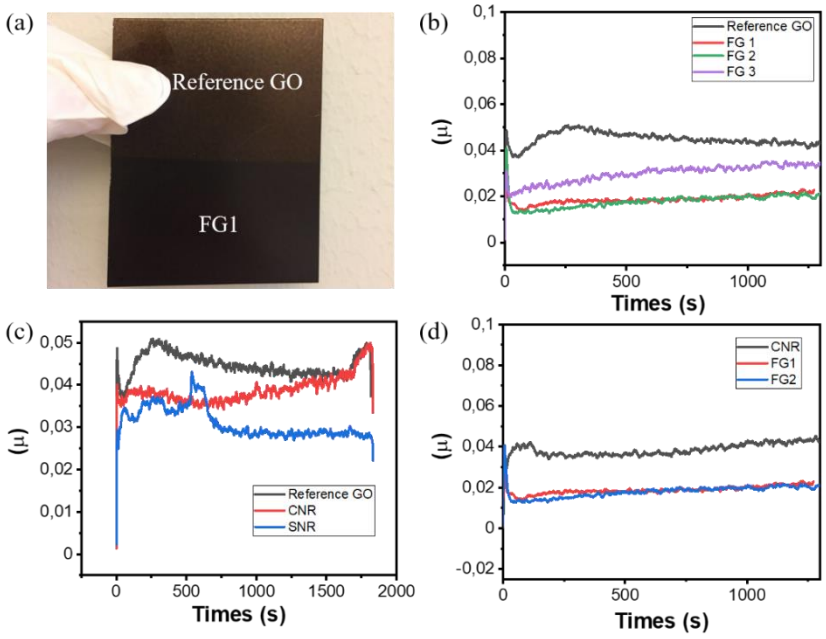

Figure 4-7. (a) The optical images of FG1 and reference GO enhanced epoxy coatings (Tricolit TSC, Applied Nano Surface AB). (b) The abrasion tests on stainless-steel plates (4 N, 200 rpm, 30 min, dry contact) of the reference GO, FG1, FG2, and FG3. (c) The abrasion tests on stainless-steel plates (4 N, 200 rpm, 30 min, dry contact) of the reference GO, CNR, and SNR. (d) The abrasion tests on stainless-steel plates (4 N, 200 rpm, 30 min, dry contact) of the reference CNR, FG1 and FG2.

In the dry contact, the coefficient of friction (COF) of the graphene-free Tricolit TSC Coatings is 0.75. After formulated with FG, the COF decreases to 0.02, almost 30 times less! Notably, less COF corresponds to better anti-friction behavior. The same coatings using graphene oxide filler give the COF around 0.05. Whereas the CNR and SNR provide even higher COF. In the lubricated contact, all functional graphene enhanced Tricolit TSC Coatings show lower COF than that of the reference GO enhanced coatings too, see Figure 4-7 (b, c, d). In all experiments, the COF of FG3 enhanced Tricolit TSC coatings is higher than that of FG1 and FG2, indicating larger size functional graphene decreases COF more than smaller one[10].

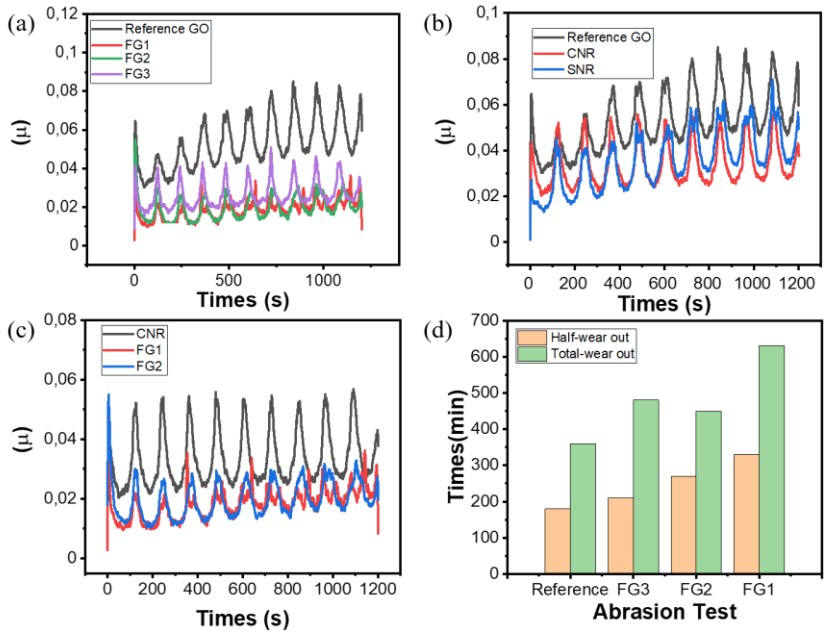

Figure 4-8. (a) Friction tests on different coated stainless-steel plates (4 N, 200 rpm, 30 min, lubricated contact) of reference GO, FG1, FG2, and FG3. (b) Friction tests on different coated stainless-steel plates (4 N, 200 rpm, 30 min, lubricated contact) of reference GO, SNR and CNR. (c) Friction tests on different coated stainless-steel plates (4 N, 200 rpm, 30 min, lubricated contact) of CNR, FG1 and FG2. (d) The wear out time of the reference GO, FG1, FG2, and FG3 enhanced epoxy coatings (Tricolit TSC, Applied Nano Surface AB).

The friction tests in lubricated contact show similar results with abrasion tests. All of the functional graphene enhanced graphene coatings show lower COF than the reference one, see Figure 4-8 (a, b, c). And FG1, FG2, exhibits lower COF than FG3. With the optimized geometry, FG1 shows more than 30% lower COF than the reference GO enhanced coatings. Further, among all samples, the FG1 enhanced Tricolit TSC Coatings possess the longest wear-out time (630 min). The wear-out time of FG1 enhanced Tricolit TSC Coatings is 1.5 times longer than the referenced GO enhanced coatings (360 min), see Figure 4-8 (d)[10]. Therefore, improved tribological properties in both the friction and wear tests have been demonstrated by adding functional graphene.

After curing, an obvious smoother surface was observed in the functional graphene enhanced Tricolit TSC Coatings, see Figure 4-9 (a, b, c, d). This improved surface evenness illustrates the functional graphene is able to improve the wear resistance for Tricolit TSC Coatings[10].

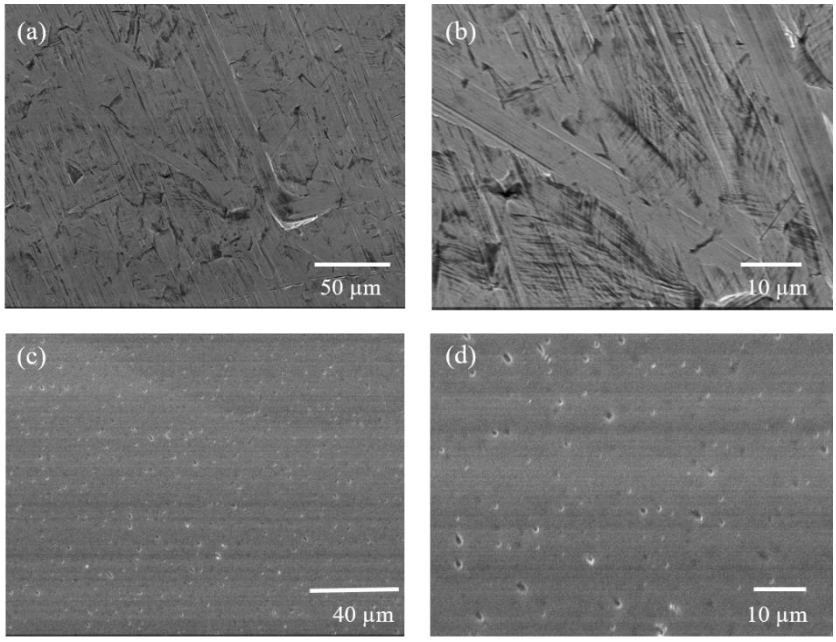

Figure 4-9. (a) The SEM image of the Tricolit TSC coatings. (b) The high-resolution SEM image of the Tricolit TSC coatings. (c) The SEM image of the diazonium salt functionalized graphene enhanced Tricolit TSC coatings. (d) The high-resolution SEM image of the diazonium salt functionalized graphene enhanced Tricolit TSC coatings.

4.2.3.3 Mass Production of Functionalized Graphene

Finally, mass production technology was developed for the functional graphene using a device shown in Figure 4-10 (a). With such a device, we are able to prepare functional graphene 300 g per batch. The concentration of functional graphene can be condensed to 55 mg mL^{-1}, see Figure 4-10 (b, c). Additionally, the same functional technology with the assistance of acid was expanded to mass-produce hydrophilic carbon fiber dispersion, see Figure 4-10 (d).

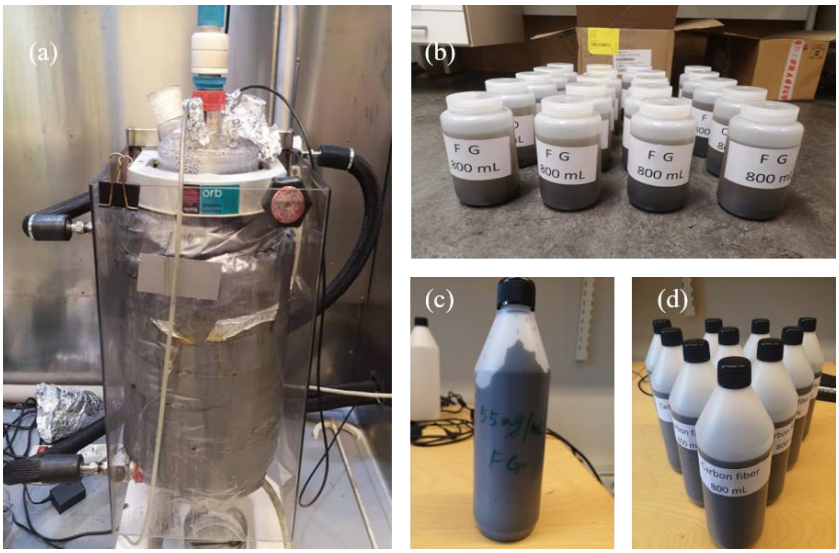

Figure 4-10. (a) The mass production device for functional graphene. (b) The optical image of mass-produced functional graphene. (c) The optical image of condensed functional graphene dispersion. (d) The optical image of mass-produced carbon fiber dispersion.

4.3 Hexagonal Boron Nitride Enhanced Cement Repair Material

4.3.1 Introduction

Concretes are widely used for buildings and constructions, such as bridges, roads, towers, etc. However, these concrete severely suffer from deterioration when exposed to sunlight, humidity, etc.[25] Currently, repair material, such as repair cement, is widely applied as an efficient and low-cost method for extending the lifetime of deteriorated concretes[25]. Enhancements in adhesion, elasticity, mechanical, rheological and permeability properties of these materials are important focused areas towards the development of future building materials. To date, there is a keen interest in developing nanotechnology, especially using 2D materials, for repairing cements[26]. Compared to the traditional material, the use of nanomaterial, such as graphene and carbon nanotubes (CNTs), exhibits outstanding advantages for reinforcing cement repair materials, such as ultra-high aspect ratios[27], extremely high strength[28], high modulus[29], and elasticity[30], etc.

However, there are few studies about using hexagonal boron nitride (h-BN) as a structure fortifier for cement repair material. It is proven that the incorporation of the hexagonal boron nitride can mechanically reinforce the cement-based materials[31, 32]. Moreover, the hexagonal boron nitride agglomeration is white in color (specified as ‘white

graphene) and this property enables the substrates to remain their original color after coated with the repair materials. However, the poor dispersed stability and compatibility with matrix limit its wide application in cement [33].

Cellulose derivatives are demonstrated as an excellent dispersant for carbon nanotubes (CNTs)[34]. Compared to sodium dodecyl sulfate (SDS), sodium carboxymethyl cellulose's (CMC) dispersing ability is twenty times higher for CNTs[35]. The long CMC molecules are thought to wrap around substrates for better dispersion. Similar to CNTs, the high specific surface area, chemical alert and strong Van der Waals force in the hexagonal boron nitride lead to the poor dispersibility of the hexagonal boron nitride[36]. In this regard, the CMC should also work as efficient dispersants for the hexagonal boron nitride. On the other hand, for cement repair materials, adhesion with substrates is one of the most common and important phenomena while considering applications[36]. Until now, CMC has widely been developed as tackifiers in water-born glue for thousands of years due to its exceptional adhesion, chemical stability, and low-cost properties[37, 38]. Therefore, the introduction of CMC in repair material would not only improve the dispersibility of the hexagonal boron nitride but also effectively raise the adhesion for substrates, such as pavements and airport runways, etc.

Furthermore, the role of hexagonal boron nitride during the hydration of cement is unrevealed. The presence of such material could impact the dissolution-precipitation mechanisms occurring when un-hydrated cement is mixed with water. The un-hydrated cement contains several mineral phases, the most important one being the tricalcium silicate (C_3S or Alite, C = CaO_2 and S = SiO_2). When mixed with water the C_3S dissolves, which leads to the precipitation of hydrates such as portlandite or calcium silicate hydrates (C-S-H). The hydration of C-S- contributes to improving the strength of the hardened material. Due to its charged surface, C-S-H is susceptible to interact with other charged species, such as the functionalized h-BN. The surface charge of C-S-H particles depends on the stoichiometry of the hydrate, which in turn depends on the pH of the pore solution of the cementitious material. For example, a C-S-H with a calcium-to-silicon ratio (Ca/Si) < 1 has a negative apparent surface charge due to the ionization of the surface silanol sites. C-S-H with a Ca/Si > 1 has a positive apparent surface charge due to an adsorption of $Ca^{2+,}$ gradually leading to the overcompensation of the surface charge[39]. In a regular hydrated Portland cement, the C-S-H has a Ca/Si between approximately 1.5 to 2[40] and therefore a positive apparent surface charge. The presence

of h-BN can potentially alter the hydration of C_3S and/or interact with C-S-H particles. A better understanding of the involved mechanisms would be beneficial to the development of repair materials enhanced with h-BN.

In this work, the CMC was used to functionalized multi-scale hexagonal boron nitride to enhance the mechanical performance of cement repair materials. The presence of hexagonal boron nitride in the hydration reaction of cement was investigated by using synthesized phases, C_3S and C-S-H. The nanoscale hexagonal boron nitride can work as a nucleation site during hydration while the microscale hexagonal boron nitride particle attribute to bond with $Si(OH)_4$ and $Ca(OH)_2$. Results show that the functional hexagonal boron nitride is able to increase C_3S for achieving high strength cement repair materials. Finally, cooperated with Lanark AB, the practical application has been conducted by using such h-BN enhanced cement materials to repair walls.

4.3.2 Materials and Experiments

4.3.2.1 Materials

Table 4-2. Materials

Name	Specifications	Manufacturers
Hexagonal Boron Nitride (h-BN)	98 wt.%	Sigma-Aldrich (Sweden) Trading Co., Ltd.
Carboxymethyl Cellulose (CMC)	M.W. 100, 000, DS 0.9	Sigma-Aldrich (Sweden) Trading Co., Ltd.
REP 920	Cement CEM II 52.5 N, Natural sand (0-4 mm)	Weber
$CaCO_3$	98 wt.%	Sigma-Aldrich (Sweden) Trading Co., Ltd.
SiO_2	200 $m^2 g^{-1}$	Algol Chemicals

4.3.2.2 Experiments

(1) Preparation of Hexagonal Boron Nitride Nanosheets

At first, 5 g hexagonal boron nitride powders were tip sonicated (VEVOR FS-1800N, Shanghai VEVOR Machinery Equipment Co., Ltd.) into a 500 mL distilled water and

isopropanol mixture solution. After that, the unexfoliated h-BN particles were removed by using a high-speed refrigerated centrifuge at 8000 rpm (CR22N, Hitachi Koki Himac Co., Ltd.), and the exfoliated BNNS were collected at 10000 rpm for 30 min.

(2) Preparation of Functionalized Hexagonal Boron Nitride

The CMC solution (5 mg mL^{-1}) was mixture with the BNNS dispersion under mechanical stirring. Afterward, centrifugation was used to isolate the product. After drying at 60 °C, the obtained functionalized hexagonal boron nitride powder can be easily dispersed in water.

(3) Preparation of the C_3S

The C_3S was synthesized as follows and respecting the method presented in another study[41]. Accordingly, 75 g of $CaCO_3$ and 15 g of SiO_2 (Aerosil 200, Algol Chemicals), 180 g of Milli-Q water were precisely weighted and introduced in the container. The geometry of milling balls (290 g) is 2 cm. The container was then tightly closed and sealed, following by put on a custom-made rotation device at low speed for 24 h. Then the obtained paste was put in smaller containers and dried at 105 °C until constant weight. Finally, the obtained powder was burned at 1600 °C for 5 hours and air quenched after calcination.

The C-S-H samples with Ca/Si of 0.8, 1.0, 1.2 and 1.4 were synthesized as suspensions as described in a previous study[41] by using calcium oxide, aerosil silica and water. Calcium oxide was obtained after decarbonization of calcium carbonate at 1000 °C for 4 hours. Before use, the water was freshly demineralized. The liquid to solid ratio (L/S) of those suspensions has been fixed to 50. Different Ca/Si was used to investigate the influence of the zeta potential on the interactions with hexagonal boron nitrides. The composition of the different samples is described in Table 4-3 (the indicated weight takes into account the solubility of the C-S-H at the laboratory temperature). Once the mix of the different reagents is made, the suspensions are transferred on a rotation device at low speed for 4 weeks to ensure the complete reaction between C-S-H and additives. In particular, 3 suspensions were made for each Ca/Si: one was kept as it is for a reference, one was mixed with 0.4 wt.% of FBN (functionalized BN) and the third one was mixed with 7 wt.% of FBN. Because the potential changes with 0.4 wt.% FBN might be challenging to detect, the system containing 7 wt.% FBN will avoid that issue, although such a high concentration is not representative of a practical system.

Table 4-3. The components of C-S-H suspensions.

Ca/Si	CaO (g)	SiO_2 (g)
0.8	2.27	3.04
1.0	2.45	2.59
1.2	2.73	2.36
1.4	3.00	2.07

4.3.2.3 Characterization

(1) Fourier-transform Infrared Spectroscopy (FTIR)

FTIR was conducted on UATR TWO (PerkinElmer, USA) at the wavenumber range of 4000-400 cm^{-1}. The FTIR sample was prepared by ground and compressed with KBr powder to form a KBr pellet.

(2) Scanning Electron Microscopy (SEM)

The micro morphologies of cement repair materials and BNNS were observed under SEM (Zeiss Supra 60 VP, Zeiss, Germany) at 20 kV.

(3) Atomic Force Microscope (AFM)

Atomic force microscopy (AFM) was used to analyze the morphology of BNNS on the Nanoscope IIIa in the tapping mode. The scan rates were between 1.0 and 2.4 Hz.

(4) Optical Images

The optical images were captured by a digital telephone (Huawei Note 20, China) with 20x resolution.

(5) Isothermal Calorimetry

The early heat developed during the hydration of the synthesized C_3S was measured by a TAM Air isothermal calorimetry over 7 days, in form of time vs. cumulative heat and time vs. heat flow curves. The dry components were precisely weighed (precision up to 0.0001 g) and mixed. The desired amount of Milli-Q water was taken with a pipette, added to the solid mix and its weight was also measured precisely. Right after, the mix was stirred for 2 min with a spatula before the introduction of approx. 5 g of the paste in

a calorimetry vial with a funnel. The weight of the sample in the vial was precisely measured before sealing the vial and introduce it into the calorimeter. The heat release was measured during the hydration of the paste over 7 days. After that time, the samples were recovered to stop the hydration by solvent exchange. The samples were submerged in isopropanol (2-propanol ≥ 98 % technical, VWR chemicals) for 7 days. During that time, the isopropanol was renewed two times the first day, and one time after during the 2nd, 3rd and 5th day. After drying, the samples were stored in a desiccator with silica gel and soda lime.

(6) Thermogravimetric Analysis (TGA)

TGA was made on ground paste samples with a Mettler Toledo TGA-DSC3 heated from 20 to 1000 °C at a rate of 10 °C min^{-1} and purging flow of 50 mL min^{-1} in N_2. The amount of portlandite (CH) are presented as the wt.% relative to the dry mass and calculated as follows:

$$CH = \frac{w_{450} - w_{500}}{w_{520}} \cdot \frac{74}{18} \qquad 4-1$$

where "w_x" represents the weight of the sample at the temperature "x".

(7) X-Ray Diffraction (XRD)

The characterization of crystalline phases was performed by XRD measurements with a Rigaku Miniflex 600 with a fast 1d solid-state detector. The scan was performed between 2 and 42°.

(8) Zeta Potential

The surface zeta potentials (ζ) and the particle sizes were conducted on a Malvern Zetasizer (Malvern Panalytical, England). Three repeats for each sample were conducted. The ζ potential measurements were made approximately one month after the FBN was added to the suspensions to ensure the systems to have reached equilibrium.

(9) Flow Behaviors

The flow behavior of the repair material with and without h-BN or FBN was characterized by the mini-cone test method. The mini cone's dimensions are: Height: 5.56 cm, Upper diameter: 1.95 cm and. Lower diameter: 3.65 cm. The tested volume of 36.05 mL may run out on a test table of frosted glass. Only the final diameter of the slump was measured.

The procedure of the mini-corn test was presented in Figure 4-11. First, a glass plate and the mini cone are humidified. The repair material, the h-BN/FBN and water are mixed for 1 min by hand and then 3 min with a mixer at low speed. The paste is inserted in the mini cone standing on the glass plate. The mini cone is lifted, allowing the paste to flow. The resulting diameter of the paste is measured. A high diameter will be obtained for a sample with high fluidity. This method was also used to adjust the amount of water when h-BN is present in the mix: in this case, the goal was to obtain the same diameter.

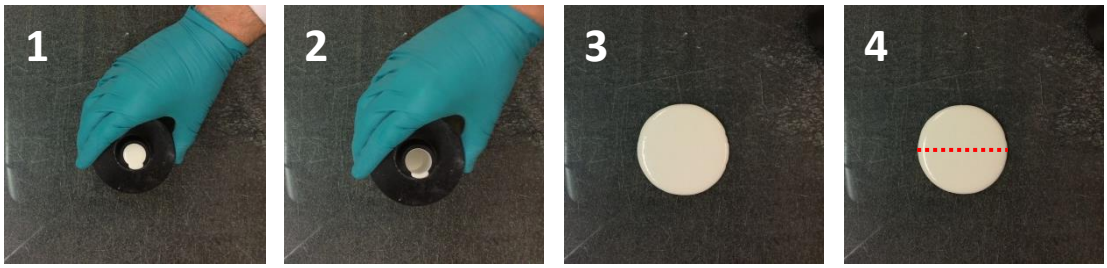

Figure 4-11. The procedure of the mini-cone test.

4.3.3 Results and Discussions

4.3.3.1 Preparation of Functionalized Hexagonal Boron Nitride

The diameter of microscale hexagonal boron nitride (h-BN) is about 0.2-4 μm with an agglomeration of 30-60 layers of single-atom layer h-BN sheets (BNNS), as shown in Figure 4-12 (a). While the diameter of the nanoscale h-BN particle is about 100 nm with few-layer BNNS, as shown in Figure 4-12 (b).

The FTIR was used to identify functional groups and thereby check the functionalization of h-BN, see Figure 4-12 (c). The broad absorption bands at 2974, 1583, 1411, 1053, and 900 cm^{-1} on the FTIR spectrum of the functional boron nitride are attributable to C-H stretching vibrations, the stretching vibrations of carboxyl groups (COO-), carboxyl groups, C-O-C stretching and 1,4-β glycoside of CMC, respectively. On the other hand, compared with the FTIR spectrum of CMC, the absorption peak of FBN shifts to higher wavenumbers. Such blue shift indicates the electron-withdrawing inductive effect by bonding with h-BN. Especially, the broad and strong peak at 3367 cm^{-1} shifts to a weak peak at 3667 cm^{-1}, suggesting a dedication of the hydrogen bond between hydroxyl

groups. Thus, these shifts provide evidence for the functionalization of the hexagonal boron nitride.

After functionalization, the dispersibility of h-BN is dramatically improved, as shown in Figure 4-12 (d). A high concentration of FBN can be dispersed in water with moderate stirring and shows a milk-like dispersion. After functionalization, the zeta potential of FBN dispersion decreases from to -5.61 mV to -55.07 mV, indicating the largely improved dispersibility than pristine h-BN[41]. The FBN dispersion is able to keep stable for 1 week.

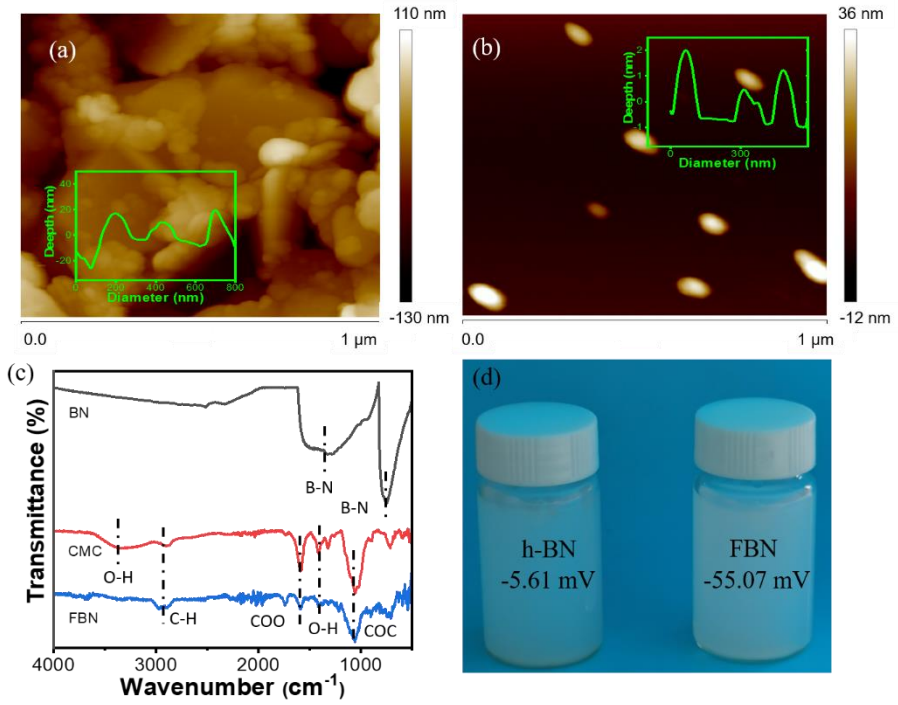

Figure 4-12. (a) The AFM image of microscale h-BN particles. (b) The AFM image of exfoliated BNNS. (c) The FTIR spectrum of h-BN, CMC, and FBN. (d) The optical images of h-BN and FBN dispersions.

4.3.3.2 Interaction of Functionalized h-BN with C-S-H Particles and C_3S

The zeta potential was used to characterize the reaction between C-S-H suspensions and FBN. After functionalization, the zeta potential of FBN particles was measured as negative charged within a pH range from 0 to 14, see Figure 4-13 (a). As presented in Figure 4-13 (a), the particles have a negative surface charge of -46.8 mV at a neutral pH environment. This can potentially lead to interactions with C-S-H particle having a Ca/Si > 1.0 and therefore a positive apparent surface charge. The reference samples, i.e. without FBN, have an expected behavior, with a negative value for a Ca/Si of 0.8, a

positive value for the other ones, and increasing with the Ca/Si. The obtained values are also similar to what is observed in the literature[42]. The presence of FBN in the suspensions does not impact the zeta potential of the particles. This indicates that there is no interaction between the FBN and the C-S-H particles, whatever their Ca/Si ratios, see Figure 4-13 (b).

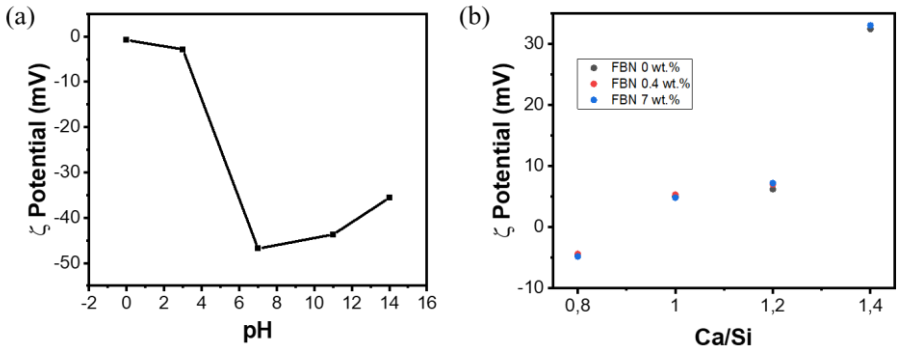

Figure 4-13. (a) The zeta potential of FBN in water under pH from 0 to 14. (b) Evolution of the zeta potential of C-S-H suspensions with various Ca/Si ratios (0.8, 1.0, 1.2 and 1.4) and mixed with 0, 0.4 and 7 wt.% of FBN.

The hydration reaction of the C_3S in the absence and presence of h-BN and FBN and measured by isothermal calorimetry with both heat flow and heat, presented in Figure 4-14. The visible peak in the heat flow corresponds to the hydration of the C_3S. The presence of h-BN or FBN does not introduce any change in kinetic. The position and the intensity of the peak are not changed when FBN presents, but slightly decreases with h-BN, see Figure 4-14 (a). Up to 1.5 days of hydration, all samples have a similar cumulative heat, see Figure 4-14 (b). After that point, the samples containing h-BN and FBN produce more heat than the reference. No differences can be seen between h-BN and FBN, meaning that the small decrease observed on the heat flow for h-BN does not influence a longer term. The higher total heat indicates that more hydrates have grown in the presence of h-BN and FBN.

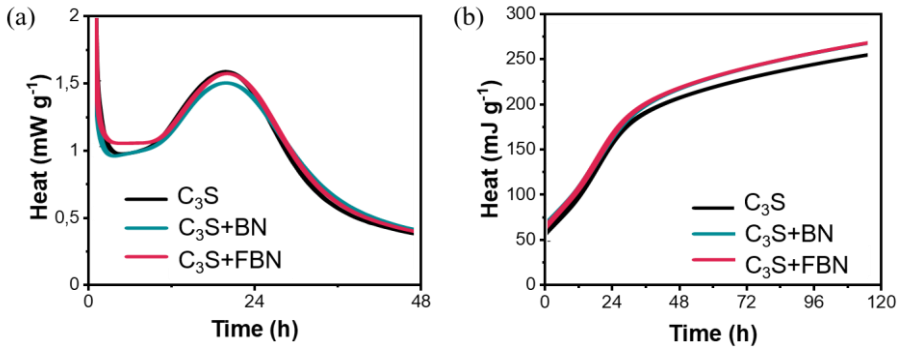

Figure 4-14. (a) The heat flow of the C_3S hydration alone or mixed with h-BN or FBN. (b) The flow of the C_3S hydration alone or mixed with h-BN or FBN.

After isothermal calorimetry, the samples were analyzed by the XRD and TGA. For the XRD, the hydrated samples are compared with the raw material, i.e. un-hydrated C_3S and h-BN. By comparing the hydrated sample to the un-hydrated C_3S, new diffraction peaks are present. The ones indicated by a * correspond to portlandite ($Ca(OH)_2$), which is one of the hydration products of C_3S together with C-S-H, see Figure 4-15. The C-S-H having a nano-crystalline structure[43], it is challenging to detect it by XRD. Another "new" peak is visible around 27°, corresponding to the presents of h-BN. No other phases are detected, showing that the h-BN did not react to form a new component.

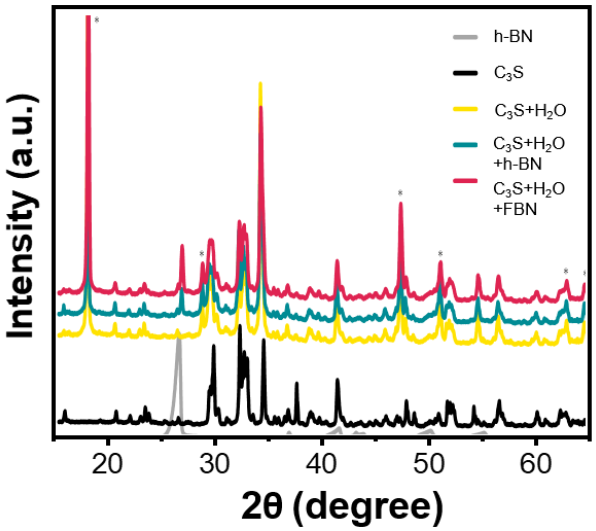

Figure 4-15. The XRD diffractograms of the raw h-BN, un-hydrated C_3S and the hydrated with or without h-BN/FBN. The pictures indicated with a * correspond to portlandite ($Ca(OH)_2$).

In Figure 4-16, the weight loss registered during the TGA analysis is similar for all samples. Only the sample containing h-BN have a slightly less important weight loss upon warming (approximately 0.3 % compared to the other samples), see Figure 4-16

(a). The derivative curves, presented on the right side, allow distinguishing the different phases present in the samples. The identification was made following the indication given in another study[44]. The portlandite is visible at approximately 450°C. The different samples present similar portlandite content, see Table 4-4. There are two other peaks, one at 130°C corresponds to the C-S-H and is similar for all samples, and the second one at 700°C, see Figure 4-16 (b). This later can be associated with either C-S-H or calcium carbonate $CaCO_3$, and is the only peak showing differences between the samples: it has a higher intensity when FBN presents. It is however not possible to conclude with certitude on which phase it is, even though the calorimetry measurement goes in favor of the formation of more hydrates.

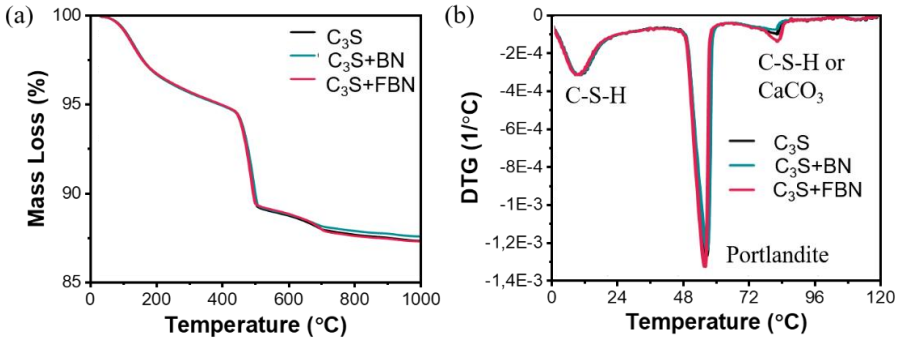

Figure 4-16. The TGA analysis of the hydrated C_3S paste with or without h-BN/FBN. Left: mass loss. Right: derivative curves.

Table 4-4. Portlandite content of the C_3S pate with or without h-BN/FBN. The amount is relative to the dry mass of the samples.

Sample	C_3S	C_3S + h-BN	C_3S + FBN
Portlandite Content (wt.%)	25.91	25.54	25.36

Finally, those three samples were also analyzed by SEM. As shown in Figure 4-17 (a-d), the introduction of h-BN and FBN dramatically enhanced the hydration process with obvious fiber-like crystal structures. The nanoscale h-BN and FBN particles might act as nucleation sites for the formation of C-S-H. Moreover, the FBN particles are more homogenously dispersed in the cement paste than BN, as shown in Figure 4-17 (d), the h-BN particle tends to form a cluster while the FBN is dispersed uniformly distributed in the cement, see Figure 4-17 (e, f). We can therefore conclude again on the success of the functionalization of the h-BN.

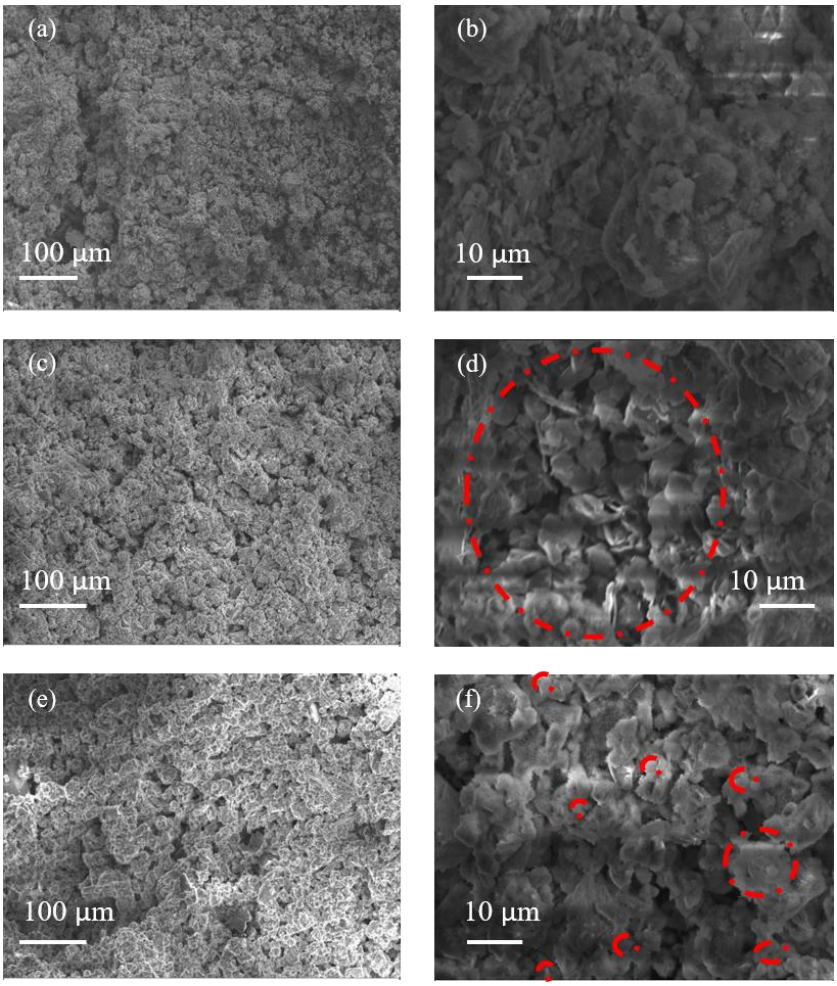

Figure 4-17. (a) The low-resolution SEM image of the C_3S paste after hydration. (b) The high-resolution SEM image of the C_3S paste after hydration. (c) The low-resolution SEM image of FBN enhanced C_3S paste after hydration. (d) The high-resolution SEM image of the FBN enhanced C_3S paste after hydration. (e) The low-resolution SEM image of the FBN enhanced C_3S paste after hydration. (f) The high-resolution SEM image of the FBN enhanced C_3S paste after hydration.

4.3.3.3 Mechanical Performances of Functional Boron Nitride Enhanced Cement Repair Materials

The potential impact of the presence of h-BN and FBN on the fluidity of the repair material Rep 920 was check using the mini-cone test. The results are presented in Table 4-5. No significant impact is measured when 0.4 wt.% h-BN is used. On the contrary, the presence of FBN drastically decrease the fluidity: the paste could not flow out of the cone when this later was lifted. This can lead to a lower adhesion of the enhanced repair material to the substrate. The loss of fluidity is probably due to the hydrophile properties of the functionalization agent (CMC): a part of the water is absorbed and not available

anymore. To overcome this issue, extra water is added to reach a fluidity similar to the h-BN free repair materials. Increasing the water-to-solid ratio from 0.084 to 0.086 was enough.

Table 4-5. The impact of the presence of 0.4 wt.% h-BN and FBN on the fluidity of the repair material ("no water adjustment") and the amount of water required to keep a similar fluidity. Measured with the so-called "mini cone test".

		No water adjustment			Water adjustment	
Mixes	Rep 920 (g)	90	89.64	89.64	89.64	89.64
	h-BN (g)	0	0.36	0	0	0
	FBN (g)	0	0	0.36	0.36	0.36
	water (g)	7.56	7.56	7.56	8.1	7.74
	water/solid	0.08	0.08	0.08	0.09	0.08
	Diameter (mm)	34	32	*	38	35

*stayed stuck in the mini cone

The compressive strength 28th of those mixes were measured, see Figure 4-18. The repair material and the mixture containing h-BN exhibits similar compressive strength (75.9 and 73.8 N mm^{-2}). The mix containing FBN has a significantly lower strength: 64.6 N mm^{-2}. This was expected due to the extra water added, which lead to a more porous structure and thus a lower compressive strength.

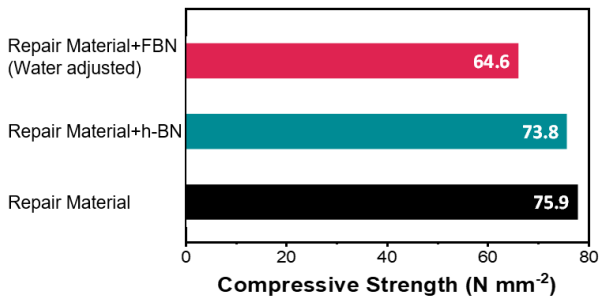

Figure 4-18. The compressive strength at 28 days of the repair material with or without h-BN/FBN. The mix with FBN was water adjusted to keep a similar fluidity.

The graphic representation of the type of failure for each mix is presented in Figure 4-19. Among the different possible failure types (i.e. in the glue, the repair material, the

concrete, or the interface repair material/concrete), a failure of the glue represents a failed test (glue possibly too thin, too dry, etc.), while a failure in the concrete is the best possibility, showing that the repair material is stronger than the concrete.

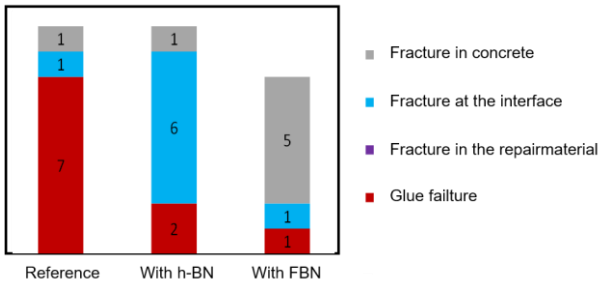

Figure 4-19. The graphic representation of the type of failure for each mix.

The repair material without h-BN or FBN shows mainly a failure of the glue (7 cases out of 9). It is thus not possible to compare this reference mix to the other ones. For the repair material containing h-BN, most of the failure happened at the interface repair material/concrete with an average load of 3.4 MPa, while it is mainly happening in the concrete for the sample containing FBN, with an average load of 4.2 MPa. This shows that the repair material containing FBN is 1) stronger than the reference concrete, 2) has a better adhesion property compared to the sample containing h-BN.

4.3.3.4 Industrial Application of Functional Boron Nitride Enhanced Cement Repair Materials

Figure 4-20. (a) The optical images of industrial applications of FBN enhanced cement repair materials. (b) Certificates of industrial applications of FBN enhanced cement repair materials.

Finally, our FBN enhanced cement repair materials have been granted for the five-stars campus project and have been used to repair the cement walls, see Figure 4-20 (a). Figure 4-20 (b) shows the certificates for these applications.

4.4 Graphene Enhanced mRNA Based Drug Delivery Platform

4.4.1 Introduction

When the diameters of graphene sheets decrease to a certain nanoscale dimension, for instance 10 nm, the quantum confinement effect can be observed, and such graphene sheets are named as graphene quantum dots (GQDs). Academically, the geometry at which graphene sheet starts to exhibit quantum confinement effects is controversial, and the thickness of graphene quantum dots is defined as 1 layer, 1-2 layer, or less than 10 layers[45]. Compared to graphene nanosheets, graphene quantum dots present quantum confinement effects, larger surface areas, more active sites, and unique photoluminescence behaviors. Coupled with good biocompatibility and dispersibility, colloidal stability, and tunable surface structure[46, 47], graphene quantum dots are attractive for drug delivery. Moreover, graphene quantum dots are able to quickly respond to physical stimuli, such as ultrasound[48], magnetic fields[49] and light[50], etc. These unique responding features allow the accurate control of drug release[46].

To date, a variety of graphene based drug delivery platforms, including electrical fields activated graphene based microcapsule platform[51], graphene oxide/carbon/mesoporous silica photo-responsive drug delivery platform[52], and graphene based photothermal therapy[53], etc. have been extensively developed. For example, Li et al. has demonstrated folic acid modified N-doped carbon dots as an efficient platform for killing 26 types of tumor cells[54]. Graphene quantum dots were proved to be able to across the blood-brain barrier and prevent α-synucleinopathy in Parkinson's disease without surface functionalization[55]. Iannazzo et al. has established a good biocompatible and cell-traceable drug delivery system based on graphene quantum dots for inserting the doxorubicin drug into DNA for cancer therapy[56]. Su et al. has synthesized a pH-sensitive graphene quantum dots nanoaircraft with variable size, which can deliver and penetrate antitumor drugs into the deep Tumor[57]. Yao et al. established a graphene quantum dots-capped magnetic mesoporous silica nanoparticles as a multifunctional platform for drug release, magnetic thermotherapy and photothermotherapy[58]. Further, graphene quantum dots can selectively interact with RNA or DNA to protect them from enzymatic degradation[57], thus increase the interest in integrating graphene quantum dots with DNA or RNA-based therapeutics.

Messenger RNA (mRNA)-based therapeutics are highly expected in drug delivery for several distinctive advantages, such as increased control of protein formation, reduced genotoxicity, high compatibility with biological systems, and no need for nuclear localization or transcription[59, 60]. The mRNA-based therapeutics offer new possibilities for treating disease, so a variety of different biomaterial-based systems have been developed for mRNA delivery, such as lipid nanoparticles[61, 62], polymeric nanoparticles[63, 64], and gold nanoparticles[65], etc. However, the biomaterial delivery systems that can stably, safely, and effectively deliver mRNA to specific sites with high selectivity and efficient protein expression are still need improvement. Furthermore, mRNA molecules are unstable in most biological fluids, carrying a negative charge and large, leads to poor cell penetration and instability. These two features limit their application for therapies. In this regard, due to the surface tunable properties and colloidal stability, graphene quantum dots and mRNA composite particles would ameliorate the challenges of poor penetration and instability[47].

However, the unmodified graphene quantum dots are negatively charged. Without functionalization, they will not bind mRNA very well. To this end, polyethyleneimine (PEI) allows the complexation of DNA and RNA, and it possesses a high cationic charge density. Recently, PEI functional carbon nanotubes have been successfully demonstrated to deliver DNA or RNA[66]. Given the similar properties of carbon nanotubes and graphene quantum dots, PEI would be a good starting point for exploring the utility of graphene quantum dots for mRNA delivery platforms.

In this work, the PEI functional graphene quantum dots were used to deliver intact and functional mRNA to Huh-7 hepatocarcinoma (liver) cells. This cell line is used as a model for the liver because most nanomedicine particles are cleared by the liver, resulting in higher levels of transfection in this organ. The result shows the transfection efficiency for functional graphene quantum dots and mRNA complexes is 25% with a formulation concentration of 4000 ng mL^{-1}. This work describes the first step towards a potentially interesting preparation method for stable and effective mRNA delivery systems.

4.4.2 Materials and Experiments

4.4.2.1 Materials

Table 4-6. Materials

Name	Specifications	Manufacturers
Citric Acid	99 wt.%	Sigma-Aldrich (Sweden) Trading Co., Ltd.
Sodium Hydroxide (NaOH)	97 wt.%	Sigma-Aldrich (Sweden) Trading Co., Ltd.
Polyethylenimine (PEI)	50 wt.%	Sigma-Aldrich (Sweden) Trading Co., Ltd.
Ethylenediamine (EDA)	98 wt.%	Sigma-Aldrich (Sweden) Trading Co., Ltd.
Dicyclohexylcarbodiimide (DCC)	99 wt.%	Sigma-Aldrich (Sweden) Trading Co., Ltd.
Erythropoietin (EPO)	/	AstraZeneca Co., Ltd.
Enhanced Green Fluorescent Protein (EGFP)	/	AstraZeneca Co., Ltd.
mRNA	/	AstraZeneca Co., Ltd.
Tris Solution	1 M	AstraZeneca Co., Ltd.
Huh-7 Hepatocarcinoma Cells	/	AstraZeneca Co., Ltd.
Fetal Bovine Serum (FBS)	1 mg mL^{-1}	AstraZeneca Co., Ltd.
L-glutamine	5 wt.%	AstraZeneca Co., Ltd.
Sodium Pyruvate	5 wt.%	AstraZeneca Co., Ltd.
MC3-based Lipid Nanoparticles	/	AstraZeneca Co., Ltd.
Hoechst 33342	98 wt.%	Sigma-Aldrich (Sweden) Trading Co., Ltd.
Propidium Iodide	94 wt.%	Sigma-Aldrich (Sweden) Trading Co., Ltd.

4.4.2.2 Experiments

(1) Preparation of Graphene Quantum Dots

At first, the citric acid solution (5-20 g mL^{-1}) was heated at 200 °C for 6 h in a 150 mL Teflon-lined stainless-steel autoclave. After cooling to room temperature, the resulting orange liquid was centrifuged and dialyzed (3.5 K MWCO) for seven days to remove unreacted and impurity chemicals, until the pH becomes 7.0. Finally, the solution was concentrated by centrifugation (8000 rpm). The concentration of the graphene quantum dots (GQDs) is 4 mg mL^{-1}, and the reduction yield is 56 wt.%.

(2) Preparation of Functionalized Graphene Quantum Dots

At first, 10 mL GQDs were dispersed in 100 mL distilled water, aminated by adding ethylenediamine (EDA) and dicyclohexylcarbodiimide (DCC) under stirring for 1 h at 80 °C. After that, 10 mL 10 wt.% PEI solution was added into the aminated GQDs solution and stirring for 8 h. The resulting solution was further purified using 3.5 K MWCO dialysis tubing for 7 days under running water, resulting in a final concentration of 2.8 mg mL^{-1} functional graphene quantum dots (FGQDs). The FGQDs fluoresce somewhat with emission in the green part of the spectrum (around 520 nm). This could be mitigated by using moderate concentrations as the fluorescence at the concentrations used here is not intense when compared with the enhanced green fluorescent protein (EGFP).

(3) Formation of the FGQDs/mRNA Complex

The molar ratios of N in FGQDs to molar ratios of P in mRNA (N/P ratio) were used to quantity FGQDs to mRNA ratios. The pH was adjusted to 7.5 using 1M Tris (pH 8). Before analysis, the FGQDs/mRNA complex was incubated for 1 h under room temperature.

(4) Cell Transfer Efficiency and Cytotoxicity Test

The Huh-7 hepatocarcinoma cells were cultured in DMEM supplemented with L-glutamine (5 wt.%), sodium pyruvate (5 wt.%), fetal bovine serum (10 wt.%), and incubated in CO_2 (5%) at 37 °C. Cells were seeded into the Cell Carrier imaging plates two days before test. FGQDs/mRNA source plates were created using acoustic dispensing (Echo 655) followed by robotic transfer (Agilent Bravo) to the Huh-7 cultures. Lipid nanoparticles (LNPs) and FGQDs were incubated together with the

growth medium normally used to maintain the cells, and the cells were incubated with FGQDs/mRNA in 2 different ways: using a 2 h pulse incubation and removing the FGQDs/mRNA with an additional 22 h incubation in a fresh growth medium or 24 h continuous incubation. As a control, MC3-based LNP were added and used. Propidium iodide and Hoechst 33342 were added directly to living cells 24 h to stain cells and nuclei, respectively. The experiments were run twice, and wells were dosed in triplicate.

4.4.2.3 Characterization

(1) Fourier Transform Infrared Spectroscopy (FTIR)

The chemical structures were identified by FTIR (NEXUS 6700, Thermo Fisher, USA) scanning from 4000 to 500 cm^{-1}. The sample is prepared by grounding with KBr powder for 10 min and pressed into pellet under 10 Mpa for 1 min.

(2) Raman Spectroscopy

Raman spectroscopy (XploRA, Thermo Fisher, USA) was used to determine the single-layer structure in graphene. The Raman spectroscopy was scanned at 532 nm for 5 s. The sample powder is dispersed on a glass sheet for measurement.

(3) Zeta Potential and Particle Size

Surface zeta potentials (ζ) and Particle sizes were conducted on a Malvern Zetasizer (Malvern Panalytical, England). Three parallel repeats were carried out for each sample. The DTS1060-folded capillary cell (750 μL) was applied as the sample holder.

(4) Atomic Force Microscopy (AFM)

Atomic force microscopy (AFM) was used to analyze the morphology of graphene quantum dots and functional graphene quantum dots on a nanoscope (IIIa) with NSC15 tips (silicon cantilever, Mikro Masch, USA). The scan rates were between 1.0 and 2.4 Hz with a tapping mode.

(5) Transmission Electron Microscopy (TEM)

TEM (Tecnai G2 20, USA) is operated at an acceleration voltage of 200 KV to show the microstructure of graphene oxide sheets. The sample solution is diluted to 1 mg mL^{-1}, and dropped on lacey support films with further drying under 60°C in an oven.

(6) Agarose Gel Electrophoresis

The FGQDs/mRNA complexes were examined by agarose gel electrophoresis (1wt.% Agarose E-GelEX, Invitrogen) at various N/P ratios (i.e. at N/P 0, 2, 4, 6, 8, 10, 20, 40 60, 100). Three replicates were performed per dose and two fields of view were acquired in each well.

(7) Confocal Images

Confocal images were acquired using a 20x objective (Olympus, NA 0.95) at two points in every well (Yokogawa CV7000). Before investigated under confocal imaging, the EGFP mRNA transgene expression was incubated for 24 h with FGQDs/mRNA. For transfection of mRNA and cytotoxicity test, 8 doses were used per formulation (as shown in Table 4-7).

Table 4-7. FGQDs/mRNA doses for cell incubation.

ng well^{-1}	ng mL^{-1}
250	8333
100	3333
40	1333
16	533
6.4	213
2.6	85
1.0	34
0	0

In detail, 15000 cells per concentration were typically analyzed, and the initial analysis extracted 16 parameters per cell. Cells were classified as EGFP-positive, PI-positive (dead), and/or PI-negative (living). Additional measurements related to cell health were also generated (cell counts, nuclear intensities, and nuclear morphological measures). Data are shown as mean from 6 wells for each point (combined data from 3 replicates in two separate experiments).

4.4.3 Results and Discussions

4.4.3.1 Preparation of Graphene Quantum Dots

At first, the GQDs were prepared from citric acid, as shown in Figure 4-21. After pyrolysis and carbonization, the carbon atoms self-assemble into interlinked hexagonal carbon rings (at the red rings site), and thus creating graphene.

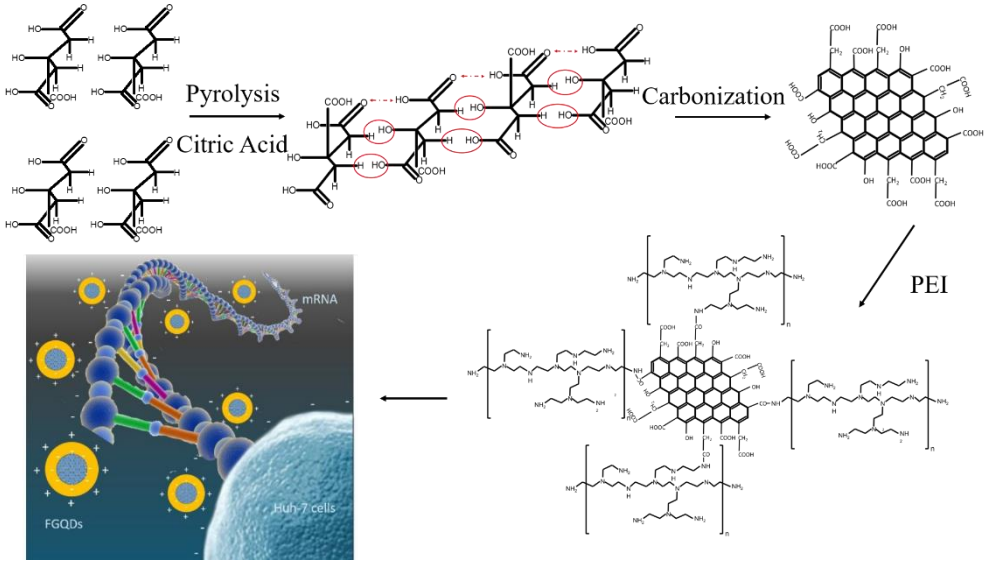

Figure 4-21. A schematic image for the synthesis of FGQDs. The red rings show the carbonization reaction sites.

4.4.3.2 Preparation of Functionalized Graphene Quantum Dots

After purification, the GQDs were functionalized by PEI following a reaction with graphene carboxyl groups. The high concentration of positively charged amino groups on PEI imparts positive surface zeta potential that permits mRNA complexation.

The FTIR was used to characterize the chemical structures of GQDs and FGQDs. After carbonization, only peaks correspond to C=C=O, C=O and C-O-C bonds are observed, while there is no peak indicate C=C bond observed in the FTIR spectrum of citric acid, as shown in Figure 4-22 (a). Additionally, the FTIR spectrum of GQDs does not reveal any absorption for C-H bonds, implying the complete carbonization of the citric acid. After functionalized by PEI, typical peaks of C-N and N-H are observed at 1550 and 1396 cm^{-1}, see Figure 4-22 (b). At the same time, the peaks at 2600-3000 cm^{-1} disappear after functionalization. Compared with the FTIR spectrum of PEI, the absorption peaks

of N-H and C-N shift to lower wavenumbers. Such blue shift suggests the polarity of these two bonds decreases after functionalization with PEI, which is caused by the forming of the C-N bond[66]. All these bonding changes provide evidence that the successful functionalization of GQDs with PEI.

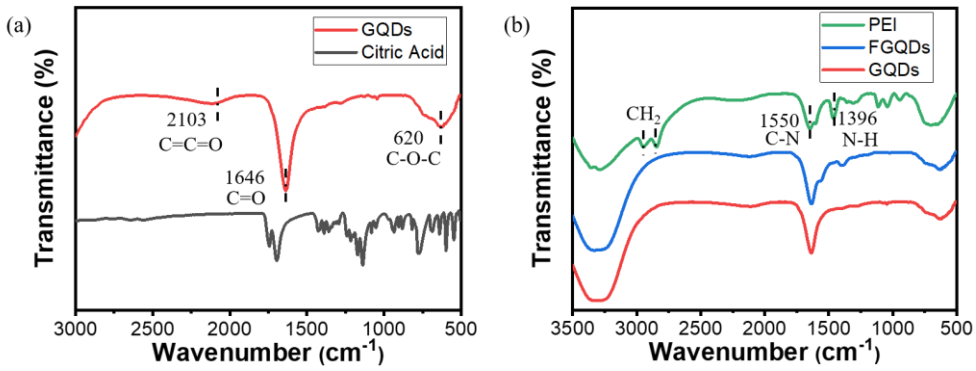

Figure 4-22. (a) The FTIR spectrums of citric acid and GQDs. (b) The FTIR spectrums of GQDs, FGQDs and PEI.

The TEM and AFM were used to analyze the geometry of GQDs and FGQDs. The average size of GQDs is 2-5 nm with a thickness less than 1 nm, indicating the GQDs are consist of 1-3 layers of graphene sheets[45], see Figure 4-23 (a, c). After functionalization, FGQDs grow to tens of nanometers, and the thickness of FGQDs is 0.33-2 nm see Figure 4-23 (b, d).

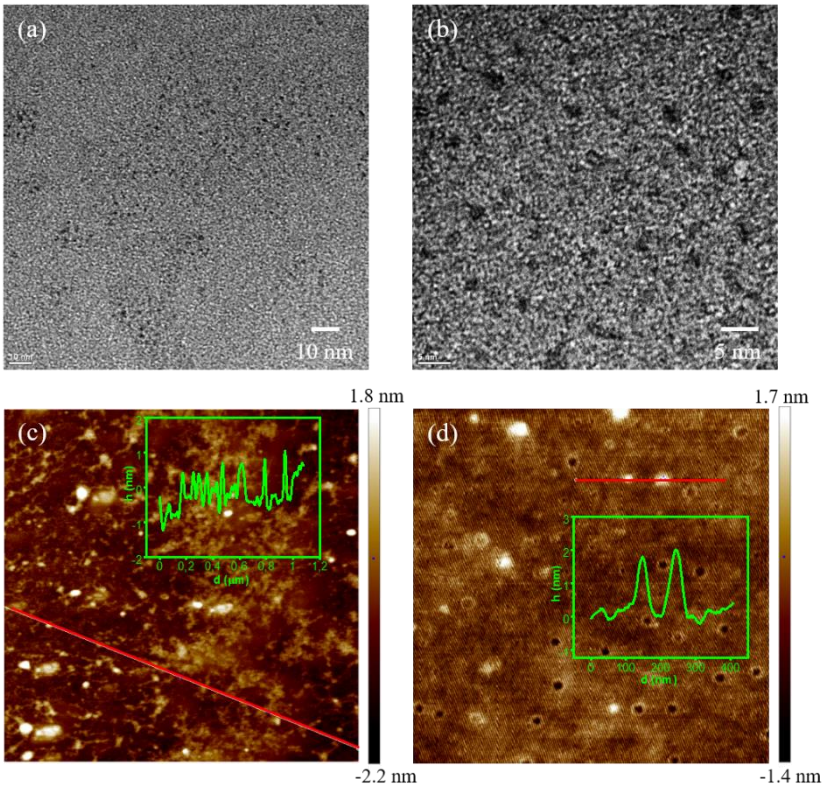

Figure 4-23. (a) The TEM photography of GQDs. (b) The TEM photography of FGQDs. (c) The AFM photography of GQDs. (d) The AFM photography of FGQDs. Insets of (c) and (d) show the heigh profiles along the indicated red lines.

Further, both GQDs and FGQDs exhibits stable, strong photoluminescence (PL) emission with a sharp (FWHM = 83 and 75 nm) PL peak at 390 nm, see Figure 4-24 (a). The zeta potential of GQDs increases from -36 V to +24.2 mV after functionalized with PEI, as a result of the introduction of high concentration positive amino groups through functionalization, see Figure 4-24 (b). Moreover, the zeta potential of our FGQDs shows pH stability. The zeta potential of FGQDs stays at the range of +22 mV to +26 mV over a pH range of 4-14. This positively charged surface enables the FGQDs to be well formulated with mRNA as a drug delivery platform[66].

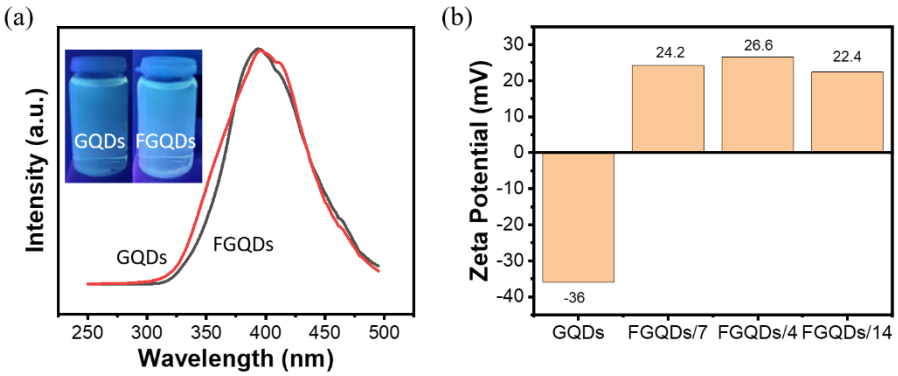

Figure 4-24. (a) The photoluminescence spectra of GQDs and FGQDs. The insets are digital images of GQDs and FGQDs aqueous solution (pH=7) under UV-light (center wavelength: 365 nm). (b) The zeta potential of the GQDs and FGQDs under various pH values.

4.4.3.3 Preparation of FGQDs/mRNA Complex

The FGQDs are positively charged, so an electrostatically driven interaction would be expected between FGQDs and negatively charged mRNA. To verify it, negative charged erythropoietin EPO-mRNA and EGFP-mRNA were used to formulate with FGQDs, respectively. While formulation, the FGQDs to mRNA ratios were expressed as the molar ratios of N in FGQDs to molar ratios of P in mRNA (N/P ratio, N/P= 0, 2, 4, 6, 8, 10, 20, 40 60, 100). The agarose gel electrophoresis results confirm that FGQDs could completely complex with both EPO-mRNA and EGFP-mRNA at all N/P ratios with the white dots disappear after formulated with FGQDs, and remained close to the loading position[62], as shown in Figure 4-25 (a, b).

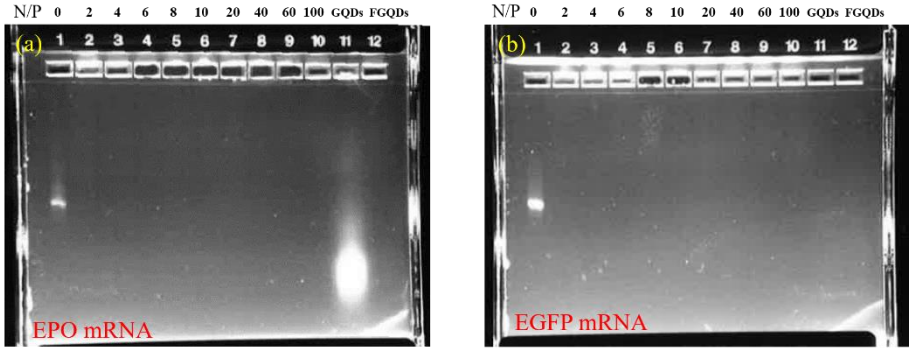

Figure 4-25. (a) EPO-mRNA gel electrophoresis at various charge N/P ratios. (b) EGFP-mRNA gel electrophoresis at various charge N/P ratios.

At first, experiments were conducted to optimize the N/P ratio between the FGQDs and the mRNA in the complex. When the N/P ratio below 20%, the average size of

FGQDs/mRNA particle decreases with increasing N/P ratio. While a sudden increase is observed when the N/P ratio reaches 40% (** $P < 0.01$, * $P < 0.05$)[64]. This is because the reduced amounts of positively charged FGQDs are available at lower N/P ratios. After 40%, the average size of FGQDs/mRNA particle decreases again when increasing the N/P ratio, see Figure 4-26 (a, b). All the FGQDs/mRNA complexes have particle sizes below 300 nm. To verify DLS results, SEM was used to observe the microstructure of FGQDs/mRNA complexes. Similarly, a higher N/P ratio leads to smaller particle geometry when formulated, see Figure 4-26 (c).

Further, the dosed particles were removed after 2 h and a fresh growth medium was added to obtain a 2 h pulsed particles. As a result, the EGFP expression shows the dose-dependent property, and low doses of FGQDs/mRNA complexes result in particle uptake, see Figure 4-26 (d).

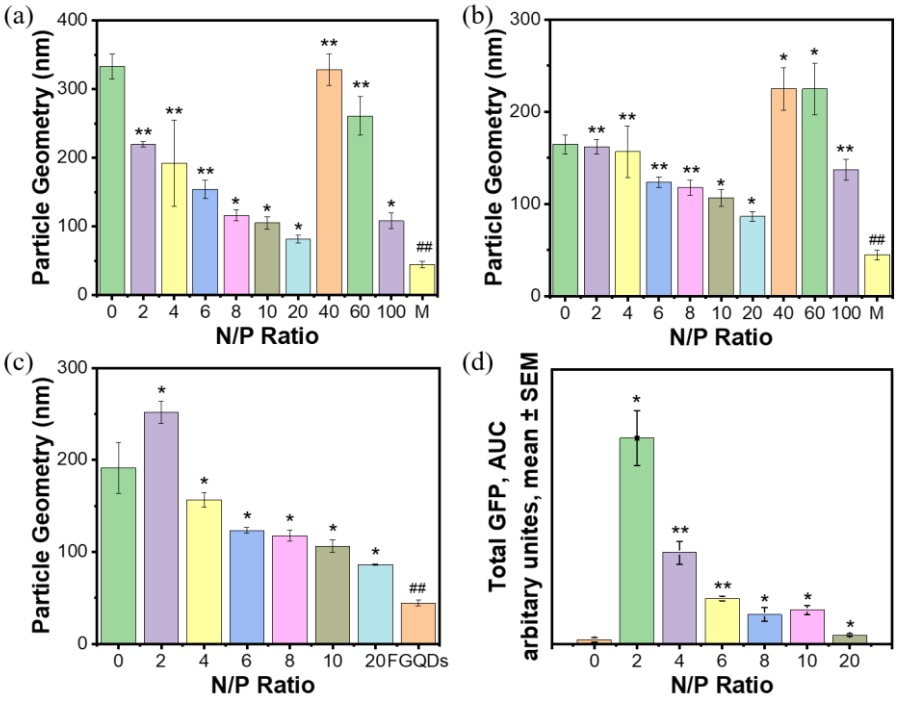

Figure 4-26. (a) The particle size of EPO-mRNA at various charge N/P ratios by DLS. (b) The particle size of EGFP-mRNA at various charge N/P ratios by DLS. (c) The particle size of EGFP-mRNA at various charge N/P ratios by SEM. (d) The total produced GFP of EGFP-mRNA at various charge N/P ratios.

4.4.3.4 Delivery of FGQDs/mRNA Complex to Cell Cultures

Here, high-throughput microscopy was used to both qualitatively and quantitatively evaluate the transfection efficiency of the FGQDs/mRNA complex by calculating the percentage of EGFP positive cells. A 24×16 plate was used for cell tests, see Figure 4-27 (a).

The reference nuclear staining with Hoechst 33342 exhibits blue under the high-throughput microscopy, see Figure 4-27 (b). And the propidium iodide staining is shown in yellow and EGFP protein production is shown in magenta.

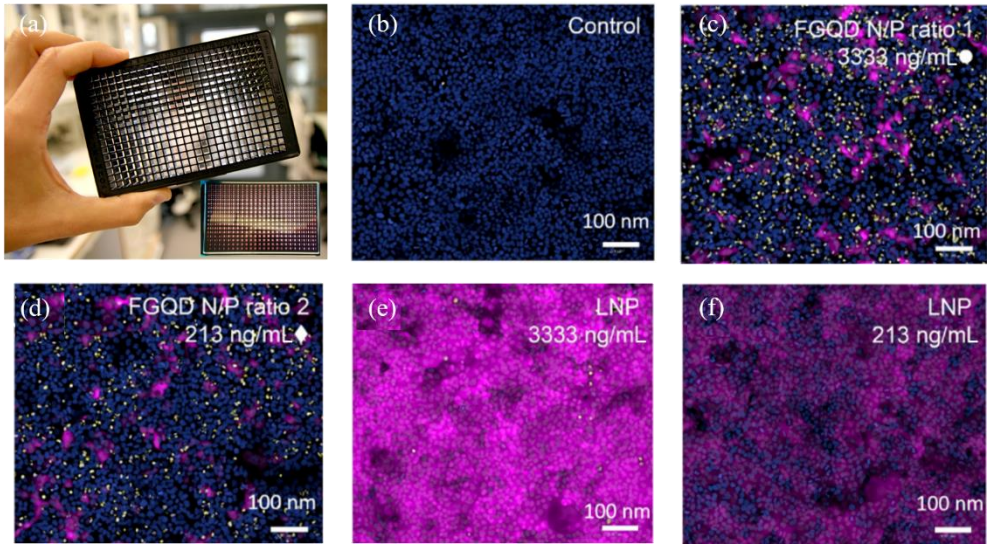

Figure 4-27. Functional cellular data obtained following transfection. (a) 24×16 plates for cell tests. (b) The high-throughput microscopy of Huh-7 cells. (c) The high-throughput microscopy of Huh-7 cells in 3333 ng mL^{-1} FGQDs functional EGFP-mRNA. (d) The high-throughput microscopy of Huh-7 cells in 213 ng mL^{-1} FGQDs functional EGFP-mRNA. (e) The high-throughput microscopy of Huh-7 cells in 3333 ng mL^{-1} lipid particle functional EGFP-mRNA. (f) The high-throughput microscopy of Huh-7 cells in 213 ng mL^{-1} lipid particle functional EGFP-mRNA.

Both the FGQDs (see Figure 4-27 (c, d)) and reference lipid nanoparticles (see Figure 4-27 (e, f)) are able to deliver EGFP-mRNA to Huh-7 cells. While qualitatively, the differences are apparent. Compared to lipid-treated Hun-7 cells, cells treated with FGQDs tended to have fewer cells expressing EGFP, but positive cells did produce a lot of protein. Likewise, FGQDs-treated wells did have more propidium iodide staining than the reference lipid-based particles, suggesting introduced greater disruption of the

plasma membrane by FGQDs. This is primarily a result of the PEI functionalization, rather than the graphene itself.

In this regard, for an N/P ratio of 2, the optimal doses and formulations occur at relatively low doses for FGQDs: 213 ng mL^{-1} mRNA when considering the ratio between cellular toxicity and EGFP production, using either Tris or PBS buffer solution.

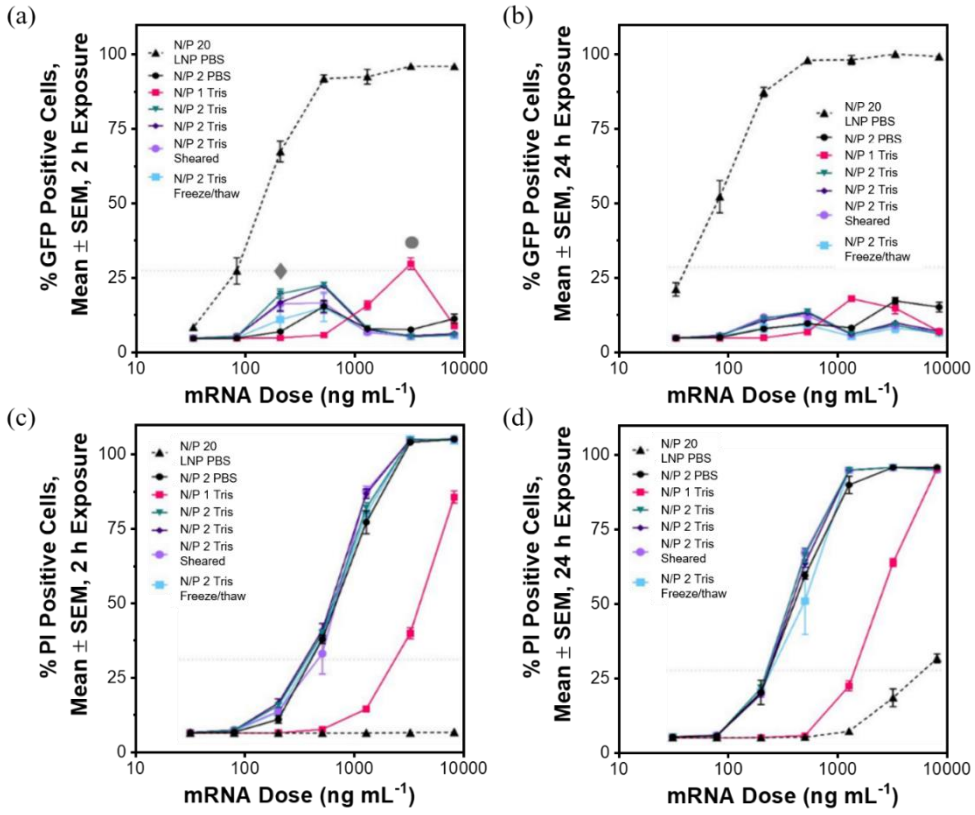

Figure 4-28. (a)The 2 h pulsed dose of EGFP positive cells. (b) The 24 h pulsed dose of EGFP positive cells. (c) The 2 h pulsed dose of propidium positive cells. (d) The 24 h pulsed dose of propidium positive cells.

After that, quantitative analysis data with various N/P ratios are counted to evaluate protein production (see Figure 4-28 (a, b)) and propidium staining (see Figure 4-28 (c, d)), following a 2 h and 24 h pulsed dose exposure. Interestingly, an N/P ratio of 1 resulted in less potent, but also fewer toxic particles, and in this case, the optimal dose was more than a magnitude higher. When increasing exposure time from 2 h to 24 h, a lower protein expression is observed, see Figure 4-28 (c, d).

Additionally, the LNPs are sensitive to the shearing force and suffer from breakage during formulation. In contrast, the FGQDs/mRNA complex still retained substantial

activity after pressed through a thin needle (27G) 20 times, indicating improved processibility for mRNA formulation.

4.5 Summary

In this chapter, we explored the application of using graphene-like 2D materials for interface enhancement applications. Three applications, including water-borne epoxy coatings, mRNA-based drug delivery and cement repair materials have been investigated in this chapter.

At first, graphene was used to enhance the tribological performance for the Tricolit TSC Coatings. To improve the dispersibility of graphene flakes, an aryl diazonium salt was used to functionalize graphene. Such functionalized graphene can act as reactive filler in a water-borne epoxy coating formulation. The geometry of functionalized graphene flakes is optimized by formulating three sizes with coatings. With optimized geometry and loading, 30 times less coefficient of friction than graphene-free coatings were achieved. And the wear-out time is more than 2 times higher than the commercial products. Finally, mass production technology up to 300 g per batch was developed for preparing functional graphene. This functionalization strategy was further promoted for achieving high hydrophilic carbon nanotubes. This work paves the way for commercial applications of functionalized graphene for mechanical enhancement in coatings.

Secondly, a mixture of nanoscale and microscale functional hexagonal boron nitride was prepared for improving the strength of cement repair materials. After functionalized with carboxymethyl cellulose, the hexagonal boron nitride nanoparticles can be easily dispersed in water and formulated with cement repair materials. Compared to pristine hexagonal boron nitride particles, functional hexagonal boron nitride largely improves and the dispersion in cement repair materials matrix and the adhesion with substrates. Together with a local cement company, this work has demonstrated the commercial application as repair materials for buildings. This work provides a feasible approach to utilizing hexagonal boron nitride as a reinforcing filler for concrete repair materials.

And finally, a novel graphene quantum dots based mRNA delivery platform was developed. To be able to formulate with mRNA and cells, the covalent functionalization with PEI was used to achieve positively charged graphene quantum dots. Our results show that functional graphene quantum dots were able to complex mRNA and deliver it intact to the cytoplasm of Huh-7 hepatocarcinoma cells. Furthermore, unlike the lipid

nanoparticles, the FGQDs/mRNA complex is not very sensitive to shearing force. The transfection efficiency for FGQDs/mRNA complexes is 25% with a formulation concentration of 4000 ng mL^{-1}, but comparable transfection efficiencies could be achieved at much lower doses if the ratio between the carrier and the cargo was optimized. This work describes the first step towards a potentially interesting preparation method for stable and effective mRNA delivery systems.

Reference

[1] Kumar A., Sharma K., Dixit A. R. A review of the mechanical and thermal properties of graphene and its hybrid polymer nanocomposites for structural applications [J]. J. Mater. Sci., 2019, 54(8): 5992-6026.

[2] Omrani E., Menezes P. L., Rohatgi P. K., et al. Mechanical and tribological properties of self-lubricating metal matrix nanocomposites reinforced by carbon nanotubes (CNTs) and graphene - A review [J]. Compos. Part B-Eng., 2015, 77: 402-420.

[3] Wang J., Jin X., Li C., et al. Graphene and graphene derivatives toughening polymers: toward high toughness and strength [J]. Chem. Eng. J., 2019, 370: 831-854.

[4] Mittal G., Dhand V., Rhee K. Y., et al. A review on carbon nanotubes and graphene as fillers in reinforced polymer nanocomposites [J]. J. Ind. Eng. Chem., 2015, 21(1): 11-25.

[5] Song K., Zhang Y., Meng J., et al. Structural polymer-based carbon nanotube composite fibers: understanding the processing-structure-performance relationship [J]. Materials, 2013, 6(6): 2543-2577.

[6] Almessiere M. A., Chaudhary K., Ali J., et al., Graphene-based composite materials [M]. John Wiley & Sons, 2019.

[7] Lim J., Yeo H., Goh M., et al. Grafting of polyimide onto chemically-functionalized graphene nanosheets for mechanically-strong barrier membranes [J]. Chem. Mater., 2015, 27(6): 2040-2047.

[8] Huang Y. J., Qin Y. W., Zhou Y., et al. Polypropylene/graphene oxide nanocomposites prepared by in situ ziegler-natta polymerization [J]. Chem. Mater., 2010, 22(13): 4096-4102.

[9] Kim H., Miura Y., Macosko C. W. Graphene/polyurethane nanocomposites for improved gas barrier and electrical conductivity [J]. Chem. Mater., 2010, 22(11): 3441-3450.

[10] Liu Y., Xia C., Zehri A., et al. Surface modification of graphene for use as a structural fortifier in water-borne epoxy coatings [J]. Coatings, 2019, 9(11): 754.

[11] Berman D., Erdemir A., Sumant A. V. Graphene: a new emerging lubricant [J]. Mater. Today, 2014, 17(1): 31-42.

[12] Li Y. L., Wang S. J., Wang Q. Enhancement of tribological properties of polymer composites reinforced by functionalized graphene [J]. Compos. Pt. B-Eng., 2017, 120: 83-91.

[13] Lv T., Huang S. Q., Hu X. D., et al. Tribological and machining characteristics of a minimum quantity lubrication (MQL) technology using GO/SiO_2 hybrid nanoparticle water-based lubricants as cutting fluids [J]. Int. J. Adv. Manuf. Technol., 2018, 96(5-8): 2931-2942.

[14] Wu P., Chen X. C., Zhang C. H., et al. Synergistic tribological behaviors of graphene oxide and nanodiamond as lubricating additives in water [J]. Tribol. Int., 2019, 132: 177-184.

[15] Li X., Chen B. B., Jia Y. H., et al. Enhanced tribological properties of epoxy-based lubricating coatings using carbon nanotubes-ZnS hybrid [J]. Surf. Coat. Technol., 2018, 344: 154-162.

[16] Li H. Y., Shi N. Q., Ji J., et al. Preparation of microcapsules containing double-component lubricant and self-lubricating performance of polymer composites [J]. Mater. Res. Express, 2018, 5(5): 055302.

[17] Bandeira P., Monteiro J., Baptista A. M., et al. Influence of oxidized graphene nanoplatelets and [DMIM] [NTf_2] ionic liquid on the tribological performance of an epoxy-PTFE coating [J]. Tribol. Int., 2016, 97: 478-489.

[18] Qi Y. Z., Liu J., Zhang J., et al. Wear resistance limited by step edge failure: the rise and fall of graphene as an atomically thin lubricating material [J]. Acs. Appl. Mater. Inter., 2017, 9(1): 1099-1106.

[19] Kumar R., Sahoo S., Joanni E., et al. Recent progress in the synthesis of graphene and derived materials for next generation electrodes of high performance lithium ion batteries [J]. Prog. Energy Combust. Sci., 2019, 75: 100786.

[20] Papageorgiou D. G., Kinloch I. A., Young R. J. Mechanical properties of graphene and graphene-based nanocomposites [J]. Prog. Mater. Sci., 2017, 90: 75-127.

[21] Kuila T., Bose S., Mishra A. K., et al. Chemical functionalization of graphene and its applications [J]. Prog. Mater. Sci., 2012, 57(7): 1061-1105.

[22] Rasheed A. K., Khalid M., Rashmi W., et al. Graphene based nanofluids and nanolubricants - review of recent developments [J]. Renew. Sust. Energ. Rev., 2016, 63: 346-362.

[23] Presser A., Huefner A. Trimethylsilyldiazomethane - a mild and efficient reagent for the methylation of carboxylic acids and alcohols in natural products [J]. Cheminform, 2004, 135(8): 1015-1022.

[24] Li Z., Young R. J., Wang R., et al. The role of functional groups on graphene oxide in epoxy nanocomposites [J]. Polymer, 2013, 54(21): 5821-5829.

[25] Yang Q. b., Zhu B. R., Wu X. Characteristics and durability test of magnesium phosphate cement-based material for rapid repair of concrete [J]. Mater. Struct., 2000, 33(4): 229-234.

[26] Manzur T., Yazdani N., Emon M., et al. Potential of carbon nanotube reinforced cement composites as concrete repair material [J]. J. Nanomater., 2016, 2016: 142959.

[27] Zheng L., O'connell M., Doorn S., et al. Ultralong single-wall carbon nanotubes [J]. Nat. Mater., 2004, 3(10): 673-676.

[28] Yu M. F., Files B. S., Arepalli S., et al. Tensile loading of ropes of single wall carbon nanotubes and their mechanical properties [J]. Phys. Rev. Lett., 2000, 84(24): 5552.

[29] Salvetat J. P., Bonard J. M., Thomson N., et al. Mechanical properties of carbon nanotubes [J]. Appl. Phys. A. Mater., 1999, 69(3): 255-260.

[30] Walters D., Ericson L., Casavant M., et al. Elastic strain of freely suspended single-wall carbon nanotube ropes [J]. Appl. Phys. Lett., 1999, 74(25): 3803-3805.

[31] Wang W., Chen S. J., de Souza F. B., et al. Exfoliation and dispersion of boron nitride nanosheets to enhance ordinary Portland cement paste [J]. Nanoscale, 2018, 10(3): 1004-1014.

[32] Rafiee M. A., Narayanan T. N., Hashim D. P., et al. Hexagonal boron nitride and graphite oxide reinforced multifunctional porous cement composites [J]. Adv. Funct. Mater., 2013, 23(45): 5624-5630.

[33] Bouville F., Deville S. Dispersion of boron nitride powders in aqueous suspensions with cellulose [J]. J. Am. Ceram. Soc., 2014, 97(2): 394-398.

[34] Minami N., Kim Y., Miyashita K., et al. Cellulose derivatives as excellent dispersants for single-wall carbon nanotubes as demonstrated by absorption and photoluminescence spectroscopy [J]. Appl. Phys. Lett., 2006, 88(9): 093123.

[35] Wen X. Y., Joshi R. 2D materials-based metal matrix composites [J]. J. Phys. D-Appl. Phys., 2020, 53(42): 423001.

[36] Panesar D. K., Zhang R. X. Performance comparison of cement replacing materials in concrete: limestone fillers and supplementary cementing materials - a review [J]. Constr. Build. Mater., 2020, 251: 118866.

[37] Inphonlek S., Sunintaboon P., Leonard M., et al. Chitosan/carboxymethylcellulose-stabilized poly(lactide-co-glycolide) particles as bio-based drug delivery carriers [J]. Carbohydr. Polym., 2020, 242: 116417.

[38] Long L. Y., Weng Y. X., Wang Y. Z. Cellulose aerogels: synthesis, applications, and prospects [J]. Polymers, 2018, 10(6): 28.

[39] Labbez C., Nonat A., Pochard I., et al. Experimental and theoretical evidence of overcharging of calcium silicate hydrate [J]. J. Colloid Interf. Sci., 2007, 309(2): 303-307.

[40] Lothenbach B., Nonat A. Calcium silicate hydrates: solid and liquid phase composition [J]. Cement Concrete Res., 2015, 78 (SI): 57-70.

[41] Li X., Ouzia A., Scrivener K. Laboratory synthesis of C_3S on the kilogram scale [J]. Cement Concrete Res., 2018, 108: 201-207.

[42] Imura T., Yanagishita H., Ikegami T. Drastic improvement in trapping efficiency and dispersibility for phosphatidylcholine liposomes in the pPresence of divalent metal ions [J]. Journal of Oleo Science, 2003, 52(12):673-679.

[43] Plusquellec G., Nonat A. Interactions between calcium silicate hydrate (CSH) and calcium chloride, bromide and nitrate [J]. Cement Concrete Res., 2016, 90: 89-96.

[44] Scrivener K., Snellings R., Lothenbach B., et al. A practical guide to microstructural analysis of cementitious materials [M]. CRC Press, 2016.

[45] Xu A., Wang G., Li Y., et al. Carbon-based quantum dots with solid-state photoluminescent: mechanism, implementation, and application[J]. Small, 2020, 16: 2004621.

[46] Gu Z., Zhu S., Yan L., et al. Graphene-based smart platforms for combined cancer therapy [J]. Adv. Mater., 2019, 31(9): 1800662.

[47] Sanchez V. C., Jachak A., Hurt R. H., et al. Biological interactions of graphene-family nanomaterials: an interdisciplinary review [J]. Chem. Res. Toxicol., 2011, 25(1): 15-34.

[48] Dai C., Zhang S., Liu Z., et al. Two-dimensional graphene augments nanosonosensitized sonocatalytic tumor eradication [J]. Acs Nano, 2017, 11(9): 9467-9480.

[49] Peng E., Choo E. S. G., Chandrasekharan P., et al. Synthesis of manganese ferrite/graphene oxide nanocomposites for biomedical applications [J]. Small, 2012, 8(23): 3620-3630.

[50] Yang K., Hu L., Ma X., et al. Multimodal imaging guided photothermal therapy using functionalized graphene nanosheets anchored with magnetic nanoparticles [J]. Adv. Mater., 2012, 24(14): 1868-1872.

[51] Liu H. W., Huang W. C., Chiang C. S., et al. Arrayed rGOSH/PMASH microcapsule platform integrating surface topography, chemical cues, and electrical stimulation for three-dimensional neuron-like cell growth and neurite sprouting [J]. Adv. Funct. Mater., 2014, 24(24): 3715-3724.

[52] Chen Y. W., Chen P. J., Hu S. H., et al. NIR-triggered synergic photo-chemothermal therapy delivered by reduced graphene oxide/carbon/mesoporous silica nanocookies [J]. Adv. Funct. Mater., 2014, 24(4): 451-459.

[53] Yang K., Zhang S., Zhang G., et al. Graphene in mice: ultrahigh in vivo tumor uptake and efficient photothermal therapy [J]. Nano Lett., 2010, 10(9): 3318-3323.

[54] Li J., Yang S., Deng Y., et al. Tumor therapy: emancipating target-functionalized carbon dots from autophagy vesicles for a novel visualized tumor therapy [J]. Adv. Funct. Mater., 2018, 28(30):1870206.

[55] Donghoon K., Min Y J., Heehong H., et al. Graphene quantum dots prevent α-synucleinopathy in Parkinson's disease [J]. Nat. Nanotechnol., 2018, 13(9):812-818 .

[56] Iannazzo D., Pistone A., M Salamò., et al. Graphene quantum dots for cancer targeted drug delivery [J]. Int. J. Pharm, 2017, 518(1-2):185-192.

[57] Su Y. L., Yu T. W., Chiang W. H., et al. Hierarchically targeted and penetrated delivery of drugs to tumors by size-changeable graphene quantum dot nanoaircrafts for photolytic therapy [J]. Adv. Funct. Mater., 2017, 27(23):1700056.

[58] Yao X. X., Niu, X. X., Ma K., et al. Graphene quantum dots-capped magnetic mesoporous silica nanoparticles as a multifunctional platform for controlled drug

delivery, magnetic hyperthermia, and photothermal therapy [J]. Small, 2017, 13(2): 1602225.

[59] Li B., Zhang X., Dong Y. Nanoscale platforms for messenger RNA delivery [J]. Wires. Nanomed. Nanobi., 2019, 11(2): e1530.

[60] Chalbatani G. M., Dana H., Gharagouzloo E., et al. Small interfering RNAs (siRNAs) in cancer therapy: a nano-based approach [J]. Int. J. Nanomed., 2019, 14: 3111.

[61] Zohra F. T., Maitani Y., Akaike T. mRNA delivery through fibronectin associated liposome-apatite particles: a new approach for enhanced mRNA transfection to mammalian Cell [J]. Biol. Pharm. Bull., 2012, 35(1): 111-115.

[62] Bao Y., Jin Y., Chivukula P., et al. Effect of PEGylation on biodistribution and gene silencing of siRNA/lipid nanoparticle complexes [J]. Pharm. Res-dordr, 2013, 30(2): 342-351.

[63] Menon J. U., Ravikumar P., Pise A., et al. Polymeric nanoparticles for pulmonary protein and DNA delivery [J]. Acta Biomater., 2014, 10(6): 2643-2652.

[64] Su Z., Erdene-Ochir T., Ganbold T., et al. Design of curdlan-based pH-sensitive polymers with endosome buffering functionality for siRNA delivery [J]. Inter. J. Biol. Macromol., 2020, 146: 773-780.

[65] Kumar S., Diwan A., Singh P., et al. Functionalized gold nanostructures: promising gene delivery vehicles in cancer treatment [J]. RSC Adv., 2019, 9(41): 23894-23907.

[66] Wang L., Shi J., Zhang H., et al. Synergistic anticancer effect of RNAi and photothermal therapy mediated by functionalized single-walled carbon nanotubes [J]. Biomaterials, 2013, 34(1): 262-274.

CHAPTER 5

Summary

In this thesis, we studied the preparation and the application of using graphene-like 2D materials for heat dissipations, energy storages and interface enhancements. To improve the heat dissipation for electronics, graphene enhanced heat pipe and hexagonal boron nitride enhanced heat spreader were developed. In energy storage, graphene enhanced electric double-layer capacitors and graphene based in-plane micro-supercapacitors were investigated. Finally, as to the interface enhancements, graphene enhanced water-borne epoxy coatings, graphene enhanced mRNA drug delivery platform and hexagonal boron nitride enhanced cement repair materials. Furthermore, to obtain low-cost, less-defects and uniform products, mass production technology was developed for functional graphene and hexagonal boron nitride. Some of the work in this thesis has been demonstrated prototypes by the author in a relevant environment and produced commercial products.

(1) *Graphene Enhanced Heat Pipe*

In this work, a unique lightweight and high thermal performance graphene heat pipe was firstly designed and developed. At first, the inner structures of graphene enhanced heat pipe were optimized, including the alignment of graphene flakes, high thermal conductivity graphene film, wicker structure and filling volume of the working fluid. Compared to the conventional copper-based heat pipe, our graphene heat pipe improves the specific cooling capacity more than 3 times. COMSOL Multiphysics was used to build the cooling model for graphene enhanced heat pipe, providing the equation for calculating the contribution factor from the container at the first time. Finally, a graphene/copper composite heat pipe was fabricated to improve the reliability and mechanical strength of graphene enhanced heat pipe. The interface between graphene and copper was investigated to decrease the thermal interface resistance.

(2) *Hexagonal Boron Nitride Enhanced Heat Spreader*

High thermally conductive while electrically insulation materials have been urgently demanded for thermal management in electronics as they won't disturb the function of main circuits when removing heat. In this regard, hexagonal boron nitride has attracted extensive interest as it possesses high in-plane thermal conductivity (751 W m^{-1} K^{-1}) and a wide bandgap (5.9 eV). In this work, a hexagonal boron nitride based heat spreader was prepared by electrospinning with polyvinylpyrrolidone. At first, the exfoliation technic and the geometry of h-BN were optimized. The result shows that nanoscale hexagonal boron nitride particles contribute to achieving higher thermal conductivity than microscale. After that, electrospinning was used to prepare hexagonal based fiber, and thus aligned hexagonal boron nitride particles for increasing the heat transfer pathway. With the optimized exfoliated media, geometry and loading, the in-plane thermal conductivity of the hexagonal boron nitride based heat spreader reaches 22 W m^{-1} K^{-1}, this value is comparable to most of the reported work. Such electrospinning process is simple, constant and scalable, showing high potential for mass production.

(3) *Graphene Enhanced Electric Double-layer Capacitor*

In this work, a scalable graphene foam preparation technology was developed to realize high performance supercapacitor through tailoring specific area and wettability. The unique porous structure, low ohm resistance, doping and high electrical conductivity largely improve the electrochemical performance of graphene foam electrodes and thus achieve ultrahigh specific capacity, cycling stability and outstanding rate capability. Further, density functional theory simulation was firstly used to reveal why increasing the polarity of graphene improves its wettability.

(4) *Graphene Based In-plane Micro-supercapacitor*

In the past decades, searching for a replacement for silicon wafers has become one of the most urgent issues for next-generation microelectronics. In this work, graphene assembled film was used to replace the conventional silicon wafer to fabricate flexible and high thermal performance micro-supercapacitors. The result shows that such replacement can decrease the surface temperature by 4 °C but will not influence the electrochemical behavior of MSCs.

(5) *Graphene Enhanced Water-borne Epoxy Coating*

In this work, graphene was used to lower the coefficient of friction and extend the lifetime of the Tricolit TSC Coating, a commercial water-borne epoxy coating. To improve the dispersibility of graphene and the compatibility with epoxy, p-hydroxybenzene diazonium salt was prepared to functional graphene at first. In addition, amino groups on the functional graphene can bond with epoxy to further improve the mechanical strength of coatings. With optimized geometry and loading, 30 times less coefficient of friction than graphene-free coatings were achieved. And the wear-out time is more than 2 times higher than the commercial products. Finally, mass production technology up to 300 g per batch was developed for preparing functional graphene. This functionalization strategy was further developed for carbon nanotubes to improve their dispersion too.

(6) *Hexagonal Boron Nitride Enhanced Cement Repair Material*

In this work, a mixture of nanoscale and microscale functional hexagonal boron nitride was prepared for improving the strength of cement repair materials. After functionalized with carboxymethyl cellulose, the hexagonal boron nitride nanoparticles can be easily dispersed in water and formulated with cement repair materials. Compared to pristine hexagonal boron nitride particles, functional hexagonal boron nitride largely improves the dispersion in cement repair materials matrix and the adhesion with substrates. Together with a local cement company, this work has demonstrated the commercial application as repair materials for walls.

(7) *Graphene Enhanced mRNA Drug Delivery Platform*

In this work, functional graphene quantum dots were firstly used to deliver intact mRNA to Huh-7 hepatocarcinoma cells. To interact with cells, the zeta potential of graphene quantum dots was tailored to positive by functionalized with PEI. The transfection efficiency for functional graphene quantum dots and mRNA complexes was as high as 25% with a formulation concentration of 4000 ng mL^{-1}, but comparable transfection efficiencies could be achieved at much lower doses if the ratio between the carrier and the cargo was optimized. This work describes the first step towards a potentially interesting preparation method for stable and effective mRNA delivery systems.

CHAPTER 6

Future Outlook

With the extensive development in the past 15 years, most of the basic physical and chemical properties of graphene-like 2D materials have been discovered, and a few products have been introduced in market. Now the development of graphene-like 2D materials heavily towards commercialization. Being consist of single-layer of atoms, graphene-like 2D materials present unprecedent behaviors in chemical, mechanical, thermal, electrical and optical, etc. For instance, chemically, graphene-like 2D materials provide protection to corrosion and penetration due to their chemical alertness and anisotropic layered structure. Mechanically, electrically and thermally, graphene-like 2D materials is able to largely improve the performance of surrounding matrix.[1] However, among all of the applications of graphene-like 2D materials, including energy storage, thermal dissipation, composites, etc., their performance is still far from reaching their theoretical properties. This is mainly because graphene-like 2D materials inevitably suffer from defects, π-π stacking and their unique chemical and physical properties significantly deteriorate while increasing layers and defects.

Together with the efforts for graphene perfection, it is crucial to identify the markets that can utilize the special properties of graphene-like 2D materials. Nowadays, the industry has been extensively pursuing graphene for consumer electronics, involving heat dissipation and high-performance electronics. However, the significant anisotropic thermal behavior heavily limits the applications of using graphene-like 2D materials for cooling applications. While the justification for transistors has slow down over time due to challenges in generating a sizable bandgap. In this regard, the killer applications of graphene-like 2D materials is remain unrevealed.[2]

To be widespread on the market, new revolutionary solutions should either create new market opportunities or be able to provide significant performance improvements. For today's 2D materials industry, the performance improvement is too moderate to replace the well-established conventional technology. To make graphene-like 2D materials industry-friendly, efforts should be focused to provide specified, uniform high-quality

products and reduce cost in synthesis, storage, and processing. In this regard, the price of graphene has rapidly and steadily reduced, for example, the price of mechanical exfoliated graphene decreases from 250 to 20 \$ Kg^{-1} in last decade.[1] Further, to penetrate the markets, graphene-like 2D materials must firstly be compatible with the existing technology in terms of preparation and application. In this regard, scientific communities, as well as companies, are required to collaborated to seek convincing high-performance applications for scalable products.

Reference

[1] Kong W., Kum H., Bae S. H., et al. Path towards graphene commercialization from lab to market [J]. Nat. Nanotechnol., 2019, 14(10): 927-938.

[2] Sharon M., Sharon M., Shinohara H., et al. Graphene: an introduction to the fundamentals and industrial applications [M]. Scrivener, 2015.

CHAPTER 7

Summary of Papers

LIST OF PUBLICATIONS

This thesis is based on the following appended papers:

Paper I

Egg albumen templated graphene foams for high-performance supercapacitor electrodes and electrochemical sensors

Ya Liu, Xiaoli Zhao, Cancan Wang, Long Zhang, Mengxiong Li, Yunmei Pan, Johan Liu and Hongbin Lu, Journal of Materials Chemistry A, 2018, 6(37): 18267-18275.

This paper presents a scalable graphene foam preparation technology to realize high performance supercapacitor. The unique porous structure, low ohm resistance, doping and high electrical conductivity largely improve the specific gravimetric capacity, cycling stability and rate capability. Further, density functional theory simulation was used to reveal why increasing the polarity of graphene improves its wettability.

My contribution: Concept Development, Data collection, analysis, and paper writing.

Paper II

A lightweight and high thermal performance graphene heat pipe

Ya Liu, Shujing Chen, Yifeng Fu, Davide Mencarelli, Luca Pierantoni, Hongbin Lu, and Johan Liu, *NanoSelect*, 2020, 2: 1-9,

This paper presents a new class of graphene heat pipe and graphene/copper heat pipe. Graphene film press technology, wicker, working fluid were optimized for graphene heat pipe. Thermal transfer model of graphene heat pipe was built by COMSOL Multiphysics.

My contribution: I developed the concept together with Johan Liu. I designed the detail structures of graphene heat pipe, test set-ups, and the fabrication method based on previous research and did all experiments and characterizations. I wrote the paper.

Paper III

Surface Modification of Graphene for Use as a Structural Fortifier in Water-Borne Epoxy Coatings

Ya Liu, Chao Xia, Abdelhafid Zehri, Lilei Ye, Nan Wang, Boris Zhmud, Hongbin Lu and Johan Liu. *Coatings*, 2019, 9(11), 754.

This paper presents a functional graphene for improving tribological performance of epoxy-based coatings. The geometry of graphene flakes was optimized to extend lifetime of coatings. A possible enhancing mechanism was built between functionalized agents and epoxy groups.

My contribution: I developed the concept together with Johan Liu. I designed the detail structures of graphene heat pipe, test set-ups, and the fabrication method based on previous research and did all experiments and characterizations. I wrote the paper.

Paper IV

A novel graphene quantum dot-based mRNA delivery platform

Ya Liu, Zhao Changhong, Alan Sabrish, Ye Lilei, Wu Xiaoqiu, Lu Hongbin and Liu Johan. *ChemistryOpen*, 2021, 10: 202000200.

This paper presents a novel Polyethyleneimine (PEI) functional graphene quantum dots based mRNA drug delivery platform. With a formulation concentration of 4000 ng mRNA mL^{-1}, the transfection efficiency for FGQDs/mRNA complexes was 25%. This work describes the first steps towards a potentially interesting preparation method for stable and effective mRNA delivery systems.

My contribution: I developed the concept together with J. L., X. W. and A. S. I investigated the preparation parameters for GQDs and complete the chemical functionalization. I did the material characterization with the assistance form X.W. and A. S. I wrote the draft manuscript while revised together with X. W. and A. S.

Paper V

Thermally Conductive and Electrically Insulating PVP/Boron Nitride Composite Films for Heat Spreader

Ya Liu, Nan Wang, Lilei Ye, Abdelhafid Zehri, Andreas Nylander, Amos Nkansah, Hongbin Lu and Johan Liu, *IMAPS Nordic Conference on Microelectronics Packaging (NordPac)*, 2019.

This paper investigates a hexagonal boron nitride based heat spreader by electrospinning with polyvinylpyrrolidone. With the optimized hexagonal boron nitride particle geometry and loading, the in-plane thermal conductivity of hexagonal boron nitride based heat spreader reaches 22 W m^{-1} K^{-1}.

My contribution: I developed the concept and prepared the samples. I did the characterization with assistance from A.N. and A.Z. I wrote the paper.

Paper VI

Effect of Boron Nitride Particle Geometry on the Thermal Conductivity of a Boron Nitride Enhanced Polymer Composite Film

Ya Liu, Lilei Ye, Hongbin Lu, and Johan Liu. *The 25th edition of the International Workshop on Thermal Investigation of ICs and Systems (Therminic)*, 2019.

This paper optimized the geometry of boron nitride nanosheets as thermal conductive filler for polymers.

My contribution: I oversaw the construction. I did all fabrication and characterization of the materials. I wrote the paper.

Acknowledgements

While this thesis represents the sum of my own work during the past four years, there are several wonderful people, who work as stars and sunlight, I wish to thank for their supports. Without the help from them, I will not be able to present the thesis today.

First and foremost, I would like to address my sincere thanks to Hongbin Lu and Johan Liu, my two main supervisors, for giving me this double doctoral program opportunity, guiding my researches, and trusting me to an extent I am not sure I would have myself. Thank you two for the knowledgeable supervision and generous encouragements.

In my daily work, it has been my co-supervisor, Yifeng Fu, who have guided my work. Thank you for helping me and for caring about my research and my progress as a PhD candidate.

Thanks to all my colleges in Fudan University, including Jiajia Zhang, Yingbo Ruan, Minqiang Sun, Peng wang, Yunmei Pan, Cancan Wang, Zedong Zhao, Yicheng Liu, Peiying Liu, Zhimin Zhai, Yuanhang Ge, Tianqi Wu, Bo Hu, Zhiqiang Chen, Lequan Wang. Thanks for your lovely accompany, which make research adventures full of interesting.

I also would like to thank my colleges in Chalmers, Abdelhafid Zehri, Andreas Nylander, Josef Hansson to accompany with the two and half wonderful days.

Thanks to my smart industry collaborators, Lilei Ye, Törbjorn Thringer, Törbjorn Nilsson, Gilles Plusquellec, Chao Xia, Davide Mencarelli, Luca Pierantoni, Xiaoqiu Wu, Alan Sabirsh, Lars Nilsson, Perter Merlin, Dag Andersson, etc. The help from all of you have largely broaden my research interests and reshaped my research attitude.

Thanks to my beloved one, my husband, Kun Li. You are like the sunshine in my life. Without the encourage and love from you, I would never be me.

Finally, the deepest gratitude to my family. Thank you so much for the endless support and love.

Journal of Materials Chemistry A

PAPER

View Article Online
View Journal | View Issue

Cite this: J. Mater. Chem. A, 2018, 6, 18267

Egg albumen templated graphene foams for high-performance supercapacitor electrodes and electrochemical sensors†

Ya Liu,[ab] Xiaoli Zhao,[a] Cancan Wang,[a] Long Zhang,[a] MengXiong Li,[a] Yunmei Pan,[a] Yifeng Fu,[b] Johan Liu*[bc] and Hongbin Lu *[a]

Received 16th May 2018
Accepted 17th August 2018

DOI: 10.1039/c8ta04561e

rsc.li/materials-a

We demonstrate a simple and scalable strategy to obtain N, S and Si co-doped biocompatible graphene foams (GFs) with different shapes using egg albumen as the template. The unique porous structure and element doping endow the GFs with a high charge–discharge rate and good wettability, which largely improve the electrochemical performance of the electrodes, including ultrahigh specific capacitance (534 F g^{-1} at 1 A g^{-1}), and excellent rate capability (308 F g^{-1} at 100 A g^{-1}) and cycling performance (96.1% retention of the initial capacitance after 10 000 cycles at a high current density of 10 A g^{-1}). Besides, when used as an electrochemical sensor for dopamine, the GF exhibits a detection limit as low as 1.2 μM with a linear response up to 70 μM, due to the low equivalent series resistance. These reveal great potential for promoting the application of 3D graphene in energy storage and electrochemical sensors.

Introduction

Graphene is a promising material for an extensive range of applications in view of its outstanding physical and chemical properties.[1–4] Unfortunately, graphene sheets, in particular those derived from graphene oxide (GO), inevitably suffer from agglomeration owing to the van der Waals interaction between adjacent sheets.[1,5–9] Such re-stacking gives rise to an undesired compromise of graphene's properties.[10] Recently, using three-dimensional (3D) graphene, such as foams, aerogels, sponges, monoliths, *etc.*, has emerged as an effective strategy to counter this re-stacking issue.[8,11] Generally, synthesis techniques of 3D graphene can be classified into template-free (*e.g.*, hydrothermal, solvothermal, and 3D printing technology)[12,13] and template-based methods. Template-based approaches include chemical vapor deposition (CVD),[14] hard template (*e.g.*, PU sponge and MgO)[1,6] and soft template (*e.g.*, air bubble)[15] methods. Template-free methods offer the merit of self-assembly but lack the control of pore structure. By comparison, template-based methods provide an alternative to effectively control the pore distribution and pore size.[16] However, the removal of CVD templates is time- and energy-consuming; furthermore, hard templates are only used to obtain 3D graphene with simple shapes. Air bubble soft templates need freeze-drying technology to keep the pore structure, which limits their practical application. Therefore, it remains a critical issue to develop a facile approach for the preparation of 3D graphene with an integrated structure.

On the other hand, the surface of graphene is highly hydrophobic, which causes a weak interfacial contact with the electrolyte and thus leads to deterioration of its electrochemical properties.[10] Recently, heteroatom doping has been considered as the best approach to improve the wettability of graphene because the doping can tailor its surface structure without sacrificing the morphological advantages of graphene.[17–19] Dopants such as nitrogen (N), phosphorus (P), sulfur (S), silicon (Si) and boron (B) have been doped into carbon materials to obtain high performance electrochemical products.[17,18,20–23] Moreover, previous studies have demonstrated that the N dopant can tune the electronic properties of graphene and the S dopant can promote its Faradaic charge transfer.[19] And the incorporation of Si does not bring about extra defects but can modify the electronic distribution of graphene.[17,24] Thus graphene doped with N, S and Si may show great potential in promoting the electrochemical performance of graphene.

Based on the above insights, we here propose a simple foam slurry template strategy to prepare N, S, and Si co-doped 3D graphene with the assistance of egg albumen. Conventionally, stable egg albumen foams (EF) can be obtained by mechanical

[a]State Key Laboratory of Molecular Engineering of Polymers, Department of Macromolecular Science, Collaborative Innovation Center of Polymers and Polymer Composites, Fudan University, 2005 Songhu Road, Shanghai 200433, China. E-mail: hongbinlu@fudan.edu.cn

[b]Electronics Materials and Systems Laboratory (EMSL), Department of Microtechnology and Nanoscience (MC2), Chalmers University of Technology, Kemivägen 9, SE-412 96 Göteborg, Sweden. E-mail: johan.liu@chalmers.se

[c]SMIT Center, Shanghai University, No 20, Chengzhong Road, Shanghai, 201800, China

† Electronic supplementary information (ESI) available. See DOI: 10.1039/c8ta04561e

stirring while making cakes and can be solidified at a relatively low temperature, *e.g.*, 60 °C. Inspired by this process, we mix a GO slurry with the as-prepared EF. Then, graphene foams (GFs) could be obtained by further calcination. Moreover, N, S and Si contained in egg albumen are able to dope the graphene skeleton, and finally we obtain N, S, and Si co-doped GFs. Moreover, we prove that the introduction of heteroatoms into graphene sheets is preferable to improve their wettability. Besides, the unique 3D structure contributes to a large surface area and provides channels for a fast charge–discharge rate. Thus, the obtained GFs exhibit ultrahigh gravimetric capacitance and electrochemical sensing performance. Furthermore, the unique liquid-like morphology of the GO foam (GOF) slurry guarantees the preparation of GFs with various shapes. Totally taking the high performance, convenient and low-cost process into consideration, this research provides a new strategy to prepare GFs and boosts their applications in energy storage and electrochemical sensors.

Experimental

Preparation of GFs

Briefly, the egg albumen solution was subjected to powerful magnetic stirring for 15 minutes at a speed of 1500 rpm until all of the liquid substance was converted into white viscous foams, and the total volume of the foam slurry became approximately four times as large as that of the original solution. Subsequently, a GO dispersion with a concentration of 5.6 mg mL^{-1} was mixed with the foams (weight ratio 3 : 10) at room temperature (25 °C) to obtain a uniform GOF slurry. Then, the GOF slurry was transferred into a vacuum oven for solidification at 60 °C. After that, the solidified GOF was annealed in a tube furnace under a nitrogen atmosphere for 2 h with a heating rate of 10 °C min^{-1}. During the calcination, the GOF was reduced to GF and egg albumen was decomposed simultaneously.

Preparation of GF electrodes

Typically, Ni foam was washed with acetone, hydrochloric acid, ethanol and distilled water to remove the oxide on the surface, followed by annealing at 1000 °C under a nitrogen atmosphere for 2 h.

Then the GOF slurry was coated on the Ni foam to be solidified (Ni-GOF) and further annealed in a tube furnace for 2 h under a nitrogen atmosphere to obtain GF deposited on Ni foams (GF-Ni). Then, the GF-Ni was used as a freestanding electrode for supercapacitors in this work. The mass loading was 0.7 mg. On the other hand, GF was mixed with 0.5 wt% PTFE solution to fabricate electrodes for electrochemical sensors. Subsequently, the obtained dispersion was coated on a polished glassy carbon electrode (GCE) and further dried under an infrared lamp for 10 minutes.

Characterization

Rheological performances were tested on a HAAKE MARS III rotary rheometer. GF's chemical structures were investigated by Fourier transform infrared (FT-IR) spectroscopy (NEXUS 470) and Raman spectroscopy (XploRA, at 532 nm). The morphologies of GFs were observed with field emission scanning electron microscopy (FESEM, Ultra 55) and transmission electron microscopy (TEM, Tecnai G20). Energy dispersive spectroscopy (EDS) was applied to study elemental distribution. X-ray photoelectron spectroscopy (XPS) was carried out on an AXIS UltraDLD system. N_2 adsorption–desorption isotherms were measured with an ASPS2020 instrument. Dynamic water contact angles were measured using an OCA20 contact angle instrument to determine the hydrophilicity of GF. Thermal decomposition curves were obtained with a Mettler Toledo thermogravimetric analyzer (TGA) under a nitrogen atmosphere with a heating rate of 10 °C min^{-1} from 50 to 800 °C. X-ray powder diffraction (XRD) patterns were recorded using a diffractometer (X'Pert PRO, Panalytical B.V., Netherlands) with a Cu Kα radiation source (λ = 1.5406 Å). Electrical conductivities were measured using a four-point probe (ST2262).

Electrochemical measurements

Electrochemical measurements for both supercapacitors and electrochemical sensors were performed with a three-electrode system (CHI660D, Chenhua Instruments, China) with 6 M KOH solution and 0.1 M PBS (containing 0.1 M KCl) solution as the electrolyte. Conventionally, an Ag/AgCl electrode and a Pt wire were used as the reference electrode and counter electrode, respectively. Electrochemical performances of the obtained GF electrodes were characterized by cyclic voltammetry (CV), electrochemical impedance spectroscopy (EIS), chronopotentiometry (CP), cycling stability, and differential pulse voltammetry (DPV) measurements. The CV tests were carried out with scan rates from 5 to 200 mV s^{-1}. The CP measurements were performed with current densities from 1 to 100 A g^{-1}. The specific capacitances were obtained from the discharge process according to the following equation:

$$C = \frac{I \times \Delta t}{m \times \Delta V}$$

where I is the current loaded (A), Δt is the discharge time (s), ΔV is the potential change (V), and m is the mass of the active material (g).[25] The EIS measurements were performed in the frequency range from 0.01 Hz to 100 kHz. The capacitance was calculated from discharge curves, which were recorded from −1.0 V to 0 V, given that the graphene electrode was used as the negative electrode of supercapacitors. DPV tests were carried out from −0.1 to 0.4 V with the applied parameters as follows: 50 s pulse time, 50 mV modulation amplitude, and 0.5 s pulse period.

Results and discussion

The preparation process of GF is illustrated in Fig. 1a. For comparison, the GFs fabricated at 400, 600 and 800 °C are designated as GF-400, GF-600 and GF-800, respectively. FTIR spectroscopy was applied to determine the functional groups in egg albumen, reduced graphene oxide (RGO), and GF, respectively. And the preparation of RGO is depicted in the ESI.† In

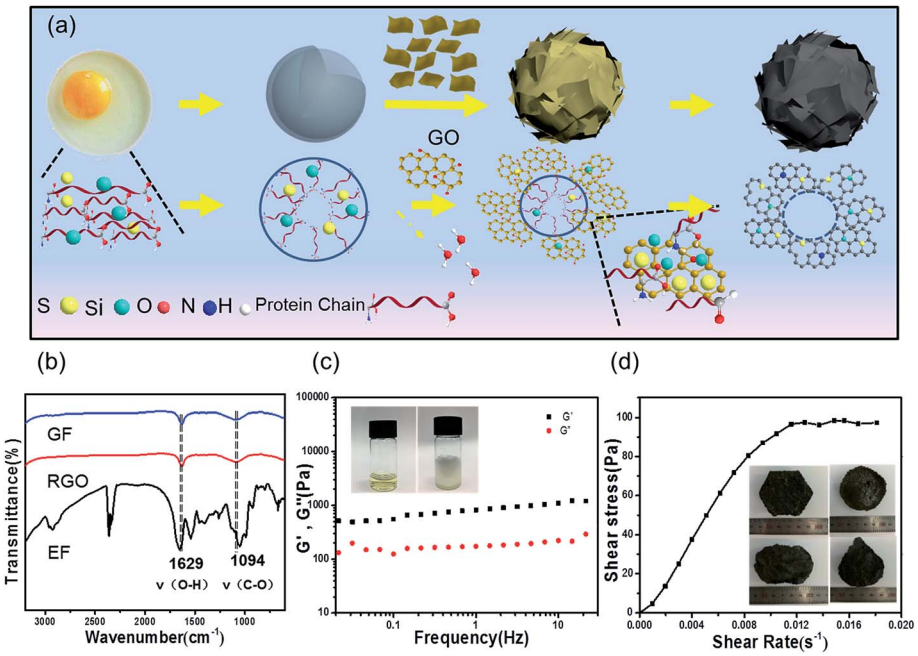

Fig. 1 (a) Schematic illustration of the preparation of GF. (b) FT-IR spectra of RGO, GF and EF. (c) Frequency sweep test of GOF (the insets are the pictures of the egg albumen solution and its foam). (d) Rheological curve of GOF (the insets are GFs with different shapes).

Fig. 1b, the broad peak at 1629 cm^{-1} is attributed to the O–H vibrations of water adsorbed on the surface of samples. Another broad band around 1094 cm^{-1} represents the C–O stretching vibration. It is noteworthy that the spectrum of GF matches well with that of RGO obtained from freeze-drying but those peaks (650 to 3000 cm^{-1}) observed in EF totally disappear after treatment at 800 °C for 2 h. This indicates that the egg albumen suffered from complete pyrolysis in this process. These results are consistent with TGA results of the egg albumen (Fig. S1, ESI†) and the Raman data of GF (Fig. S2, ESI†). The rheological behaviour of GOF was investigated by frequency sweep and steady shear scanning. Fig. 1c shows that both the loss modulus (G') and storage modulus (G'') of GOF increase with increasing frequencies within 0.01–30 Hz and the rheological curve reveals a noticeable characteristic of pseudo-plastic fluids (Fig. 1d), where the apparent viscosity decreases with increasing shear rates. This enables the preparation of various shapes of GF by using different moulds. To illustrate this, several samples with hexagonal, spherical, elliptical and drop shapes were prepared respectively, as shown in the insets of Fig. 1d. After demoulding, all GF monoliths keep the shape of the moulds.

The morphologies of GFs and GO were investigated by SEM and TEM. SEM images suggest that the GFs have honeycomb-like interconnected porous structures with relatively thin graphene skeletons, which come from egg albumen templates (Fig. S3, ESI†). The diameters of pores range from several nanometers to hundreds of microns. The nitrogen adsorption/desorption isotherm shows a typical IV isotherm with a small hysteresis at a high relative pressure ($P/P_0 = 0.9$), suggesting the coexistence of macropores and mesopores. Additionally, the surface area determined by the Brunauer–Emmett–Teller (BET) calculation is 1020 $m^2\ g^{-1}$. The pore size distribution was calculated using a density functional theory (DFT) model and the result shows that there is a large amount of pores centred at 4 nm. Such a 3D multiscale porous structure is beneficial for achieving a high specific surface area and can provide channels for fast charge (ion and electron) transfer; the latter is important for electrochemical capacities and large detection ranges. In addition, EDS was performed to confirm the element distribution in GF-800. As shown in Fig. 2c, except for C and O, abundant S and Si are observed in the mapping photograph, implying the incorporation of S and Si into the skeleton of the GF. To this end, XPS provides further evidence. As is known, it is hard for EDS to image elements that possess a relatively small atomic number with a little dose, such as N. But XPS can provide evidence for these atoms. As shown in Fig. 2d, the N 1s phase in GF actually exists in different modes, with the bonding states of pyridinic (398.5 eV), pyrrolic (399.7 eV), graphitic (401.5 eV) and oxidized nitrogen (406.8 eV). The S 2p peak of GF can be resolved into two peaks at the binding energies of 163.9 and 168.9 eV, suggesting the presence of S 2p3 (for the –C–S–C– bond) and SO*x*. The Si 2p spectrum can be divided into three characteristic peaks at 100.96, 102.1 and 103.6 eV, corresponding to the binding energies of Si–C, Si–O and Si=O, respectively. Moreover, elemental analysis provides further evidence for the existence of N and S. The relative content of N and S for GF-800 by elemental analysis is 4.87 and 0.32%, respectively (Table S2, ESI†), and the content of Si by XPS analysis is 6.69% (Fig. S4, ESI†). It is recognized that N and S doped graphene can generate new electronic states to create plenty of electrical charges, thus significantly enhancing the electrochemical performance.[19] Besides, abundant oxygen-containing functional groups can be introduced into graphene sheets by the incorporation of S and Si, which are

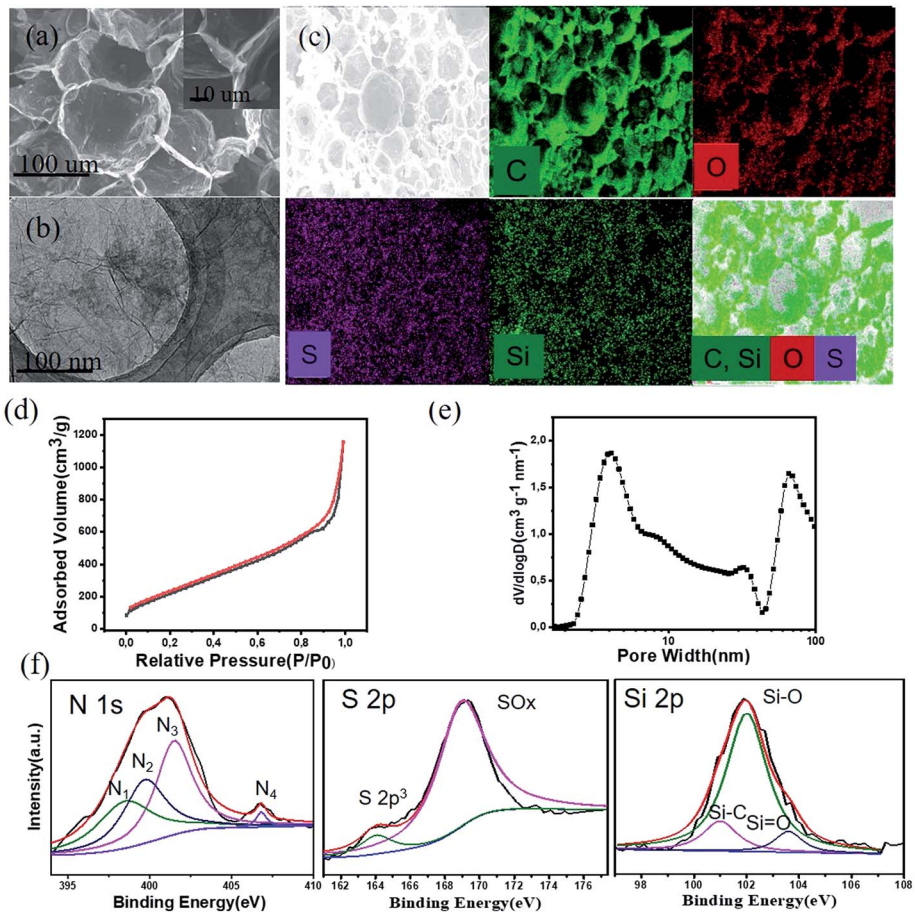

Fig. 2 (a) SEM image of GF (the inset is a SEM image with higher resolution). (b) TEM image of GF. (c) SEM and element mapping images of GF. (d) Nitrogen adsorption/desorption isotherms of GF-800. (e) Pore size distributions of GF-800. (f) High resolution N 1s, S 2p and Si 2p XPS spectra and corresponding fitting peaks.

responsible for improving their capacitance.[19] Furthermore, such element doping provides potential for improving the wettability of graphene, which is super important for performance optimization of electrochemical devices.[20,26,27]

The dynamic water contact angle measurements of GFs and RGO were performed to confirm the effect of N, S, and Si doping on surface wettability. As shown in Fig. 3a, the RGO sample is quite hydrophobic with a nearly unchanged water contact angle of 116°. In contrast, GF-400, GF-600 and GF-800 are more hydrophilic than RGO with the initial contact angles of 40°, 62.8° and 96.5°, respectively, and water droplets are completely absorbed within 60 s. These results demonstrate an expected improved wettability of GF by doping graphene with heteroatoms, which can introduce polar bonds and oxygenic groups.[26] As is known, as electrical double layer capacitors (EDLCs), graphene stores energy by adsorbing electrolyte ions on its surface.[26] Hence this improved wettability is beneficial for enhancing the performance of electrochemical devices, such as supercapacitors and electrochemical sensors.

Density functional theory calculations were performed to verify the influence of N, S, and Si doping on the electronic properties of GF with the CASTEP computer program. The generalized gradient approximation (GGA) with the interpolation formula of Perdew, Burke, and Ernzerhof (PBE) was applied to optimize geometries and calculate electronic structures. Accordingly, the energy cutoff was set at 380 eV, and a $3 \times 3 \times 1$ supercell was used for calculation.[28] As shown in Fig. 4, the regular hexagonal honeycomb structures display a slight deformation in the plane direction, and the bond angle of –C–C–C– (120°) and the bond length of –C–C– (1.42 Å) change a lot after doping with C, S, and Si atoms. And defects on the graphene sheets can affect their crystal structures. On the other hand, partial densities of states and band structures (Fig. S5, ESI†) demonstrate that more sophisticated electronic states can be observed at the position close to the Fermi energy of graphene. And the distribution of charge density difference indicates that the balanced electronic density of graphene is broken owing to the different electronegativity values of C, N, S and Si atoms. These demonstrate that the introduction of N, S and Si atoms into graphene can enhance its polarity, which results in the improved wettability of graphene and may improve its electrochemical properties.

To verify the improved electrochemical performance, we next investigated the supercapacitive properties of GF using a three electrode system with 6 M KOH solution applied as the electrolyte. Fig. 5a shows the CV curves of GF at the voltages from

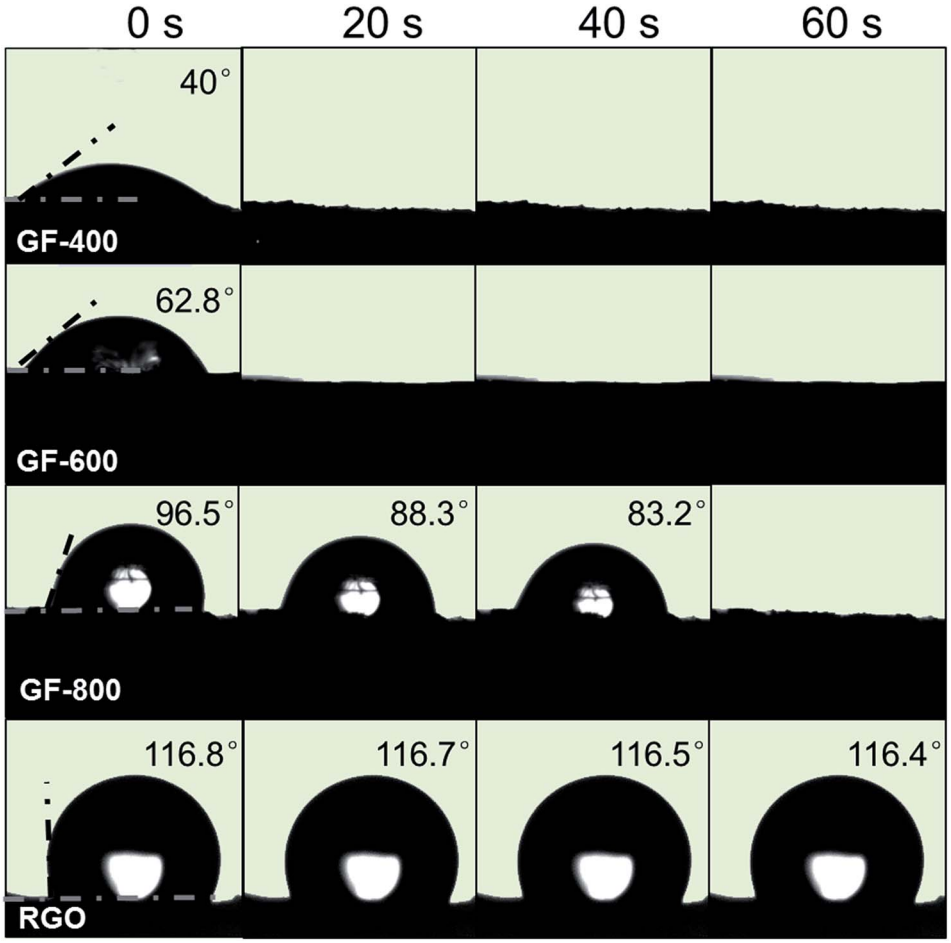

Fig. 3 The dynamic water contact angle tests of GF-400, GF-600, GF-800 and RGO.

−1 to 0 V and the scan rates from 5 to 200 mV s^{-1}. All curves exhibit a rectangle-like shape, suggesting a typical electrical double-layer capacitance behavior. Besides, no peaks indicating pseudo-capacitance contributed by $Ni(OH)_2$ are observed in the CV curves, and the XRD patterns of GO, GF, and Ni foams (before and after annealing at 800 °C) (Fig. S6, ESI†) show that the crystal of Ni foam was unchanged. These two lines of evidence indicate that the Ni-foam keeps stability during the calcination. Based on this, we can exclude the influence of $Ni(OH)_2$ and totally attribute the obtained capacitance to our GFs. Fig. 5b shows the galvanostatic charge and discharge curves of GF-400, GF-600 GF-800, GF-900 and GF-1000 at 10 A g^{-1}. The capacitance increases at first while increasing the calcination temperature due to the decomposition of egg albumen and the reduction of graphene. After 800 °C, because of re-stacking of graphene sheets, the supercapacitor performance tends to decrease with increasing temperature. Therefore, it is necessary to balance conductivity and surface area to optimize the performance of supercapacitors. The CP curves of GF-800 (Fig. 5b) reveal a specific capacitance as high as 534 F g^{-1} at 1 A g^{-1}, which is almost equivalent to the theoretical value (550 F g^{-1}) of graphene. Notably, this value is comparable to those of previously reported work involving porous carbon materials, indicating a great potential of GF-800 for use as a supercapacitor electrode (Table S3, ESI†). Moreover, even at 100 A g^{-1}, the specific capacitance still remains at 308 F g^{-1}, and nearly no IR drops are observed at such a high current density. This reflects the exceptional rate capability of GF. In addition, the GF sample exhibits excellent cycle stability; 96.1% capacitance retention is obtained after 10 000 cycles at a high current density of 10 A g^{-1}.

To further figure out the origin of this ultrahigh performance of GF-800, a GO slurry without the egg albumen template under the same conditions was prepared as well. As shown in Fig. S7 (ESI†), the RGO electrode exhibits a capacitance of only 147 F g^{-1} at 1 A g^{-1}, indicating that the interconnected pores and element doping contribute a large part of the capacitance. Subsequently, the GF-800 foam was mixed with PTFE (weight ratio 9 : 1) to form a GF-800/PTFE electrode, which shows a specific capacitance of 471 A g^{-1} at 1 A g^{-1} (Fig. S8, ESI†). This implies that the free-standing structure of GF-800 contributes to improving the capacitance and rate capability due to a 100% active substance ratio and lower ohmic resistance. The Nyquist plots of GF obtained under different annealing temperatures reveal that a high calcination temperature is beneficial for lowering the resistance (enhancing the structural integrity of

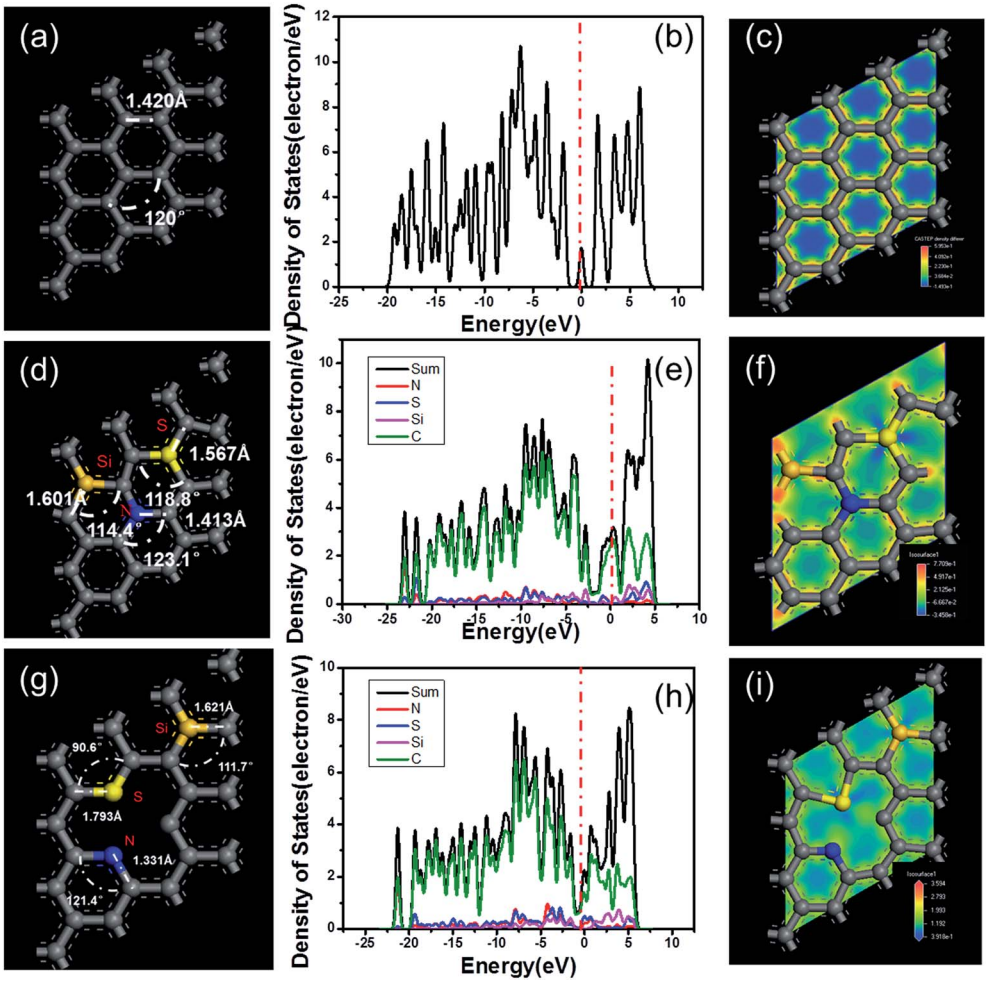

Fig. 4 The computational models and details of graphene and GF. The relaxed structures of (a) pristine graphene, (d) N, S, and Si doped flawless graphene, and (g) N, S, and Si doped defective graphene; partial densities of states of (b) pristine graphene, (e) N, S, and Si doped flawless graphene, and (h) N, S, and Si doped defective graphene; distributions of charge density difference of (c) pristine graphene, (f) N, S, and Si doped flawless graphene, and (i) N, S, and Si doped defective graphene.

graphene). For GF-800, its ohmic resistance is as small as 0.3 Ω, along with a nearly ideal vertical slope in the low-frequency region, suggesting that there exist fast electron transfer and ion diffusion within the electrode. The super-low resistance would arise from a high electrical conductivity (6.99×10^5 S m^{-1}) and better interactions with the electrolyte due to the presence of large pores and N, S, and Si doping.[6] Moreover, in the Bode Plots (Fig. S9, ESI†), the phase angle of GF-800 is close to $-90°$ in the low frequency region, indicating an ideal capacitive behaviour as well. The characteristic frequencies (f_0) of GF-400, GF-600, GF-800, GF-900 and GF-1000 at a phase angle of $-45°$ are 18, 3, 112, 11 and 65 Hz, corresponding to the time constants τ_0 ($\tau_0 = 1/f_0$) of 0.05, 0.3, 0.009, 0.09 and 0.015 s, respectively. These results imply that the time constant varies with temperature and GF-800 has the fastest charge–discharge rate (comparable to the reported work, Fig. S9 and Table S1, ESI†), corresponding to an ultrahigh specific capacitance.[26] It is believed that the super-high capacitance of GF-800 would originate from the combination of the 3D porous structure, element doping, freestanding electrode structure and high electrical conductivity.

On the other hand, owing to their low charge-transfer and diffusion resistances, it is anticipated that GFs also exhibit potential as electrochemical sensors.[29] We choose dopamine (DA) to study the detection capability of GFs as electrochemical sensors. DA is an indispensable neurotransmitter in the central nervous system to help transfer chemicals among cells.[30] Thus it is of great importance to detect DA while treating neurological diseases, for instance, Parkinson's disease. For most bio-sensors, their detection depends on enzymes, which are not only expensive but also highly susceptible to environmental conditions such as temperature, humidity, *etc.* In this regard, egg albumen-derived GF has good biocompatibility and great potential as a bio-sensor.

Cytotoxicity experiments were first carried out to determine the biocompatibility of GF. It is observed that, compared to untreated cells, there are no significant cytotoxic responses at all examined doses, indicating the good biocompatibility of GF. As shown in Fig. 6b, GF-400, GF-600 and GF-800 show sharper

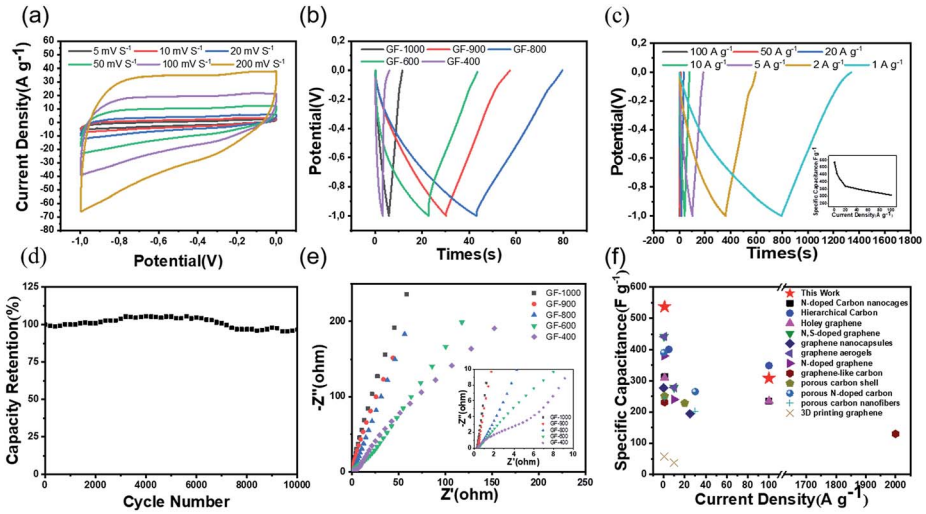

Fig. 5 (a) CV curves of GF-800 at 5, 10, 20, 50, 100, and 200 mV s^{-1}. (b) Galvanostatic charge and discharge curves of GF-400, GF-600, GF-800, GF-900 and GF-1000 at 10 A g^{-1}. (c) Rate capability of GF-800. (d) Cycling stability of GF-800 at 10 A g^{-1}. (e) Nyquist plots of GF-400, GF-600, GF-800, GF-900, and GF-1000; the inset shows the comparison in the high frequency region. (f) Comparison of the supercapacitor performance of the GF in this study and carbon materials from the literature.

response peaks than a GCE in 0.1 mM $K_3[Fe(CN)_6]$ solution, indicating an enhanced response sensitivity of the GF samples. Contrast tests, including different pH (Fig. S10, ESI†) and proportions (Fig. S11, ESI†), were performed to realize that GF-600 exhibits the best detection sensitivity for DA.

As shown in the inset of Fig. 6c, the CV curve of the PBS solution without DA shows no peak. In contrast, remarkable current peaks can be observed for the electrolytes with DA at different scan rates (5–200 mV s^{-1}), corresponding to the oxidation and reduction of DA. And both the intensities of oxidation peaks (I_{pa}) and reduction peaks (I_{pc}) are linearly dependent on the scan rates, suggesting that the DA molecule on the GF undergoes a surface-controlled process. Thus the porous structure of GFs is advantageous for DA detection. To obtain the detection limit and the linear detection range of GF electrodes, differential pulse voltammetry (DPV) measurements were carried out in 0.1 M PBS solution. Obviously, an oxidation peak at around +0.16 V appears with the addition of DA and the intensity of the peak gradually increases during the test process. The shift of the oxidation peak results from disturbance during tests and the difference signal function for CV and DPV. Furthermore, a linear dependence relationship in a large concentration range of DA from 1.25 to 70 μM can be achieved. The linear regression equation is acquired as $I\,(\mu A) = 0.436263 +$

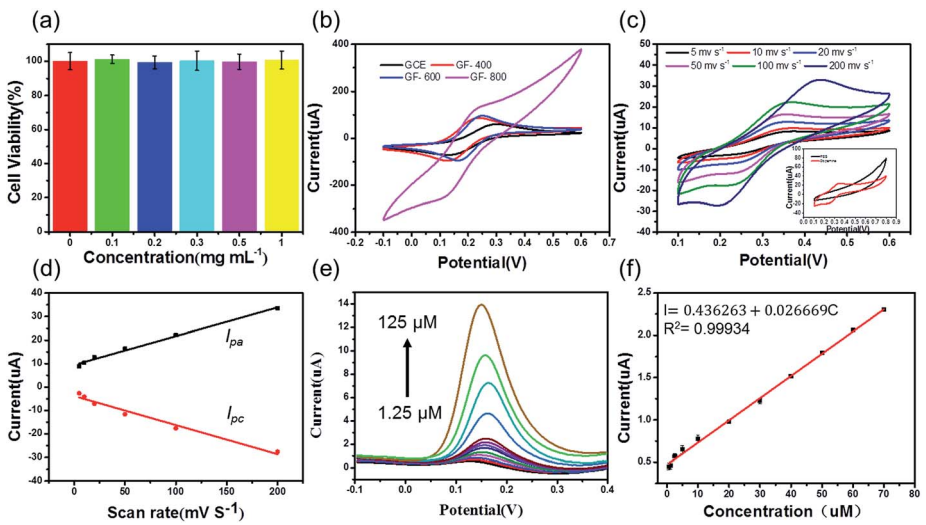

Fig. 6 Detection of DA in 0.1 M PBS (pH = 7) solution with the GF electrode. (a) Cytotoxicity tests using GF-600 dispersed in cell culture fluid with different concentrations (0, 0.1, 0.2, 0.3, 0.5, and 1 mg mL^{-1}). (b) CV curves of GCE, GF-400, GF-600 and GF-800 measured in 0.1 mM $K_3[Fe(CN)_6]$. (c) CV curves with DA at different scan rates of 5, 10, 20, 50, 100, and 200 mV s^{-1}. (d) The plots of CV peak current *versus* the scan rates. (e) DPV curves obtained in 0.1 M PBS solution in the presence of various concentrations of DA (1.25, 2.5, 5, 10, 20, 30, 40, 50, 60, 70, 80, 90, 100, and 125 μM), at a scan rate of 100 mV s^{-1}. (f) Linear relationship between the intensity of current peaks and the concentration of DA.

0.026669C (μM) ($R^2 = 0.99934$). Thus, the detection limit for DA with the GF electrode can be calculated as 1.2 μM. Comparing the electrochemical sensing performance of GF with reported work, our GF has comparable detection properties with a relatively simple preparation process (Table S4, ESI†).

Conclusions

In summary, we demonstrate a new and scalable approach to fabricate N, S, and Si co-doped biocompatible GFs with a wide variety of shapes with egg albumen used as the template. Then, supercapacitors and chemical sensors are fabricated using the obtained GFs. Among them, GF-800 exhibits ultrahigh gravimetric capacitance up to 534 F g^{-1} at 1 A g^{-1} and 308 F g^{-1} at 100 A g^{-1} with 96.1% capacitance retention after 10 000 cycles at a high current density of 10 A g^{-1}. These values are among the highest reported gravimetric capacitances of carbon-based materials. Benefiting from the hierarchical porous structure and low resistance, the prepared GF displays comparable electrochemical detection capacity. A detection concentration as low as 1.2 μM and a linear dependence up to 70 μM can be observed for the GF electrode. N, S, and Si co-doping and the unique 3D structure are considered to contribute to the excellent wettability, electron transfer and ion transport rate, which lead to a good electrochemical performance. Ultimately, we believe that this work will open a facile route to prepare three-dimensional graphene and boost its electrochemical applications.

Conflicts of interest

There are no conflicts to declare.

Acknowledgements

The authors are grateful for the financial support by the 973 project (2011CB605702), the National Natural Science Foundation of China (51173027), and the Shanghai key basic research project (14JC1400600). Y. Liu and J. Liu acknowledge the financial support from the Swedish Board for Strategic Research (SSF) with the contract No: SE13-0061 and GMT14-0045, from Formas with the contract No: FR-2017/0009 and from STINT for the double degree PhD collaboration program with the contract No: DD2016-6502, the Production Area of Advance at Chalmers University of Technology, Sweden. The authors also acknowledge the financial support by the Key R&D Development Program from the Ministry of Science and Technology of China with the contract No: YS2017YFGX020059 and Shanghai Municipal Education Commission (Shanghai University High Education Peak Discipline Program).

References

1 J. Xu, Z. Q. Tan, W. C. Zeng, G. X. Chen, S. L. Wu, Y. Zhao, K. Ni, Z. C. Tao, M. Ikram, H. X. Ji and Y. W. Zhu, *Adv. Mater.*, 2016, **28**, 5222–5228.
2 J. Yan, Q. Wang, T. Wei and Z. J. Fan, *Adv. Energy Mater.*, 2014, **4**, 1300816.
3 J. X. Zhu, D. Yang, Z. Y. Yin, Q. Y. Yan and H. Zhang, *Small*, 2014, **10**, 3480–3498.
4 H. Yu, D. Ye, T. Butburee, L. Wang and M. Dargusch, *ACS Appl. Mater. Interfaces*, 2016, **8**, 2505–2510.
5 X. Yang, J. Zhu, L. Qiu and D. Li, *Adv. Mater.*, 2011, **23**, 2833–2838.
6 J. Zhao, Y. Jiang, H. Fan, M. Liu, O. Zhuo, X. Wang, Q. Wu, L. Yang, Y. Ma and Z. Hu, *Adv. Mater.*, 2017, **29**, 1604569.
7 Y. Zhu, S. Murali, M. D. Stoller, K. J. Ganesh, W. Cai, P. J. Ferreira, A. Pirkle, R. M. Wallace, K. A. Cychosz and M. Thommes, *Science*, 2011, **332**, 1537–1541.
8 S. Ye, J. Feng and P. Wu, *ACS Appl. Mater. Interfaces*, 2013, **5**, 7122–7129.
9 V. Kuzmenko, N. Wang, M. Haque, O. Naboka, M. Flygare, K. Svensson, P. Gatenholm, J. Liu and P. Enoksson, *RSC Adv.*, 2017, **7**, 45968–45977.
10 J. Zhao, H. W. Lai, Z. Y. Lyu, Y. F. Jiang, K. Xie, X. Z. Wang, Q. Wu, L. J. Yang, Z. Jin, Y. W. Ma, J. Liu and Z. Hu, *Adv. Mater.*, 2015, **27**, 3541–3545.
11 F. Liu, S. Song, D. Xue and H. Zhang, *Adv. Mater.*, 2012, **24**, 1089–1094.
12 Y. Xu, G. Shi and X. Duan, *Acc. Chem. Res.*, 2015, **48**, 1666–1675.
13 S. Liu, A. K. Bastola and L. Li, *ACS Appl. Mater. Interfaces*, 2017, **9**, 41473–41481.
14 Z. Chen, W. Ren, L. Gao, B. Liu, S. Pei and H. M. Cheng, *Nat. Mater.*, 2011, **10**, 424–428.
15 L. X. Lv, P. P. Zhang, H. H. Cheng, Y. Zhao, Z. P. Zhang, G. Q. Shi and L. T. Qu, *Small*, 2016, **12**, 3229–3234.
16 K. Shehzad, Y. Xu, C. Gao and X. Duan, *Chem. Soc. Rev.*, 2016, **45**, 5541–5588.
17 R. Lv, M. C. dos Santos, C. Antonelli, S. M. Feng, K. Fujisawa, A. Berkdemir, R. Cruz-Silva, A. L. Elias, N. Perea-Lopez, F. Lopez-Urias, H. Terrones and M. Terrones, *Adv. Mater.*, 2014, **26**, 7593–7599.
18 X. M. Feng, Y. Zhang, J. H. Zhou, Y. Li, S. F. Chen, L. Zhang, Y. W. Ma, L. H. Wang and X. H. Yan, *Nanoscale*, 2015, **7**, 2427–2432.
19 T. Ngoc Quang, B. K. Kang, M. H. Woo and D. H. Yoon, *ChemSusChem*, 2016, **9**, 2261–2268.
20 X. Yu, Y. Kang and H. S. Park, *Carbon*, 2016, **101**, 49–56.
21 Y. X. Huang, S. L. Candelaria, Y. W. Li, Z. M. Li, J. J. Tian, L. L. Zhang and G. Z. Cao, *J. Power Sources*, 2014, **252**, 90–97.
22 C. B. Jin, W. K. Zhang, Z. Z. Zhuang, J. G. Wang, H. Huang, Y. P. Gan, Y. Xia, C. Liang, J. Zhang and X. Y. Tao, *J. Mater. Chem. A*, 2017, **5**, 632–640.
23 C. Ricca, F. Labat, C. Zavala, N. Russo, C. Adamo, G. Merino and E. Sicilia, *J. Comput. Chem.*, 2018, **39**, 637–647.
24 Z. S. Qian, X. Y. Shan, L. J. Chai, J. J. Ma, J. R. Chen and H. Feng, *ACS Appl. Mater. Interfaces*, 2014, **6**, 6797–6805.
25 L. Zhang, L. Dong, M. Li, P. Wang, J. Zhang and H. Lu, *J. Mater. Chem. A*, 2018, **6**, 1412–1422.
26 J. Zhao, H. Lai, Z. Lyu, Y. Jiang, K. Xie, X. Wang, Q. Wu, L. Yang, Z. Jin and Y. Ma, *Adv. Mater.*, 2015, **27**, 3541–3545.

27 K. Gopalsamy, J. Balamurugan, T. D. Thanh, N. H. Kim and J. H. Lee, *Chem. Eng. J.*, 2017, **312**, 180–190.
28 W. J. Yan, Q. Xie, X. M. Qin, C. H. Zhang, Z. Z. Zhang and S. Y. Zhou, *Comput. Mater. Sci.*, 2017, **126**, 336–343.
29 X. C. Dong, H. Xu, X. W. Wang, Y. X. Huang, M. B. Chan-Park, H. Zhang, L. H. Wang, W. Huang and P. Chen, *ACS Nano*, 2012, **6**, 3206–3213.
30 X. Dong, X. Wang, L. Wang, H. Song, H. Zhang, W. Huang and P. Chen, *ACS Appl. Mater. Interfaces*, 2012, **4**, 3129–3133.

Received: 13 October 2020 | Revised: 7 November 2020 | Accepted: 9 November 2020

DOI: 10.1002/nano.202000195

RESEARCH ARTICLE

nano select Open Access WILEY

A lightweight and high thermal performance graphene heat pipe

Ya Liu[1,2] | **Shujing Chen**[3] | **Yifeng Fu**[1] | **Nan Wang**[4] | **Davide Mencarelli**[5] | **Luca Pierantoni**[5] | **Hongbin Lu**[2] | **Johan Liu**[1,3]

[1] Electronics Materials and Systems Laboratory, Department of Microtechnology and Nanoscience, Chalmers University of Technology, Kemivägen 9, Gothenburg 41296, Sweden

[2] State Key Laboratory of Molecular Engineering of Polymers, Department of Macromolecular Science, Collaborative Innovation Center of Polymers and Polymer Composites, Fudan University, Songhu Road 2005, Shanghai 200433, China

[3] SMIT Center, Department of Mechanical Engineering and Automation, Shanghai University, Chengzhong Road 20, Shanghai 201800, China

[4] SHT Smart High Tech-AB, Kemivägen 6, Gothenburg 41258, Sweden

[5] Marche Polytechnic University, Via Brecce Bianche, Ancona 60131, Italy

Correspondence
Johan Liu, Electronics Materials and Systems Laboratory, Department of Microtechnology and Nanoscience, Chalmers University of Technology, Kemivägen 9, Gothenburg 41296, Sweden.
Email: johanliu@shu.edu.cn; johan.liu@chalmers.se

Hongbin Lu, State Key Laboratory of Molecular Engineering of Polymers, Department of Macromolecular Science, Collaborative Innovation Center of Polymers and Polymer Composites, Fudan University, Songhu Road 2005, Shanghai 200433, China.
Email: hongbinlu@fudan.edu.cn

Abstract

Heat pipe is one of the most efficiency tools for heat dissipation in power systems. Currently, heat pipes are usually made of copper or aluminum. However, due to their relatively high density and limited heat transmission capacity, heat pipes are facing urgent challenges in power electronics. In this paper, a new class of graphene enhanced heat pipe that can cope with these issues is reported. The graphene enhanced heat pipe is made of high thermal conductivity graphene assembled film with nanostructure enhanced inner surfaces. The study shows that the dramatically improved heat dissipation capacity, 7230 W m^{-2} K^{-1} g^{-1}, about 3.5 times higher than that of copper based commercial heat pipes can be achieved. This paves the way for using graphene enhanced heat pipe in lightweight and large capacity cooling applications, as required in many systems such as automotive electronics, hand-sets and space electronics.

KEYWORDS
graphene heat pipe, lightweight, thermal performance

1 | INTRODUCTION

Nowadays, the power density in integrated circuits (ICs) can reach over 1000 W m^{-2}.[1,2] Thus, efficiency heat dissipation is essential for keeping the performance and extending the lifetime of electronics and power systems.[3] For instance, heat pipe, a two-phase flow heat dissipation device, has attracted intensive interest because of its high efficiency and unique ability to transfer heat over large distances with minimal losses.[4–7] Today, heat pipes are mainly made of metals with high thermal conductivity and good mechanical strength, such as copper,[8]

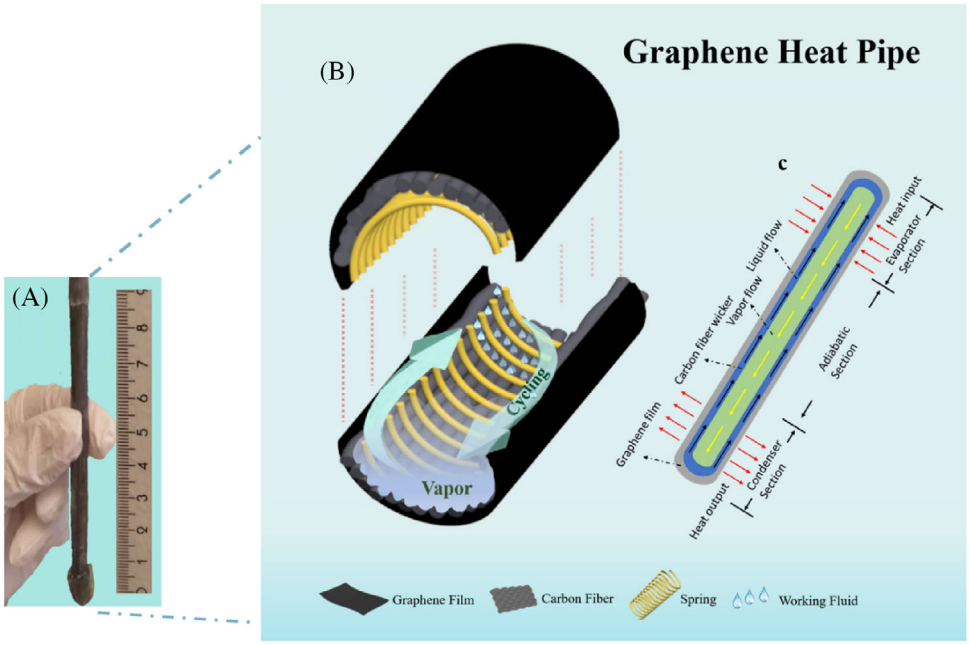

FIGURE 1 Design and image of the GHP. A, Image of a real GHP; B, schematic designing of the GHP; C, working principle of the GHP

aluminum,[8,9] or their alloys.[10] However, with the development of terrestrial and portable electronics, traditional metals could no longer be the best choice because lightweight has become the first priority in these applications.[8,11] Currently, several attempts have been made to lighten heat pipes by using light-metal and alloys, epoxy-impregnated carbon fiber with thin aluminum shells or metal/matrix composites.[8] However, light-metal suffers from issues such as corrosion and low thermal conductivity,[10] while the incorporation of epoxy or polymer matrix sharply increases thermal resistance.[12] Therefore, it remains an urgent challenge to develop a lightweight and high thermal performance heat pipe.

Compared to metal materials, graphene shows overwhelming advantages[13] such as lightweight, good stability and superior in-plane thermal conductivity (up to 5000 W m^{-1} K^{-1} at room temperature),[14,15] far better than that of copper (402 W m^{-1} K^{-1}) and aluminum (237 W m^{-1} K^{-1}).[16,17] Furthermore, compared with single layer graphene film, graphene assembled films (GF) reach a good compromise between thermal conductivity, scalable preparation and applicable mechanical strength.[18] For instance, GF with thickness at 1–2 microns has exhibited thermal conductivities up to 2500 W m^{-1} K^{-1} and tensile strength of 78 ± 6 MPa.[16] More importantly, GF has little corrosion risks even under acid, alkali and moisture exposure than metal based materials.[19] Taken all of these advantages into consideration, graphene possesses promising potential to boost heat dissipation performance of heat pipes.

In this work, we demonstrate a strategy to constitute a new class of lightweight and highly thermal conductive heat pipe based on GF. Such graphene heat pipe (GHP) exhibits a cooling capacity up to 7230 W m^{-2} K^{-1} g^{-1} under a 10 W heat loading, which is about 3.5 times better than that of commercial copper based heat pipes with the same geometry (2053 W m^{-2} K^{-1} g^{-1}). Besides, simulation results reveal that the GF contributes over 30% to the total heat dissipation ability of the heat pipe due to its outstanding thermal conductivity. Heat transfer modeling suggests that increasing thermal conductivity of wall material (container) can significantly improve its heat dissipation capacity.

2 | RESULTS AND DISCUSSION

2.1 | Design and fabrication of GHP

The GHP consists of three key components, including container, wick structure and working fluid (Figure 1A, B). To improve the mechanical strength of the GHP container, a copper spring was inset in GHP. On one hand, the ultra-high in-plane thermal conductivity of graphene film endows heat conduct from the evaporator section to the condenser section rapidly. On the other hand, the working fluid is evaporated when heat enters GHP at its evaporator section. The evaporated fluid creates a pressure gradient to force the vapor to move towards the condenser section. While vapor reaches the condenser section, the vapor

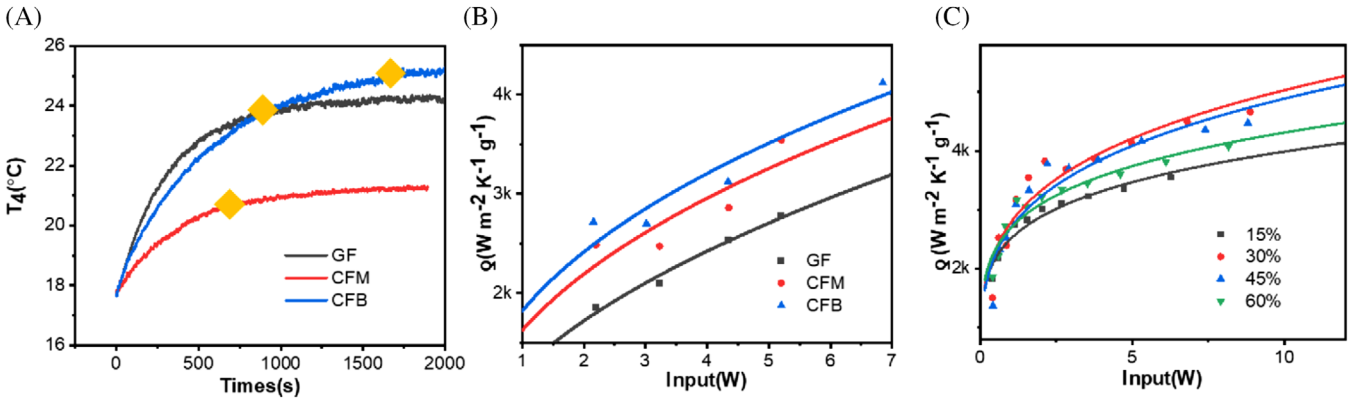

FIGURE 2 Optimization of wick structure and working fluid's filling volume. A, Start-up time of GHP with three wick structures; B, specific thermal transfer coefficient of GHP with three wick structures; C, specific thermal transfer coefficient of GHP with various filling volume of working fluid

condenses and releases its latent heat of evaporation by external devices that is, heat sink. After that, the working fluid is relatively or passively pumped to the evaporator section for re-evaporation by the capillary force of wick structure (Figure 1C).[5] Thus, by using this liquid-vapor phases changes, heat transport in GHP becomes extremely fluent and efficiency.[20]

First, microstructures of the GF were investigated by small angle X-ray scattering (SAXS, Figure S1) to verify the alignment of the graphene flakes. According to the SAXS results (Figure S2), the well-ordered graphene flakes ensure high thermal conductivity of GF by increasing thermal transfer pathway and lowering thermal interface resistance.[20,21] Based on such a theory, and following the previously developed method,[16] a 25 μm thickness GF with in-plane thermal conductivity of 1400 W m^{-1} K^{-1} was selected as the container for GHP.

In order to optimize the wick structure in GHP, three porous structures, including O_2 plasma treated GF, carbon fiber mesh (CFM) and carbon fiber bunch (CFB) were investigated (Figure S3). After treated by O_2 plasma, all these three wick structures exhibit hydrophilic property with working fluid (ethanol solution), corresponding to an instant wetting angel of 22.05, 0 and 20.34 deg (Figure S4). Among these three wick structures, the GHP with CFB wick structure shows the fastest start-up time and the highest specific thermal transfer coefficient (ϱ, **Figure 2A, B**). The start-up time refers to the time when the evaporator section needs to reach the steady state.[1] To further understand the above result, capillary pressures of three wick structures were calculated to explain the relationship between wick structure and heat transfer performance. When the heat pipe is operated under steady state, the capillary pressure of wick structure is expressed as

$$\Delta p = 2\delta cos\theta / r \tag{1}$$

where δ is the surface tension of working fluid (23.82 mN m^{-1}),[22] θ is the instant wetting angle, r is the effective capillary radius or pores of the wick structure.[7]

For the three wick structures, r is calculated as

$$r_{GF} = (s + d_s)/2 \tag{2}$$

$$r_{CFM} = (s + d_s)/2 \tag{3}$$

$$r_{CFB} = s \tag{4}$$

where s is the pore diameter, d_s is the wire diameter.[7,23]

Therefore, the capillary pressure of three wick structures are calculated as 4.76, 6.35, 15.88 KPa, respectively.

Meanwhile, the critical heat flux (CHF, q) of the three wick structures were calculated to support the capillary pressure calculation (Figure S5).

Generally, the CHF for a wicking surface can be calculated by equation as below:

$$q_w = q_{nw} + \Delta q \tag{5}$$

$$\Delta q = V \rho_f h \left(\frac{A_1}{A_t} \right) \tag{6}$$

where subscripts w and nw indicate wicking and nonwicking, Δq is the increase in CHF by a wick structure, V, ρ_f, h, A_1 and A_t are the volumetric flux of liquid wicked into the surface at CHF, working fluid density, latent heat, liquid phase surface area and total heated surface area, respectively.[15,24]

Because GF, CFM and CFB are composed of carbon, q_{nw} of these three wick structures can be considered as the same. Therefore, the difference of CHF comes from Δq.

According to Equation (6) and the infrared camera results of wetting area of the three wick structures with 150 μL working fluid (Figure S5), the CHF increased by wick structure in GF, CFM, and CFB are 34.04, 52.57, and 100.12 J, which keep consistence with the capillary pressure of the three wick structures.

In corporation with thermal transfer capability of GHP made from the three wick structures, it demonstrates that the structure of CFB has the largest contribution to the thermal transfer efficiency by improved capillary pressure and CHF.

In addition, we studied the filling volume of working fluid in GHP. Taking boiling point and wettability with graphene into consideration, an ethanol solution (V_{Water}:$V_{Ethanol}$ = 1:4) is used as working fluid in GHP. To optimize the filling volume, GHP with 6 mm outer diameter and 130 mm length filled with 15, 30, 45, 60 vol.% ethanol solution were tested, respectively. As shown in Figure 2c, the ϱ increases when the filling volume is <30 vol.% of the inner volume of GHP. When the filling amount is >30 vol.%, ϱ starts to decrease. Such tendency is because too high or too low vapor pressure will result in no-flow or low-flow behavior in a heat pipe.[5] The saturated evaporation pressure of working fluid is shown in Figure S6. Accordingly, 30 vol.% of working liquid is the optimized filling volume for the GHP.

2.2 | Heat dissipation performance of GHP

With these optimized parameters, GHPs with various lengths (90, 130, 150 mm) were fabricated to investigate the relationship between length and specific thermal transfer coefficient of GHP. When the length of the 6 mm outer-diameter GHP decreases from 150 to 90 mm, temperature on the evaporator section decreases from 77 to 42°C (**Figure 3**A-C) with 10 W heat loading (the measurement setup and position of thermal couples 1–5 are shown in Figure S7). Meanwhile, the ϱ increases with shortened length of GHP and reaches 7230 W m^{-2} K^{-1} g^{-1} with a heat loading of 10 W (Figure 3D). It is demonstrated that the heater temperature decreases with shortened pipe length (Figure 3E), consistent with the trends of ϱ. With a 10 W heat loading, temperature of the heater containing a 90 mm GHP goes to 42°C with a 15.4 mins start-up time in steady state (Figure 3F, T_4 is the temperature at thermal couple 4), far lower than that (86°C) of the independent heater without graphene pipe. These provide evidence that shorter GHP carries more power than longer pipe since capillary limit is an inverse function of the length.[9,22] On the other hand, the start-up time of GHP significantly shorts with higher heat loading. Such tendency is because higher heat loading provides sufficient pressure difference between inlet and outlet of evaporator section to activate GHP.[25]

Meanwhile, a commercial copper heat pipe with the same diameter (CHP, Spread Fast AB, 6 mm) was used as a reference to evaluate the thermal dispassion behavior of GHP. In the CHP, copper and sintered copper powder works as container and wick structure (Figures 3G and S8). Similar temperature distribution (Figure S9) and start-up behavior are observed from GHP and CHP, as shown in Figure 3H. While compared to CHP, the start-up time of GHP decreases 35%. Such improvement maybe because the rough and flexible surface property of GF, which decrease contact resistance between the heat pipe and heat source. Moreover, the GHP shows a significant advantage on specify thermal transfer coefficient (Figure 3I). A standard 90 mm GHP weights 2.1 g while the weight of the same diameter CHP is 12.9 g. The specific thermal transfer coefficient of GHP is improved by 3.5 times compared to that of the CHP. Therefore, such a high specific thermal transfer coefficient makes GHP an ideal candidate for thermal management on lightweight applications such as in spacecraft, avionics, automotive and consumer systems where performance versus weight is of great concern.

2.3 | Heat transfer modelling for GHP

The contributions from the container's thermal conductivity and phase change process were assessed numerically by COMSOL Multiphysics solver. Models of 6 mm outer diameter GHPs with length of 90, 130, and 150 mm have been designed by COMSOL and set for simulation (**Figure 4**A). In particular, thermal conductivity of container was set as 400, 900, and 1400 W m^{-1} K^{-1} to figure out the contribution from the container in a GHP. Similar to the experimental results, it was found that the shorter GHP, the lower temperature is on the heat pipe. Additionally, with the same GHP diameter and length, the temperature on the heater decreases by improving the thermal conductivity of GF (Figure 4C-E). This observation implies that improving thermal conductivity of the container would effectively promote heat dissipation of GHP. To figure out how much thermal conductivity of the GF contributing to the thermal dissipation in GHP, we define the contribution factor as γ. Notably, the through-plane thermal conductivity of GF is measured as15 W m^{-1} K^{-1} by steady state heat-flow method (ASTM standard D5470).[26] As shown in Figure S10, the temperature distribution on GHP shows similar behavior with anisotropic and isotropic thermal conductivity of GF. Therefore, to simply the thermal transfer model,

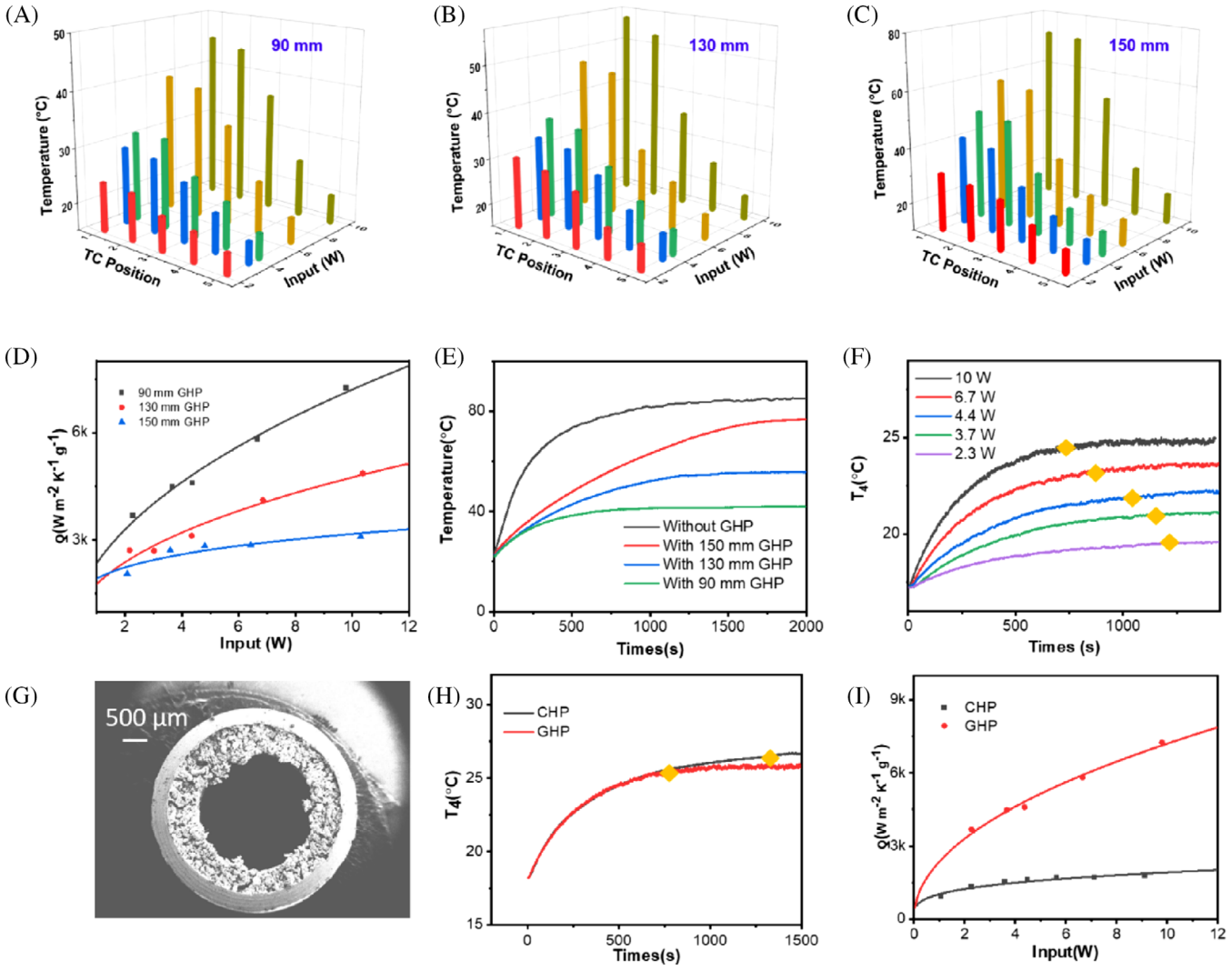

FIGURE 3 Heat dissipation performance of a 6 mm GHP. A, B, C, Temperature distribution along GHP with lengths as 90, 130, and 150 mm; D, specific thermal transfer coefficient of GHP with length as 90, 130, and 150 mm (R^2 = 0.98607, 0.96344, 0.84614); E, temperature distribution on heater with 90, 130, and 150 mm GHP under 10 W input; F, start-up times of 90 mm GHP under various heat loading; G, cross-section SEM image of CHP; H, start-up times of GHP and CHP with 10 W heat loading; I, specific thermal transfer coefficient of GHP and CHP

we considered the GHP model as isotropic for contribution factor calculation.

Typically, there are two main heat dispassion paths in heat pipe, including heat conducted by GF and heat absorbed by phase change. The contribution factor from containers can be defined as

$$\nu = \frac{Q_c}{Q_c + Q_p} \tag{7}$$

where Q_c and $Q_p$are heat delivered by the intrinsic thermal conductivity of graphene film and phase change. Similarly, the thermal transfer coefficient was used to evaluate the heat transferability. Empty GHP without working fluid was simulated to calculate the contribution from the graphene film. Therefore, we can rewrite the contribution factor equation as below:

$$V_c = \frac{\frac{Qe}{A\Delta T_e}}{\frac{Qf}{A\Delta T_f}} = \frac{\frac{Qe}{\Delta T_e}}{\frac{Qf}{\Delta T_f}} \tag{8}$$

The Qe, Qf is power of empty and filled GHP; ΔT_e, $\Delta T_f$is the temperature difference between the evaporator and condenser section in empty and filled GHP; A is cross-section area of the GHP.

To quantify such an improvement, the contribution factor of the container (γ_c) has been calculated (Figure 4B inset). Specifically, γ_c exhibits a negatively linear relationship with the length of the GHP. While reducing the pipe

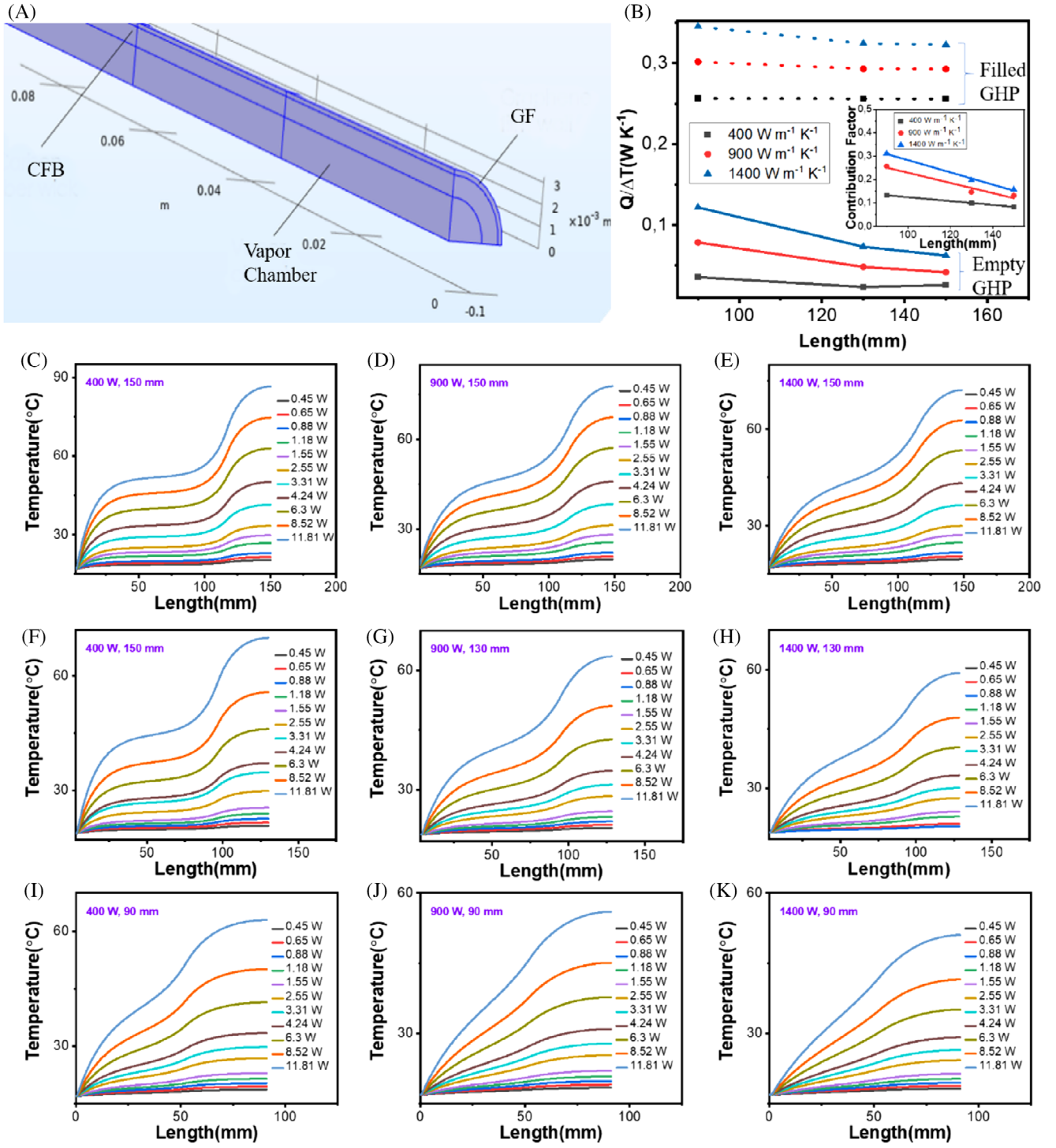

FIGURE 4 COMSOL Multiphysics solver modeling results of GHP. A, COMSOL model of GHP; B, Thermal transfer performance of phase change and GF, the inset is contribution factor of container for GHP; C-E, simulation results of 150 mm GHP with thermal conductivity as 400, 900, and 1400 W m^{-1} K^{-1}; F-H, simulation results of 130 mm GHP with thermal conductivity as 400, 900, and 1400 W m^{-1} K^{-1}; I-K, simulation results of 90 mm GHP with thermal conductivity as 400, 900, and 1400 W m^{-1} K^{-1}

length, the heat conducted by the container increases. Hence, it explains why the shorter GHP, the better its heat transfer performance. Meanwhile, it is observed that the higher thermal conductivity, the higher γ_c from the container. As a result, when thermal conductivity of a graphene film reaches 1400 W m^{-1} K^{-1}, γ_c can goes up to 0.31. This explains why highly thermally conductive graphene film can help achieve high-efficiency heat pipe. Based on these results, we build the heat transfer model for the GHP.

The total transferred heat is expressed as

$$Q = Q_c + Q_p \tag{9}$$

According to the definition of thermal conductivity and Riedel equation,

$$Q_c = \frac{A\Delta T\lambda}{L} \tag{10}$$

$$Q_{pc} = 1.093mR_sT_c\ln(P_c - 1)/18(0.93 - T_b) \tag{11}$$

where ΔT is temperature difference between evaporator and condenser section, λ represents thermal conductivity of the graphene film, L is the length of the heat pipe, m is the weight of working fluid, $R_s$is gas constant, T_c is tested temperature, P_c is critical pressure, T_b is reduced temperature at the normal boiling point.[23,24]

For a certain case, container's contribution factor is

$$\upsilon_c = A\Delta T\lambda(0.93 - T_b)/[(0.93T_bA\Delta T\lambda L) + 1.093mRT_cLln(P_c - 1)] \tag{12}$$

While inset heat parameters, container's contribution factor is rewritten as

$$\upsilon_c = 1.44\lambda(0.93 - T_b)/[(0.0168\lambda + 191T_cln(P_c - 1)] \tag{13}$$

Because of $191T_cln(P_c - 1) \gg 0.0168\lambda$, container's contribution factor is simplified as

$$\upsilon_c = 1.44\lambda(0.93 - T_b)/191T_cln(P_c - 1) \tag{14}$$

T_b is known. Thus, Equation (14) suggests that the contribution factor of container increases by using a higher thermal conductivity material. Meanwhile, the heat dissipated by phase change is mainly decided by the inner structure of heat pipe, involving inner pressure, wick structure, volume, diameter and working fluid.[6] Therefore, with the same inner structure, the Equation (14) indicates that increasing thermal conductivity of wall material (container) can significantly improve heat dissipation capacity of heat pipes.

3 | CONCLUSION

In summary, we have demonstrated, for the first time, the application of using graphene to build heat pipes for cooling purpose. With optimized wick structure, a GHP exhibits specific thermal transfer coefficient as high as 7230 W m^{-2} K^{-1} g^{-1}, which is 3.5 times higher efficiency than the well-designed commercial copper based heat pipe. Besides, a heat transfer model was built to explain the contribution of GF in the GHP. It opens the possibility to use graphene for thermal dissipation, especially in situations where lightweight is required as priority.

4 | EXPERIMENTAL SECTION/METHODS

Materials and methods

GF is prepared by a reported method.[16] In a typical experiment, 10 mg mL^{-1} GO slurry was uniformly spread in a clean plain glass substrate with a dismountable frame with the same size as the aluminum substrate was fixed onto the aluminum substrate surface. Then the aluminum substrate was transferred onto a pre-balanced heating board with temperature in the range of 50–90°C to dry the GO solution. After drying, certain volume of liquid nitrogen was slowly added to the top surface of the film until the film completely separated from the substrate. After that, the peeled off graphene oxide film was fixed between two pieces of polished graphite plates and then transfer into a furnace annealing under 2850°C for 1 hour After that, the graphitized film was pressed under 1000 KN for 6 hours to densify GF by Operator 2008SFX (Dongy Manufacturing Technology Co., Ltd., China).

CFM (1064) and CFB (1069) are purchased from Fibre Glast, USA.

Fabrication of GHP

At first, the CFB was soaked into acetone for 2 days to remove coated polymers. After drying, the CFB was transferred into a plasma chamber at 50 W for 1 minute to oxidize its surface. Then CFB was attached to GF to act as wick structure by a waterproof adhesive (Plexus MA300). A copper spiral was set inside the graphene pipe to hold the pipe during vacuuming. After that, one end of the pipe was sealed by two-component epoxy, while a V-shape plastic pipe was attached on the other end of the graphene pipe. Then the V-shape part was connected to a vacuum system to exhaust the inside air (Figure S11). After that, valve 1 was closed and valve 2 was turned on to fill in a certain amount of ethanol solution. Finally, a heat gun was used to seal the V-shape plastic pipe. The heat pipe was soaked in water to check its tightness during vacuum. The GF and CFM heat pipes are fabricated by the same method.

Measurement of GHP performance

As shown in Figure S7, five thermal couples were attached on the position of 1, 2, 3, 4, and 5. In a typical experiment, an enclosure heating element (70 W, RS component Co. Ltd, Sweden) was used as a heater. The heater was connected to

a DC power supply (Agilent E3612A). GHP was embedded in the middle of the heater with the assistance of an aluminum box. Thermal grease (Loctite TG100, 3 W m^{-1} K^{-1}, China) was used to fill in the gap between GHP and aluminum box. As to the condenser section, a copper blocker was tightly connected with the cooling water system. Temperature of the cooling water keep stable at 17.5°C. Then the other end of the GHP was embedded in the copper block. All of the data was acquired under steady state. SEM images were captured on a Zeiss Supra 60 VP (Germany) with acceleration voltage 15 kV. Specific effective thermal transfer coefficient.

For the evaporator part, the inner temperature of the heat pipe was calculated from the equation as below:

$$T_{hi} = T_{ho} - \frac{Qln\left(\frac{d_o}{d_i}\right)}{2\pi\lambda L_h} \tag{15}$$

For the condenser section, the inner temperature of the heat pipe was calculated from the equation as below:

$$T_{ci} = T_{co} - \frac{Qln\left(\frac{d_o}{d_i}\right)}{2\pi\lambda L_c} \tag{16}$$

where, L_h, $L_c$are the length of the heating part and cooling part; d_o, d_i is the out and inner diameter of heat pipe; λ is the thermal conductivity of the wall materials; Q is the heat flow go through heat pipe; T_{ho}, T_{co} is the temperature on out-wall of the evaporator and condenser section; T_{hi}, T_{ci} is the temperature on heat pipe inner-wall of the evaporator and condenser section.[18]

Specify thermal transfer coefficient (φ) was used to evaluate the performance of heat pipe by the equation as below:

$$\mathrm{g} = \frac{Q}{A\ (T_{hi} - T_{ci})\, m} \tag{17}$$

where A is the cross-section area of heat pipe; m is the weight of the heat pipe.

Simulation

COMSOL Multiphysics was used to simulate the performance of GHP, assuming the same geometrical and physical parameters of the experiments. Heat transfer in wick structure is simplified as conduction with an effective heat transfer coefficient. In the simulation, the effective thermal conductivity of carbon fiber wick structures was calculated by the following expression:

$$k_{eff} = \frac{k_f\left(k_f + k_s - (1-\varphi)\left(k_f - k_s\right)\right)}{k_f + k_s + (1-\varphi)\left(k_f - k_s\right)} \tag{18}$$

where, $k_{eff}$is the effective conductivity; k_f is conductivity of working fluid; k_s is the thermal conductivity of solid carbon; φ is the effective porosity of CFB. Vapor density was assumed as ideal gas as below:

$$\rho_v = \frac{p}{R_s T} \tag{19}$$

where ρ_v is vapor density; R_s is gas constant; T is temperature. Indicating with h the latent heat, with $p_{ref}$the room pressure, and with T_{ref} the evaporation temperature of the mixture, the inlet flow at evaporator side of wick/vapor interface and the outlet flow at condenser side are self-consistent with the saturation pressure given by:

$$p = p_{sat}(T) = p_{ref} \cdot exp\left(\frac{\lambda}{R_s}\left(\frac{1}{T_{ref}} - \frac{1}{T}\right)\right) \tag{20}$$

ACKNOWLEDGMENTS

The authors acknowledge the financial support from the Swedish Board for Strategic Research (SSF) with the contract No: SE13-0061 and GMT14-0045, from the Swedish Board for Innovation (Vinnova) under the Siografen program, from Formas with the contract No: FR-2017/0009 and from STINT for the double degree PhD collaboration program with the contract No: DD2016-6502, from the Swedish National Science Foundation with the contract No: 621-2007-4660 as well as from the Production Area of Advance at Chalmers University of Technology, Sweden. S.C. and J.L. also acknowledge the financial support by the Key R&D Development Program from the Ministry of Science and Technology of China with contract No: 2017YFB0406000 as well as from the National Natural Science Foundation of China (No: 51872182). H.L thanks for the financial support from Shanghai International Collaboration research project (No: 19520713900) and State Key Laboratory of Molecular Engineering of Polymers at Fudan University.

CONFLICT OF INTEREST

The authors declare that they have no competing interests.

REFERENCES

1. a) S.-C. Lin, K. Banerjee, *IEEE Trans. Electron Devices*. **2007**, *55*, 245; b) R. S. Gaugler (General Motors), Am., 1944469649, **1944**.
2. S. Naghibi, F. Kargar, D. Wright, C. Y. T. Huang, A. Mohammadzadeh, Z. Barani, R. Salgado, A. A. Balandin, *Adv. Electron. Mater.* **2020**, *6*, 1901303.
3. a) K. Xu, Y. Lu, T. Yamaguchi, T. Arie, S. Akita, K. Takei, *ACS Nano*. **2019**, *13*, 14348; b) G. Zhang, S. Jiang, W. Yao, C. Liu, *ACS Appl. Mater. Interfaces.* **2016**, *8*, 31202.
4. L. Trefethen, *GE Tech. Info.*, **1962**, *615*, 114.
5. B. Zohuri, *Heat Pipe Design and Technology*, Boca Raton, FL: CRC Press. **2011**, 33487.

6. B. Zohuri, *Heat Pipe Design and Technology: Modern Applications for Practical Thermal Management*, Springer, New York **2016**.
7. X. Yang, Y. Yan, D. Mullen, *Appl. Therm. Eng.* **2012**, *33*, 1.
8. B. Rassamakin, S. Khairnasov, V. Zaripov, A. Rassamakin, O. Alforova, *Solar Energy*. **2013**, *94*, 145.
9. Z. Zuo, A. Faghri, *Int. J. Heat Mass Transfer.* **1998**, *41*, 1473.
10. F. Czerwinski, *Magnesium Alloys: Corrosion and Surface Treatments, BoD–Books on Demand*, IntechOpen Limited, London **2011**.
11. N. Narendra Babu, H. C. Kamath, *Materials Today Proc.*, *1469*, 2.
12. G. Xin, T. Yao, H. Sun, S. M. Scott, D. Shao, G. Wang, J. Lian, *Science*. **2015**, *349*, 1083.
13. Z. Xiong, X. Wang, K. H. K. Lee, X. Zhan, Y. Chen, J. Tang, *ACS Appl. Mater. Interfaces.* **2018**, *10*, 9211.
14. a) F. Pulizzi, O. Bubnova, S. Milana, D. Schilter, D. Abergel, A. Moscatelli, *Nat. Nanotechnol.* **2019**, *14*, 914; b) Q. Cai, D. Scullion, W. Gan, A. Falin, S. Zhang, K. Watanabe, T. Taniguchi, Y. Chen, E. J. Santos, L. H. Li, *Sci. Adv.* **2019**, *5*, 129; c) P. Goli, H. Ning, X. Li, C. Y. Lu, K. S. Novoselov, A. A. Balandin, *Nano Lett*. **2014**, *14*, 1497; d) X. Meng, H. Pan, C. Zhu, Z. Chen, T. Lu, D. Xu, Y. Li, S. Zhu, *ACS Appl. Mater. Interfaces.* **2018**, *10*, 22611; e) Y. Xu, Z. Li, W. Duan, *Small*. **2014**, *10*, 2182.
15. T. M. Tritt, *Thermal conductivity: theory, properties, and applications*, Springer Science & Business Media, Berlin **2005**.
16. N. Wang, M. K. Samani, H. Li, L. Dong, Z. Zhang, P. Su, S. Chen, J. Chen, S. Huang, G. Yuan, *Small*. **2018**, *14*, 1801346.
17. L. Peng, Z. Xu, Z. Liu, Y. Guo, P. Li, C. Gao, *Adv. Mater.* **2017**, *29*, 1700589.
18. a) V. S. Sastri, *Green corrosion inhibitors: theory and practice*, John Wiley & Sons, **2012**; b) S. Böhm, *Nat. Nanotechnol*. **2014**, *9*, 741.
19. a) J. H. Seol, I. Jo, A. L. Moore, L. Lindsay, Z. H. Aitken, M. T. Pettes, X. Li, Z. Yao, R. Huang, D. Broido, *Science*. **2010**, *328*, 213; b) G. Yao, T. Duan, E. Chi, P. Guo, Y. Li, Z. Wang, *R. Soc. Open Sci*. **2019**, *6*, 181866.
20. S. Chi, *Heat Pipe Theory and Practice*, Hemisphere Pub. Corp, Washington, DC **1976**.
21. a) G. Vazquez, E. Alvarez, J. M. Navaza, *J. Chem. Eng. Data.* **1995**, *40*, 611; b) I. Lokteva, M. Koof, M. Walther, G. Grübel, F. Lehmkühler, *Small*. **2019**, *15*, 1900438.
22. S. Wang, W. Zhang, X. Zhang, J. Chen, *Int. J. Heat Mass Transfer.* **2011**, *54*, 1002.
23. A. Vetere, *Ind. Eng. Chem. Res.* **1991**, *30*, 2487.
24. R. P. Tye, *Thermal Conductivity*, Academic Press, Cambridge, MA, **1969**.
25. W. M. Rohsenow, J. P. Hartnett, Y. I. Cho, *Handbook of Heat Transfer*, Vol. *3*, McGraw-Hill New York **1998**, Ch. 3.
26. Y. Liu, N. Wang, L. Ye, A. Zehri, A. Nylander, A. Nkansah, H. Lu, J. Liu, Thermally Conductive and Electrically Insulating PVP/Boron Nitride Composite Films for Heat Spreader *Nordpac* **2019**.

SUPPORTING INFORMATION

Additional supporting information may be found online in the Supporting Information section at the end of the article.

How to cite this article: Liu Y, Chen S, Fu Y, et al. A lightweight and high thermal performance graphene heat pipe. *Nano Select*. 2020;1-9. https://doi.org/10.1002/nano.202000195

coatings

MDPI

Article

Surface Modification of Graphene for Use as a Structural Fortifier in Water-Borne Epoxy Coatings

Ya Liu [1,2], Chao Xia [3], Abdelhafid Zehri [1], Lilei Ye [4], Nan Wang [4], Boris Zhmud [3], Hongbin Lu [2,*] and Johan Liu [1,5,*]

1 Electronics Materials and Systems Laboratory (EMSL), Department of Microtechnology and Nanoscience (MC2), Chalmers University of Technology, Kemivägen 9, SE-412 96 Göteborg, Sweden; yaliu@chalmers.se (Y.L.); hafid@chalmers.se (A.Z.)
2 State Key Laboratory of Molecular Engineering of Polymers, Department of Macromolecular Science, Collaborative Innovation Center of Polymers and Polymer Composites, Fudan University, 2005 Songhu Road, Shanghai 200433, China
3 Applied Nano Surfaces AB, Knivstagatan 12, SE 753 23 Uppsala, Sweden; chao.xia@appliednanosurfaces.com (C.X.); boris.zhmud@appliednanosurfaces.com (B.Z.)
4 SHT Smart High Technology AB, Kemivägen 6, SE 412 58 Gothenburg, Sweden; lilei.ye@sht-tek.com (L.Y.); Nan.wang@sht-tek.com (N.W.)
5 SMIT Center, School of Mechanical Engineering and Automation, Shanghai University, No. 20, Chengzhong Road, Shanghai 201800, China
* Correspondence: hongbinlu@fudan.edu.cn (H.L.); johan.liu@chalmers.se (J.L.)

Received: 21 September 2019; Accepted: 11 November 2019; Published: 13 November 2019

Abstract: Graphene, the typical two-dimensional sp^2 hybridized carbon allotrope, is widely used as a filler for improving the mechanical performance of polymers. However, its superhydrophobic surface makes it a big challenge to obtain stable graphene dispersions, especially in water-borne systems. On the contrary, graphene oxide (GO) shows excellent dispersibility in water, but strong oxidants and acids destroy its structure and degrade its mechanical properties. This largely limits its application in water-borne coatings. In this work, graphene from mechanical exfoliation was surface modified by p-aminophenol derived diazonium salt to achieve a homogenous dispersion. Moreover, the hydroxyl groups in p-aminophenol are able to combine with epoxy resins during the curing process to improve mechanical performance of the final coatings. The result shows that functionalized graphene shows a lower coefficient of friction and better abrasion resistance compared to GO.

Keywords: functionalized graphene; water-borne epoxy; tribological properties

1. Introduction

Epoxy resins (ER) are an important engineering material featuring outstanding corrosion resistance, high mechanical strength, and strong adhesion to heterogeneous substrates [1,2]. ERs can be used as adhesives, protection coatings, composites, laminating materials, etc. In recent years, a tremendous interest has been raised in scientific and industrial communities to apply epoxy composites as sliding components, aiming to increase the product service life and performance.

Sliding, rolling, or rotating contacts ubiquitous in a variety of manmade systems all generate friction. If the friction is not efficiently controlled, it often leads to high wear, shorter service life, and reduced reliability [3]. In this regard, the deposition of low-friction coatings, such as high-strength epoxy coatings, has become an effective strategy for extending the service life of coated parts. Considering the environmental issues and the improvement in tribological properties, water-borne epoxy coatings are a promising option [4]. Nowadays, for improving wear-resistance of water-borne coatings, an effective

and widely accepted method is to use nano-fillers, such as SiO_2 [5], nanodiamonds [6], carbon nanotubes [7], graphene [8], graphene oxide, [9] etc.

As a typical 2D material, graphene offers unique friction and wear properties that are not usually observed in conventional materials [10]. Besides its exceptional thermal, electrical, optical, and mechanical properties, graphene can also serve as a solid lubricant. The high chemical inertness and excellent shear-slide capability make graphene a promising alternative for constructing wear-resisting coating layers [11]. Ultrathin graphene layers, even in multilayer configurations, can be applied to nano- or microsystems such as microelectromechanical systems (MEMS) and nanoelectromechanical systems (NEMS) with oscillating, rotating, and sliding contacts to reduce friction and wear [12].

When used in water-borne coating systems, the primary challenges is to produce stable homogenous graphene dispersions. To address this issue, surface modifications, involving covalent and noncovalent hydroxyl and carboxyl functionalization, have been performed on the surface of graphene through the edges or defect sites to improve graphene's dispersibility [3,13]. Besides that, epoxy groups are able to react with the functional groups grafted onto graphene, including hydroxyl, amino, etc., [14] to build a stable crosslinked network between functional graphene and an epoxy binder [15]. Such crosslinking is favorable for the mechanical performance of graphene-filled composites.

In this work, a diazonium salt with hydroxyphenyl groups was used to modify the surface of graphene. The hydroxyl groups and benzene rings in the hydroxyphenyl moiety help adjust the surface hydrophilicity of graphene: The functionalized graphene can be readily dispersed in water to form a stable dispersion. On the other hand, the hydroxyl groups are able to further react with the epoxy groups to build a strong bonding between the graphene flakes and the epoxy binder, significantly improving the tribological properties of the epoxy coating. Compared with graphene oxide (GO), the functionalized graphene (FG) sample exhibits a lower coefficient of friction and higher abrasion resistance.

2. Materials and Methods

2.1. Preparation of Graphene (G)

Graphene powder was purchased from Carbonene (Product XTG-P-0762, Deyang, China). GO was purchased from Applied Graphene Materials (Product A-GNP10, Redcar, England). The p-aminophenol and sodium hydroxide were purchased from Sigma-Aldrich (Saint Louis, MO, USA) with purity <98%. The 37% hydrochloric acid and sodium nitrite (for analysis) were purchased from Sigma-Aldrich (Saint Louis, MO, USA). All chemicals were used without additional purification.

2.2. Preparation of Diazonium Salt (DS)

By analogy with the Sandmeyer reaction, 2 g *p*-aminophenol was added to 100 mL 5% sodium hydroxide solution at 50 °C and stirred for 30 min. Then 20 mL 0.1 M sodium nitrite solution was added to the dispersion. Subsequently, the dispersion was transferred to an ice-water bath with a temperature of about 0–4 °C. In the next step, 15 mL 1 M hydrochloric acid was added into the dispersion and stirred for 30 min. Afterwards, centrifugation was used to isolate the product. The yield of *p*-hydroxybenzene diazonium chloride was 80%. Note that due to its tendency to self-decomposition, the diazonium salt should be prepared immediately before the surface modification.

2.3. Preparation of Functionalized Graphene

First, 0.5 g graphene powder was dispersed into 100 mL distilled water in an ultrasonic bath. Then pH value was adjusted to 10 by adding the sodium hydroxide solution. After that, 2 g 5 wt. % diazonium salt solution was gradually added to the graphene dispersion under mechanical stirring for 8 h and continuous cooling using the ice-water bath. In the end, centrifugation was used to remove excess chemicals and impurities from the solution. The yield of modified graphene was 72% based on graphene weight.

2.3.1. Preparation of Water-Borne Coatings Containing Functionalized Graphene

Water-borne epoxy coatings were formulated by Applied Nano Surfaces Sweden AB (Uppsala, Sweden). Typically, 1 g functional graphene (FG) powder was dispersed in 30 mL distilled water under ultrasonification. Subsequently, the FG dispersion was added to the commercial Tricolit TSC coating base with mechanical stirring for 30 min. Next, the obtained coating slurry was sprayed onto steel plates with a spray gun to achieve a dry film with a thickness between 15 to 25 µm. The sprayed plates were dried at room temperature for 30 min, and then transferred to a furnace with a temperature profile of 50 °C for 30 min, 90 °C for 1 h, 120 °C for 1 h, and 250 °C for 0.5 h for final curing.

2.3.2. Characterization

Fourier transform infrared spectroscopy (FT-IR, PerkinElmer, UATR Two, 4000–500 cm^{-1}, Waltham, MA, USA) and X-ray photoelectron spectroscopy (XPS, PHI 5000 VersaProbe III, monochromatic Al *Kα* X-ray, Kanagawa, Japan) were employed to identify the chemical structures of graphene (G) and functionalized graphene (FG). Thermalgravimetric analysis (TGA, PerkinElmer, Pyris 1, Waltham, MA, USA) was applied to determine the mass ratio of functional groups in FG from 60 to 600 °C under nitrogen atmosphere. Transmission electron microscopy (TEM, FEI Tecnai, T20, 300 KV, Hillsboro, OR, USA) was used to observe the morphologies of G and FG. The morphology of the epoxy coating film was analyzed by scanning electron microscopy (SEM, Zeiss Supra 60 VP, Oberkochen, Germany) with acceleration voltage 6–12 KV. Raman spectra were obtained with LabRAM HR-800 (Horiba, Kyoto, Japan) with 514 nm laser and ×100 objective.

2.3.3. Tribological Tests

Friction tests were performed using a reciprocating ball-on-disc test rig (Figure 1). The 100Cr6 steel balls with Ø11 mm and Ra 0.065 µm were used during the tests. Dry abrasion tests were conducted for 30 min using a constant velocity of 200 rpm and stroke length of 10 mm under dry condition, with a load of 4 N. Lubricated friction tests were conducted using velocity ramps of 0 to 100 to 0 rpm (10 circles), stroke length of 10 mm, and a load of 3 N. Castrol Edge 0W-40 motor oil (Castrol, Germany) was used as the lubricant. Wear tests were carried out in a customized rig (see Figure 2c) resembling the industry-standard Taber abraser (ASTM D-4060). The tests were used for the relative ranking of wear resistance (one coating vs. another). A nylon ring was rotating with a speed of 130 rpm and a load of 1 N against the coating on the stainless-steel substrate. The time required for total wear out of the coating was recorded: The longer coating breakdown time, the better the abrasion resistance was.

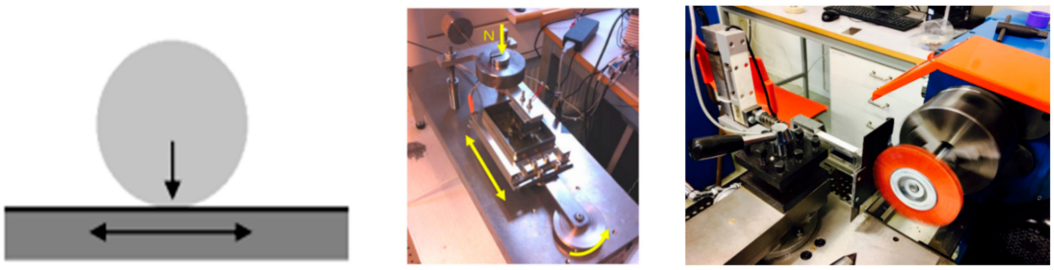

Figure 1. (**a**) Ball-on-flat friction and wear test setup, (**b**) tribological test rig, (**c**) abrasion test rig.

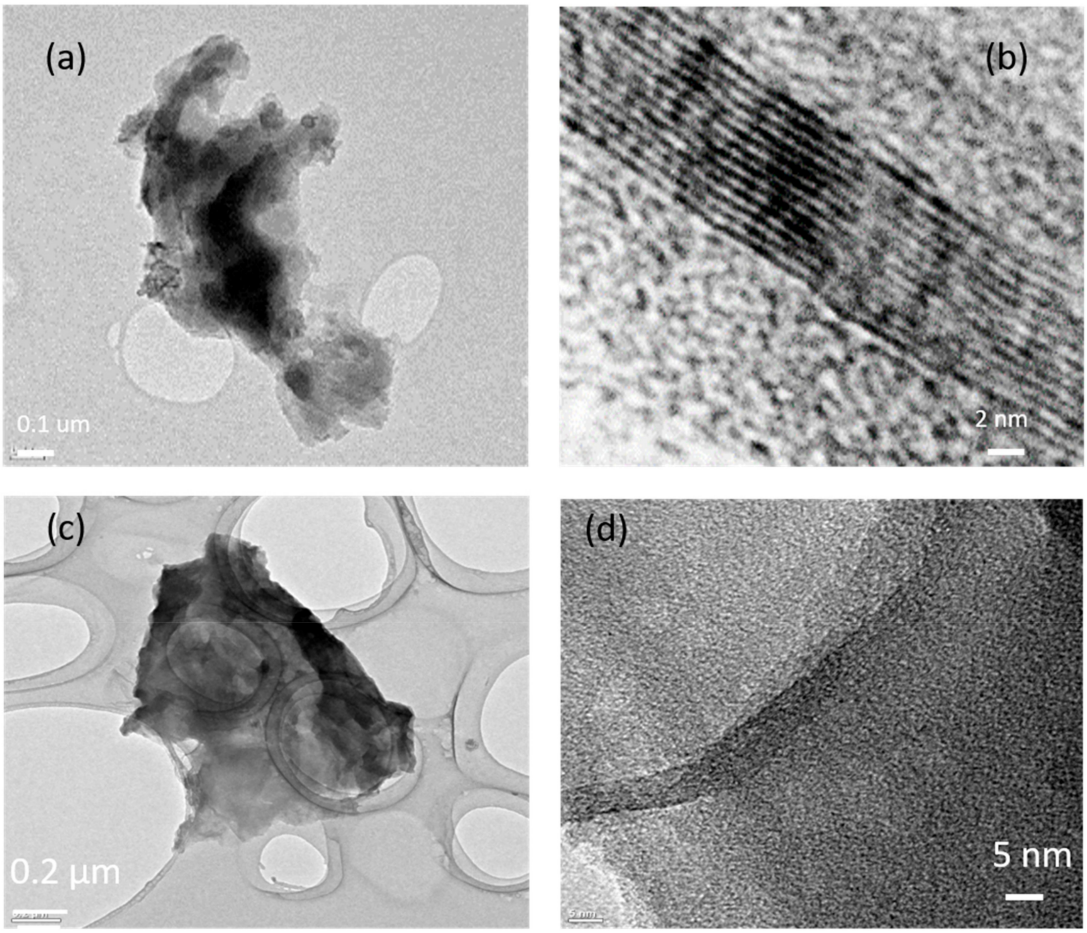

Figure 2. TEM images of graphene (G) and functionalized graphene (FG). (**a**) Low-resolution and (**b**) high-resolution TEM images of G; (**c**) low-resolution and (**d**) high-resolution TEM images of FG.

3. Results and Discussion

3.1. Characterization of Functional Graphene

TEM was used to observe the influence of functionalization on graphene morphology. As shown in Figure 2, the pristine graphene sheets consist of approximately 10 graphene layers (see Figure 2b). After functionalization, a new grafted layer was observed on the surface of graphene (see Figure 2d). In the high-resolution TEM image of FG, its crystal structure was not as sharp as graphene. This may be due to the functional groups attached to the graphene surface.

FTIR spectroscopy was applied to determine the functional groups in pristine graphene and FG. As shown in Figure 3a, a small peak at 1201 cm^{-1} corresponding to C–O stretching vibrations appears at the FTIR spectrum of pristine graphene, indicating the presence of a small amount of oxidized sites. A peak at 2120 cm^{-1} corresponds to the N≡N stretching vibrations in aryl diazonium salts. After functionalization with the prepared DS, the peak at 2120 cm^{-1} disappears. Other indicative peaks are at 1191 cm^{-1} due to C–O stretching, and at 1730 cm^{-1} due to C=O stretching. Further, the peak at 1061 cm^{-1} corresponds to the C–O stretching vibrations in the phenol group. Finally, the broad peak around 1564 cm^{-1} can be attributed to the C=C stretching vibrations in the aromatic rings.

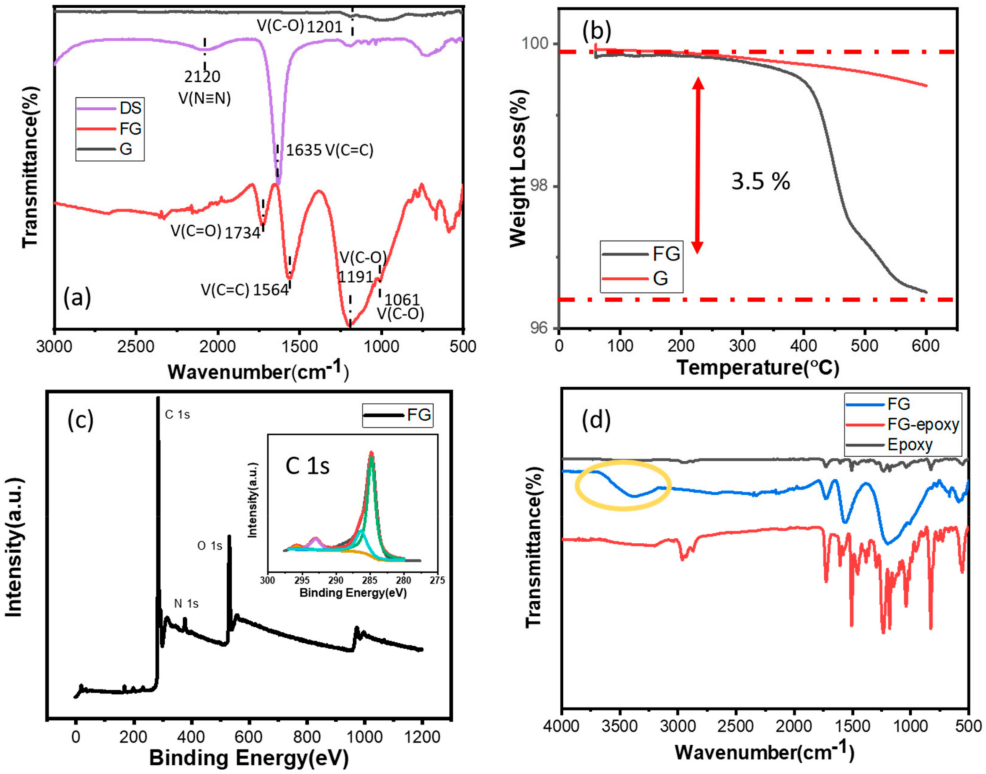

Figure 3. (**a**) The infrared spectrum of modified graphene platelets (FG), prepared diazonium salt (DS), and pristine graphene platelet (G); (**b**) TGA data of FG and G; (**c**) XPS spectrum of FG (the inset is the C 1*s* fitting curves); (**d**) infrared spectrum of epoxy, FG, and FG enhanced epoxy coatings.

One possible grafting mechanism is represented in Figure 4 and presumes the presence of oxidation sites/defects on graphene sheets. First, a heteropolar bond between carboxyl and diazonium moieties is formed due to ion exchange, and then the unstable diazonium carboxylate releases nitrogen. This mechanism is similar to the well-known reaction of methylation of carboxylic acids with diazomethane [16].

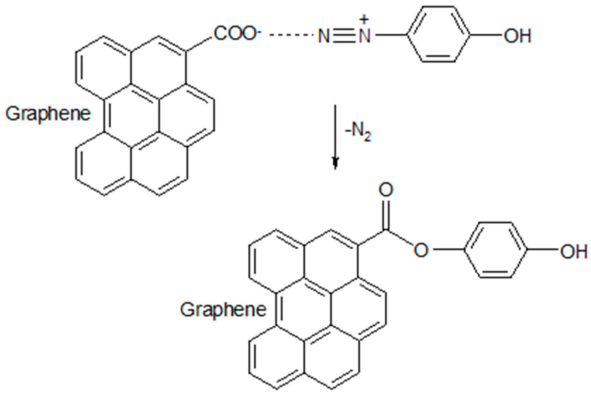

Figure 4. A possible mechanism of graphene functionalization using a diazonium salt.

One may question if the oxidized sites on graphene sheets can be directly reacted with epoxy groups. They cannot since, post-exfoliation, these sites appear to be in a nonreactive ester form, and they only get activated during the Sandmeyer reaction due to saponification with NaOH.

The above findings are further supported by the TGA analysis of G and FG (Figure 3b). TGA curves of unmodified graphene show a weight loss from 50 to 600 °C, with a sharp weight decrease starting

around 200 °C corresponding to the graft elimination from FG. TGA results show 3.5 wt. % of phenolic groups are grafted on the surface of graphene sheets.

XPS measurements give more detail regarding the bonding between graphene and the aminophenol moiety. As shown in Figure 3c, except for carbon, the peaks of N and O can be observed at the same time. Furthermore, the C 1*s* peak can be curve-fitted into three peaks, which are corresponding to C–C (284.8 eV), π–π satellite (293 eV), and C–O (286 eV), respectively, as shown in Figure 3c inset. All this gives solid evidence of successful surface modification of graphene with diazonium salt.

As shown in Figure 3d, the FTIR peak at around 3500 cm^{-1} corresponding to the hydroxyl groups on FG is no longer present in the spectrum of the FG-epoxy coating, indicating the successful combination of the hydroxyl and epoxy groups. This suggests that FG acts as a reactive cross-linker as intended [17].

3.2. Tribological Performance of FG Enhanced Epoxy Coating

To investigate the influence of the FG particle size on the rheological properties (sprayability and film levelling) of the coating, three batches of FG material were prepared by mechanical grinding. According to SEM analysis (see Figure 5), the average particle size of FG1, FG2, and FG3 was 3–6 um, 1–3 um, and 0.5–1 um.

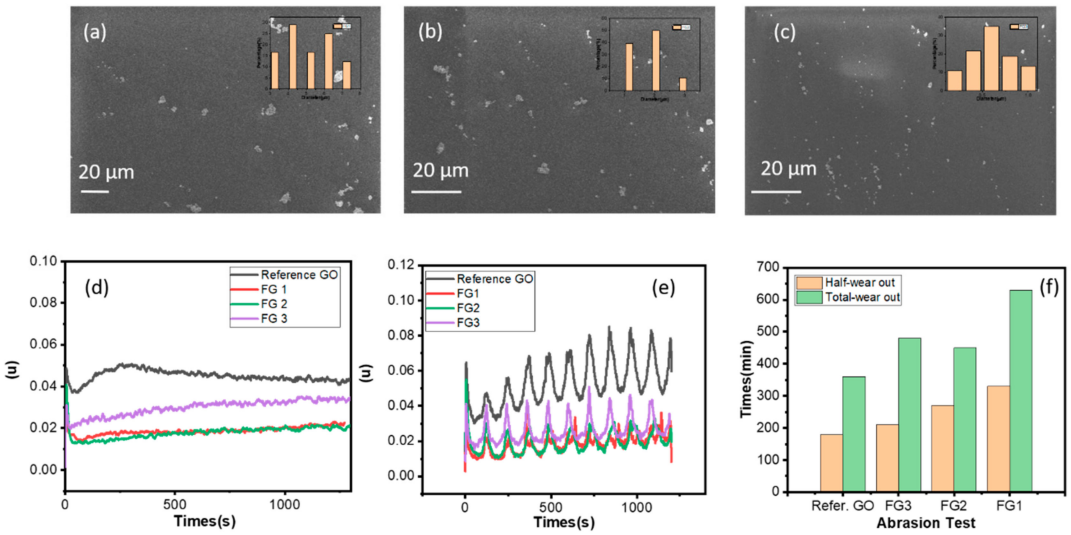

Figure 5. (**a**–**c**) SEM images of FG1, FG2, and FG3 (insets are size distributions); (**d**) abrasion tests on stainless-steel plates (4 N, 200 rpm, 30 min, dry contact) of reference GO, FG1, FG2, and FG3; (**e**) friction tests on different coated stainless-steel plates (4 N, 200 rpm, 30 min, lubricated contact) of reference GO, FG1, FG2, and FG3; (**f**) wear data for the reference GO and FG1, FG2, and FG3.

As shown in Figure S1, the structure of reference GO is similar with pristine G. The coefficient of friction (COF) of graphene-free epoxy coating against steel in a dry contact is 0.75, as shown in Figure S2. The same coating using GO filler gives the COF around 0.05, some 15 times less! FG1, FG2, and FG3 show further decrease of COF compared to GO. FG1 and FG2 samples have the lowest COFs, close to 0.02, while FG3 has a slightly higher COF ~0.03.

In a lubricated contact, all the FG samples have lower COF than that of the reference GO sample, see Figure 5e. COF of FG3 is somewhat higher than that of FG1 and FG2.

Relative lifetimes (total wear out) of wear tests are displayed in Figure 5f. FG1 sample has the longest relative lifetime (630 min) which is almost 1.5 times longer than the reference GO coating (360 min).

In summary, both in the friction and wear tests, FG modified coatings demonstrated improved tribological properties. Overall, tribological performance of FG sample is FG1 > FG2 > FG3. This indicates that large size graphene sheets exhibit superior self-lubricating capacity.

3.3. Coating Morphology

SEM was used to analyze the coating surface morphology. As shown in Figure 6c,d, the FG flakes are homogeneously dispersed in the epoxy matrix, the average particle size being 1–2 um. Compared with the FG-free epoxy coating, the FG modified coating shows a smoother surface, while the FG-free coating looks more stretched. This indicates the enhanced abrasion resistance of FG modified coatings.

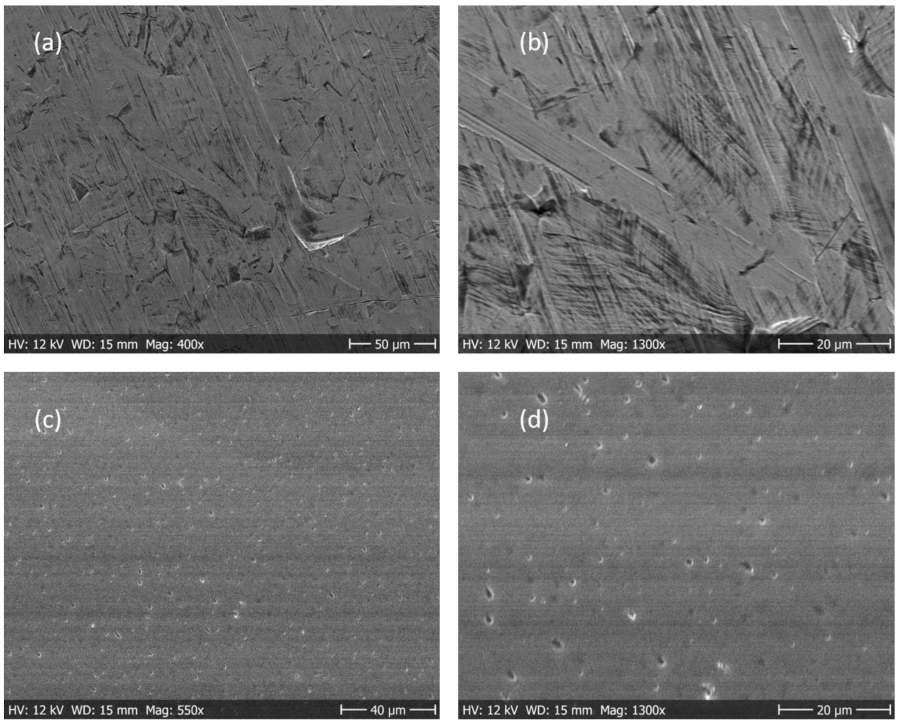

Figure 6. (**a**) SEM image of epoxy coating; (**b**) high-resolution SEM image of epoxy coating; (**c**) SEM image of epoxy coating with FG; (**d**) high-resolution SEM image of epoxy coating with FG.

4. Conclusions

Mechanically exfoliated graphene was surface modified using an aryl diazonium salt in order to improve its dispersibility in water. Such functionalized graphene was successfully used as reactive filler in a water-borne epoxy coating formulation. Coatings modified by functionalized graphene demonstrated improved tribological properties in terms of friction and wear. This work paves the way for future applications of functionalized graphene for mechanical enhancement of polymer-bonded coatings.

Supplementary Materials: The following are available online at http://www.mdpi.com/2079-6412/9/11/754/s1: Figure S1, (a) SEM images of the pristine graphene (the inset shows its size distribution), (b) SEM image of the reference GO (the inset shows its size distribution), (c) the infrared spectrum of GO, (d) raman spectrum of GO; Figure S2, Abrasion test on stainless-steel plates of pristine epoxy binder (4N, 200rpm, 30min, dry contact).

Author Contributions: Conceptualization, Y.L., L.Y., J.L., N.W., C.X. and B.Z.; Methodology, Y.L., C.X. and B.Z.; Software, Y.L.; Validation, Y.L., C.X. and L.Y.; Formal analysis, Y.L. and C.X.; Investigation, Y.L., L.Y., J.L., C.X. and B.Z.; Resources, J.L., L.Y., B.Z. and H.L.; Data curation, Y.L.; Writing—original draft preparation, Y.L., C.X. and A.Z.; Writing—review and editing, J.L., B.Z. and H.L.; Visualization, J.L. and B.Z.; Supervision, J.L., L.Y., B.Z. and H.L.; Project administration, L.Y.; Funding acquisition, J.L., L.Y., B.Z. and H.L.

Funding: This research was funded by the Swedish Board for Innovation (Vinnova) under the Sioagrafen program, by the Swedish Board for Strategic Research (SSF) with the contract No: SE13-0061 and GMT14-0045, by Formas with the contract No: FR-2017/0009 and by STINT for the double degree PhD collaboration program with the contract No: DD2016-6502, by the Swedish National Science Foundation with the contract No: 621-2007-4660 as well as by the Production Area of Advance at Chalmers University of Technology, Sweden. J.L. also acknowledges the financial support by the Key R&D Development Program from the Ministry of Science and Technology of China with the contract No: 2017YFB0406000 as well as from the National Natural Science Foundation of China (No: 51872182). H.L. thanks financial support from Shanghai International Collaboration research project (19520713900) and State Key Laboratory of Molecular Engineering of Polymers in Fudan University.

Conflicts of Interest: The authors declare no conflict of interest.

References

1. Cui, M.J.; Ren, S.M.; Zhao, H.C.; Xue, Q.J.; Wang, L.P. Polydopamine coated graphene oxide for anticorrosive reinforcement of water-borne epoxy coating. *Chem. Eng. J.* **2018**, *335*, 255–266. [CrossRef]
2. Guo, Q.B.; Lau, K.T.; Zheng, B.F.; Rong, M.Z.; Zhang, M.Q. Imparting Ultra-Low Friction and Wear Rate to Epoxy by the Incorporation of Microencapsulated Lubricant? *Macromol. Mater. Eng.* **2009**, *294*, 20–24. [CrossRef]
3. Berman, D.; Erdemir, A.; Sumant, A.V. Graphene: A new emerging lubricant. *Mater. Today* **2014**, *17*, 31–42. [CrossRef]
4. Li, Y.L.; Wang, S.J.; Wang, Q. Enhancement of tribological properties of polymer composites reinforced by functionalized graphene. *Compos. Part B Eng.* **2017**, *120*, 83–91. [CrossRef]
5. Lv, T.; Huang, S.Q.; Hu, X.D.; Ma, Y.L.; Xu, X.F. Tribological and machining characteristics of a minimum quantity lubrication (MQL) technology using GO/SiO2 hybrid nanoparticle water-based lubricants as cutting fluids. *Int. J. Adv. Manuf. Technol.* **2018**, *96*, 2931–2942. [CrossRef]
6. Wu, P.; Chen, X.C.; Zhang, C.H.; Luo, J.B. Synergistic tribological behaviors of graphene oxide and nanodiamond as lubricating additives in water. *Tribol. Int.* **2019**, *132*, 177–184. [CrossRef]
7. Li, X.; Chen, B.B.; Jia, Y.H.; Li, X.F.; Yang, J.; Li, C.S.; Yan, F.Y. Enhanced tribological properties of epoxy-based lubricating coatings using carbon nanotubes-ZnS hybrid. *Surf. Coat. Technol.* **2018**, *344*, 154–162. [CrossRef]
8. Li, H.Y.; Shi, N.Q.; Ji, J.; Wang, H.Y. Preparation of microcapsules containing double-component lubricant and self-lubricating performance of polymer composites. *Mater. Res. Express* **2018**, *5*, 8. [CrossRef]
9. Bandeira, P.; Monteiro, J.; Baptista, A.M.; Magalhaes, F.D. Influence of oxidized graphene nanoplatelets and DMIM NTf2 ionic liquid on the tribological performance of an epoxy-PTFE coating. *Tribol. Int.* **2016**, *97*, 478–489. [CrossRef]
10. Papageorgiou, D.G.; Kinloch, I.A.; Young, R.J. Mechanical properties of graphene and graphene-based nanocomposites. *Prog. Mater. Sci.* **2017**, *90*, 75–127. [CrossRef]
11. Qi, Y.Z.; Liu, J.; Zhang, J.; Dong, Y.L.; Li, Q.Y. Wear Resistance Limited by Step Edge Failure: The Rise and Fall of Graphene as an Atomically Thin Lubricating Material. *ACS Appl. Mater. Interfaces* **2017**, *9*, 1099–1106. [CrossRef] [PubMed]
12. Tambe, N.S.; Bhushan, B. Scale dependence of micro/nano-friction and adhesion of MEMS/NEMS materials, coatings and lubricants. *Nanotechnology* **2004**, *15*, 1561–1570. [CrossRef]
13. Kuila, T.; Bose, S.; Mishra, A.K.; Khanra, P.; Kim, N.H.; Lee, J.H. Chemical functionalization of graphene and its applications. *Prog. Mater. Sci.* **2012**, *57*, 1061–1105. [CrossRef]
14. Song, J.; Dai, Z.; Li, J.; Zhao, H.; Wang, L. Silane coupling agent modified BN–OH as reinforcing filler for epoxy nanocomposite. *High Perform. Polym.* **2019**, *31*, 116–123. [CrossRef]
15. Rasheed, A.K.; Khalid, M.; Rashmi, W.; Gupta, T.; Chan, A. Graphene based nanofluids and nanolubricants-Review of recent developments. *Renew. Sustain. Energy Rev.* **2016**, *63*, 346–362. [CrossRef]
16. Presser, A.; Hüfner, A. Trimethylsilyldiazomethane–a mild and efficient reagent for the methylation of carboxylic acids and alcohols in natural products. *Monatshefte Für Chem. Chem. Mon.* **2004**, *135*, 1015–1022.
17. Li, Z.; Young, R.J.; Wang, R.; Yang, F.; Hao, L.; Jiao, W.; Liu, W. The role of functional groups on graphene oxide in epoxy nanocomposites. *Polymer* **2013**, *54*, 5821–5829. [CrossRef]

A Novel Graphene Quantum Dot-Based mRNA Delivery Platform

Ya Liu[+],[a, b] Changhong Zhao[+],[a, f] Alan Sabirsh[+],[c] Lilei Ye,[d] Xiaoqiu Wu,*[c] Hongbin Lu,*[b] and Johan Liu*[a, e]

Abstract: During the last decades, there has been growing interest in using therapeutic messager RNA (mRNA) together with drug delivery systems. Naked, unformulated mRNA is, however, unable to cross the cell membrane and is susceptible to degradation. Here we use graphene quantum dots (GQDs) functionalized with polyethyleneimine (PEI) as a novel mRNA delivery system. Our results show that these modified GQDs can be used to deliver intact and functional mRNA to Huh-7 hepatocarcinoma cells at low doses and, that the GQDs are not toxic, although cellular toxicity is a problem for these first-generation modified particles. Functionalized GQDs represent a potentially interesting delivery system that is easy to manufacture, stable and effective.

1. Introduction

In recent years, graphene quantum dots (GQDs) have emerged as an attractive platform for bio-applications, involving biosensing, biomedical imaging and drug delivery. This is because various desirable attributes from GQDs: dispersibility, good biocompatibility, large surface area, colloidal stability, and tunable surface structure. Moreover, GQDs are able to respond to physical stimuli, such as magnetic fields, ultrasound[3] and light. These unique responding features allow the accurate control of drug release.[1a] To date, some exciting examples, include a graphene oxide/carbon/mesoporous silica photo-responsive drug delivery platform, an electrical fields activated graphene based microcapsule platform, and graphene based photothermal therapy[7] have been reported. Notably, GQDs are able to selectively interact with DNA or RNA and protect them from enzymatic degradation,[1b] suggests the possibility of integrating GQDs with DNA or RNA-based therapeutics.

Messenger RNA (mRNA)-based therapeutics are a promising class of drugs with a range of advantages, including reduced genotoxicity, increased control of product (protein) formation, no need for nuclear localization or transcription and better compatibility with biological systems. Structurally, mRNA is a single-strand poly nucleotide that in cells is transcribed from a DNA template prior to translation into protein. mRNA molecules are, however, large, carrying a net charge and unstable in most biological fluids. These poor cell penetration and instability characteristics limit their use as therapeutic agents. To cope with this issue, composite particles made from mRNA and GQDs would ameliorate many of these problems due to the surface properties and colloidal stability of GQDs.[1b]

Unmodified GQDs will not, however, bind mRNA very well so GQDs need to be functionalized. In this regard, Polyethyleneimine (PEI) possess a high cationic charge density and allows the complexation of RNA and DNA. Besides, PEI functionalized carbon nanotubes (CNTs) have been designed successfully for nucleic acid delivery. Given the similar surface properties of GQDs and CNTs, we hypothesized that PEI would be a good starting point for exploring the utility of GQDs as an mRNA delivery system.

In this work, GQDs were prepared from citric acid, and surface zeta potential of GQDs were tailored by PEI. The GQDs/mRNA complexes were prepared by combining the functional-

[a] Y. Liu,[+] Prof. C. Zhao,[+] Prof. J. Liu
Department of Microtechnology and Nanoscience
Chalmers University of Technology
9 Kemivägen, Gothenborg
412 96 (Sweden)
E-mail: johan.liu@chalmers.se
[b] Y. Liu,[+] Prof. H. Lu
Department of Macromolecular Science
Collaborative Innovation Center of Polymers and Polymer Composites
Fudan University
2005 Songhu Road Shanghai 200433 (China)
E-mail: hongbinlu@fudan.edu.cn
[c] Dr. A. Sabirsh,[+] Dr. X. Wu
Advanced Drug Delivery, Pharmaceutical Sciences, R&D
AstraZeneca, Gothenburg, Sweden
1 Pepparedsleden, Mölndal
431 50 (Sweden)
E-mail: Xiaoqiu.Wu@astrazeneca.com
[d] Dr. L. Ye
SHT Smart High Tech AB
6 Kemivägen
Gothenburg 412 58 (Sweden)
[e] Prof. J. Liu
SMIT Center, School of Mechanical Engineering and Automation
Shanghai University
20 Chengzhong Road
Shanghai 201800 (China)
E-mail: johanliu@shu.edu.cn
[f] Prof. C. Zhao[+]
School of Life Science and Technology
Xinxiang Medical University
601 Jinshui Road,
Xinxiang Henan 453003 (China)
[+] These authors contributed equally to this work.

Supporting information for this article is available on the WWW under https://doi.org/10.1002/open.202000200

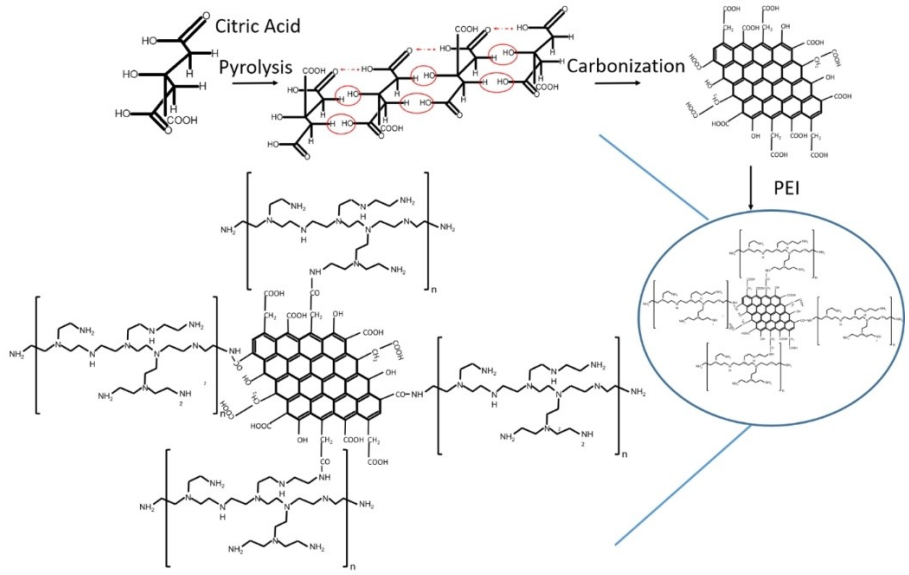

Figure 1. A schematic overview of the FGQDs synthesis. The red ring and arrow show the carbonization reaction sites.

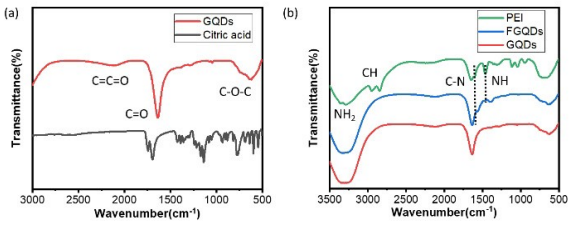

Figure 2. (a) FTIR spectrums of GQDs and citric acid; (b) FTIR spectrums of PEI, FGQDs and GQDs.

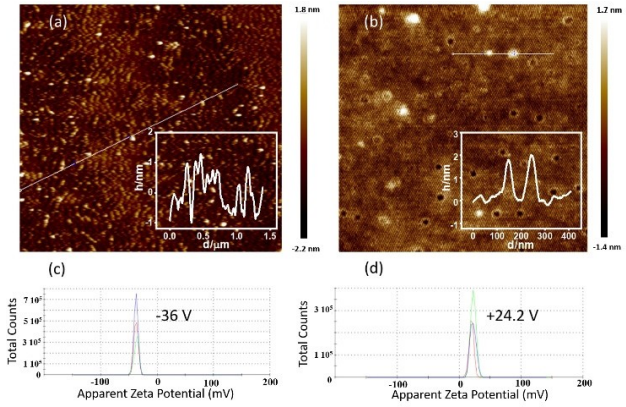

Figure 3. Atomic force microscopy images of (a) GQDs and (b) FGQDs. Insets show image intensities along the indicated lines. Panels (c) and (d) show the surface charge of the GQDs before and after PEI functionalization respectively (repeated three times).

ized GQDs (FGQDs) with mRNA. The mRNA molecules bind to the particles as a result of simple charge interactions. Finally, the novel FGQDs were used to deliver intact and functional mRNA to Huh-7 hepatocarcinoma (liver) cells. This cell line is used as a model for the liver because most nanomedicine particles are cleared by the liver, resulting in higher levels of transfection in this organ.

2. Results and Discussion

GQDs were prepared from citric acid, as shown in Figure 1. After pyrolysis and carbonization, the carbon atoms grow to form interlinked hexagonal carbon rings (at the red ring site), and thus creating graphene. After that, PEI was used to functionalize the surface of the GQDs following a reaction with graphene carboxyl groups. The high concentration of positively charged amino groups on PEI imparts a surface zeta potential that permits mRNA complexation.

FTIR was used to characterize the GQDs and PEI-GQDs. After pyrolysis, only peaks at 620, 1646, 2103 cm^{-1} are observed on the FTIR spectrum of GQDs, corresponding to C–O–C, C=O and C=C=O groups, as shown in Figure 2(a), indicating the successful preparation of GQDs. Additionally, the GQDs spectra do not reveal any absorption caused by C–H bonds, suggesting the complete carbonization of citric acid. After PEI functionalization, typical peaks of C–N and N–H are observed in the FTIR spectrum of FGQDs at 1550 and 1396 cm^{-1}, see Figure 2(b). Compared with the absorption peak of PEI, the position of C–N and N–H absorption peaks tend to shift to lower wavenumber. Such a blue shift phenomenon suggests a decrease in the polarity of these two bonds and can be attributed to the formation of the C–N bond between GQDs and PEI.

As shown in Figure 3(a), the average size of GQDs is 2–5 nm with a thickness less than 1 nm, indicating the GQDs were composed of 1–3 layers of graphene sheets. After functionalization with PEI, FGQDs grows to tens of nanometers. While FGQDs consist of 1–6 layers of graphene sheets with a thickness of 0.33–2 nm. Such results keep consistent with the TEM images of GQDs, see Figure S1. The surface zeta potential of GQDs is

−36 V due to the oxygen-containing functional groups, including hydroxyl and carboxyl groups. Following PEI functionalization, the surface zeta potential of FGQDs increases to +24.2 V. This increase is a result of the positively charged amino groups on PEI. Notably, the surface zeta potential of prepared FGQDs exhibits pH stability, as shown in Figure S2. The surface zeta potential of FGQDs stays at around +22 V over a pH range of 4–14. This positively charged surface enables the GQDs to combine with mRNA. Additionally, UV absorption and fluorescence properties of GQDs and FGQDs were investigated in Figure S3. Both GQDs and FGQDs are able to absorb UV light at 360 nm and emit blue fluorescence.

The FGQDs have a positively charged surface, so an electrostatically driven interaction would be expected between FGQDs, and negatively charged EEGFP mRNA. FGQDs to mRNA ratios were expressed as molar ratios of N in FGQDs to molar ratios of P in mRNA (N/P ratio). As shown in Figure 4, agarose gel electrophoresis confirmed the formation of a complex between FGQDs and mRNA at various N/P ratios (i.e. at N/P 2, 4, 6, 8, 10, 20, 40 60, 100). At all N/P ratios, mRNA completely complexed with FGQDs, and remained close to the loading position. The particle size of the FGQDs/mRNA complexes formed at various N/P ratios demonstrate that higher N/P ratios lead to smaller particle sizes as a result of reduced amounts of positively charged FGQDs being available at lower N/P ratios (Figure 5(a)). All the FGQDs/mRNA complexes have particle sizes below 300 nm.

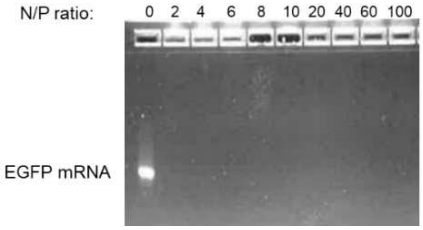

Figure 4. eGFP mRNA gel electrophoresis is retarded following complexation with FGQDs at various charge (N/P) ratios (0–100).

2.1. Delivery of Functional mRNA to Cell Cultures

mRNA-based therapeutics offer new possibilities for treating disease, so a variety of different biomaterial-based systems have been developed for mRNA delivery, such as lipid nanoparticles,[10] polymeric nanoparticles,[11] and gold nanoparticles.[12] However, it is still necessary to find novel biomaterial delivery systems that can stably, safely and effectively deliver mRNA to specific sites with high selectivity and efficient protein expression. Here, FGQDs were employed to deliver mRNA, and the transfection efficiency was evaluated both qualitatively and, quantitatively by calculating the % EGFP positive cells in the images obtained using high-throughput microscopy.

Our investigation of FGQDs/mRNA complexes began with experiments to determine the optimum ratio between FGQDs and the mRNA cargo. We created particles using various ratios, and DLS measurements indicated that particle size increased following mRNA addition and, that as expected, particle size decreased if mRNA condensation was then encouraged by adding more FGQDs and thus more charge (Figure 5(a)). Note that unbound mRNA (N/P 0) assumes a spherical form in aqueous buffers. The functional cellular experiments were performed at relatively low doses and exposures were short because of the acidic nature of this first round of formulations. Decreased eGFP production at higher doses of the FGQDs/mRNA complexes (Figure 5(b)) is the result of media acidity, rather than FGQDs toxicity. A clear relationship was seen where an increasing proportion of FGQDs was less effective (Figure 5(c)). Encouraged by this, and the fact that protein production was seen at very low doses, we continued with a second round of functional experiments with an improved formulation that was much less acidic.

Both the reference lipid nanoparticle (Figure 6(a) and (c)) and the FGQDs ((b) and (d)) could deliver functional EGFP mRNA to Huh-7 cells. Qualitatively, differences are apparent. Wells treated with FGQDs tended to have fewer cells expressing EGFP, but positive cells did produce a lot of protein. This is in contrast to the more uniform expression obtained following

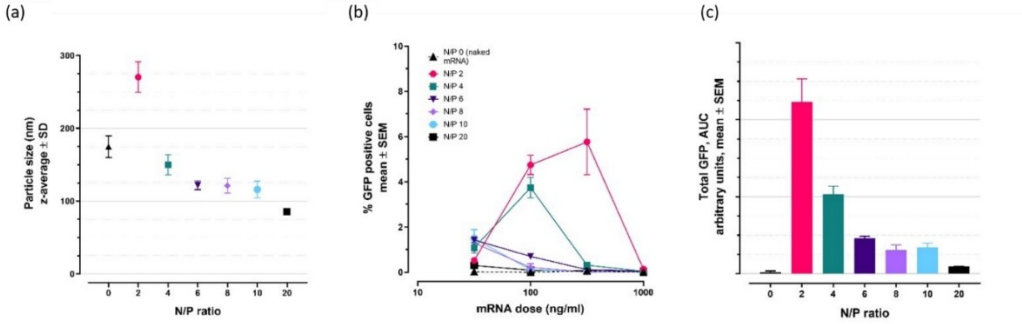

Figure 5. Particle size and function at various FGQDs to mRNA ratios. (a) As the proportion of FGQDs increases in relation to the number of mRNA molecules in a solution, increased mRNA condensation results in smaller particle sizes. (b) A 2 h pulse of particles was created by removing dosed particles after 2 h and adding fresh growth medium. Imaging and quantification occurred at 24 h. Low doses of FGQDs/mRNA complexes resulted in particle uptake and dose-dependent eGFP expression. (c) The amount of eGFP protein produced, shown as the total area under the curve for all particle doses together, was inversely proportional to the N/P ratio, with lower ratios resulting in more protein production. n = 3 for all data points. 24 h continuous dosing produced similar data (not shown) but with lower protein expression due to cellular toxicity (see discussion).

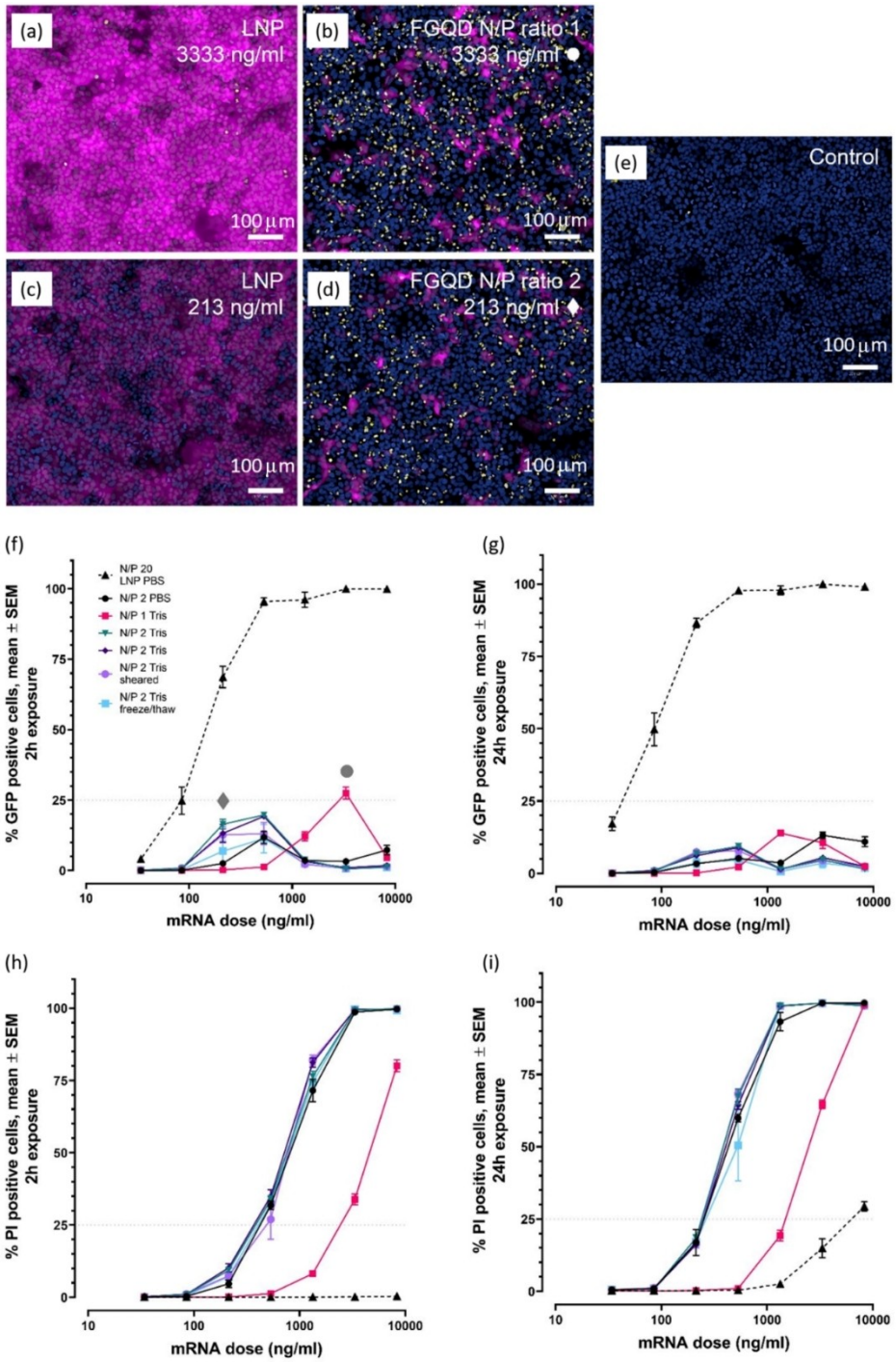

Figure 6. Functional cellular data obtained following transfection. Shown are representative images, of Huh-7 cells exposed to LNPs (a and c) FGQDs (b and d) and control cells dosed with buffer (e), taken 24 h following the start of a 2 h pulsed exposure to either LNPs or FGQDs complexed with mRNA encoding for eEGFP (the entire 2 h data set is shown in f and h below). FGQDs images are taken from wells that produced the most EGFP: an N/P ratio of 1 at 3333 ng/mL mRNA (b) and an N/P ratio of 2 at 213 ng/mL mRNA (d). The corresponding points on the curves in panel f are noted with circle ● and diamond ♦ symbols. Images from wells receiving LNPs at the same doses and time points are shown in a and c. EGFP protein production is shown in magenta, propidium iodide staining in yellow and nuclear staining with Hoechst 33342 is shown in blue; scale bars show 100 µm. Qualitatively similar images were obtained following 24 h of continuous exposure but with more PI signal (intensity and % positive cells). Quantitative image analysis data is shown in panels f and g for eEGFP (protein production) and h and i for PI staining (cell viability). The left panels (f and h) show data obtained at 24 h following a 2 h pulsed dose, while the right panels (g and i) show data obtained following continuous 24 h exposure. Curves show responses to FGQDs or reference LNPs complexed with mRNA at different charge ratios (N/P ratios). Data is shown as mean ± SEM from 6 wells for each point (combined data from 3 replicates in two separate experiments for all data points).

LNP transfection. Likewise, FGQDs-treated wells did have more propidium iodide staining than the reference lipid-based particles, indicating greater disruption of the plasma membrane, a likely side-effect of the PEI functionalization, rather than the graphene itself.

GQDs are reported to be biocompatible and have great promise for drug delivery,[13] however, the size, functionalization of GQDs can influence their cytotoxicity in different ways.[14] To facilitate cellular uptake, nanoparticles are often designed to be catatonically charged, which can enhance the interaction of the particles with the anionic cell membrane, however, this results in cytotoxic effects as well.[15] The optimal doses and formulations, if one considers the ratio between EGFP production and cellular toxicity, occur at relatively low doses for FGQDs: 213 ng/mL mRNA is optimal for an N/P ratio of 2, using either PBS or Tris as a buffer system, and a 2 h pulsed dose (Figure 6(f) and (h)). Longer, 24 h exposures increase cellular toxicity, resulting in lower protein expression (Figure 6(g) and (i)). The cell health data in Figure S4 shows similar results. Interestingly, an N/P ratio of 1 between the FGQDs and the mRNA cargo resulted in less potent, but also less toxic particles, and in this case, the optimal dose was more than a magnitude higher.

The FGQDs tested here were both less effective and more toxic than the reference LNP-based mRNA delivery system, but this was not unexpected as these are the first generation of functionalized graphene-based delivery systems we have developed, while the LNPs represent a more mature technology. Furthermore, because the toxicity is primarily a result of functionalization[16] and the resulting particle charge, alternative functionalization strategies have the potential to produce less toxic particles. Hybrid particles, consisting of GQDs in complex with lipids, are an interesting possibility. GQDs do, however, have other desirable properties as well including a large surface area and the ability to respond to external stimuli such as ultrasound, magnetic fields and light. Since LNPs are sensitive to shearing force during formulation (AstraZeneca unpublished data), a shear tolerance test was performed on the FGQDs/mRNA complex formed at N/P 2. The sample was pressed through a thin needle (27G) 20 times. The performance of the FGQDs/mRNA complex was not very sensitive to this treatment and retained substantial activity, Figure 6(f–i). Finally, we found that one freeze-thaw cycle did have an effect on the potency of the complexes but did not reduce cellular toxicity.

3. Conclusion

In this work, we prepared a novel mRNA delivery platform based on GQDs. Covalent functionalization of the GQDs surface with PEI was used to achieve positively charged GQDs (termed functionalized GQDs or FGQDs). Our results show that FGQDs were able to successfully complex mRNA and deliver it intact to the cytoplasm of Huh-7 hepatocarcinoma cells. Furthermore, unlike LNP, the FGQDs/mRNA complex is not very sensitive to shearing force. The transfection efficiency for FGQDs/mRNA complexes was as high as 25% with a formulation concentration of 4000 ng mRNA/mL, but comparable transfection efficiencies could be achieved at much lower doses if the ratio between the carrier and the cargo was optimized. This work describes the first steps towards a potentially interesting preparation method for stable and effective mRNA delivery systems based on GQDs.

Experimental Section

Materials

50 wt% polyethylenimine (PEI, Mw 60,000 by GPC) solution and citric acid were purchased from Sigma-Aldrich Co. Ltd, Sweden. EEGFP mRNA (5moU) was purchased from Trilink BioTechnologies, Inc., USA. The huh-7 hepatocarcinoma cell line was obtained from AstraZeneca AB, Sweden and originally sourced from ATCC. pH test paper was purchased from Fisher Scientific Co. Ltd, Sweden. The chemicals were analytically pure and used as received.

Preparation of GQDs

GQDs were prepared using a typical bottom-up method. Briefly, 1 g citric acid was dissolved in 80 mL distilled water while stirring for 30 min at room temperature. Then, the prepared transparent solution was transferred in a 150 mL Teflon-lined stainless-steel autoclave. After that, the autoclave was put into a muffle furnace at 200 °C for 6 h. The resulting orange liquid was used to prepare GQDs by adding it drop by drop into 100 mL of 10 mg /mL NaOH solution, under vigorous stirring. After adjusting the pH to 7.0, an aqueous solution of GQDs was obtained. This solution was filtered and dialyzed (3.5 kDa cut-off) for 7 days under running water. After concentrating the solution using centrifugation (8000 r/min), an orange solution of GQDs (4 mg/mL) was obtained. The production yield was calculated to be about 56%.

Preparation of Functionalized GQDs (FGQDs)

PEI was used to modify the surface zeta potential of pre-prepared GQDs. GQDs were aminated by adding ethylenediamine (EDA) and dicyclohexycarbodiimide (DCC) in 100 mL GQDs solution stirred for 1 h at 80 °C. After that, 10 wt% PEI solution was added into the aminated GQDs solution with stirring for 8 h. The resulting solution was further purified using 3.5 K MWCO dialysis tubing for 7 days under running water, resulting in a final concentration of 2.8 mg/mL FGQDs. FGQDs fluoresce somewhat with emission in the green part of the spectrum (around 520 nm), This could be mitigated by using moderate concentrations as the fluorescence at the concentrations used here is not intense when compared with eEGFP.

Formation of FGQDs/mRNA Complex

FGQDs to mRNA ratios were expressed as molar ratios of N in FGQDs to molar ratios of P in mRNA (N/P ratio). FGQDs/mRNA complex was formed by mixing varied volumes of FGQDs and mRNA solution to achieve the desired N/P ratio in water or adjusted to pH 7.5 using 1 M Tris pH 8 and incubated for 1 h at RT before analysis. The obtained FGQDs/mRNA complexes were examined by agarose gel electrophoresis (1% Agarose E-GelEX, Invitrogen). The particle sizes were measured using a Zetasizer APS (Malvern Instrument).

Cell Transfer Efficiency and Cytotoxicity Test

Huh-7 hepatocarcinoma cells were cultured in DMEM supplemented with 10% fetal bovine serum, 5% L-glutamine, 5% sodium pyruvate and incubated at 37 °C in 5% CO_2. Cells were seeded into 384 well Perkin Elmer Cell Carrier imaging plates two days prior to test. FGQDs/mRNA source plates were created using acoustic dispensing (Echo 655) followed by robotic transfer (Agilent Bravo) to the Huh-7 cultures. LNPs and FGQDs were incubated together with the growth medium normally used to maintain the cells, and the cells were incubated with FGQDs/mRNA in 2 different ways: 24 h continuous incubation or, using a 2 h pulse incubation followed by removal of the FGQDs/mRNA and an additional 22 h incubation in fresh growth medium. MC3-based lipid nanoparticles (LNP) were added and used as a control. Hoechst 33342 and propidium iodide were added directly to living cells 24 h to stain nuclei and cells with compromised membranes respectively. Confocal images were acquired using a 20×objective (Olympus, NA 0.95) at two points in every well (Yokogawa CV7000). Wells were dosed in triplicate and the experiment was run twice.

Particles Characterisation

Fourier-transform infrared (FTIR) and Raman spectroscopy were used to characterize the chemical structure of GQDs and FGQDs. The value of zeta potentials was measured using a Malvern zetasizer (Malvern Panalytical, England). Atomic force microscopy (AFM) was used to analyse the morphology of GQDs and FGQDs in tapping mode on a Nanoscope IIIa (Digital Instruments) with NSC15 tips (silicon cantilever, MikroMasch). High resolution transmission electron microscopy (HRTEM) observations were made on a Tecnai G2 F20S-TWIN 200KV electron microscope. UV-Vis absorption was characterized using a UV/Vis/NIR spectrophotometer (Agilent Cary 60). All FL spectra were obtained by an FL spectrophotometer (Cary Eclipse, Varian). pH values were obtained using pH test paper.

Data Analysis

The eEGFP mRNA transgene expression was investigated using confocal imaging after 24 h of incubation with FGQDs/mRNA. For transfection of mRNA and cytotoxicity test, 8 doses were used per formulation (as shown in Table S1), 3 replicates were performed per dose and two fields of view were acquired in each well. Columbus (ver2.9; Perkin Elmer) was used for automated analysis of the images. 15000 cells/concentration were typically analysed, and initial analysis extracted 16 parameters/cell. Cells were classified as EGFP-positive, PI-positive (dead), and/or PI-negative (living). Additional measurements related to cell health were also generated (cell counts, nuclear intensities and nuclear morphological measures).

Acknowledgements

The authors acknowledge financial support from the Swedish Board for Innovation (Vinnova) under the Siografen program, from the Swedish National Science Foundation with the contract No: 621-2007-4660, from the Swedish Board for Strategic Research (SSF) with the contract No: SE13-0061, from Formas with the contract No: FR-2017/0009 and from STINT for the double degree PhD collaboration program with the contract No: DD2016-6502 as well as from the Production Area of Advance at Chalmers University of Technology, Sweden. J.L. also acknowledges the financial support from the National Natural Science Foundation of China (No: 51872182). H.L thanks for the financial support from Shanghai International Collaboration research project (No: 19520713900) and State Key Laboratory of Molecular Engineering of Polymers at Fudan University.

Conflict of Interest

The authors declare no conflict of interest.

Keywords: drug delivery · functionalization · graphene quantum dots · hepatocarcinoma · mRNA

[1] a) Z. Gu, S. Zhu, L. Yan, F. Zhao, Y. Zhao, *Adv. Mater.* **2019**, 31, 1800662; b) V. C. Sanchez, A. Jachak, R. H. Hurt, A. B. Kane, *Chem. Res. Toxicol.* **2011**, *25*, 15–34.
[2] E. Peng, E. S. G. Choo, P. Chandrasekharan, C. T. Yang, J. Ding, K. H. Chuang, J. M. Xue, *Small* **2012**, *8*, 3620–3630.
[3] C. Dai, S. Zhang, Z. Liu, R. Wu, Y. Chen, *ACS Nano* **2017**, *11*, 9467–9480.
[4] K. Yang, L. Hu, X. Ma, S. Ye, L. Cheng, X. Shi, C. Li, Y. Li, Z. Liu, *Adv. Mater.* **2012**, *24*, 1868–1872.
[5] Y. W. Chen, P. J. Chen, S. H. Hu, I. W. Chen, S. Y. Chen, *Adv. Funct. Mater.* **2014**, *24*, 451–459.
[6] H. W. Liu, W. C. Huang, C. S. Chiang, S. H. Hu, C. H. Liao, Y. Y. Chen, S. Y. Chen, *Adv. Funct. Mater.* **2014**, *24*, 3715–3724.
[7] K. Yang, S. Zhang, G. Zhang, X. Sun, S.-T. Lee, Z. Liu, *Nano Lett.* **2010**, *10*, 3318–3323.
[8] a) B. Li, X. Zhang, Y. Dong, *Wires. Nanomed. Nanobi.* **2019**, *11*, e1530; b) G. M. Chalbatani, H. Dana, E. Gharagouzloo, S. Grijalvo, R. Eritja, C. D. Logsdon, F. Memari, S. R. Miri, M. R. Rad, V. Marmari, *Int. J. Nanomed.* **2019**, *14*, 3111.
[9] L. Wang, J. Shi, H. Zhang, H. Li, Y. Gao, Z. Wang, H. Wang, L. Li, C. Zhang, C. Chen, *Biomaterials* **2013**, *34*, 262–274.
[10] a) F. T. Zohra, Y. Maitani, T. Akaike, *Biol. Pharm. Bull.* **2012**, *35*, 111–115; b) Y. Bao, Y. Jin, P. Chivukula, J. Zhang, Y. Liu, J. Liu, J.-P. Clamme, R. I. Mahato, D. Ng, W. Ying, Y. Wang, L. Yu, *Pharm. Res.* **2013**, *30*, 342–351.
[11] a) J. U. Menon, P. Ravikumar, A. Pise, D. Gyawali, C. C. W. Hsia, K. T. Nguyen, *Acta Biomater.* **2014**, *10*, 2643–2652; b) Z. Su, T. Erdene-Ochir, T. Ganbold, H. Baigude, *Int. J. Biol. Macromol.* **2019**, *143*, 118-125..
[12] S. Kumar, A. Diwan, P. Singh, S. Gulati, D. Choudhary, A. Mongia, S. Shukla, A. Gupta, *RSC Adv.* **2019**, *9*, 23894–23907.
[13] F. Chen, W. Gao, X. Qiu, H. Zhang, L. Liu, P. Liao, W. Fu, Y. Luo, *Front. Lab. Med.* **2017**, *1*, 192–199.
[14] M. Nurunnabi, Z. Khatun, K. M. Huh, S. Y. Park, D. Y. Lee, K. J. Cho, Y. K. Lee, *ACS Nano* **2013**, *7*, 6858–6867.
[15] D. Fischer, Y. Li, B. Ahlemeyer, J. Krieglstein, T. Kissel, *Biomaterials* **2003**, *24*, 1121–1131.
[16] Y. Liu, X. Zhao, C. Wang, L. Zhang, M. Li, Y. Pan, Y. Fu, J. Liu, H. Lu, *J. Mater. Chem. A* **2018**, *6*, 18267–18275.

Manuscript received: January 21, 2021
Revised manuscript received: January 28, 2021

FULL PAPERS

Message delivered! A novel graphene quantum dots based mRNA drug delivery platform was prepared. The results show that these modified GQDs can deliver intact and functional mRNA to Huh-7 hepatocarcinoma cells at low doses. The transfection efficiency for FGQDs/mRNA complexes was 25% with a formulation concentration of 4000 ng mRNA/mL, but comparable transfection efficiencies could be achieved at much lower doses if the ratio between carrier and cargo was optimized. This work describes the first steps towards a potentially interesting preparation method for stable and effective mRNA delivery systems.

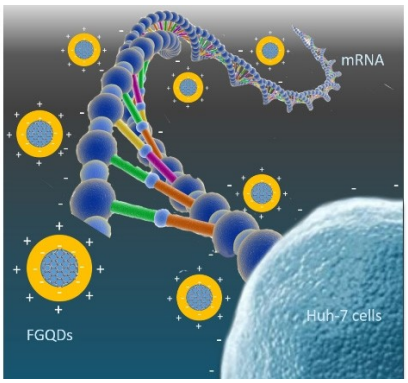

Thermally Conductive and Electrically Insulating PVP/Boron Nitride Composite Films for Heat Spreader

Ya Liu*,‡, Nan Wang†, Lilei Ye†, Abdelhafid Zehri*, Andreas Nylander*, Amos Nkansah†, Hongbin Lu‡, Johan Liu*, §
*Electronics Materials and Systems Laboratory (EMSL), Department of Microtechnology and Nanoscience (MC2), Chalmers University of Technology, Kemivägen 9, SE 412 96 Göteborg, Sweden
†Smart High Technology AB, Kemivägen 6, SE 412 58 Gothenburg, Sweden
‡ State Key Laboratory of Molecular Engineering of Polymers, Department of Macromolecular Science, Collaborative Innovation Center of Polymers and Polymer Composites, Fudan University, 2005 Songhu Road, Shanghai 200433, China
Email: hongbinlu@fudan.edu.cn
§ SMIT Center, School of Mechanical Engineering and Automation, Shanghai University, No 20, Chengzhong Road, Shanghai, Box 808, 201800, China
Email: johan.liu@chalmers.se

Abstract—Thermally conductive materials with electrically insulating properties have been extensively investigated for thermal management of electronic devices. The combined properties of high thermal conductivity, structural stability, corrosion resistance and electric resistivity make hexagonal boron nitride (h-BN) a promising candidate for this purpose. Theoretical studies have revealed that h-BN has a high in-plane thermal conductivity up to 400 - 800 W m^{-1} K^{-1} at room temperature. However, it is still a big challenge to achieve high thermally conductive h-BN thick films that are commercially feasible due to its poor mechanical properties. On the other hand, many polymers exhibit advantages for flexibility. Thus, combining the merits of polymer and the high thermal conductivity of h-BN particles is considered as a promising solution for this issue. In this work, orientated PVP/h-BN films were prepared by electrospinning and a subsequent mechanical pressing process. With the optimized h-BN loading, a PVP/h-BN composite film with up to 22 W m^{-1} K^{-1} and 0.485 W m^{-1} K^{-1} for in-plane and through-plane thermal conductivity can be achieved, respectively. We believe this work can help accelerate the development of h-BN for thermal management applications.

Keywords—thermal management, electrical resistvity, PVP/BN composite film; orientation, die attach

I. INTRODUCTION

With rapid increase in power density in electronics, efficient heat removal has become an emerging demand for electronic devices because the higher a microprocessor's cooling rate, the faster it can operate and therefore providing better performance. Electrically non-conductive materials have attracted great interest for thermal management in electronics as they won't disturb the function of main circuits[1]–[3]. For instance, polymers show an excellent electrical insulation properties and flexibility used in several industry applications. However, the super low intrinsic thermal conductivity of plastic materials significantly limit its application as thermal management solutions. Thus, adding high thermal conductivity fillers, such as Al_2O_3 and boron nitride into a polymer matrix to make composite materials is widely considered as an effective solution [4], [5]. Accordingly, a compromise between mechanical properties of the mixture and its thermal properties has to be well defined in order to obtain optimal performance via the introduction of fillers and combine its flexibility and electrical insulation performance of pristine polymers.

Previous research have focused on increasing the thermal conductivity of polymer-based materials, including formation of 3D interconnected structures, orientation, self-assembly and preferential localization[6], [7]. Up until now, it is still challenging to achieve materials with simultaneous adequate electrical resistivity and high thermal transfer performance. It is widely believed that one solution to this issue is building interconnected thermal conduction paths with thermally conductive fillers through orientated polymer chains [7]. Therefore, it is expected that using polymer fibers with highly aligned fillers would make it possible to obtain high thermal conductivity polymer composites.

In this work, we used hexagonal boron nitride sheets (h-BN) with its high in-plane thermal conductivity of 400-800 W m^{-1} K^{-1} and wide band gap, about 5.9 eV[7], as a filler to prepare a Polyvinylpyrrolidone (PVP)/h-BN composite film. Electrospinning under a high electric field was applied to achieve orientated PVP/h-BN composite fibers. Further mechanical compression and UV curing were used to help achieve a uniform film with mechanical stability. Inside this fiber, h-BN sheets are oriented and interconnected along the in-plane direction of the PVP. We have also demonstrated the fabrication using the electrospinning process that shows the advantage of simplicity for large-scale industrial manufacturing.

978-91-519-2090-0/$31.00 ©2019 CFP19M25-ART

II. EXPERIENTAL SECTION

A. Preparation of PVP/h-BN composite film

PVP/h-BN composite films with a varied loading were fabricated using an electrospinning process, as shown in Fig. 1.

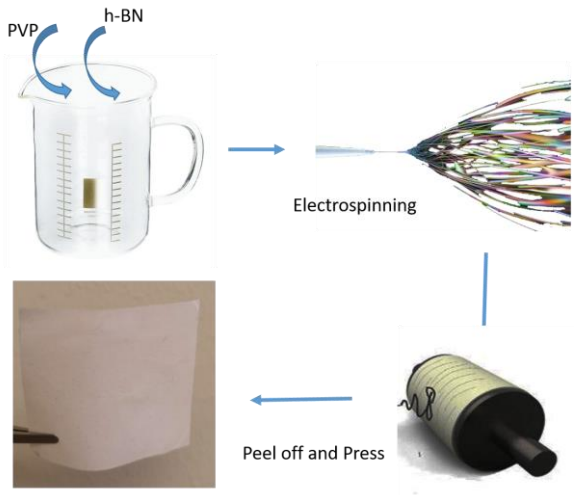

Fig. 1. Schematic of preparation of PVP/h-BN composite film.

Briefly, the precursor solution for electrospinning was prepared by dissolving PVP and the specific amount of h-BNs in ethanol. During the electrospinning process, the work distance between the spinneret and collector was 15 cm and the voltage was set at 13 kV. The solution flow was adjusted to 0.3 mL per hour by a syringe pump. The fibers were spun at room temperature; at an ambient humidity was 10% relative humidity. After spun, the PVP/h-BNs nanofiber membrane was peeled off from aluminum foil. Then, the obtained freestanding PVP/h-BN fiber sheet was pressed under 15 Mpa for 10 mins at room temperature. For comparison purposes, a pure PVP fiber reference film was also prepared by electrospinning.

B. Characterization

Scanning electron microscope (SEM) and X-ray scattering (WAXS) were used for characterization of the morphological structures of the PVP and PVP/h-BN fiber film. SEM observation was conducted using a Zeiss Supra 60 VP microscope for assessment of the alignment of the electrospunned fiber. In order to observe the h-BN alignment in the PVP/h-BN fiber, the samples were sintered in a furnace at 600 °C for 3 h. Wide angle X-ray scattering (WAXS, SAXSLAB Mat:Nordic) was used to analyze the orientation of PVP chains with the following equation.

$$II=(180°-H°)/180° \qquad (1)$$

Where II is the orientation degree and H is the full width half maximum of the strongest peak at equatorial direction of WAXS images.

Specific heat (Cp, J Kg^{-1} K^{-1}) analysis was carried out using a transient plane source apparatus (TPS 2500s, Hot disk Sweden). The In-plane thermal diffusivity (D, mm^2 s^{-1}) was measured by the laser flash method (LFA-467, NETZSCH, Germany) using an in-plane measurement sample holder accessory. In a laser flash method, an energy pulse heats one side of a plane-parallel sample and the resulting time dependent temperature rise on the backside due to the energy input is detected. The higher the thermal diffusivity of the sample, the faster the energy reaches the backside. In a one-dimensional, adiabatic case, the thermal diffusivity D is calculated from this temperature rise as follows:

$$D = 0.1388*d^2/t_{1/2} \qquad (2)$$

Where, d is the thickness of the sample (mm); $t_{1/2}$ is the time to the half maximum (s).

The density (ρ, g cm^{-1}) was calculation by weight-divided volume. Thermal conductivity k (W m^{-1} K^{-1}) was calculated as

$$k = \rho \times Cp \times D \qquad (3)$$

Fig. 2 Steady state heat-flow setup for through-plane thermal conductivity measurement.

Through-plane thermal conductivity of PVP, PVP/h-BN film was measured by a steady state heat-flow method (ASTM standard D5470), as shown in Fig.2. In the steady-state measurement, the thermal conductivity and interfacial thermal conductance are determined by measuring the temperature difference at a separation (distance)under the steady-state heat flow through the sample. Three samples were measured for each h-BN loading. The total thermal resistance of samples with varied thickness was measures as R. Accordingly,

$$R= R_{c1}+R_{c2}+BLT/k \qquad (4)$$

Where R_{c1} and R_{c2} is the interface thermal resistance, respectively. BLT is the thickness of PVP/h-BN film and k is the through-plane thermal conductivity. R_{c1} and R_{c2} can be

calculated as the constant of linear fitting curves of R at different thicknesses and should be accounted for before finding the through plane conductivity of the film. The thermal conductivity at certain filler loading can be calculated from equation (4).

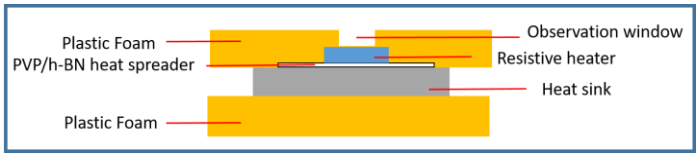

Fig. 3 Model for verifying thermal transfer performance of PVP/h-BN fiber.

Samples were cut into the size as 40 × 50 mm, were pressed in-between a heater and an aluminum heat sink to demonstrate its performance as a heat spreader, as shown in Fig.3. The heater was connected to a DC power supply with the input power kept constant at about 4 W. The surface temperature profile was captured by an infrared thermograph (FLIR-A655 SC).

III. Results and Discussion

SEM was used to observe the morphology of the PVP and PVP/h-BN fibers, as shown in Fig. 4(a) and 4(b). The PVP/h-BN composite solution was spun to PVP/h-BN fiber by electrospinning. This fiber fabrication process is able to orientate the PVP chains along the fiber direction for an increased thermal and mechanical performance. The orientation degree of PVP fiber is 95% according to the WAXS results, as shown in Fig. 4(e) and 4(f).The orientation of the PVP chains is important and will improve the thermal transfer performance of the manufactured film [8]. To investigate impact of electrospinning on the h-BN sheets alignment, a pressed sample of h-BN powder (Fig.4(c)) was compared to the prepared fiber (Fig.4(d)). After sintered at 600 ^{o}C for 3 h, we are able to obtain a pure h-BN film. The element mapping of this h-BN film show only boron and nitride, as shown in the inset of Fig.4(d), indicating the fully decomposition of PVP. Compared to the structure of the pressed h-BN film, the h-BN flakes inside this PVP/h-BN fiber forms an interconnected continuous network which adds to the thermal conductive path already formed by the PVP chains in the fiber [7].

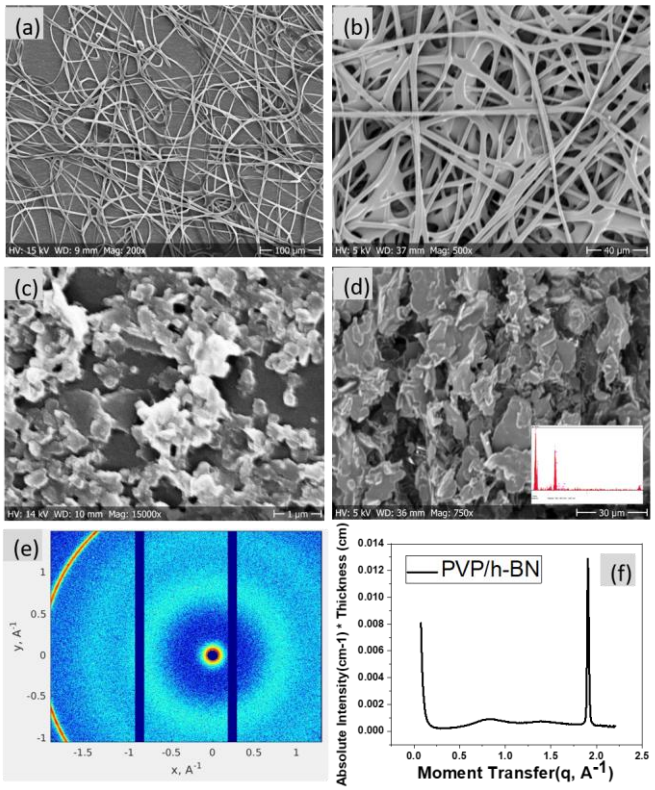

Fig.4 The morphology of PVP/h-BN fiber with (a) low and (b) high resolutions. (c) The morphology of h-BN composite film by mechanical pressing h-BN powder and h-BN fiber film (sintering PVP/h-BN fibers at 600 ^{o}C for 3 h). The inset is the element mapping of h-BN film. (e) WAXS images of PVP/h-BN film and (f) its corresponding intensity curve.

Four-point probe electrical measurements was employed to assess the electrical resistivity of PVP/h-BN film. However, no electrical response was observed which indicates promising electrical resistivity but may also indicate a bad contact to the surface. This property should be further investigated in future studies regarding the h-BN polymer composite film.

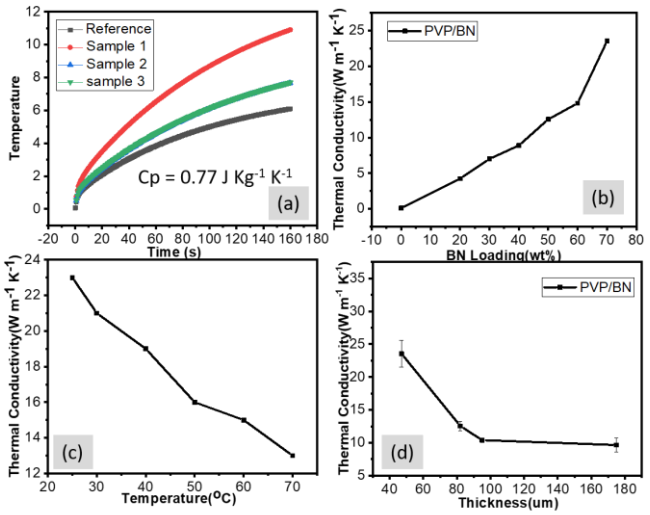

Fig. 5. (a) Cp of PVP/h-BN composite film; (b) In-plane thermal conductivity of PVP/h-BN film with different h-BN loading; (c) In-plane thermal conductivity of PVP/h-BN film at different temperature ; (d) In-plane thermal conductivity of PVP/h-BN film with different thickness.

The measured Cp of the PVP/h-BN is 0.77 J Kg^{-1} K^{-1}, as shown in Fig. 5(a). The in-plane thermal conductivity measured using the flash method of the prepared PVP/h-BN decreased with increasing film thickness. This can be explained as the thermal interface resistance is relatively high between the different h-BN sheets and due to the high aspect ratio (L/D) of the h-BN sheets this material benefit in terms of thermal conductivity by minimizing the total fiber thickness without reaching below the percolation limit[9]. Accordingly, the in-plane thermal conductivity of this PVP/h-BN film was found to reach up to 22 W m^{-1} K^{-1} at room temperature at a thickness of 40 um at 70% h-BN loading, as shown in Fig.5(b) and (d). However, further development is required due to the decrease thermal performance with increase temperature in the range 20 – 70 °C, which is shown in Fig.5(c). This temperature reliability may come from the disorientation process of PVP chains. When temperature increase, the PVP chain tends to move to a random distribution.

Through-plane thermal conductivity was measured using a custom-made steady state heat-flow setup. Similar as the in-plane thermal conductivity, through-plane thermal conductivity decreases with an increased film thickness at different h-BN loading. Unlike the in-plane thermal conductivity, the through-plane thermal conductivity of the PVP/h-BN film reaches a maximum at 60 % h-BN filler content. It was possible at this loading to achieve a through-plane thermal conductivity of 0.485 W m^{-1} K^{-1}, which is more than 5 times of an improvement compared to the PVP fiber reference sample.

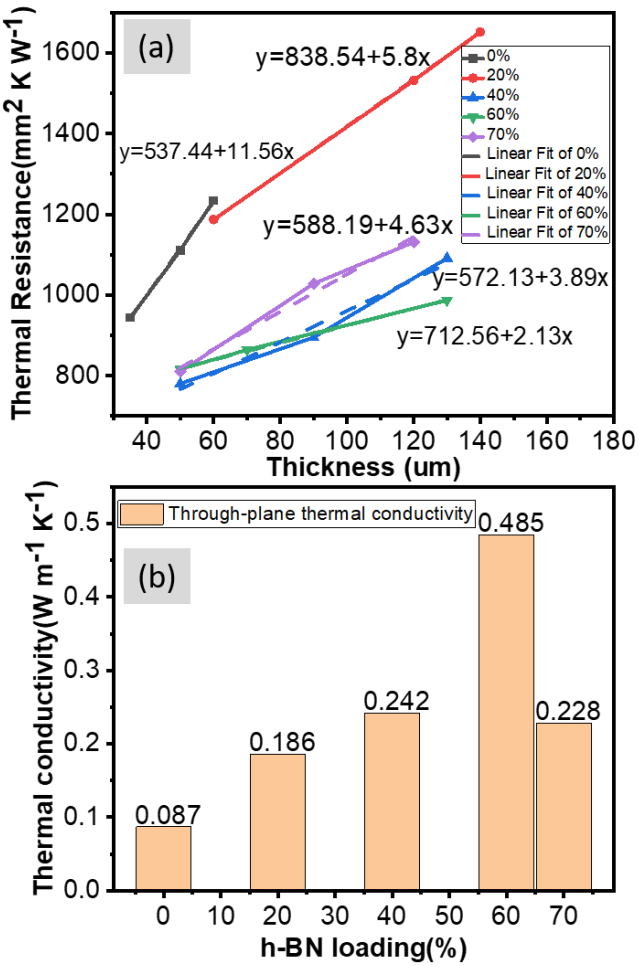

Fig. 6. (a) Thermal resistance and its linear fit curves of PVP/h-BN film with different h-BN loading; (b) Extracted through-plane thermal conductivities of PVP/h-BN films with different h-BN loading.

To verify the heat spreading performance, a setup with a resistive heater and a solid aluminum block was used as a heat sink as shown in Fig.7 (a). This setup was used with and without the PVP/h-BN film in-between to demonstrate how such a film would perform as a heat spreader in a simulated environment similar to a thermal package. Plastic foams were used on the bottom and up to minimize heat transfer from these two sides. An IR camera was used to capture surface temperature of the heater top surface through a window in the plastic foam. Consequently, the case with oriented PVP/h-BN fibers manage to successfully cool the heater with about 25 °C compared to the reference case at an input heater effect of 4 W. This demonstrates that the PVP/h-BN fiber composite could be a viable solution as a heat spreader in thermal packages, which is consistent with the result of their thermal conductivity.

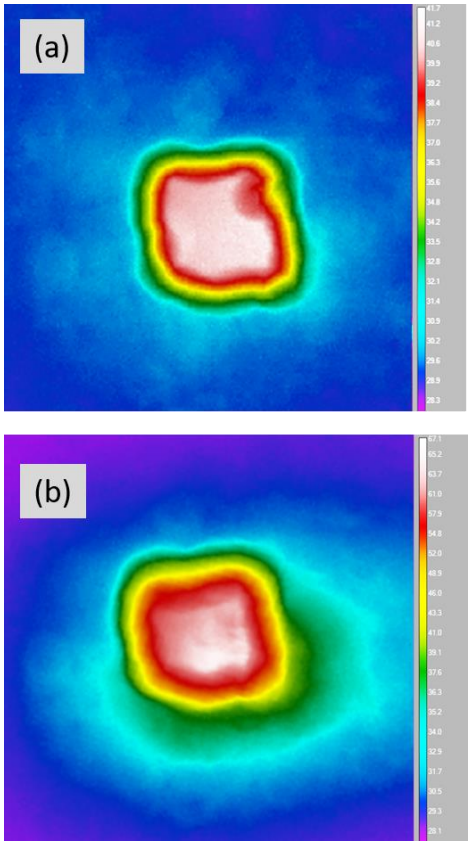

Fig. 7. (a) Infrared thermal images of observation windows; (b) Temperature distribution of heater with and without PVP/h-BN film.

IV. Conclusion

In this work, we prepared a non-conductive thermal heat spreader using a PVP/h-BN composite by electrospinning. At a h-BN loading of 70%, the prepared composite film was able to exhibit an in-plane thermal conductivity as high as 22 W $m^{-1} K^{-1}$. The best through-plane thermal conductivity was observed with a h-BN loading at 60%, this corresponded to an improvement of more than 5 times compared to pure PVP fiber film. The heat spreading performance was demonstrated for the PVP/h-BN film by deploying it-between a heater and heatsink to simulate the conditions in a thermal package. The use of the PVP/h-BN film decreased the temperature with 25 °C. Thus, this electrospinning method extends the application of polymer based composite film as a non-conductive heat spreader. However, further development is required to improve the temperature stability of this composite film in order to keep the heat spreading capabilities under conditions expected in thermal management applications.

Acknowledgment

The authors acknowledge the financial support from the Swedish Board for Strategic Research (SSF) with the contract No: SE13-0061 and GMT14-0045, from Formas with the contract No: FR-2017/0009 and from STINT for the double degree PhD collaboration program with the contract No: DD2016-6502, from the Swedish National Science Foundation with the contract No: 621-2007-4660 as well as from the Production Area of Advance at Chalmers University of Technology, Sweden. The authors also acknowledge the financial support by the Key R&D Development Program from the Ministry of Science and Technology of China with the contract No: 2017YFB0406000. The authors are grateful for the financial support by the 973 project (2011CB605702), the National Natural Science Foundation of China (51173027 and 51872182), and the Shanghai key basic research project (14JC1400600). We greatly acknowledge also the financial support from EU Horizon 2020 program “Smartherm”.

References

[1] Q. Li *et al.*, “Flexible high-temperature dielectric materials from polymer nanocomposites,” *Nature*, vol. 523, no. 7562, p. 576, 2015.
[2] A. L. Moore and L. Shi, “Emerging challenges and materials for thermal management of electronics,” *Materials today*, vol. 17, no. 4, pp. 163–174, 2014.
[3] C. Zhi, Y. Bando, T. Terao, C. Tang, H. Kuwahara, and D. Golberg, “Towards thermoconductive, electrically insulating polymeric composites with boron nitride nanotubes as fillers,” *Advanced Functional Materials*, vol. 19, no. 12, pp. 1857–1862, 2009.
[4] H. Chen *et al.*, “Thermal conductivity of polymer-based composites: Fundamentals and applications,” *Progress in Polymer Science*, vol. 59, pp. 41–85, 2016.
[5] Z. Kuang *et al.*, “Fabrication of highly oriented hexagonal boron nitride nanosheet/elastomer nanocomposites with high thermal conductivity,” *Small*, vol. 11, no. 14, pp. 1655–1659, 2015.
[6] Z. Yang *et al.*, “Thermally conductive, dielectric PCM–boron nitride nanosheet composites for efficient electronic system thermal management,” *Nanoscale*, vol. 8, no. 46, pp. 19326–19333, 2016.
[7] J. Chen, X. Huang, B. Sun, and P. Jiang, “Highly Thermally Conductive Yet Electrically Insulating Polymer/Boron Nitride Nanosheets Nanocomposite Films for Improved Thermal Management Capability,” *ACS nano*, vol. 13, no. 1, pp. 337–345, 2018.
[8] Y. Xu *et al.*, “Nanostructured polymer films with metal-like thermal conductivity,” *Nature communications*, vol. 10, no. 1, p. 1771, 2019.
[9] H. Song, J. Liu, B. Liu, J. Wu, H.-M. Cheng, and F. Kang, “Two-dimensional materials for thermal management applications,” *Joule*, vol. 2, no. 3, pp. 442–463, 2018.

Effect of Boron Nitride Particle Geometry on the Thermal Conductivity of a Boron Nitride Enhanced Polymer Composite Film

Ya Liu[1,3], Nanwang[2], Lilei Ye[2], Hongbin Lu[3], Johan Liu[1, 4]

[1] Electronics Materials and Systems Laboratory (EMSL), Department of Microtechnology and Nanoscience (MC2), Chalmers University of Technology, Göteborg, Sweden
[2] SHT Smart High Technology AB, Gothenburg, Sweden
[3] State Key Laboratory of Molecular Engineering of Polymers, Department of Macromolecular Science, Collaborative Innovation Center of Polymers and Polymer Composites, Fudan University, Shanghai, China
[4] SMIT Center, School of Mechanical Engineering and Automation, Shanghai University, Shanghai, China

* Corresponding Author: johan.liu@chalmers.se ,+46 31 772 30 67

Abstract

Hexagonal Boron Nitride (h-BN) has been considered as a promising enhancement filler for thermal management due to its high thermal conductivity, structural stability, and super electrical resistivity. Numerus studies have reported using BN as an enhancement filler to achieve high thermally conductive polymer based thermal management materials. However, there are limited data regarding the influence of the flake size of BN sheets to the thermal management property of BN filled composites. In this work, three h-BN size geometries, including microscale h-BN powder, h-BN nanosheets, and a mixture of micro and nanoscale h-BN, were studied regarding its thermal transfer performance. The results show that h-BN nanosheets are able to achieve the highest in-plane thermal conductivity with loading from 0 - 5 wt% while for the through-plane thermal conductivity, all three geometries show similar thermal property when the filler loading less than 5 wt%. Through-plane thermal conductivity exhibits a sudden increase to 5.69 W m^{-1} K^{-1} at a loading of 5 wt%..

1 Instructions

In recent years, tremendous progress has developed in the field of power devices. The increased packaging density put further larger requirement on the heat dissipation capacity of the packaging materials. One possible solution is introducing highly thermal conductivity fillers, including aluminum oxide, Hexagonal Boron Nitride (h-BN), graphene, Silicon carbide (SiC), etc, into the polymer part of the device.[1] Plenty of studies regarding using h-BN as an enhancement agent for improving thermal dissipation capacity have been reported in recent years. However, there are still few data about the influence of h-BN size/geometry on the thermal performance. Multi-modal particle size mixing of h-BN and c-BN was used to fabricate an epoxy resin composite film to achieve a mechanical strength enhancement up to 217% by K.C. Yung and H. Liem.[2] Therefore, studying the influence of particle size on the thermal performance would help in this regard.

Compared with SiC and AlN, BN, especially h-BN shows advantages of high thermal conductivity (400 - 800 w m^{-1} k^{-1}) and outstanding electrical insulation performance. Therefore, the incorporation of BN and polymers becomes an effective strategy to improve its thermal conductive coefficient with low dielectric constant. There are lots of studies regarding using BN as an enhancement filler to achieve high thermal conductive polymer-based thermal management materials, including BN filled polybenzoxazine[2], BN for epoxy resin,[3-4] polyimide composites with h-BN,[5] PTFE with BN[6] and PVA with BN[7]. Building 3D thermal conductive pathway[8], interface modification of BN nameplates[9] and orientation BN sheets,[10-12] are also believed as effective methods to further improve thermal performance of BN and polymer composites. However, there are limited data related to the influence of the flake size of BN sheets on the thermal dissipation capacity of BN filled composites. Filler particle size, aggregation, orientation, and polymer chain rigidity were taken into consideration for h-BN filled polyimide films by Shinji Ando's group.[13] However, the specified influence of BN particle size on thermal performance was not concluded by his work.

In this work, h-BN size with nanoscale and microscale were used to investigate the influence of h-BN flake size on the thermal dissipation property of BN filler composite. Briefly, the few-layer h-BN nanosheets were prepared by a mechanical exfoliation method. A polymer material of carboxymethyl cellulose (CMC) was selected as the polymer agent due to its good compatibility with h-BN. Its unique six-membered ring structure is able to combine with BN sheets to modification BN's dispensability in water. Three comparison experiments were conducted for thermal conductivity measurement respectively.

ISBN 978-1-7281-2078-2

2 Experiments

2.1 Preparation of BN and CMC composite film

Commercially available h-BN powder from Sigma-Aldrich was used as the large size of h-BN and the source of BNNS. The mixture of isopropanol (IPA) and deionized water was used as a solvent for both dispersion and exfoliation. For fabrication of CMC composite film, CMC powder with average molecular weight (M.W) of 700000 was dissolved in hot water by magnetic stirring at first. Then separately prepared suspension of BN sheets in isopropyl alcohol was added dropwise to the aqueous polymer solution at room temperature. The mixture was concentrated by evaporating water with vigorous stirring at 60 °C for 24 h. The resulting polymer blend with dispersed BN sheets was cast into a thin film with a targeted thickness of about 50 μm on a cell-culture dish, and then the free-standing film can be obtained by peeling off for subsequent characterization and measurements, as shown in Fig.1.

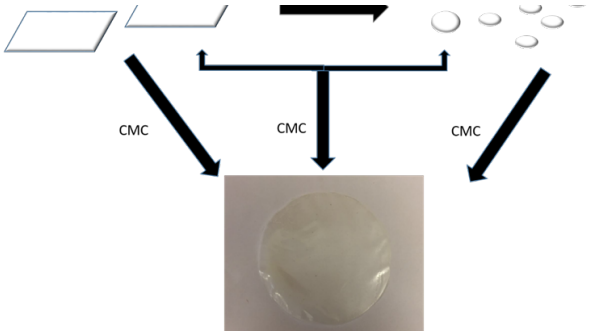

Fig. 1. Schematic of preparation of BN and CMC composite film.

2.2 Characterization

Scanning electron microscopy (SEM) was used to analyze the micromorphology of pristine BN powder under 15 KV.

Atomic force microscopy (AFM) were carried out using a Nanoscope III scanning probe microscope (Digital Instruments with Santa Barbara, CA) in tapping mode. XPS was used to investigate the chemical structure of h-BN after exfoliation. Fourier-transform infrared (FT-IR) was conducted with a PerkinElmer II instrument over the range of 4000- 400 cm^{-1}.

The In-plane and through-plane thermal diffusivity (D, mm^2 s^{-1}) was measured by a laser flash method (LFA-467, NETZSCH, Germany) using an in-plane and through-plane measurement sample holder accessory separately. In a laser flash method, an energy pulse heats one side of a plane-parallel sample and the resulting time-dependent temperature rise on the backside due to the energy input is detected. The higher the thermal diffusivity of the sample, the faster the energy reaches the backside. In a one-dimensional, adiabatic case, the thermal diffusivity D is calculated from this temperature rise as follows:

$$D = 0.1388*d^2/t^{1/2} \quad (1)$$

Where, d is the thickness of the sample (mm); $t^{1/2}$ is the time to the half maximum (s).

The density (ρ, g cm^{-1}) was calculation by weight-divided volume. Thermal conductivity k (W m^{-1} K^{-1}) was calculated as

$$k = \rho \times Cp \times D \quad (2)$$

Where, Cp is the thermal capacity of the sample (J g^{-1} k^{-1});

3 Results and Discussion

Fig. 2(a) is the XPS full survey of BNNS. Except for Boron and Nitride element, a significant oxygen peak can be observed at the position of 531 eV. XPS peak analyses were used to further understand the chemical structure of oxygen. As shown in fig.2 (b) and 2 (c), oxygen is introduced to h-BN sheets after exfoliation in IPA and water solution. Both Boron and Nitride show the combination with oxygen with specifying peaks at 198 and 405 eV, respectively. FTIR was used to analyze the chemical bonding between CMC and h-BN and h-BNNS, as shown in fig. 2(d). The characteristic peaks of BN and CMC can be observed on the FTIR images of CMC-BN and CMC-BNNS, indicating the preparation of BN-CMC and BNNS-CMC composite material Compared with CMC-BN, the peak at the position of 1598 cm-1 disappear on the FTIR data of CMC-BNNS. This peak corresponding to the –C=O group, indicating the addition reaction between BNNS and CMC.

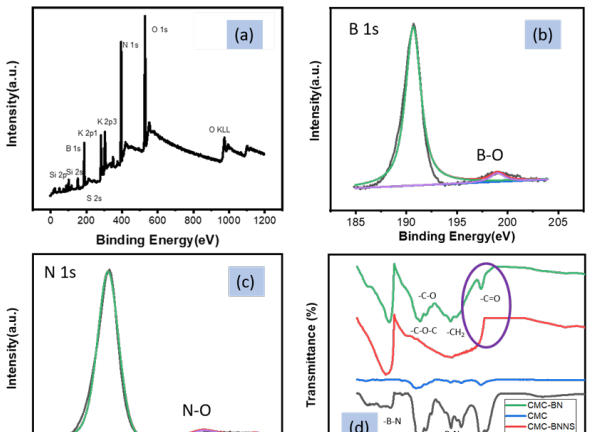

Fig. 2. (a) XPS full survey of BNNS; (b) B 1s XPS Spectra; (c) N 1s XPS spectra; (d) FTIR spectrum of pristine BN, CMC, CMC-BN, and CMC-BNNS.

ISBN 978-1-7281-2078-2

SEM and AFM were used to study the morphology of BN and BNNS. The pristine h-BN flakes show a size around 1-5 um with a layer accumulation structure, as shown in fig 3 (a) and 3 (b). Mechanical exfoliation was used to prepared BNNS. As shown in Fig. 3 (c) and (d), after mechanical exfoliation, the morphology of h-BN changed from Irregular polygon to a small round shape after strong mechanical exfoliation. The edge of pristine h-BN sheets become smooth after mechanical exfoliation. Generally, the size of pristine h-BN decreased to 10 - 100 nm with a thickness of about 2 - 20 nm, as shown in Fig. 3 (e) and 3 (f). According to the thickness of the single layer atom is around 0.33 - 1 nm[14], the prepared BNNS are piled up by few-layer to tens layers of h-BN sheets.

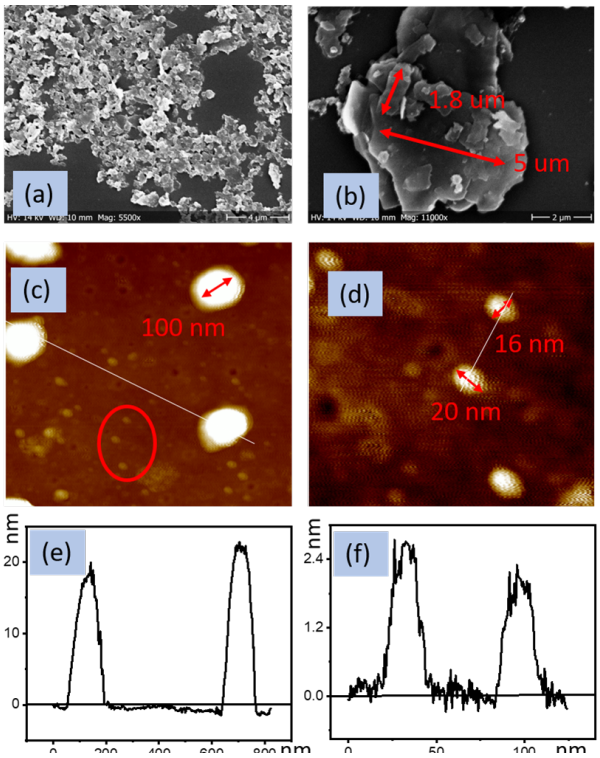

Fig. 3. (a) SEM image of pristine BN powder; (b) High-resolution SEM image of pristine BN powder; (c) AFM image of BNNS ; (d) High-resolution AFM image of BNNS; (e) and (f) Height profile of BNNS.

To investigate the influence of h-BN particle size on the thermal conductivity of its composite materials, three receipts were used to prepared h-BN filled CMC composite films. Pristine h-BN powder, h-BNNS after mechanical exfoliation, and a mixture of h-BN and h-BNNS were added into CMC solution to prepare CMC-BN, CMC-BNNS, and CMC-BN+BNNS composite film, respectively. With a loading varying from 0 to 5 wt%, the CMC-BNNS shows the highest In-plane thermal conductivity, while CMC-BN shows the lowest In-plane thermal conductivity, as shown in Fig, 4 (a). When it comes to through-plane thermal conductivity, the BNNS-CMC exhibits a sudden increase to 5.69 W m^{-1} K^{-1} at a loading of 5 wt%. While when the filler's loading less than 5 wt%, there is no big difference between the three samples, as shown in Fig. 4 (b). These results indicate that when h-BN used as thermal management filler agent, the contribution of BN flake size to the thermal transfer performance should be taken into consideration.

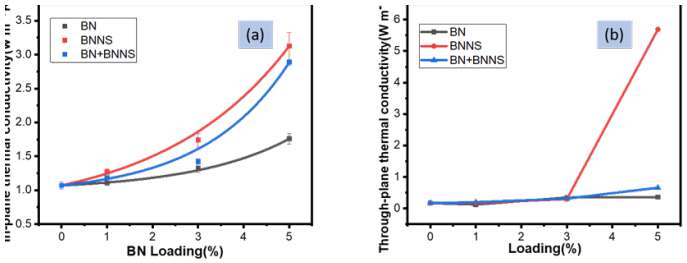

Fig.4. (a) In-plane thermal conductivity of BN, BNNS, and BN+BNNS composite film with different filler loading; (b) Through-plane thermal conductivity of BN, BNNS and BN+BNNS composite film with different filler loading.

To further investigate how the geometry of h-BN influence thermal performance of h-BN filled CMC films, SEM was used to observe the alignment of h-BN sheets in CMC. Compared with BN, the BNNS show a tendency to agglomerate to build an interconnected network inside CMC, as shown in Fig 5 (a), (b), (c) and (d). Except for the pristine higher thermal conductivity of BNNS, this interconnected network may contribute to In-plane thermal performance improvement of BNNS-CMC. Cross-section image was used to study the influence of h-BN geometry to Through-plane thermal conductivity. The BN-CMC shows a clear layer structure, while BNNS-CMC tends to form an integral structure. This may indicate BNNS seem to exhibit better compatibility with CMC than h-BN sheets due to the introducing of oxidant group in the exfoliation process. However, this cross-section image cannot give us evidence regarding why this BNNS-CMC exhibit a sudden increase of through-plane thermal conductivity. More experiments with loading more than 5 wt% should be conducted in the future to explain this phenomenon.

ISBN 978-1-7281-2078-2

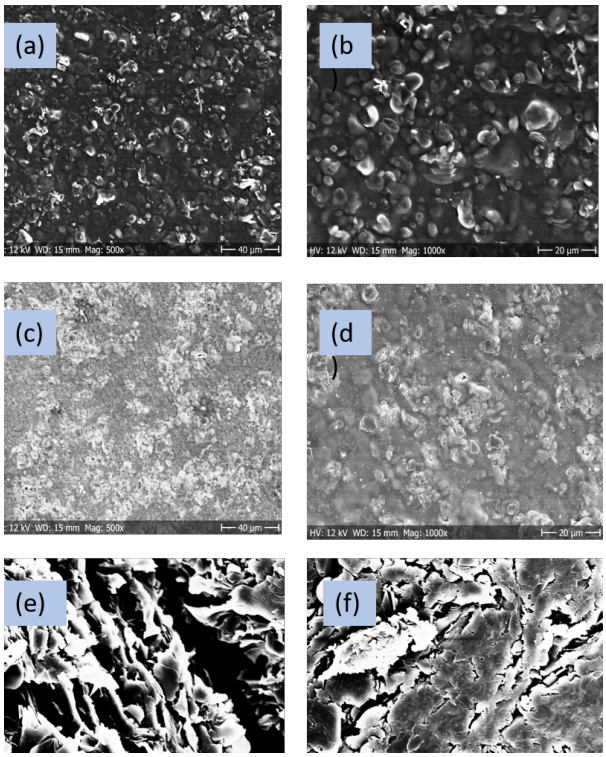

Fig.5. (a) SEM image of BN composite film with 5 wt% loading; (b) High-resolution SEM image of BN composite film with 5 wt% loading; (c) SEM image of BNNS composite film with 5 wt% loading; (d) High-resolution SEM image of BNNS composite film with 5 wt% loading; (e) Cross-section SEM image of BN composite film with 5 wt% loading; (f) Cross-section SEM image of BNNS composite film with 5 wt% loading.

4 Conclusion

In this work, three receipts with different BN size composition and loading were investigated to study the influence of h-BN filler size and geometry on the thermal conductivity of its composite films. Compared with BN and mixture of BN and BNNS, the BNNS composite film exhibits obvious advantages for In-plane thermal conductivity. While through-plane thermal conductivity depends on the additive filler's loading. When the filler's loading less than 5 wt%, three receipt shows similar through-plane thermal conductivity. The Through-plane thermal conductivity of BNNS-CMC composite film exhibits a suddenly increase when BNNS's loading up to 5 wt%. In the future, more study can be conducted on the filler loading large than 5 wt%.

Acknowledgements

The authors acknowledge the financial support from the Swedish Board for Strategic Research (SSF) with the contract No: SE13-0061 and GMT14-0045, from Formas with the contract No: FR-2017/0009 and from STINT for the double degree PhD collaboration program with the contract No: DD2016-6502, from the Swedish National Science Foundation with the contract No: 621-2007-4660 as well as from the Production Area of Advance at Chalmers University of Technology, Sweden. The authors also acknowledge the financial support by the Key R&D Development Program from the Ministry of Science and Technology of China with the contract No: 2017YFB0406000. The authors are grateful for the financial support by the 973 projects (2011CB605702), the National Natural Science Foundation of China (51173027 and 51872182), and the Shanghai key basic research project (14JC1400600). We greatly acknowledge also the financial support from the EU Horizon 2020 program "Smartherm".

Literature

[1] J. Gu, Z. Lv, Y. Wu, Y. Guo, L. Tian, H. Qiu, et al., "Dielectric thermally conductive boron nitride/polyimide composites with outstanding thermal stabilities via in-situ polymerization-electrospinning-hot press method," Composites Part A: Applied Science and Manufacturing, vol. 94, pp. 209-216, 2017.

[2] K. Yung and H. Liem, "Enhanced thermal conductivity of boron nitride epoxy-matrix composite through multi-modal particle size mixing," Journal of Applied Polymer Science, vol. 106, pp. 3587-3591, 2007.

[3] Y. X. Fu, Z. X. He, D. C. Mo, and S. S. Lu, "Thermal conductivity enhancement with different fillers for epoxy resin adhesives," Applied Thermal Engineering, vol. 66, pp. 493-498, May 2014.

[4] H. Liem and H. S. Choy, "Superior thermal conductivity of polymer nanocomposites by using graphene and boron nitride as fillers," Solid State Communications, vol. 163, pp. 41-45, Jun 2013.

[5] K. Sato, H. Horibe, T. Shirai, Y. Hotta, H. Nakano, H. Nagai, et al., "Thermally conductive composite films of hexagonal boron nitride and polyimide with affinity-enhanced interfaces," Journal of Materials Chemistry, vol. 20, pp. 2749-2752, 2010.

[6] C. Pan, J. Zhang, K. Kou, Y. Zhang, and G. Wu, "Investigation of the through-plane thermal conductivity of polymer composites with in-plane oriented hexagonal boron nitride," International Journal of Heat and Mass Transfer, vol. 120, pp. 1-8, 2018.

[7] W. L. Song, P. Wang, L. Cao, A. Anderson, M. J. Meziani, A. J. Farr, et al., "Polymer/boron nitride nanocomposite materials for superior thermal transport

performance," Angewandte Chemie International Edition, vol. 51, pp. 6498-6501, 2012.
[8] J. Chen, X. Huang, Y. Zhu, and P. Jiang, "Cellulose nanofiber supported 3D interconnected BN nanosheets for epoxy nanocomposites with ultrahigh thermal management capability," Advanced Functional Materials, vol. 27, p. 1604754, 2017.
[9] J. Yu, X. Huang, C. Wu, X. Wu, G. Wang, and P. Jiang, "Interfacial modification of boron nitride nanoplatelets for epoxy composites with improved thermal properties," Polymer, vol. 53, pp. 471-480, 2012.
[10] Z. Kuang, Y. Chen, Y. Lu, L. Liu, S. Hu, S. Wen, et al., "Fabrication of highly oriented hexagonal boron nitride nanosheet/elastomer nanocomposites with high thermal conductivity," Small, vol. 11, pp. 1655-1659, 2015.
[11] J. Chen, X. Huang, B. Sun, and P. Jiang, "Highly thermally conductive yet electrically insulating polymer/boron nitride nanosheets nanocomposite films for improved thermal management capability," ACS nano, vol. 13, pp. 337-345, 2018.
[12] Y. Liu, N. Wang, L. Ye, A. Zehri, A. Nylander, A. Nkansah, et al., "Thermally Conductive and Electrically Insulating PVP/Boron Nitride Composite Films for Heat Spreader," in 2019 IMAPS Nordic Conference on Microelectronics Packaging (NordPac), 2019, pp. 1-5.
[13] M. Tanimoto, T. Yamagata, K. Miyata, and S. Ando, "Anisotropic thermal diffusivity of hexagonal boron nitride-filled polyimide films: effects of filler particle size, aggregation, orientation, and polymer chain rigidity," ACS applied materials & interfaces, vol. 5, pp. 4374-4382, 2013.
[14] P. Nemes-Incze, Z. Osváth, K. Kamarás, and L. Biró, "Anomalies in thickness measurements of graphene and few layer graphite crystals by tapping mode atomic force microscopy," Carbon, vol. 46, pp. 1435-1442, 2008.

ISBN 978-1-7281-2078-2